Dilute Nitride Based Vertical Cavity Enhanced Photodetector

MOHAMMAD SYAHMI BIN NORDIN

A thesis submitted for the degree of Doctor of Philosophy (Ph.D.) in Applied Physics

School of Computer Science and Electronic Engineering

University of Essex

March 2018

Abstract

The research reported in this thesis is aimed at developing and demonstrating the performance of a p-i-n / vertical cavity enhanced (VCE) photodetector structure with different material compositions of dilute nitride. The tunable selectivity is taken into account during the development in order for the VCE photodetector to be able to perform as a tunable receiver. In the first part, the performance of p-i-n photodetectors with 10 and 20 quantum wells are presented. The 20 quantum well photodetector exhibits the highest ever reported quantum efficiency of 80% at -5V bias for applications at 1.0μm wavelength. However, variation in the absorption's thickness equates to a trade-off between speed, bandwidth, noise-equivalent-power, and detectivity. A GaInNAs/GaAs VCE photodetector with an internal gain of 1.55 for room temperature operation at 1.3μm wavelength is next demonstrated. This is the first internal gain ever reported using a GaInNAs VCE photodetector with a 1.7nm FWHM and an overall quantum efficiency of 67%. The proposed VCE photodetector of GaInNAs/GaNAs showed impressive multiplication at a low reverse bias of 0.5V. The internal gain is detected to be 2.45 at -2V bias with a responsivity of 1.63A/W for room temperature operation. The responsivity and gain of the sample can be enhanced by increasing small range of temperature but then suffered from temperature-induced broadening of the full width half maximum (FWHM). Finally, an avalanche VCE photodetector is proposed, where the preliminary outcome shows the current oscillation behaviour under illumination at room temperature operation. The sample produces very low responsivity of 2.15mA/W due to growth problems with the charge layer which affect the electric field in the multiplication region.

ACKNOWLEDGEMENTS

In the name of ALLAH, the Beneficent and the Merciful, Alhamdulillah, all praises to ALLAH for the strengths and His blessing in completing this thesis. I am very much thankful to my supervisor Professor Anthony J. Vickers, for his guidance, advice and encouragement throughout my PhD studies. I would like to thank to Professor Ayse Erol from Istanbul University who has helped me a lot after my former supervisor, Professor Naci Balkan passed away on June 2015. Thank you also to Dr. Ville-Markus Korpijarvi and Prof. Mircea Guina from Optoelectronic Research Centre (ORC), Technical University of Tampere for growing the samples.

My special thanks go to all current and previous members of Optoelectronic Research Group at the University of Essex; Dr. Hagir Khalil, Dr. Simone Mazzucato, Dr. Benjamin Royall, Dr. Faten, Dr. Nadir Khan, Dr Marinah Othman and Dr. Mustafa Gunes who helped me for theoretical and experimental works. Particular thanks go to Mr. Adrian Boland-Thoms for his help in cleanroom as well as extensive technical support. I am also grateful to all my colleagues and friends at University of Essex.

My wonderful wife, Nurulain Samat deserves enormous amounts of my warmest appreciation. She has been so amazing over the past years that there are no words to describe how grateful I am to her, except to say that I love her very much. To my two daughters (Anis and Areen) who have to sacrifice living separately from me for few months, I love both of you.

Finally, I am forever indebted to my wonderful parents (Nordin and Noor Jannah) for their everlasting love, support and prayers that make this dream come true. I can't thank them enough for everything that they have done. Thanks to all my siblings (Fakhrin, Akhyar and Syazwan) which without their encouragement, support and understanding it would have been impossible for me to finish my study.

Symbols used in Thesis

Fundamental Constants

c	speed of light in a vacuum	=	$3x10^{8}$ m / s
ε_0	Electric constant	=	$8.85x10^{-12}$ $m^{-3}Kg^{-1}s^{4}A^{2}$
h	Plank's constant	=	$6.63x10^{34}$ m^2 kg / s
ħ	Planks constant / 2π	=	1.055×10^{34} m^2 kg / s
k_B	Boltzmann's constant	=	1.38×10^{-23} Kg $s^{-2}K^{-1}$
q	Elementary charge	=	1.6×10^{-19} C

List of Symbols

A	Area of the sample
α	Absorption coefficient
α_e	Electron impact ionisation rate
β_h	Hole impact ionisation rate
C_{NM}	Fitting parameter in BAC model
χ	Electron affinity
E_a	Effective band gap of a quantum well
E_c	Conduction band level
E_v	Valence band level
E_F	Fermi level
E_g	Band gap
E_i	Threshold energy for ionisation
E_M	Extended state in the conduction band
E_N	Extended state in the nitrogen localised state
E_{imp}	Impact ionisation energy
G	Generated rate for the electron-hole pair
G_n	Minority electron generation rate
G_p	Minority hole generation rate
γ	Fitting parameter for effect of N concentration on localised acceptor level E_N
η	Emission efficiency
P_{nr0}	Probability non-radiative processes independent of temperature
P_r	Probability for a radiative transition
P_0	Optical beam intensity
J	Current density
J_{dark}	Dark current density
J_{sc}	Short circuit current density
J_0	Saturation current coefficient
J_{pg}	Photogenerated current density
J_{diff}	Diffusion current
k_s	Thomas-Fermi screening wave number
λ	Wavelength
λ_{de}	De-Broglie wavelength
L_w	Quantum well thickness
L_b	Barrier thickness
d	depletion width
μ_w	Carrier mobility in the well
μ_b	Carrier mobility in the barrier
μ_h	Hall mobility
m^*_e	Electron effective mass

m^*_h	Hole effective mass
m^*_{eh}	Electron-hole effective mass
m^*_{ew}	Electron effective mass at the well
m^*_{hw}	Hole effective mass at the well
n_w	Carrier density in the well
n_b	Carrier density in the barrier
n	Refractive index
b	Optical bowing parameter
ħw	Photon energy
λ	Wavelength
L_m	Mean free path
N_a	Acceptor concentration
N_d	Donor concentration
N_c	Conduction band density of states
N_v	Valence band density of states
n_i	Intrinsic carrier density
n_p	Photogenerated electron population in p-type material
n_w	Carrier density in the well
n_b	Carrier density in the barrier
P_{in}	Incident power
P_{out}	Output power
R	Responsivity
D*	Detectivity
R_{th}	Thermal escape rate from quantum well
R_t	Tunnelling rate from quantum well
R_r	Radiative recombination rate
R_T	Total recombination rate
R_{nr}	Non-radiative recombination rate
σ	Conductivity
T	Temperature
τ	Minority carrier lifetime
τ_n	Electron lifetime
τ_p	Hole lifetime
τ_{sc}	Average scattering time
V	Voltage
V_{app}	Applied voltage
V_{bi}	Built in voltage of a pn junction
V_H	Hall voltage
V_j	Total voltage across the depletion region
V_m	Maximum power point voltage
V_{NM}	$V_{MN} = C_{NM}\sqrt{y}$
ν_d	Drift velocity
W_d	Depletion width
W_n	Depletion width of the n-type side of the pn junction
W_p	Depletion width of the p-type side of the pn junction

CONTENTS

CHAPTER 1

Introduction

1.1 Thesis Outline

Chapter one starts off with an overview of the outline of the thesis. It then looks at the background of fibre optic communication system and the GaInNAs material. The incorporation of Antimony into the dilute nitride material and the usage of GaNAs have been discussed. A review of the development of the GaInNAs-based cavity enhanced photodetector, as well as the research objectives, concludes the chapter.

Chapter two focuses on the materials and devices for optical communication and the semiconductor principles, with particular emphasis on the photodetectors. This chapter also presents the theoretical calculation for dilute nitride bandgap that will be used to design the active region for the proposed device, beginning by introducing some basic concepts of the material and the quantum well, followed by discussions on theories used in the calculations, taking into account the effect of the quantum confinement with varying nitrogen composition.

Chapter three mainly covers the design and modelling of the GaInNAs(Sb)/GaNAs vertical cavity enhanced (VCE) photodetector. Discussions will include the additional inputs made during the development process of the devices. All the numerical formula used along the entire process are laid out in this chapter as well. Chapter four mainly focuses on the experimental works and includes an overview of the growth technique using the molecular beam epitaxy (MBE). The theoretical background, and justification, for the experimental work carried out, have also been included.

Chapter five covers the results of both the growth samples and other samples used. Discussions and analysis of every experiment are detailed, along with comparative studies between the devices. The proposed device's performance will then be elaborated upon from the view of vertical cavity enhanced (VCE) photodetectors.

Chapter six presents the proposed avalanche photodetector design and structure development based on the VCE photodetector design described in chapter three, and includes a discussion on the initial experimental results. Finally, chapter seven concludes the thesis with a summary of the work done, along with suggestions for future work.

1.2 State-of-the-art

The idea of optoelectronic devices was raised in the late 1980s. However, it has turned out to be one of the intensely pursued research fields within the most recent decade, driven principally by the rapid development of the communication technology. As internet-based communications continue to grow, and transistor sizes reduces according to Moore's law, the conventional technology based on copper has been pushed to its breaking point and could no longer fulfil the demand for high-speed and large bandwidth. Underlying this condition, optoelectronic devices are destined to have an imperative role in present day communications system owing to its high speed transmission and excellent low-noise properties. Recent developments have proven that optoelectronic devices could deliver low-cost and high-performance solutions for the communication technology such as chip-to-chip, fibre-to-the-premise, and intra-chip applications[1].

At present, the majority of data transmission corresponds to the minimum optical loss window for silica optical fibres. Therefore, various optoelectronic devices have been developed within the said optical windows wavelength such that they can be directly connected to external servers without wavelength conversion, where here, photodetectors are placed at the end of the optical path to convert optical into electrical signals, with the conversion quality greatly affecting the overall performance of the entire system. An ideal photodetector ought to have a high responsivity and quantum efficiency, low dark currents and noise level, a high detection speed, large bandwidth and low applied voltage-bias supplies. However, the most important principle

for a photodetector is its compatibility with the optoelectronic integrated circuit (IC) technology. Even though most of the main substrate used for ICs is Silicon, some of the III-V compounds of the periodic table such as Gallium Arsenide (GaAs), are preferred for high-speed integrated circuits. GaAs has some electrical properties that are superior to that of the Silicon. It has higher saturated electron velocity and higher drift mobility, allowing it to function at much higher frequencies or higher speed digital devices [2]. GaAs devices generate less noise than Silicon devices and can be operated at higher power levels than the equivalent Silicon device because of higher breakdown voltages. Furthermore, GaAs substrates have the advantages of low cost and large area in wafers.

The integration of commercial GaAs electronic (Metal-Semiconductor-Field-Effect-Transistor, MESFET) ICs has reached very-large-scale integration (VLSI) levels in recent years. This integration uses only noncompliant metals in contact with the semiconductor as well as Silicon IC upper-level interconnect and passivation technologies [3]. These advances provide much higher levels of optoelectronic integration through epitaxial growth of the III-V heterostructures on the GaAs-based VLSI electronics and simultaneously overcoming the materials problems inherent in growing the III-Vs on Silicon [4]. Most 10-Gbps application specific integrated circuits (ASICs) have been implemented on GaAs and Silicon Germanium (SiGe) technologies with 0.5 μm line width [5].

GaAs devices are relatively insensitive to overheating owing to their wider direct energy bandgap. Therefore, GaAs can be used to absorb and emit light efficiently compared to Silicon that has an indirect bandgap. The regularly embraced photodetection system exploits the inter-band transition from the band gap of a semiconductor to retain the photon. Additionally, the photodetection wavelength can be adjusted by choosing semiconductor materials having a suitable band gap, or creating the band gap with band engineering techniques. $In_xGa_{1-x}As$ alloy is currently the most mature and commercialised material system for photodetection at

telecommunications wavelengths. The $In_xGa_{1-x}As$ based photodetector currently outperforms Silicon and Germanium owing to its direct band gap properties and relatively large absorption coefficient. The band gap of $In_xGa_{1-x}As$ can be tuned for longer wavelength than 1μm although this will result in lattice mismatching with the GaAs based substrate.

A 1.5 μm thick graded $In_xGa_{1-x}P$ buffered on a GaAs substrate was effectively demonstrated to overcome the ~4% lattice mismatch at 10-Gbps operation of the $In_{0.53}Ga_{0.47}As$/GaAs p-i-n photodiode [6]. However, the whole procedure is relatively expensive and involved a complex fabrication process in comparison to InP substrate application. The $In_xGa_{1-x}As$ based on InP substrate has demonstrated high responsivities exceeding 1 A/W [7], high quantum efficiencies of more than 90% [7-8], low dark currents of less than 10 pA [7,9], large bandwidths up to 100 GHz [9-10], and high speeds up to 50 Gb/s [11-12] for telecommunication technologies. However, the limitation of having an 8.1% lattice mismatch between InP and Silicon [13] and a 3.9% lattice mismatch between InP and GaAs [14] makes it difficult to integrated $In_xGa_{1-x}As$ based photodetectors with other optoelectronic ICs.

The introduction of a small amount of Nitrogen (so-called dilute nitride) into the $In_xGa_{1-x}As$ material offers the flexibility of tailoring both the bandgap and the lattice parameter to better match the GaAs substrate. GaInNAs/GaAs has a much larger conduction band offset due to the decreased curvature of the new conduction band in dilute nitrides. This consequently increases the electron effective mass. With a deeper quantum well and increment of electron mass, GaInNAs provides a better confinement of the carriers in quantized sub-band and a better match of the valence band and conduction band densities of states. These properties allows the GaInNAs quantum wells to produce a much larger gain compared to a bulk semiconductor medium, and leads to a better room temperature operation especially when using the cavity based structure. Hence, the ability of resonant cavity photodetector using

GaInNAs quantum wells technology enhancement is expected to outperform the delinquent of the current Silicon and InP technology.

1.3 Background

Back in the early 90's, the interchange texts or messages via emails and World Wide Web pages were enough for people to communicate with each other. However, in the coming of the 21st century, people started to share high quality files (video and pictures) over the internet. The development of new generations of internet services such as YouTube, Facebook, E-bay and Bit-Torrent motivates the users to share high definition (HD) movies, watch live streaming video, do online shopping, and play online games. Thus, this critical situation has led to the need for higher bandwidth requirements and the need of internet upgrading mainly in the Metro Area Network (MAN) and the Local Area Network (LAN). The upgrading has motivated a great deal of effort into the development of smaller and faster electronics devices. The limitless desire for such devices has driven an increasing demand for a greater capacity of information processing and high-speed data transmission. In low cost data transmission applications, such as fibre to the home, LAN, and free-space optical interconnects, devices operating with emission at 0.85μm wavelength is a widely used technology. The devices are appropriate for short distance multi-mode fibre based interconnects because of their low output power and cost. Optical fibres can transmit light over a wide range of wavelengths up to near infrared application. Longer wavelengths application in the range of 1.3 to 1.55μm provide for longer transmission distances (hundred kilometres) at high bit rates due to diminished effects from attenuation and dispersion. This further enhances network speed and efficiency by reducing the need for additional components such as repeaters or amplifiers. Therefore, longer wavelength operating devices are desirable in developing fibre-optic communication of MAN [15]. The operation at the 1.3μm or 1.55μm of telecommunication windows has been used because of the minimum dispersion at

1.3μm and the minimum attenuation at 1.55μm. However, the telecommunication window of 1.55 μm is already very heavily utilised in long haul communication systems [16], while 1.3μm is more suited for MAN networks. Moreover, many of today's medium haul systems operate in the 1.3μm window, and if transceiver systems could be made economical, then they could be used in local area networks.

The fibre-optic communication system comprises a transmitter, an optical fibre channel for light transmission, and a receiver. A photodetector is used to convert the optical signals into electrical signals at the receiving end. The operating wavelength of a photodetector is based on the bandgap of the absorption material. Commonly, the InP and Silicon based semiconductor material such as InGaAs or InGaAsP [17-20] is used. However, those materials are typically influenced by a strong dependence of temperature [21], and relatively small conduction band offset [22-23]. Increasing temperature reduces the available gain because the efficiency decreases due to electrons leaking out of the quantum well (QW). Thus, an external cooling package is needed to minimise the thermal-related problem and ensure a stable operation. This however increases the cost because expensive thermoelectric cooling systems often dominate the cost of individual components. Furthermore, the current commercial InP based photodetectors are already costly in nature because of the high substrate cost and expensive processing technology. Other than the cost issues, the InP based materials also have low refractive index contrast value for cavity mirrors application which are important in cavity devices such as vertical cavity surface emitting laser (VCSEL) [24], Vertical Cavity Semiconductor Optical Amplifier (VCSOA) [25] and Vertical Cavity Enhanced Photodetector (VCEPD) or known as Resonant Cavity Enhanced Photodetector (RCEPD) [26]. The refractive index contrast for the Silicon and InP based systems such as GaInAsP/InP and AlGaInAs/AlInAs are small, and need more than 50 pair of mirrors to contain sufficient light for reflectivity application [27]. Therefore, a GaAs based structure is introduced to offer a more economical solution for lower cost of fabrication process,

and an easy growth and reliable processing of the AlAs/GaAs pairs for the Distributed Bragg Reflector (DBR) system due to better lattice matching. The AlAs/GaAs mirror system has high refractive index contrast and high thermal conductivity thus the incident light confinement within the cavity requires the use of less than 30 pairs. In addition, GaAs-based material systems have better thermal conductivity than InP and Silicon based materials which helps to enhance the heat dissipation [28].

Even though GaAs based materials have advantages over InP and Silicon based materials, the composition of Indium for InGaAs bandgap of over 1μm results in a lattice mismatched alloy to the GaAs. This led to significant effort towards introducing Nitrogen into the InGaAs materials to provide absorption up to the near infrared wavelength, known as dilute nitride [33]. Interest in quaternary dilute nitrides for long wavelength application began in the mid 90's after Kondow *et.al.* published results on the quaternary alloy, GaInNAs [29-30]. This novel alloy allowed independent control over the In:Ga and N:As ratios. Increasing the In:Ga ratio causes a reduction in bandgap and an increase in lattice parameter, while increasing the N:As ratio also causes bandgap reduction, but will decrease the lattice parameter. Therefore, GaInNAs gives the flexibility of tailoring both the bandgap and lattice parameter due to the flexibility of material composition which makes it possible to be used for lasers [31] and photodetectors [32] applications. The materials were expected to have very good temperature characteristics resulting from the predicted large electron confinement. In addition, being based on GaAs, dilute nitrides would be easily integrated with the established GaAs technology including DBR mirrors. However, producing high quality dilute nitride has proven to be difficult, with increasing nitrogen fraction resulting in reduced optical quality [29, 33-37]. Post-growth annealing was soon found to improve the optical quality but the increase in optical quality was usually accompanied by a blue shift [70], which partly offsets the red shift induced by nitrogen incorporation. Despite these problems, early research led to the demonstration of a

range of devices and a gradual improvement in material quality [38]. As for the compositions of GaInNAs near 1300nm emission, the band discontinuity is typically around 80% in the conduction band [39]. This research on GaInNAs has also revealed that it has a larger conduction band offset and a larger electron effective mass than GaInAsP [29, 40], thus providing better confinement for electrons and better match of the conduction and valence band densities of states, leading to better temperature stability, higher operating temperature, and higher efficiency[41].

In the GaInNAs material system, Indium atoms are used to counter-balance the tensile strain induced by the incorporation of Nitrogen. However, when Antimony is used in place of the Indium atoms, due to its properties as a reactive incorporation [42-43] and its large atomic size, it allows for more room for Nitrogen to be incorporated without excessively increasing the lattice free energy. Nevertheless, the growth of dilute nitride materials, such as GaNAsSb and GaInNAs at low temperature (<500˚C) and the difference between the size of nitrogen atoms and the size of replaced group-V atoms lead to the formation of mid-gap arsenic antisite and nitrogen-related defects [44-48]. These defects contribute to such materials having short carrier lifetimes [49-50] and low photoluminescence (PL) efficiency [51]. In addition, the presence of Antimony during GaInNAs growth has been thought to act only as a surfactant to improve quantum-well (QW) planarity and PL [52-53]. V. Gambin *et. al*. observed a sharp increase in radiative recombination with high Indium samples beyond 1.3μm and found it to not only act as a surfactant, but is a significant alloy constituent, further red-shifting the optical emission [54]. The need of high concentration of Indium (30-40%) for longer wavelength operation has resulted in a high compressive strain in the QW even with the lattice constant reduction from Nitrogen incorporation, while the addition of Antimony, affects the strain effect to the GaAs barriers in dilute nitride even though it offers an important step toward achieving a high optical quality in quaternary dilute nitride QWs. Thus, GaNAs barriers were proposed as a way to compensate this

high compressive strain, by providing an opposing tensile strain below and above the GaInNAs(Sb) layer [55-58]. In addition to improving the quality of a GaInNAs(Sb) single QW, strain compensation provided by GaNAs barriers also helps with growing multiple QWs. These occurrences have been demonstrated by a few researchers using three well (of high quality) grown QWs of GaInNAs(Sb) for VCSEL application [59-61], and single QW for high performance edge-emitting lasers [62-63]. However, the quality of GaNAs itself remains relatively poor with a high concentration of point defects [64-66]. The small bandgap of GaNAs also means smaller band offset between GaInNAs(Sb) and GaNAs layers, resulting in more carriers in the GaNAs barriers when compared to the GaAs barriers.

The advantages of GaInNAs material for longer wavelength and DBR technology brings with it an improvement in the development of the resonant cavity enhanced devices, especially the RCEPD. Many of the fundamental physical concepts required for resonant cavity devices have been known for over a century. It started in the 19th century when Charles Fabry and Alfred Perot developed the Fabry-Perot etalon, consisting of two reflecting surfaces placed in parallel. An etalon is a device consisting of two reflecting glass plates, employed for measuring small differences in the wavelength of light using the interference it produces. This interferential phenomenon has since resulted in numerous applications, especially in optical device technology [67-68]. In terms of the RCEPD, the resonant cavity is essentially a Fabry-Perot etalon where the resonance condition of the etalon is the operating wavelength of the photodetector. RCEPDs are considered promising candidates for high speed optical communications and interconnections operating in the near infrared. In these high performance photodetectors, high speed, high external quantum efficiency and wavelength-selectivity can be achieved simultaneously because of the constructive interference occurring within the DBR cavity to enhance the amplitude of the internal optical field [69]. The optical and electrical path lengths can be decoupled to break the trade-off between bandwidth and quantum efficiency in a standard bulk p–i–n structure.

Furthermore, the quantum well structure is inferior in absorption efficiency and high speed performance compared to the bulk p-i-n structure, while the optical coupling normal to the surface makes RCE structures physically compatible with VCSEL due their inherent features such as narrow spectral line width and easy coupling [71]. For high speed photodetectors, the optimum absorption coefficient due to thickness is typically required so that a bottom DBR with a reflectivity close to 99% is essential for unity quantum efficiency [72].

There have been limited studies on quaternary GaInNAs based cavity enhanced photodetector for 1.3μm operation in the literature. *Heroux et al.* made the first attempt and reported a remarkable quantum efficiency (QE) of between 48% and 72% at considerably high bias voltages up to -7V with a rather large FWHM of 11nm [73]. However, the method they used to obtain quantum efficiency is not mentioned explicitly which put some doubt on the figures given for efficiency. Furthermore, the FWHM of the QE is very poor which is associated with bad DBR quality. *RuiKang et al.* demonstrated the operation at 1.3μm with three 6.8 nm wide QWs sandwiched between 11 and 5 pairs of GaAs/AlGaAs top and bottom mirrors, respectively. Their device shows a low quantum efficiency of 12% with a 5.8nm full width at half maximum (FWHM) [74], in part due to the small number of QWs in their device where the incident light is not fully absorbed. Furthermore, the small number of pairs for the top and bottom DBR mirrors of their device produces very low reflectivity, which might not be suitable for 1.3μm optical communication systems which required high selectivity. The most recent work was by A. Pfenning *et. al*. on the adaptation of resonant tunnelling diode in the cavity. However, as their device demonstrated a very low QE of 18.3% operated at -3V reverse bias [75], it could not be considered in applications for optical communication systems.

The application of long-haul fibre optic communication systems for high bandwidth are always affected by signal losses, hence a photodetector with internal gain is essential to amplify the signal. Therefore, an avalanche photodiode (APD) is chosen in order to reduce the number of

repeaters and amplifiers. The multiplication region of an APD plays an important role in the determination of gain, multiplication noise and gain-bandwidth-product (GBP). The impact ionisation parameter is the key for an APD which with a high impact ionisation coefficient, will contribute to lower multiplication noise and higher bandwidth. APD structures requires that $\beta/\alpha \approx 0$ (pure electron ionisation) or $\alpha/\beta \approx 0$ (pure hole ionisation), where α and β are the electron and hole ionisation coefficient, respectively. Low noise and high gain-bandwidth product have been reported on APDs with multiple multiplication regions [76-83].

1.4 Thesis Motivation and Objective

1.3µm photodetectors plays an important role in the expansion of fibre optic systems into mid haul (<10km) data communication networks. Most of the mid haul fibre optic systems operate at wavelength of 1.3µm. Common fibre optic systems are employed in long haul data communication systems such as intercontinental networks and intercity networks. Due to the increasing demand for bandwidth which can no longer be met by the copper wires, the use of fibre optics has been expanded to MAN. The current InP and Silicon based semiconductor devices are known to incur high production costs due to the complex and expensive fabrication processes involved [84-85], with poor reflectivity performance of the DBR technology. Thus, the development of optical semiconductor device has been optimised to overcome the requirement of a high speed and higher bandwidth at low cost production. The novel quaternary GaInNAs material system that can be lattice matched to GaAs based devices has been introduced as a contender to replace the InP and Silicon based technology. Recent years have witnessed the realization of the promising potential of GaInNAs-based devices to be used in optical communication for near infrared application. Furthermore, the GaInNAs enables the use of high reflectivity (of over 99%, with lesser number of pairs) GaAs/AlAs DBR mirrors due to lattice matching with GaAs. The use of this DBR is important in developing the structure of the vertical

cavity enhanced (VCE) photodetector devices. A cavity device is preferred due to its ease of coupling characteristic and narrow spectral line width output. Additionally, the device which is able to operate with internal gain is favoured to amplify low signal during longer transmission.

The GaInNAs material has been extensively used for laser and photodetector applications for many years. However, its competency for cavity photodetector at 1.3μm wavelength operation is still being a big question. Research have shown negative but promising results. As of 2014, GaInNAs based VCE photodetector with internal gain for operation at 1.3μm is yet to be demonstrated. Hence, the aim of this thesis is to develop and demonstrate the performance of a vertical cavity structure based on quaternary dilute nitride (GaInNAs) material with internal gain at 1.3μm operation for optical communication. The work done in this thesis is mainly focused on the photodetector's main parameters such as quantum efficiency, sensitivity, selectivity, Noise Equivalent Power (NEP), and possible gain at room temperature operation. The tunable selectivity approach has been considered during the development of the VCE photodetector as an alternative method towards improving the quantum efficiency and sensitivity if required. The photodetector structures reported in this thesis are entirely surface illuminated.

References

1. J. Wang and S.J. Lee, Sensors, 11, 696 (2011)
2. M. Kuzuhara and S.Tanaka, JSAP International, No.3, 4 (2003)
3. B. Green. and C. Weitzel, IEEE Microwave, 120 (2015)
4. A. Saha and N. Manna, Optoelectronics and Optical Communications, University Science Press, 488 (2011)
5. I. Kaminow, and T. Li, "Optical fibre telecommunications", IVA components, San Diego, California: Elsevier Science, Chapter 16 (2002)
6. C-K Lin, H-C Kuo, Y-S Liao, and G-R Lin, Proceedings of SPIE Vol. 5624, 399 (2005)
7. Z. Sheng, L. Liu, J. Brouckaert, S. He, D.V. Throurhout, Optics Express, 18, 1756 (2010)
8. J.H. Kim, H.T. Griem, R.A. Friedman, E.Y. Chan, S. Ray, IEEE Photon. Technol.Lett., 4, 1241 (1992)
9. L.E. Tarof, D.G. Knight, K.E. Fox, C.J. Miner, N. Puetz, H.B. Kim, Appl. Phys. Lett., 57, 670 (1990)
10. B.M. Onat, M. Gokkavas, E. Ozbay, E.P. Ata, E. Towe, M.S. Unlu, IEEE Photon. Technol. Lett., 10, 707 (1998)
11. M. Nada, H. Yokoyama, Y. Muramoto, T. Ishibashi, H. Matsuzaki, Opt. Express, 22, 14681 (2014)
12. . R. Valivarthi, I. Lucio-Martinez, A. Rubenok, P. Chan,F. Marsili, V.B Verma, M.D. Shaw, J.A. Stern, J.A. Slater, D. Oblak, S.W. Nam, W. Tittel, Opt. Express, 22, 24497 (2014)
13. M. Casalino, G. Coppola, R.M. De La Rue and D.F. Logan, Laser Photonics Rev. 10, No. 6, 895 (2016)
14. . I. Mathews, D. O'Mahony, A. Gocalinska, M. Manganaro, E. Pelucchi, M. Schmidt, A. P. Morrison and B. Corbett1, Applied Physics Letter, 102, 033906, 2013

15. H. Riechert, A. Ramakrishnan, G. Steinle, Semiconductor Science Technology, 17, 892, (2002)
16. F. Sarcan , M.S. Nordin, F. Kuruoglu, A. Erol and A.J. Vickers, Superlattices and Microstructures, 102, 27 (2017)
17. J. C. Campbell, W. T. Tsang, G. J. Qua, and J. E. Bowers, Appl. Phys. Lett., vol. 51, pp. 1454-1456, 1987.
18. F. Capasso, K. Alavi, A. Y. Cho, P. W. Foy, and C. G. Bethea, Appl. Phys. Lett., vol. 43, pp. 1040-1042, 1983.
19. C. Lenox, H. Nie, P. Yuan, G. Kinsey, A. L. Holmes, Jr., B. G. Streetman, and J. C. Campbell, IEEE Photon. Technol. Lett., vol. 11, pp. 1162-1164, (1999)
20. G. Roelkens, J. Brouckaert, D. Taillaert, P.r Dumon, W. Bogaerts, D.V. Thourhout, R. Baets, No.25, (2005)
21. A. F. Phillips, S. J. Sweeney, A. R. Adams, and P. J. A. Thijs, IEEE Journal of Selected Topics in Quantum Electronics. 5, (1999).
22. M. Yano, H. Imai, and M. Takusagawa, J. Appl. Phys. 52, 3172 (1981).
23. N. K. Dutta and R. J. Nelson, Appl. Phys. Lett 38, 407 (1981).
24. A. Larsson, C. Carlsson, J. Gustavsson, A. Haglund and P. Modh, Microwave Photonics, (2004)
25. F.A.I. Chaqmaqchee, N. Balkan and J.M.U. Herrero, Nanoscale Research Letters, 7 (2012)
26. Q. Han, X.H. Yang, Z.C. Niu, H.Q. Ni, Y.Q. Xu, S.Y. Zhang, Y. Du, L.H. Peng, H. Zhao, C.Z. Tong, R.H. Wu, Q.M. Wang, Appl. Phys. Lett. 87, 11 (2005)
27. V. Gambin, , Ph.D. thesis, Stanford University, (2000)
28. J. Piprek and S. J. B. Yoo, Electron. Lett., vol. 30, pp. 866 (1994)
29. M. Kondow, K. Uomi, A. Niwa, T. Kitatani, S. Watahiki and Y. Yazawa, Jpn. J. Appl. Phys., 35, 1273 (1996)
30. M. Kondow, T. Kitatani, S. Nakatsuka, M. Larson, K. Nakahara, Y. Yazawa and M. Okai, IEEE J. Select. Topics Quantum Electron, 3, 719 (1997).
31. J. S. Harris, Semiconductor Science and Technology, 17, 880 (2002)
32. D. Jackrel, H. Yuen, S. Bank, M. Wistey, J. Fu, X. Yu, Z. Rao, and J. S. Harris, presented at Semiconductor Photodetectors II, San Jose, CA, USA, (2005)
33. M. Weyers, M. Sato and H. Ando Jpn. J. Appl. Phys., 31, L853 (1992)
34. I.A. Buyanova, W.M. Chen, G. Pozina, J.P. Bergman, B. Monemar, H.P. Xin and C.W. Tu, Appl. Phys. Lett., 75, 501 (1999).
35. A. Markus, A. Fiore, J.D. Ganiere, U. Oesterie, J.X. Chen, B. Deveaud, M. Ilegems and H. Riechert, Appl. Phys. Lett., 80, 911 (2002)
36. S. Sato, Y. Osawa and T. Saitoh, Jpn. J. Appl. Phys., 36, 2671 (1997).
37. I.A. Buyanova, W.M. Chen and B. Monemar, MRS Internet J. Nitride Semi. Research, 6, 2 (2001).
38. S. Shirakata, M. Kondow, T. Kitatani, Appl. Phys. Lett., 80, 2087 (2002).
39. M. Hetterich, M. D. Dawson, A. Y. Egorov, D. Bernklau, and H. Riechert, Appl. Phys. Lett. 76, 1030 (2000).
40. W. Shan, W.Walukiewicz, J. W. A. III, E. E. Haller, J. F. Geisz, D. J. Friedman, J. M. Olson, and S. R. Kurtz, Journal of Applied Physics, vol. 86, no. 4, 2349 (1999)
41. M. Kondow, S. Natatsuka, T. Kitatani, Y. Yazawa, and M. Okai, Electronics Letters, no. 24, 2244 (1996)
42. K. Volz, V. Gambin, W. Ha, M. A. Wistey, H. Yuen, S. Bank, and J. S. Harris, Journal of Crystal Growth, vol. 251, no. 1-4, 360 (2003)
43. H. B. Yuen, S. R. Bank, M. A. Wistey, J. S. H. Jr, and A. Moto, Journal of Applied Physics, no. 11, 6375 (2004)
44. R. J. Kaplar, D. Kwon, S. A. Ringel, A. A. Allerman, S. R. Kurtz, E. D. Jones, and R. M. SiegSolar Energy Materials and Solar Cells, vol. 69, 85 (2001)
45. W. K. Loke, S. F. Yoon, S. Wicaksono, K. H. Tan, and K. L. Lew, Journal of Applied Physics, 102, 054501 (2007)
46. S. Wicaksono, S. F. Yoon, W. K. Loke, K. H. Tan, K. L. Lew, M. Zegaoui, J. P. Vilcot, D. Decoster, and J. Chazelas, Journal of Applied Physics, 102, 044505-7 (2007)
47. W. K. Loke, S. F. Yoon, K. H. Tan, S. Wicaksono, and W. J. Fan, Journal of Applied Physics, 101, 033122-5 (2007)
48. W. M. Chen, I. A. Buyanova, C. W. Tu, and H. Yonezu, Physica B: Condensed Matter, 376, 545 (2006)
49. A. J. Ptak, S. W. Johnston, S. Kurtz, D. J. Friedman, and W. K. Metzger, Journal of Crystal Growth, 251, 392 (2003)
50. R. A. Mair, J. Y. Lin, H. X. Jiang, E. D. Jones, A. A. Allerman, and S. R. Kurtz, Applied Physics Letters, 76, 188 (2000)
51. S. Wicaksono, S. F. Yoon, K. H. Tan, and W. K. Loke, Journal of Vacuum Science and Technology B: Microelectronics and Nanometer Structures, 23, 1054 (2005)
52. H. Shimizu, K. Kumada, S. Uchiyana, and A. Kasukawa, IEEE J. Select. Topics Quantum Electron. 7, 355 (2001)
53. X. Yang, M. J. Jurkovic, J. B. Heroux, andW. I.Wang, Appl. Phys. Lett., 75, 178 (1999)
54. Vincent Gambin, Wonill Ha, Mark Wistey, Homan Yuen, Seth R. Bank, Seongsin M. Kim, and James S. Harris, IEEE Journal Of Selected Topics in Quantum Eelectronics, 8, 4 (2002)

55. S. G. Spruytte, PhD thesis, Stanford University, (2001)
56. S. G. Spruytte, M. C. Larson, W. Wampler, C. W. Coldren, H. E. Petersen, and J. S. Harris, Journal of Crystal Growth, 227, 506 (2001)
57. E.-M. Pavelescu, T. Jouhti, C. S. Peng, W. Li, J. Konttinen, M. Dumitrescu, P. Laukkanen, and M. Pessa, Journal of Crystal Growth, no. 1, 31 (2002)
58. A. Y. Egorov, D. Bernklau, B. Borchert, S. Illek, D. Livshits, A. Rucki, M. Schuster, A. Kaschner, A. Hoffmann, G. Dumitras, M. C. Amann, and H. Riechert, Journal of Crystal Growth, 227, 545 (2001)
59. M. A. Wistey, S. R. Bank, H. B. Yuen, L. L. Goddard, and J. S. Harris, Electronics Letters, 25, 1822 (2003)
60. M. A. Wistey, S. R. Bank, H. P. Bae, H. B. Yuen, E. R. Pickett, L. L. Goddard, and J. S. Harris, Electronics Letters, 5, 282 (2006)
61. T. Sarmiento, H. Bae, T. D. O'Sullivan, and J. S. Harris, Conference on Lasers and Electro-Optics, p. CTuY4, (2009)
62. W. Ha, V. Gambin, S. Bank, M. Wistey, H. Yuen, K. Seongsin, and J. S. J. Harris, IEEE Journal of Quantum Electronics, 9,1260 (2002)
63. M. A. Wistey, PhD thesis, Stanford University, 2004.
64. P. Krispin, V. Gambin, J. S. Harris, and K. H. Ploog, Journal of Physics, 93, 6095 (2003)
65. J. S. Wang, A. R. Kovsh, L. Wei, J. Y. Chi, Y. T. Wu, P. Y. Wang, and V. M. Ustinov, Nanotechnology, 12, 430 (2001)
66. H. B. Yuen, S. R. Bank, M. A. Wistey, J. S. H. Jr, and A. Moto, Journal of Applied Physics, 11, 6375 (2004)
67. M.S. Unlu, Optoelectronics World Magazine, 3, 15 (1998)
68. M.S. Unlu and S. Strite, J. Appl. Phys., 2, 607 (1995)
69. Y. M. El-Batawy and M. J. Deen, Proceedings of SPIE - The International Society for Optical Engineering 4999 (2003)
70. R.J. Potter, S. Mazzucato N. Balkan, M.J. Adams, P.R. Chalker, T.B. Joyce and T.J. Bullough, Superlattice Microst., 29, 169 (2001)
71. R. Sceats, N. Balkan, M.J Adams and J. Masum, Turkey Journal of Physics, 23 (1999)
72. J.B. H´eroux and W.I. Wang, Dilute Nitride Photodetector and Modulator Devices, Dilute III-V Nitride Semiconductors and Material Systems, edited by A. Erol, Springer-Verlag Berlin Heidelberg, 563 (2008).
73. J.B. Hereoux, X. Yang, W.I. Wang, Appl. Phys. Lett., 75, 18, (1999)
74. Z. Ruikang, Acta Ohoton. Sin. 31, 3, (2002)
75. A. Pfenning, F. Hartmann, F. Langer, S. Höfling, M. Kamp, L. Worschech, Appl. Phys. Lett., 104 (2014).
76. C. Hu, K. A. Anselm, B. G. Streetman and J. C. Campbell, Appl. Phys. Lett., 69, 3734 (1996)
77. C. Lenox, P. Yuan, H. Nie, O. Baklenov, C. Hansing, J. C. Campbell, and B. G. Streetman, Appl. Phys. Lett., 73, 783 (1998)
78. K. F. Li, D. S. Ong, J. P. R. David, G. J. Rees, R. C. Tozer, P. N. Robson, and R. Grey, IEEE Trans. Electron Dev., 45, 2102 (1998)
79. P. Yuan, H. Chad, K. A. Anselm, C. Lenox, H. Nie, H. L. Holmes, B. G. Streetman, and J. C. Campbell, IEEE J. Quantum Electron., 36, 198 (2000)
80. J. S. Ng, S. L. Tan, Y. L. Goh, C. H. Tan, J. P. R. David, J. Allam, S. J. Sweeney and A.R. Adams, IEEE Proceeding International Conference on Indium Phosphide & Related Materials (IPRM), (2010)
81. Y. M. El-Batawy and M.J. Deen, IEEE Transactions on Electron Devices, 52, 3 (2005)
82. Y. M. El-Batawy and M.J. Deen IEEE Transactions on Electron Devices, 50, 3 (2003)
83. N. D. Shuling, W.F. Ma, N.Li, J.C. Campbell, C. Wang and L.A. Coldren, IEEE Photonics Technology letters, 17, 8 (2005)
84. A. Syrbu, A. Mircea, A. Mereuta, A. Caliman, C.A. Berseth, G. Suruceanu, V. Iakovlev, M. Achtenhagen, A. Rudra, E. Kapon, Photonics Technol. Lett. 16, 5, (2004)
85. G. Boehm, M. Grau, O. Dier, K. Windhorn, E. Roenneberg, J. Rosskopf, R. Shau, R. Meyer, M. Ortsiefer, M.-C. Amann, J. Cryst. Growth, 301 (2007)

CHAPTER 2

Literature Review

2.1 Review of Materials and Devices for Optical Communications

Since the demonstration of the first laser in 1958 [1] and the first forward-biased GaAs p-n junction in 1962 [2], optoelectronics, which deals with the interaction of electronic, light and optical processes [3], has made enormous progress. Optoelectronic devices are based on semiconductors, which are the materials that bridge the gap in electrical conductivity between metals and insulators [4] ranging between of 10^{-8} to 10^{3} $\Omega^{-1}cm^{-1}$ [5]. Elemental semiconductor such as Silicon which is the leading material in microelectronics, has an indirect bandgap [6]. This means that the minimum of the conduction band and the maximum of the valence band do not have the same wave vector, so any optical transition near the bandgap energy requires an additional conservation of momentum. Typically this additional momentum comes from phonons. Since the additional energy associated with this particle is lost as heat to the lattice, the devices based on these materials have very weak interaction with light and therefore are not suitable for efficient optical applications. As an example of indirect semiconductor, the band structure of Silicon is represented in Fig.2.1(a).

Direct bandgap compound semiconductors are ideal for optoelectronic applications. Composed of elements from different columns of the periodic table, they offer the possibility to design the electronic properties of the material alloy by altering the alloy composition and properties, in a process called “bandgap engineering”. Direct gaps result in a much stronger optical absorption and emission. The reason for this is that the photon has negligible momentum. Optical transitions, in the simplest model, involve raising an electron from the valence band into the conduction band. Such transitions, which generally conserve momentum, are always vertical when viewed in a band structure diagram, whereby in a direct gap semiconductor, they occur near the bandgap energy (for k=0).

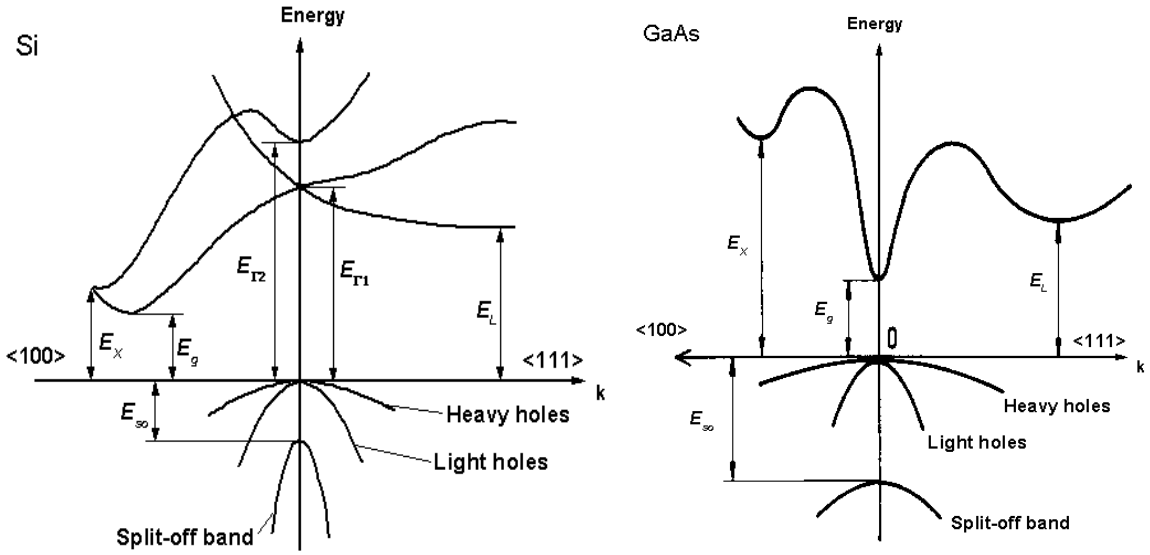

(a) (b)

Figure 2.1: Band structure of (a) Silicon and (b) GaAs [6]

The most common and useful compound semiconductors in optoelectronics are the III-V materials made from elements from the Group III (Ga, In, Al) and the Group V (As, P, Sb, N) in the periodic table, such as GaAs. The elemental semiconductors Si and Ge are the Group IV material that has been widely used as photodetectors as well. II-VI materials and, to a lesser extent, IV-VI materials (for example PbTe), can also be used, but usually for different applications. However, the remarkable advantage of the III-V modulation doping is the reduced remote impurity scattering [7] due to the spatial separation of the carriers and their parent dopants, thus leading to increased carrier mobility. The remote impurity scattering can be further reduced by inserting a spacer layer, which is normally an undoped part of the barrier.

This research project is limited to the III-V compounds. Of all the III-V semiconductors, GaAs has been extensively studied, especially in the 1980s [8], and it is now the most used material in optoelectronics. The bandgap structure of GaAs in Fig.2.1(b) and that of the Silicon's in Fig.2.1(a) shows the difference between direct and indirect semiconductors. Nowadays the optical and electrical properties of GaAs have been well understood and a lot of devices have been successfully developed based on this material.

Normally the selection of semiconductor compounds for optoelectronic devices is based on a few reasons :- the combination of different materials used that allows control the of the flow of the electrons and holes in the devices, energy bandgap and mirror structures that can be designed and fabricated (it is possible to make structures in which only certain sections absorb or emit light at the wavelengths of interest with the other parts being transparent) and the ability to confine the carriers in advanced thin layer semiconductor materials.

The most important relation in this design connects the lattice of a certain compound with its expected bandgap energy. Fig.2.2 shows the resulting graph for the various semiconductor alloys. In the figure, the possible binary and ternary alloys are represented by direct and indirect bandgap material. For example, the line connecting GaAs and InAs represents the direct bandgap of GaInAs compound.

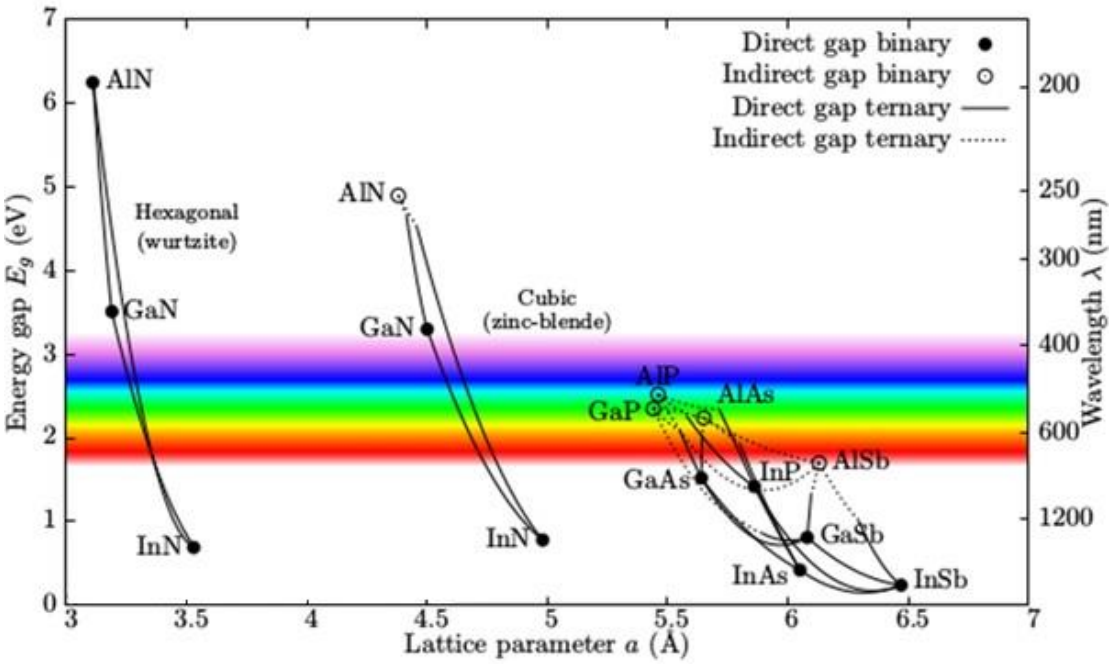

Figure 2.2: Bandgap vs. lattice constant for various semiconductor materials [8]

The facility of making a certain alloy depends upon the chemical properties of the individual components. This growth process is much easier when the alloy parental materials have similar ionic radius and electronegativity, for example when replacing Ga with Al in GaAs to form AlGaAs. If this is not the case, then the components are said to have a large miscibility

gap and alloy growth becomes difficult. Instead of forming miscible (random) alloys, these materials tend to form clusters or phase separated layers, resulting in poor quality devices. In addition, the simple lattice constant versus energy bandgap relation ceases to be valid once phase separation occurs. The only way around this is to use non-equilibrium growth conditions so that the natural repulsion of the materials can be overcome and a metastable random alloy can be formed [9].

The lattice constant is very important in deciding the type of heterostructures which can be made. In most cases, to successfully grow one crystalline material on another, the lattice constants of the two components need to be very close [10]. If they are not, the junction may have a very large number of crystalline defects, which will often (though not always) stop the device from functioning as desired. In light-emitting devices, for example, a large number of defects will usually lead to a short device lifetime, rendering the device useless. However, it is possible to grow very thin layers even when there is substantial lattice mismatch, known as strain. Proposed in 1982 by G.C. Osbourn [11], strain became a new and additional tool to modify band structures in a predictable and useful way, increasing the number of semiconductor alloys that could be fabricated [12-13]. The layer thickness above which defects and imperfections start appearing when an epilayer with lattice constant a_w is grown on a substrate with lattice constant a_s is called critical thickness d_c where ε is in-plane strain defined as [14]:

$$d_c \approx \frac{a_w}{2|\varepsilon|} \quad \ldots\ldots (2.1)$$

with

$$\varepsilon = \frac{a_s - a_w}{a_w} \quad \ldots\ldots (2.2)$$

Fig.2.3 represents the different possible strain conditions when growing one semiconductor on a different one, together with the corresponding implications on the alloy bandgap profile [12]. In the presence of the strain, the valence band splits into heavy hole (E_{HH}) and light hole (E_{LH})

levels removing the degeneracy at zone centre (k=0). Under tensile strain, the band gap is reduced and the light hole band moves towards the valence band edge, while under compressive strain, the bandgap increases and the heavy hole moves towards the valence band edge [13]. Compressive strain (stress) breaks the cubic symmetry of the lattice resulting in the splitting of the degeneracy, which is known as the splitting-off energy. Compressive strain takes place when a semiconductor layer of a larger lattice constant is grown on a layer that has a smaller lattice constant. Vice versa, the tensile strain is constructed.

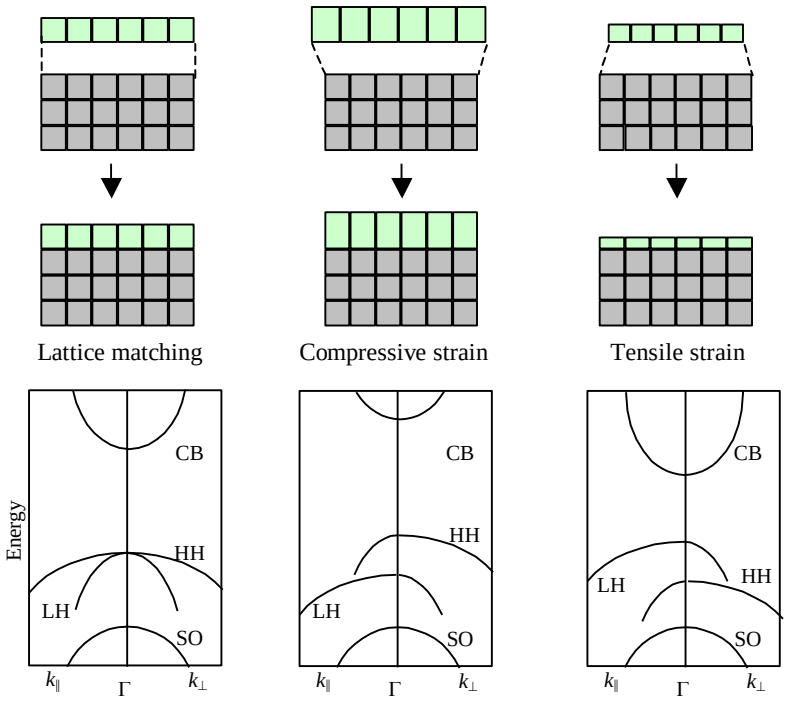

Figure 2.3: Deformation of the epilayer lattice under different strain conditions, and consequences on the bandgap profile [14]

The issues of lattice mismatch has brought many further development in material system for communication devices. At present, InGaAs is the most promising and commercialised material system compared to Silicon and Germanium technology. The tuneable band gap of InGaAs from 850 nm to 3600 nm makes it suitable for a wide range of photodetection applications. The performance of InGaAs applications has been briefly explained in the previous chapter. However, InGaAs material photodetector is difficult to be integrated with other

complementary-metal-oxide-semiconductor (CMOS) and GaAs technology due to the lattice mismatch between Silicon, GaAs and InP. At present, Germanium is becoming a very competitive semiconductor material due to the smaller lattice mismatch with Silicon substrate (approximately 4.2%) thus resolving the compatibility issue with the CMOS circuits. Ge-on-Si photodetectors have shown as good as performance to the InGaAs photodetectors with a high quantum efficiency of 90% [15], high responsivity of 1.76 A/W at a 5V input voltage [16], high speed of 43 Gb/s, bandwidth of more than 30 GHz [17], and low dark currents of 0.2 pA [18] being reported in literature. In addition to the Silicon photodetector being impeccably compatible with just CMOS components, its photodetection wavelength is fair at below 1100 nm [19]. The manipulation of Silicon band structure such as via doping or surface engineering are required to enable sub-band gap photon absorption. At this time, only the all Silicon mid-bandgap absorption (MBA) photodetector structure can be compared with the commercialised InGaAs photodetectors. Comparable outcomes reported for certain performances include high responsivity between 0.5–10 A/W at a high input voltage of 60 V [20], bandwidth of more than 35 GHz [21] and low bit-error-rate of less than 10^{-12} [22]. Other structures such as surface state absorption (SSA) [23-24], internal photon emission (IPE) [25-28] or two-photon absorption (TPA) [29-33] photodetectors are still limited by low responsivity and quantum efficiency.

On the other side, HgCdTe is possibly the most favourable of other semiconductor material for near infrared photodetection application in the spectrum of 0.7–2.5 μm. The direct bandgap semiconductor with good lattice-matching between HgCdTe tertiary alloy and the CdZnTe substrate ensures high-quality crystal growth. In fact, it is the only material that maintains approximately the same lattice constant regardless of the composition of each element while having reasonable dielectric permittivity and low thermal expansion coefficient to ensure a small device capacitance and overall device stability [34]. At present, the development of the HgCdTe photodetector has reached the third-generation products [35]. The tremendously small

ionisation ratio of 0.1 for HgCdTe avalanche photodetector structure leads to a high quantum efficiency of more than 90%, high responsivity of more than 13 A/W, low dark currents of less than 60 nA, and large gains of more than 100 [34]. However, the large mismatch of CdTe with Silicon and GaAs makes HgCdTe challenging to integrate with other integrated circuits and the toxic nature of Hg raises serious safety issues during the fabrication.

Another material option is that of the low dimensional materials such as graphene and carbon nanotube (CNT) which while are still in their early stages, have shown potential in the development of nanoscale high performance photodetectors. Graphene's unique band structure, ultrafast carrier mobility with tunable optical properties via electrostatic doping and good stability enables it to outperform other semiconductor materials for optical communications applications [36]. In addition, graphene has very good compatibility with Silicon substrate, making it convenient for low-cost and large-scale integration into the CMOS circuits [37-39]. Thus far, a bandwidth of 40 Gb/s [40], and sensitivity of 10^7 A/W [41] have been separately demonstrated in laboratories for the graphene photodetectors. Challenges in graphene technology includes the ability to increase the responsivity without sacrificing the bandwidth and effective detection area. As well as the need to improve the fabrication process for mass production prior to commercialisation. However, the inversely proportional relationship between the bandgap (0.2–1.5eV) to its size and dimension makes the CNT capable for a wide spectral of photodetection [42]. While the substantial columbic interaction between the electron and hole due to the strong quantum confinement in 1D binds them into excitons. That can undertake multiplication for better sensitivity and response speed [43]. A responsivity of 0.9–1.8 A/W has been demonstrated from visible to near-infrared for a CNT bolometric p-n diode [44]. However, the bandwidth of the CNT photodetector is usually limited within the megahertz range, delaying its application in telecommunication systems that are near the infrared region.

As shown in Fig.2.4, in the long-haul telecommunication systems, the lines at 1300nm and 1550nm wavelength represent the historical minimum of the earlier fibre's absorption spectrum although worldwide the current systems are in fact operating in either the 2nd window (1280-1325nm) or the 3rd one (1530-1565nm). The window from 1350nm to 1450nm is not available because of higher attenuation over most of the region.

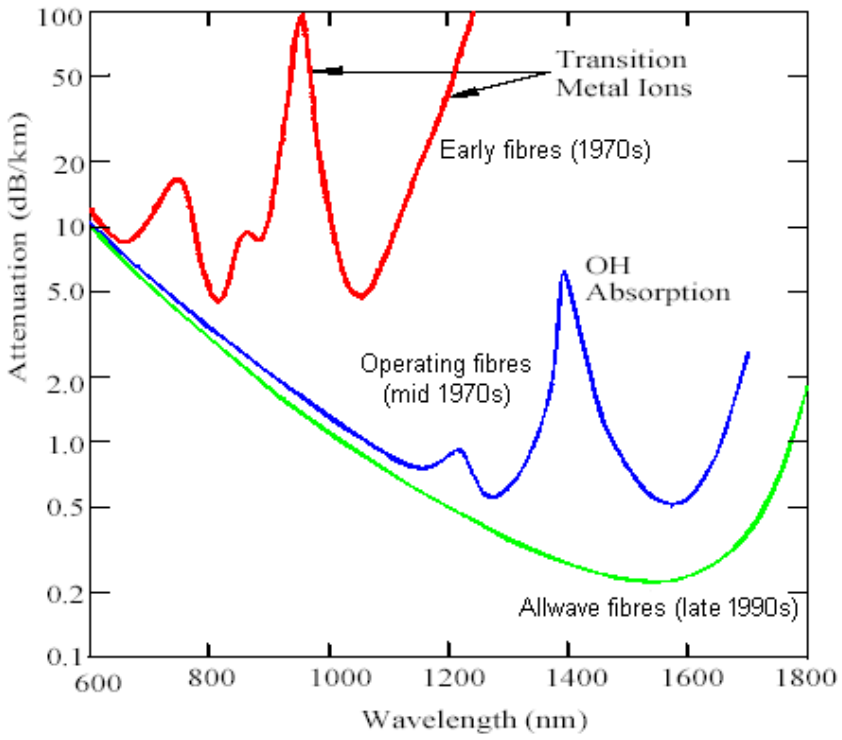

Figure 2.4: Absorption spectrum of different optical fibres [45]

This entire broadband is now available for optical data transmission. Therefore, the optoelectronic market, on which success depends upon the development of optical fibres, requires new semiconductor materials with fundamental bandgap energy in this spectrum range, ultimately in order to obtain tunable long-wavelength semiconductor lasers and detectors. Recently, there has been an increase in the demand for components for the metro and local networks of devices operating at 1.3μm, because at this wavelength the fibre dispersion coefficient is zero (Fig.2.5). Even if dispersion-shifted fibres are available at 1.55μm, for

submarine long-haul links (such as the transatlantic links), it is more economical to use the already installed fibres (operating at 1.3μm) rather than lay new ones (operating at 1.55μm) [46].

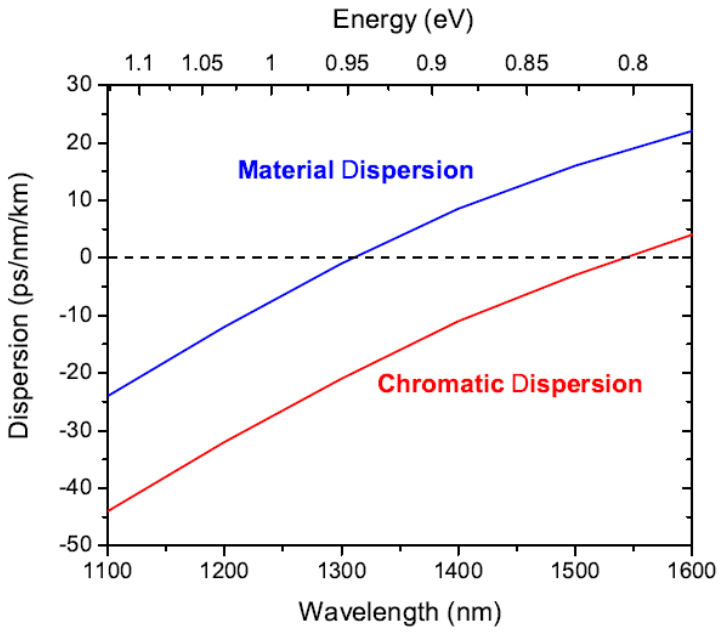

Figure 2.5: Dispersion coefficient versus wavelength in optical fibres. Red line represents the dispersion shifted case, and blue line is the zero-dispersion wavelength [47].

A typical optical communication system consists of 3 major components: signal transmitter (e.g. laser), signal transportation medium (e.g. optical fibre) and signal receiver (e.g. photodetector). Photodetector speed and sensitivity are the key issues in long-haul fibre optic communication systems [48]. Owing to its internal gain which results from impact ionisation, the avalanche photodetector (APD) is frequently the detector of choice over p-i-n photodetectors which have no gain, and therefore, low sensitivity. The multiplication region of an APD plays a critical role in determining the overall gain and gain-bandwidth product (GBP). Both the multiplication noise and the gain-bandwidth product of APDs are determined by the ratio of the electron and hole impact ionisation coefficients, which for most III-V compounds, approaches unity at high electric field intensities. In the case where only one type of carriers (for example electrons) is involved in the impact ionisation process, noise-free and wide bandwidth photodiode will be obtained while for the holes the ionisation coefficient is zero. Common APDs

for wavelengths beyond 1.1μm use separate layers for light absorption (narrow bandgap) and carrier multiplication (wide bandgap). Control of the electric field at the interface between the layers is critical. Currently most optical communications systems mainly makes use mainly InGaAs/InP APDs.

There has also been interest in devices which rely on resonant cavity effects to enhance their performance. Goedbloed and Joosten [49] demonstrated the first application of the resonant-cavity photodetector in 1976 that exhibited interference waves in its responsivity when illuminated with light of varying wavelength at the Philips Research Laboratories. Since then, the resonant-cavity-enhanced (RCE) photodetectors have established substantial attention and several works have demonstrated various degrees of enhancement in comparison to previous generations of photodetectors [50-55]. Normally, semiconductor photodetectors require a large absorption region for sufficient light collection. Larger absorption region increases the transit time and decrease the speed. Therefore, the trade-off between efficiency and speed is a limiting factor for conventional photodetectors [56-57]. This trade-off can be avoided by manipulating the properties of a resonant cavity. Typical a RCE photodetector mostly consists of an absorption layer placed into a vertical cavity with an optimized period of top and bottom (distributed Bragg reflectors) DBRs. The DBR materials must have a lattice constant very close to that of the substrate so that several microns can be grown with very little strain, preventing the formation of structural defects. DBRs are beneficial because light which is not absorbed in the first pass is reflected back into the absorption layer, repeatedly until absorbed. The cavity will enhance the light field at a specific wavelength within the absorption region and enables efficient light absorption even with a thin absorption region. Resonant-cavity enhancement also enables wavelength selectivity meaning the photodetector is highly sensitive at a specific wavelength while remaining unresponsive to off-resonance wavelengths.

The most widely used semiconductor materials for optoelectronics applications at 1.3µm and above are grown on InP substrate. However, it is quite difficult and a high-cost task to fabricate an InP-based RCE photodetectors because the InP-based vertical cavity devices have some disadvantages such as non-monolithic growth process and poor reflectivity performance of the DBR mirrors. The most common mirror systems in InP-based material are the GaInAsP/InP, AlGaInAs/AlInAs and AlGaAsSb. The refractive index contrast of GaInAsP/InP and AlGaInAs/AlInAs systems are very small and more than 50 mirror pairs are needed to contain sufficient light in the cavity [59]. Moreover, poor temperature characteristic also creates the requirement to be cooled [60]. As an alternative, the practice of using Si-based dielectric mirrors makes the grown InP-based devices more complicated and costly [61-62].

The novel GaInNAs compound material grown on GaAs substrate is another alternative approach to overcome the problem. The fact that GaInNAs can be grown being lattice matched with GaAs enables the use of GaAs/AlAs DBR stack. It consequently make the growth process of GaInNAs-based devices monolithic. In addition, the combination of GaAs/AlAs DBR stack produce a high refractive index contrast. Hence, it is possible to use less periods of GaAs/AlAs dielectric mirrors in the device design to achieve a reflectivity of over 99% compared to the number required for InP-based vertical cavity devices.

2.2 Semiconductor Principles

The working principle of a semiconductor photodetector is based on the photoelectric effect. It is the most commonly employed in engineered devices which was first initiated by Einstein in 1905 who claimed that a photon absorbed by a material creates an electron-hole pair. This section present a brief review about semiconductor photodetectors and dilute nitride.

When a large number of atoms are brought together to form a crystal, their orbital combine and energy levels will split into a large number of allowed bands. The highest full band

is known as the valence band while the lowest empty band is called the conduction band. The minimum amount of energy required to move an electron from the valence band to the conduction band of the semiconductor material is called the bandgap of the material, E_g.

As mentioned previously, the lattice constants of different semiconductor materials should match when they are grown on top of each other to prevent a large number of defects. However, growing thin layers such as quantum wells is possible to embody large mismatch in the lattice parameter of the barrier without many defects [63]. This is used in some types of devices to modify the band structure [11]. The lattice constant is related to the bandgap where the increased spacing between atoms will generally result in a decrease in bandgap.

Mainly the semiconductor is categorised by intrinsic semiconductor and extrinsic semiconductor. An intrinsic semiconductor is an undoped semiconductor such a Silicon. This means that holes in the valence band are vacancies which are created by electrons that have been thermally excited to the conduction band. On the other hand, an extrinsic semiconductor is a doped semiconductor where holes or electrons are supplied by a foreign atom acting as an impurity which is able to deeply modify its electrical properties making its presence important in devices such as diodes [49], transistors [64], lasers [65] and solar cells [66].

In order to produce current, a photodiode cell must first convert the incoming photons into free carriers via the absorption and generation process where a photon passing through the semiconductor is absorbed and in doing so gives its energy to an electron in the valence band. If the energy given to the electron is equal or more than that of the direct bandgap of the material, or if phonons are available to give the electron the momentum to make an indirect transition, the electron is promoted to the conduction band. The free electron will live for a finite amount of time before it recombines, either radiatively or non-radiatively. If a photon has energy greater than the energy bandgap, it will be absorbed and creating a mobile carrier above the conduction band. However, the excess energy will be lost in a femto second timescale through the emission

of phonons until the carrier reaches the bottom of the conduction band where it will experience the same lifetime as an electron generated there [67]. A photon which has energy less than the material bandgap, to a first approximation cannot be absorbed and will be transmitted through the material.

Therefore, the ability of a semiconductor to absorb a photon of a given energy is dependent on its direct and indirect bandgaps and is given by its absorption coefficient, α. Fig.2.6 shows the absorption coefficients of some III-V and group IV materials which are commonly used in photodiodes. In Fig.2.6, all but Silicon and Germanium are direct gap materials. Above the bandgap, the absorption coefficient of direct gap materials is between $10^4 cm^{-1}$ and $10^6 cm^{-1}$.

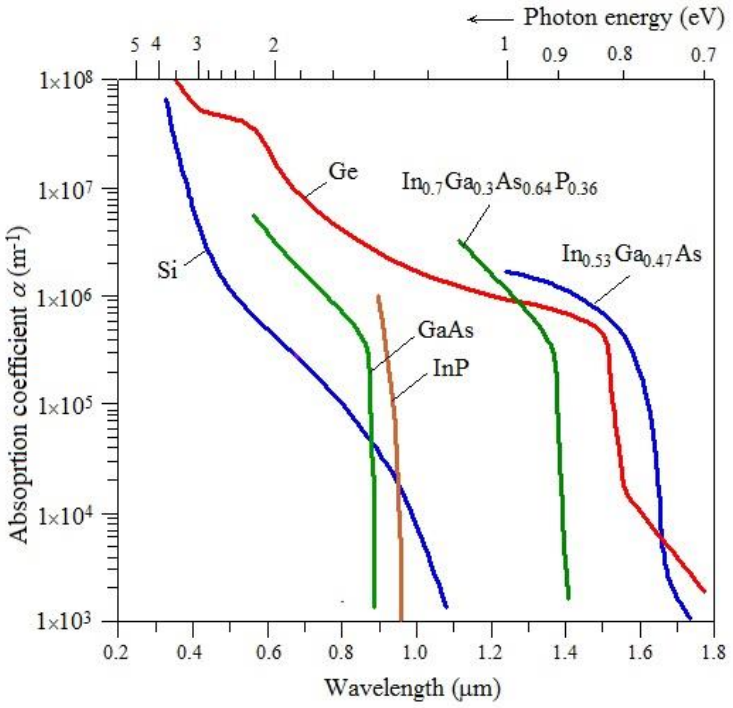

Figure 2.6: The absorption coefficient Versus Photon Energy for materials often used in photodiode. All materials shown are direct bandgap except Si and Ge [70].

Even though Germanium is an indirect bandgap material, its absorption coefficient is similar to that of a direct bandgap material due to its indirect gap being only 0.14eV lower than its direct bandgap [68]. The value of absorption coefficient has a large effect on the design structure, with

indirect bandgap semiconductors needing much thicker devices to absorb more photon. The photon excited minority carriers will only exist for a finite period of time τ, called lifetime, before recombination takes place. For the highest possible efficiencies, both radiative and non-radiative recombination should be minimal as carriers which recombine do not make a contribution to the photocurrent. However, radiative recombination is the most preferred mechanism as it enables the emitted photon to be absorbed again [69].

2.3 Carrier Generation and Recombination

Generation is the electronic excitation process to increase the quantity of an electron from the conduction band to the valence band, which stimulate an electron–hole pair, or gap from valence band into a confined state in the band hole, or from a limited state into the conduction band. These processes require an input energy.

Recombination is the relaxation process to reduce the number of carriers by decaying them from a high energy state to a lower energy state. Again, this may be from band to band, conduction band to trap state, or from trap state to valence band. In order to drop from the conduction band to the valence band, an electron needs to transfer its excess energy through the recombination process. The released energy can be given up either as a photon (radiative recombination), or as heat through phonon emission (non-radiative recombination), or as kinetic energy to stimulate an electron-hole pair (impact ionisation), or as kinetic energy to another free carrier (Auger recombination). For every generation process there is an equivalent recombination process.

2.3.1 Radiative Recombination

Radiative recombination is the recombination mechanism that dominates in direct bandgap semiconductors, the most noticeable example being the light created from a light

emitting diode (LED) [71]. There is more than one mechanism for radiative recombination. Band-to-band recombination occurs when the free electrons at the bottom of the conduction band recombine with the free holes at the top of the valence band, resulting in the emission of a photon with energy identically equivalent to the bandgap, or conduction band-to-acceptor, donor-to-acceptor, and donor-to-valence band. All these main mechanisms are depicted in Fig.2.7. In indirect band gap materials the band-to-band recombination process is slow since it involves phonons and other scattering processes, resulting in reduced radiative processes.

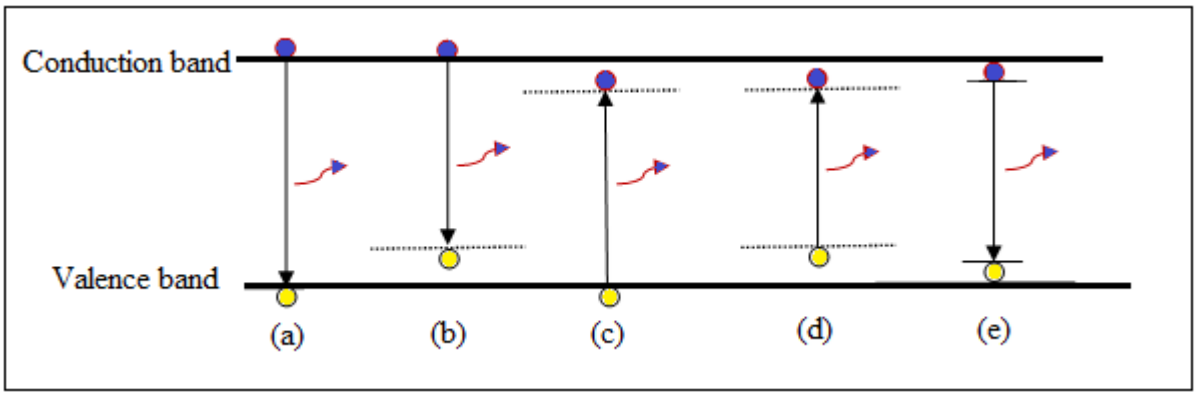

Figure 2.7: Schematic of radiative recombination processes (a) band-to-band transition (b) electron-to-acceptor transition (c) hole-to-donor transition (d) donor-to-acceptor transition (e) exciton recombination.

Excitons are electron-hole pairs bound by their mutual Coulomb interaction. If the exciton is not trapped by another centre then it is called a free exciton, which has the ability to move through the crystal. On the other hand, the exciton localized in the vicinity of a lattice defect or an impurity such as an ionised donor, acceptor or neutral atom is called a bound exciton. During radiative carrier recombination, excitonic transitions may contribute to the emission spectrum.

2.3.2 Non-Radiative Recombination

This is the recombination between an electron and hole where the energy of the electron-hole is released either via phonon emission or hot electron or hole excitation, in lieu of photon

emission [72-73]. The two main non-radiative processes are Shockley-Read-Hall (SRH) [74] and Auger recombination [75]. Some of them are illustrated in Fig. 2.8.

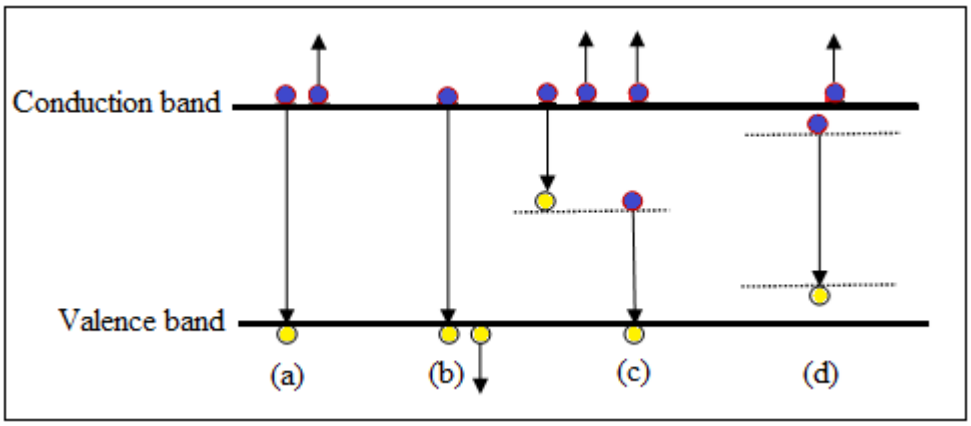

Figure 2.8: Schematic of non-radiative recombination processes (a&b) band-to-band Auger (c) electron-to-acceptor Auger (c) hole-to-trap and electron-to-trap Auger (d) donor-to-acceptor Auger

Auger recombination is the inverse of the impact ionisation process, involving the interaction of three carriers when the electron and hole recombine. Rather than emitting the excess energy as heat or as a photon, their energy is transferred to a third carrier in the conduction band. This electron then thermalises back down to the conduction band edge. A non-radiative process is most important in heavily doped/excited and narrow bandgap material (e.g. InAs). It strongly depends on the bandgap and the temperature which can be described by [76],

$$p_{nr} = p_{nr0} e^{\frac{-\Delta E}{k_B T}} \quad \ldots\ldots (2.3)$$

where p_{nr} is a coefficient independent of temperature (T=0), k_B is Boltzmann constant, and ΔE is activation energy. In experimental studies of non-radiative processes, some parameters such as emission efficiency (η) and carrier life time. In general, the emission efficiency can be described by:

$$\eta = \frac{p_r}{p_r + p_{nr}} \quad \ldots\ldots (2.4)$$

where p_r is the probability for a radiative transition. Hence the emission efficiency involving thermally activated non-radioactive transition would be in the form:

$$\eta = \frac{1}{1 + C\ exp(\frac{-\Delta E}{k_B T})} \quad \ldots\ldots (2.5)$$

where $C = p_{nr0} / p_r$ is a constant. There are many reasons for having nonradioactive recombination, such as lamentable material quality, high lattice mismatch between the structure and grown layer, intentional or unintentional impurities which produce localised trap states in the forbidden bandgap, and native defects such as vacancies, interstitials and anti-side defects.

2.4 Photodetector

The most important part of information processing is the detection of the received information. This is done using field effect transistors (FETs), bipolar junction transistors (BJTs) and diodes in electronic applications. These devices all have high gain, low noise and ability to tune and act as powerful detectors of information. However, these devices are not suitable for detecting signals with optical frequencies of more than 10^{14} Hz. The detection of optical information requires conversion of optical signal to electrical signal, which can then be processed by electronic devices. Photodetectors are the devices that measure photon flux or optical power by receiving optical signals (energy of absorbed photons) and converting them to electrical signals. Therefore, optical detectors based on photon effects which contribute to the photocurrent are preferred due to the very broad information bandwidth. Moreover, the availability of different types of semiconductors and the narrow optical bandwidth can be tolerated.

The photodetector operation utilises the photon effects based on the absorption of photons where the energy and momentum must be conserved. In such p-n or p-i-n junction diode type of detectors, the operation is based on the inter band (valence to conduction band)

absorption of light in the intrinsic (depletion) region of p-n junction. Fig.2.9 represents the conduction and valence band energies (separated by the energy gap, E_g,) in the intrinsic region of such a junction.

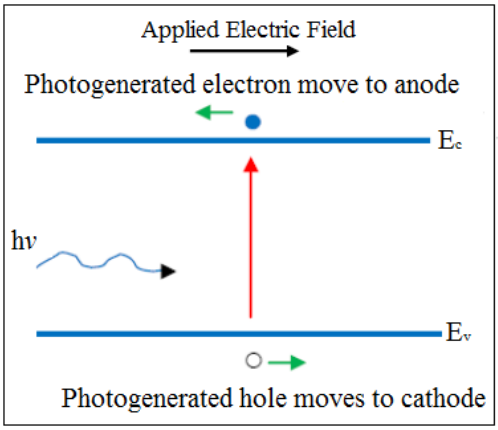

Figure 2.9: Photo-generation and motion of carriers under the influence of an applied electric field

A photon with energy, hν higher than bandgap energy, E_g is absorbed and then transfers an electron from the valence band into the conduction band, leaving a hole in the valence band. If there is an externally applied voltage to the p-n junction, the photo-generated electron hole pair will be able to move into their respective electrodes (electrons to anode and holes to cathode). Therefore when the anode and cathode are connected to the voltage supply, there will be current flow in the external circuit. The amount of current that can be generated depends on various factors such as the photon intensity, photon to charge carrier conversion factor (quantum efficiency), and the wavelength of the incident photons. The wavelength of photons above which they cannot be absorbed by the semiconductor is called the cut off wavelength. It is determined by the band gap energy of the semiconductor via [80]:

$$\lambda_{cutoff} = \frac{hc}{E_g} \quad \ldots\ldots (2.6)$$

The number of photons incident on the detector is defined as flux, Φ [81]:

$$\Phi_{\circ} = \frac{\mathrm{I}}{\mathrm{h}\nu} \quad \ldots\ldots (2.7)$$

where *I* is optical energy incident on the detector per unit area per unit second and h*v* is the energy of each photon. Most photons will be absorbed close to the surface of the photodetector because the absorption coefficient is high (especially for higher energy photons) and most carriers will be generated at a short depth from the surface. Therefore the detector will not be thick and bulky as long as the photo generated carriers are not created too close to the surface where they can recombine with the surface states resulting in a loss of mobile carriers. Hence, reduced thickness is an important requirement for photodetectors.

This is associated with the RC time constant of the detector. If the detector has a thicker depletion region, the resistance will be high and therefore the RC time constant (response time) will be long as well. Long RC time constant is not desirable and can be detrimental in high speed optical communication systems where high speed operation is essential to receive the digital signals arriving at frequencies greater than hundreds of GHz in modern optical communications networks. In an ideal photodetector, the photo-generated carrier density must be much higher than the thermally generated free carrier density. The Fermi-Dirac distribution function determines the thermal generation of electrons from valence into conduction band. In the intrinsic region of a photodetector, finite temperatures will excite electrons into the conduction band leaving holes behind. If there is an external electric field, these carriers similar to the photo generated carriers, will contribute to the current. As a result, there are two components to the current flow in the detector given by [82]:

$$J = J_{thr} + J_{pgc} \quad \ldots\ldots (2.8)$$

where J_{pgc} is the current due to the photo generated carriers and J_{thr} is the current density due to the thermally generated carriers. In order to have a sensitive detector, J_{pg} must be bigger than J_{thr}. However, for a given semiconductor, this is not always an easy condition to satisfy, especially when the detector is designed for operation at long wavelengths (hence small band gap for the semiconductor). The thermally generated current density is given by [82]:

$$J_{thr} = e(n_{thr}\mu_e + p_{thr}\mu_h) \quad \ldots\ldots (2.9)$$

where e is the electronics charge, n_{thr} and p_{thr} are the thermally generated electron and hole densities, μ_e and μ_h are the electron and hole mobilities and E is the applied electric field. If the focus is on the electrons only, the thermally generated free electron density can be written as [79]:

$$n_{th}^2 = N_c N_v exp\left(-\frac{E_g}{kT}\right) \quad \ldots\ldots (2.10)$$

where N_c and N_v are the effective density of states and T is the temperature. According to Eq.2.8 to Eq.2.10, at above room temperature, there will be a large density of thermally generated carriers across the band gap giving rise to large dark current, while for low photon intensities, J_{thr} in Eq.2.8 may be comparable to J_{pgc}. For detectors with longer wavelengths, this may become a more serious problem and the dark current may actually exceed the photocurrent. One possible solution is to cool down the detector. According to Eq.2.10, cooling down the detector will reduce n_{th} and J_{thr}. However, the band gap of semiconductors increases with decreasing temperature according Varshni's equation [83] as below:

$$E_g(T) = E_o(T = 0) - \frac{\alpha T^2}{T+\beta} \quad \ldots\ldots (2.11)$$

where E_g(T) and E_o are the band gap at a finite temperature T, and when T becomes zero respectively. The parameters α and β are material constants, the values of which depend on the semiconductor. Therefore if excessive low cooling temperature is used, the detector may be able to detect the desired long wavelengths. As a result one has to compromise between the detector sensitivity (temperature) and operating wavelength.

2.5 p-i-n Photodetector

The p-n junction photodetector may be referred to as the p-i-n photodiode if intrinsic region is placed within the depletion length, in between the junction of the p and n regions. When the junction is applied with reverse-biased, V_{bi}, a reverse current (leakage or the dark current), I_o flows through the circuit. Its value can be obtained from the diode equation as [79]:

$$I_o(V) = I_p(W_n) + I_n(-W_p) \quad \ldots\ldots (2.12)$$

where I_p and I_n are the generated current and W_p and W_n are the depletion width at the p an n regions respectively. The detection process in the p-n photodiode takes place in the intrinsic absorber region (the depletion width) in the junction as illustrated in Fig.2.10. Assuming that the light is incident on the p side of the junction of the reverse biased diode as shown in Fig.2.10 (a), if the photon energy is greater than the band gap of the semiconductor, then the incident optical power P_o will be absorbed according to [84]:

$$P_{absorbed} = P_\circ(1 - r)\left(1 - \mathrm{e}^{-\alpha \mathrm{d}}\right) \quad \ldots\ldots (2.13)$$

where α is the absorption coefficient, d is the width of the depletion width, and r is the reflectivity at the air-semiconductor interface respectively. If an anti-reflective coating is used, r is less than 1 and the expression becomes [84]:

$$P_{absorbed} = P_\circ\left(1 - \mathrm{e}^{-\alpha \mathrm{d}}\right) \quad \ldots\ldots (2.14)$$

Each absorbed photon creates an electron and hole pair. Consequently, the electron-hole pair generation will have the same positional dependence as the photon absorption as shown in Fig.2.10 (b). Additionally, as shown in Fig.2.10 (b, c), electrons and holes will be created throughout the structure; in the depletion (intrinsic) region as well as in the p and n regions of the junction. Electrons and holes created by photons within the diffusion length of the depletion region and those within the depletion region will be swept across the depletion region under the influence of the high electric field.

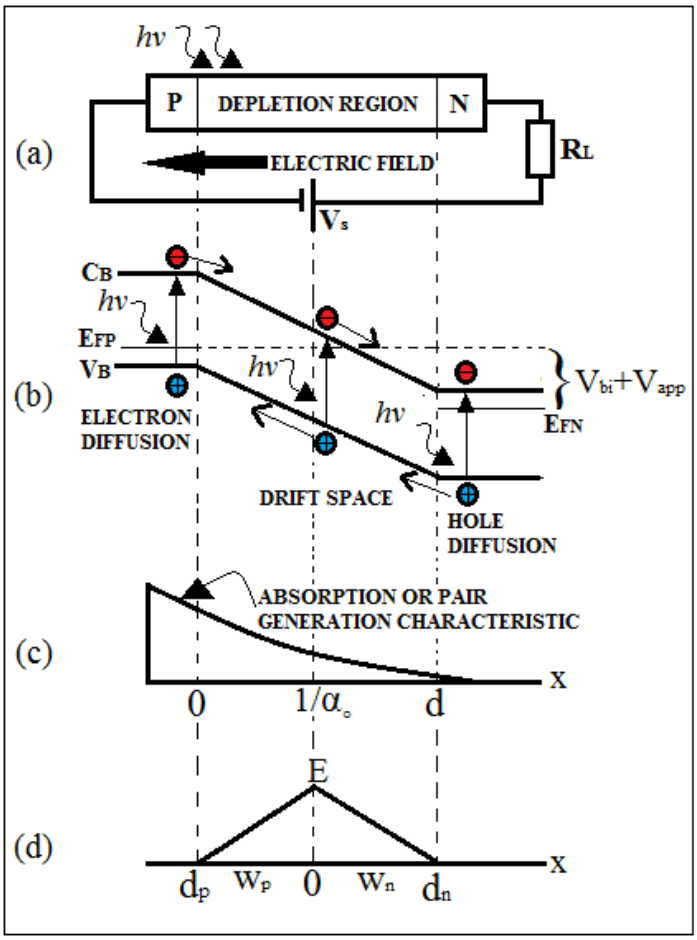

Figure 2.10: Applied reverse biased voltage under illumination. (a) Diagram of reverse pn junction with applied electric field (b) electron and hole pair generation in p, intrinsic (depletion) and n region (c) Optical power absorption and the electron hole pair generation as a function of distance from the top surface (d) The electric field distribution along depletion region [88]

A photocurrent will flow in the load resistor. The magnitude of the photocurrent will be proportionate to the optical incident power. Assuming that an antireflective coating is utilized, the expression for photocurrent is [85]:

$$I_{ph} = e\left(\frac{P_\circ}{hv}\right)\left(1 - \mathrm{e}^{-\alpha \mathrm{d}}\right) \quad \ldots\ldots (2.15)$$

where $n_p = e\left(\frac{P_\circ}{hv}\right)$ is the incident photon number per second (incident photon rate). This implies that the photocurrent increases with increasing light intensity as depicted in Fig.2.11.

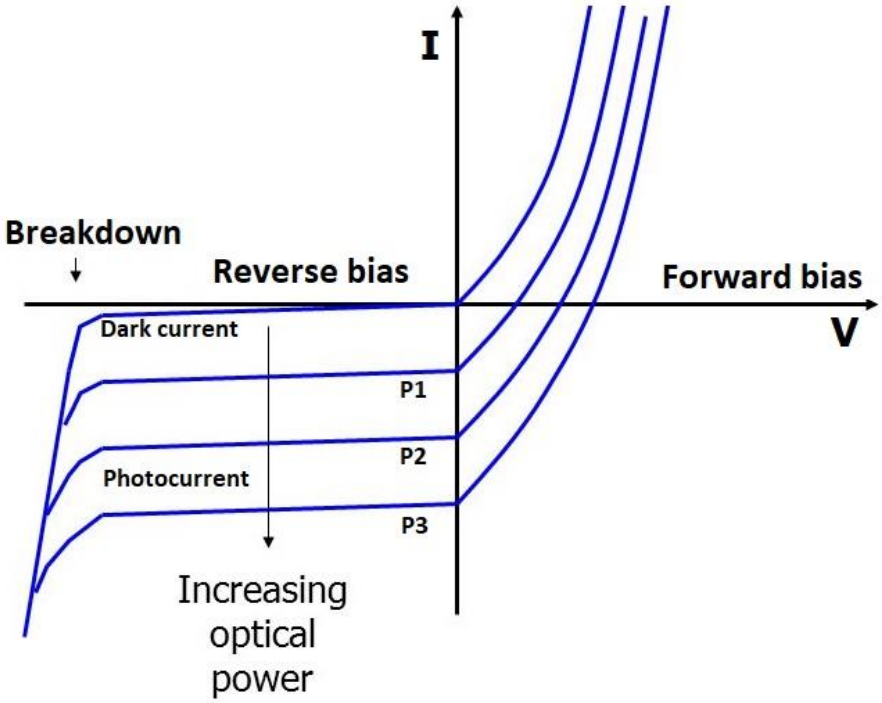

Figure 2.11: Photocurrent in a p-i-n photodetector with P3>P2>P1

2.6 Quantum Efficiency and Responsivity

The quantum efficiency, η corresponds to the ratio of photogenerated electron-hole pairs per incident photon. It can be defined as [81],

$$\eta = \frac{\frac{I_p}{e}}{\frac{P_\circ}{h\nu}} = 1 - e^{-\alpha d} \quad \ldots\ldots (2.16)$$

where I_p is the photogenerated current , P_o is the incident optical power, *hv is* the the photon energy, α is the absorption coefficient and *d* is the width of the depletion region. In an ideal detector without internal amplification, η should be as close to 1 as possible. Responsivity, *R*, is defined as the current produced at the output of the detector per optical power incident on the detector and can be written as [81]:

$$R = \frac{I_p}{P_\circ} = \frac{e\eta}{h\nu} = \frac{e\eta\lambda}{hc} = \frac{e}{h\nu}(1 - e^{-\alpha d}) \quad \ldots\ldots (2.17)$$

This equation implies that the responsivity increases linearly with the wavelength of the incident photons but abruptly tends to zero when the incident photon wavelength exceeds the cut off wavelength of the semiconductor.

2.7 Rise Time and the Bandwidth

Besides as the quantum efficiency and the responsivity, the rise time and the bandwidth of a photodetector are two other important characteristics. In order for a detector to be of use in high speed optical communication systems, its rise time needs to be short and the bandwidth to be high. The typical photodiode junction as shown in Fig.2.10 (d) with an external load resistance of R_L can be thought of as an RC circuit where the capacitance, C is the junction capacitance that can be associated with the depletion width, W as follows [79]:

$$W = W_n + W_p = \left\{\frac{2\varepsilon\varepsilon_\circ}{e} V_{bi}\left[\frac{N_A}{N_D(N_A+N_D)} + \frac{N_D}{N_A(N_A+N_D)}\right]\right\}^{\frac{1}{2}} \quad \ldots\ldots (2.18)$$

where W_n is the depletion width of the n region, W_p is the depletion width of the p region, ε is the relative permittivity, ε_o is the material permittivity, V_{bi} is the applied reverse biased, N_A is the acceptor density, and N_D is the donor density. As the reverse bias voltage is increased, the depletion width will also increase. The junction then will be observed as a parallel plate capacitor as in Fig.2.12 where the separation of the parallel plates, d corresponds to the depletion (intrinsic) layer width, W of the junction. For a junction with acceptor (donor) concentration on the p side being much higher than the donor concentration on the n-side (p-type), the depletion width can be estimated to:

$$W \approx W_{n,p} = \left(\frac{2\varepsilon\varepsilon_\circ}{e} V_{bi}\frac{1}{N_{D,A}}\right)^{\frac{1}{2}} \ldots\ldots (2.19)$$

The simplification of Eq.2.19 into the capacitance per unit area expression can be written as:

$$\frac{C}{A} = \left[\frac{\varepsilon\varepsilon_\circ N_{D,A}}{2V_{bi}}\right]^{\frac{1}{2}} \quad \ldots\ldots (2.20)$$

In order to achieve high speed detection, the capacitance, *C* value should be small (typically a few pF), and a large reverse voltage bias applied. To obtain the small value of *C*, the area, *A* should be smaller and an optimised intrinsic width, *d* is applied to reduce the RC delay time. For p-i-n photodetector, capacitance, *C* in Eq.2.20 can be written as junction capacitance, C_j and RC delay, t_{RC} can be obtained from following equation [81]:

$$C_j = \frac{\varepsilon_o \varepsilon_r A}{d} \ldots (2.21)$$

$$t_{RC} = R_L C_j \ldots (2.22)$$

where *A* is is the cross sectional area, $\mathcal{E}_r$ is the permittivity of the material, $\mathcal{E}_o$ is the permittivity of the vacuum and *d* is the depletion region. The bigger area will create a higher capacitance hence resulting in a longer delay time and lower bandwidth.

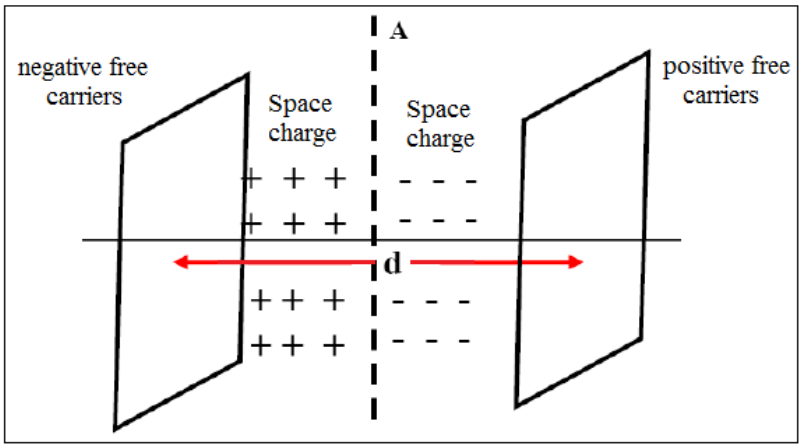

Figure 2.12: The p-n junction looks like a parallel plate capacitor with the area of the plates, *A* and the separation of the plate, *d*.

The time dependence of the electrical signal, V_{out} which is produced by a step-like light signal incident on the detector as in Fig.2.10 (a, d) [84] can be expressed by:

$$V_{out} = V_\circ \left(1 - e^{-\frac{t}{\tau}}\right) \quad \ldots\ldots (2.23)$$

where the time constant τ is the sum of the RC time constant, τ_{RC} and the transit time of charge carriers $\tau_{tr} = \frac{W}{V_d}$ across the length of the device written as:

$$\tau = \tau_{RC} + \tau_{tr} \quad \ldots\ldots (2.24)$$

The cut off frequency of the detector when RC delay dominates can be calculated by [81]:

$$t_{RC} = \frac{R_L \varepsilon_o \varepsilon_r A}{d} \ldots (2.25)$$

$$f_{RC} = \frac{1}{2\pi t_{RC}} \ldots (2.26)$$

For the maximum bandwidth application, a direct connection to the measurement device is used by having a 50Ω input impedance. The R_L can be maximised to increase the amount of voltage for a given input light if bandwidth is not important such as the continuous wave measurement. The high frequency response limitation of the photodetectors also depends on the transit time, t_{tr} of the carriers (especially holes) across the absorption layer when the transit time delay dominates. In this case, the average saturated drift velocity, v_{sat} of the slower carrier (hole saturated drift velocity) becomes the important parameter to determine the high frequency response of the photodetectors. The longer depletion width will have a bigger transit time hence a decreased bandwidth. Thus, the transit time limited cut off frequency, f_{tr} can be expressed as[86]:

$$t_{tr} = \frac{d}{v_{sat}} \ldots (2.27)$$

$$f_{t_r} = \frac{1}{2\pi t_{tr}} \ldots (2.28)$$

In the condition where neither the RC delay nor the carrier transit time delay dominates, the cut off frequency of a p-i-n photodetector can be stated as [87]:

$$\triangle f = \frac{1}{2\pi(t_{tr} + t_{RC})} \ldots (2.29)$$

2.8 Avalanche Photodetector

The wide use of p-i-n photodiode in optical communication systems is due to its low noise, high speed and low dark current. However, it operates at low bias without internal gain. Therefore, a photodetectors with high internal gain is desired when very low levels of light are to be detected in order to improve the sensitivity. The high internal gain can be obtained by an avalanche photodiode (APD). APD operates by converting each detected photon into a cascade of moving carrier at voltage levels close to the breakdown. The charge carriers therefore accelerate and acquire enough energy to excite new carriers via the process of impact ionisation[88].

Impact ionisation is the process in a material by which one energetic charge carrier can lose energy by the creation of other charge carriers. For example, in semiconductors, an electron (or hole) with enough kinetic energy can knock a bound electron out of its bound state (in the valence band) and promote it to a state in the conduction band, creating an electron-hole pair. If this occurs in a region of high electrical field, it will result in avalanche breakdown. This process is exploited in avalanche diodes, by which a small optical signal is amplified before entering an external electronic circuit. In an avalanche photodiode, the original charge carrier is created by the absorption of a photon. In some sense, impact ionisation is the reverse process to Auger recombination.

Fig.2.13 shows the schematic drawings of fundamental material parameters multiplication process for $\alpha \approx \beta$ and $\alpha >> \beta$. α and β are the impact ionisation coefficients of electrons and holes, respectively. The impact ionisation coefficients are the reciprocal of the average number of electron-hole pairs created per unit distance travelled by electrons and holes due to the electric field before they impact with the lattice to produce secondary electron-hole pairs. α and β can also be defined as ionisation probabilities per unit length (rates of ionisation, cm^{-1}). In Fig.2.13(a), since $\alpha \approx \beta$, the number of secondary electron-hole pairs generated by

electrons and holes are roughly equal. In Fig.2.13(b), since α >> β, a chain of impact ionisation events is initiated under high electric field caused by electrons. At the end of the avalanche process, five electrons are collected resulting in an avalanche gain of five. These electric field dependent coefficients are subjected to bandgap energy of semiconductor for impact ionisation [89]. Semiconductors with wide bandgaps require high electric fields to initiate the impact ionisation process.

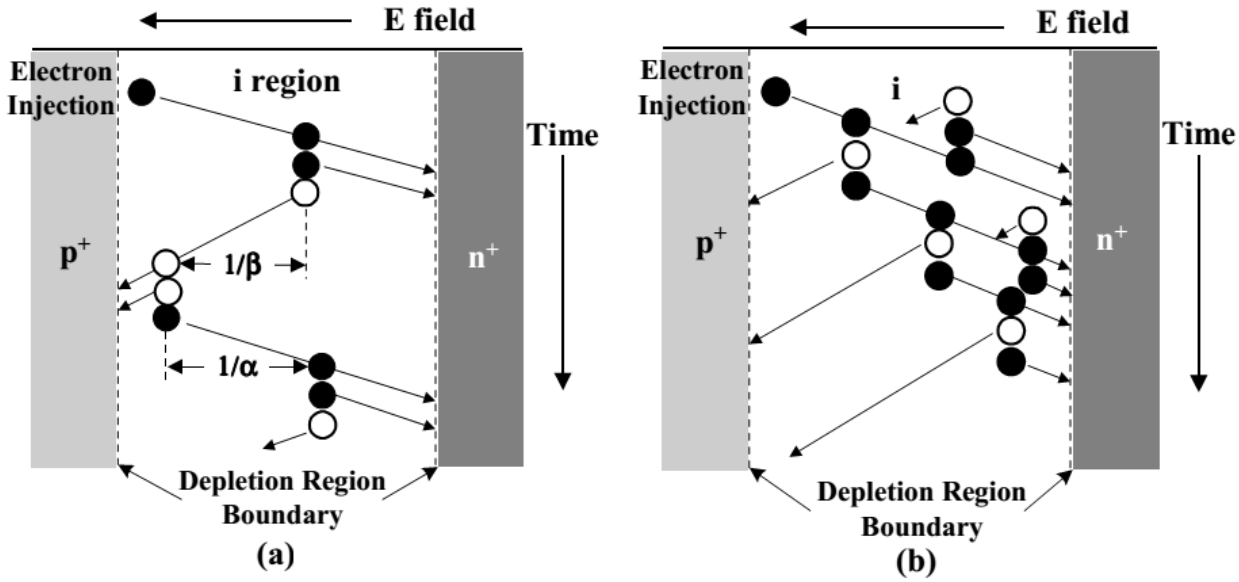

Figure 2.13: Avalanche multiplication process for (a) α≈ β and (b) α>> β [89]

Most of the ionisation is achieved by electrons when holes do not ionise appreciably. The avalanching process then proceeds principally from the p-side to the n-side. Therefore, it is desirable to fabricate APD from materials that only permit one type of carrier (either electrons or holes). If electrons have the higher ionisation coefficient, for example, optimal behaviour is achieved by injecting the electron of a photo carrier pair at the p edge of the depletion layer and by using a material whose value of α is as low as possible.

As for any photodetector, the geometry of the multiplication (avalanche) region should be thin to minimize the possibility of localized uncontrolled avalanches (instabilities or micro plasmas) being produced by the strong electric field. Greater electric-field uniformity can be

achieved in a thin region. These two conflicting requirements call for an APD design in which the absorption and multiplication regions are separated, Separate-Absorption-Multiplication-APD (SAM-APD). Photons are absorbed in a large intrinsic or lightly doped region. The photogenerated carriers drift across it under the influence of a moderate electric field, and finally enter a thin multiplication layer with a strong electric field where avalanching occurs.

2.9 Impact Ionisation

As discussed in the previous section, the phenomenon used to understand the carrier multiplication is the impact ionisation process. Over the past two decades, impact ionisation in quantum well devices has been investigated by several groups [90-92] where it operates with strong electric fields and high drift velocities in the conduction band, resulting in electron-hole pairs [93] and avalanche breakdown. In this case, the impact ionisation threshold energy is defined as the minimum energy needed for impact ionisation to occur and comparable to the energy bandgap. As a result, it may be categorised as a band-to-band process, or band-to-trap process, depending on whether the second carrier is initially in the valence band and makes a transition from the valence band to the conduction band, or whether it is initially at a localised level (trap, donor, acceptor), making a transition to a band state as illustrated in Fig.2.14. [81].

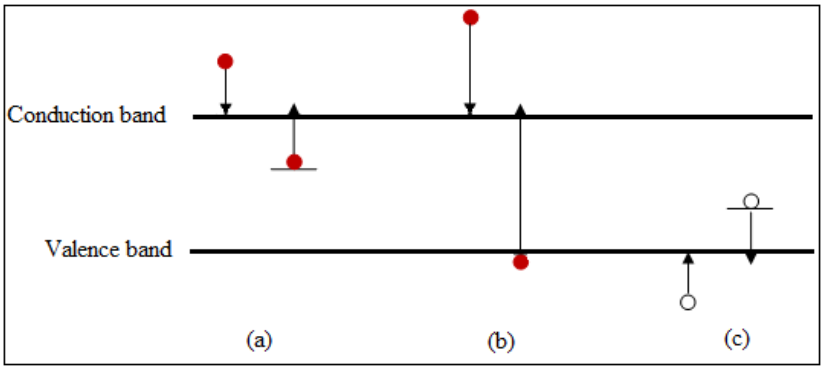

Figure 2.14: Schematic of impact ionisation processes (a) the hot electron impact ionisation of a trapped electron (b) the hot electron impact ionisation from the valence band (c) the hot hole impact ionisation of a trapped hole.

Impact ionisation of shallow impurities is responsible for the impurity breakdown at low temperature, where less energy and carrier heating is necessary for the carriers to be ionised. Band-to-band impact ionisation eventually induces the avalanche breakdown. Therefore, the shallow impact ionisation process can occur for fields starting from a few 100 V/cm, while the band-to-band impact ionisation process typically requires fields which are in the range of a few 10^5 V/cm.

In 1980, Juska and Arlauskas [94] founded the first clear experimental observation of impact ionisation in semiconductor, which was confirmed by further experimental studies [95-96]. Baraff [97] successfully calculated the impact ionisation rates in semiconductors, by computing numerically a free-carrier energy distribution function from the Boltzmann transport equation. The results show a quadratic fit curve and have been frequently used to interpret experimental data for several decades. The central assumptions of Baraff's theory are the following: (i) while drifting, electrons can gain energy only from the external electric field, (ii) electrons are subject to elastic scattering collisions characterised by their kinetic energy, which does not exceed the optical phonon energy, and (iii) carriers with kinetic energy above the optical phonon energy undergo inelastic collisions only by emitting an optical phonon of the constant energy. The impact ionisation takes place immediately after the electron acquires the kinetic energy equal to the ionisation threshold energy.

Ridley [93] suggested an analytical solution for the ionisation process known as a lucky-drift model as an alternative to the numerical Baraff curves. According to this model, the dominant contribution to the impact ionisation probability comes from the carriers, which upon drift in the electric field, undergo many collisions which destroy the momentum but enable the threshold energy for ionisation to be reached. These phenomena are investigated by measuring light emission in between 1.1 eV to 3.1 eV energy range for different points in the electrical characteristics [98]. This model was further advanced by Burt [99] and tested against a kinetic

Monte Carlo simulation [100]. The argument for ionisation presented by Ridley and Marsland [101] using Burt`s version of lucky drift fitted the experimental results. The excellent fit of the experiment obtained confirms that the nature of impact ionisation is best modelled using the lucky drift method. A Monte Carlo simulation was used by Shichijo and Hess [102] in 1981 to include the full band structure in the impact ionisation calculation. They showed that, under special conditions, the space charge associated with spatial oscillation of the field occurs.

The lucky-drift theory was offered as a simple method to calculate the impact ionisation. Later, this method was modified to include low probability of impact ionisation at threshold compared to relaxation energy [98]. No significant inconsistency was found between the simulation results from Baraff, Ridley, and Burt. Hostut and Balkan [103] reported light emission from an n-doped GaAs layer associated with impact ionisation when the device was biased in the positive regime. They showed that the light emission is due to the recombination of the impact ionisation of holes and the travelling space charge of electrons. The responsivity as a function of impact ionisation was first represented by Levine *et. al.*[104] in 1987. All these phenomena studies of impact ionisation in solid states has led to an application in optoelectronics and in medical imaging applications [105-106].

The impact ionisation process in multiple quantum well infrared photodetectors (QWIPs) was first studied by Dong *et.al.* [107] using an InGaAs/GaAs semiconductor sample. It is noteworthy that the recombination time of an electron-hole pair is in the order of nanoseconds [108] and the capture time of an electron back into the well is in the order of picoseconds [109]. Consequently, in most investigations, the recombination process has been overlooked, while the capture process plays an important role.

2.10 Photocurrent Resonant Tunnelling

Thermionic emission and tunnelling are the two main dark current mechanisms in GaInNAs/GaAs and GaAs/ $Ga_{1-y}Al_yAs$ barrier structures. The former becomes dominant at high temperature and low voltage, while the latter becomes dominant at low temperature and high voltage. Most previous studies used the standard thermionic emission [110] theory to analyse the dark current as a function of temperature (I-T characteristics) measured in various barrier structures [111-113]. However, for thick barriers, in which the electron mean free path is much smaller than the barrier thickness, collisions in the barrier are expected to dominate the vertical transport. In this case, the drift–diffusion theory is more appropriate to evaluate the thermally activated current [113-116]. When there are unintentional doped acceptors in the well, they will interact with the existing electrons in the quantum well (QW) via diffusion, and hence create a negative space charge in the barrier. The effect of negative space charge is to increase the barrier height for thermionic emission over the barrier [115, 117] and that will lead to change in the potential profile. Bishop et al. [116, 118-119] showed that, at high temperatures and low voltages, when thermionic emission dominates over the whole structure, most of the applied voltage is dropped across the QW.

Tunnelling is the process whereby a quantum particle can cross a potential barrier, which classically would be completely impenetrable because of its higher energy, to a state of equal or lower energy. The wave function of the particle extends either into, or through, the barrier when the barrier potential is finite. A non-zero particle current density through the barrier then results from the tunnelling process. Quantum mechanical tunnelling has been the basis of many semiconductor devices, starting with the Esaki tunnel diode, named after its inventor Leo Esaki [120-121]. When a particle interacts and is confined by two or more barriers of finite height and least thickness, its wave will be multiplied off each potential barrier by tunnelling. When the confining region's dimension is some multiple of the wavelength, the particle "resonates" in the

regions where its energy is greater than the local potential. At these wavelengths, the tunnelling current is amplified. Both these size quantization effects and resonance comes from the same source: the constructive interference of forward and backward waves. This is the source of the quantized energy levels that result from the confinement of the particle.

Resonant tunnelling figures prominently during the transportation of carriers through the semiconductor super lattices. It is also central to the application of these structures as electronic devices. Tunnelling calculations for semiconductor super lattices can provide this information and can be implemented in design of improved structures. By finding the transmission coefficient through the structure as a function of energy, one can locate the energy levels of the resonances. It is also possible to find the effects of an external electric field on the transmission coefficient as proposed by F. Capasso et.al. [122-123].

Resonant tunnelling occurs when the energy of the bound state in the barrier corresponds with the bound state at the well, or when the carrier density in the barrier exceeds that in the well layer. Because of the finite well thickness and narrow state in the well, the current tunnelling from the localised state into the well can be observed as a sharply peaked function of the voltage drop across the barrier. If the voltage is increased beyond the resonance peak, the current drops, as does the electron density in the quantum well. However, electron resonant tunnelling has been observed by L.L. Chang *et. al.* [124] in double barrier structures of AlGaAs/GaAs. Fox et al. [125] used tunnelling from the lowest sub-band to explain the results of photon generated carrier sweep-out measurements on samples with varying barrier thicknesses.

The resonant tunnelling of electrons between the valence band states and the conduction band due to a space charge potential has been theoretically and experimentally studied for a GaAs quantum well structure [126]. An applied reverse voltage tends to deplete the n-type layer, and the Fermi level in the conduction band moves below the Fermi level in the valence band at the p-side, as shown in Fig.2.15 resulting in possible tunnelling of occupied valence states into

the empty sub-band conduction band. The build-up of electronic space charge in the QW with double barrier devices when resonant tunnelling occurs was established by Kuan *et. al* [127]. This space charge can be transferred through barriers of different thickness or different potential heights.

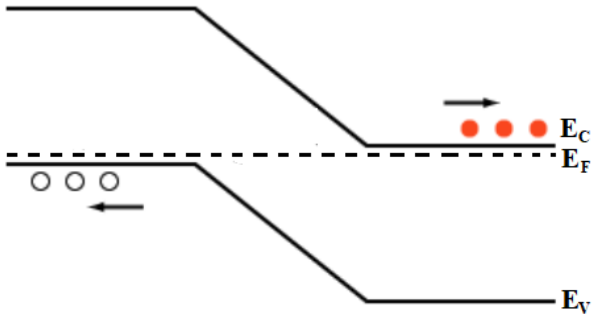

Figure 2.15: Energy band diagram of a p-n junction under applied reverse bias

For optical confinement reasons the quantum wells have a lower band gap than the rest of the cell. However, electrons can escape out of the wells after gaining enough energy from photons, thus contributing to the extra current. Geisz, and Friedman [128] initiated a technology that enhanced the quantum efficiency of solar cells by using quantum wells. The p-i-n QW consisted of a p-i-n semiconductor structure with a material of a lower bandgap added into the intrinsic region to confine the electrons to two dimensions. The quantum wells will absorb photons with lower energy than the bulk bandgap, to get higher currents by increasing the spectral response of the solar cells. The fields maintained across the intrinsic region cause photo-generated carriers that escape from the well to drift to the appropriate region before recombining, leading to an increase in the output current with high quantum efficiency [125]. The performance and characteristics of the p-i-n multi quantum well (MQW) devices, for various QW configurations, in relation to the dynamics of capture, escape, absorption and recombination of carriers in the quantum wells have been investigated [129]. It is relatively straightforward to show that the combination of the QWs and the barrier as the intrinsic region will enhance the p-i-n device current, and the output voltage is determined by the variation in the electrons and holes

Fermi level separation across the cell, as reported by M.A. Fox et al. [125]. They pointed out that in practical situations, the p-i-n device provides a high output voltage by improving the photocurrent over the QW structure material.

2.11 Dilute Nitrides Semiconductors

Significant effort has gone into understanding the physical origin of the Nitrogen (N) - introduced effects on the electronic structure of the III-V dilute nitride alloys. While the presence of minute amounts of N in GaAs results in bandgap reductions of $GaAs_{1-x}N_x$ at about 0.1eV per % of N for $x \leq 0.03$ [130], the addition of Indium into GaN_xAs_{1-x} compensates the nitrogen-induced contraction of the lattice parameter [131] while further reducing the bandgap, making it possible to grow lattice-matched GaInNAs/GaAs material systems which have energy gaps in the long wavelength range. These findings have generated significant interest and opened up the interesting possibility of using N containing group III-V alloys for various long wavelength optoelectronic applications [132-134]. Contrary to the general rules of III-V alloys where the bandgap increases with the decreasing lattice constant, a small amount of nitrogen incorporated into GaAs or GaInAs dramatically decreases the bandgap as depicted in the Fig.2.16, due to the large electronegativity of N and its small size that could cause a very strong negative bowing parameter.

By incorporating nitrogen and indium into GaAs, GaInNAs will produce the rapid decrease of bandgap to reach the long wavelength emission region with simultaneous control over bandgap and lattice constant. This allows growth of very deep GaInNAs/GaAs quantum wells, which has been proven to have excellent high temperature performance. GaInNAs is a potential material for a multi-junction stack as well as a metastable material system that can be grown lattice matched to GaAs or Germanium substrates for telecommunication application.

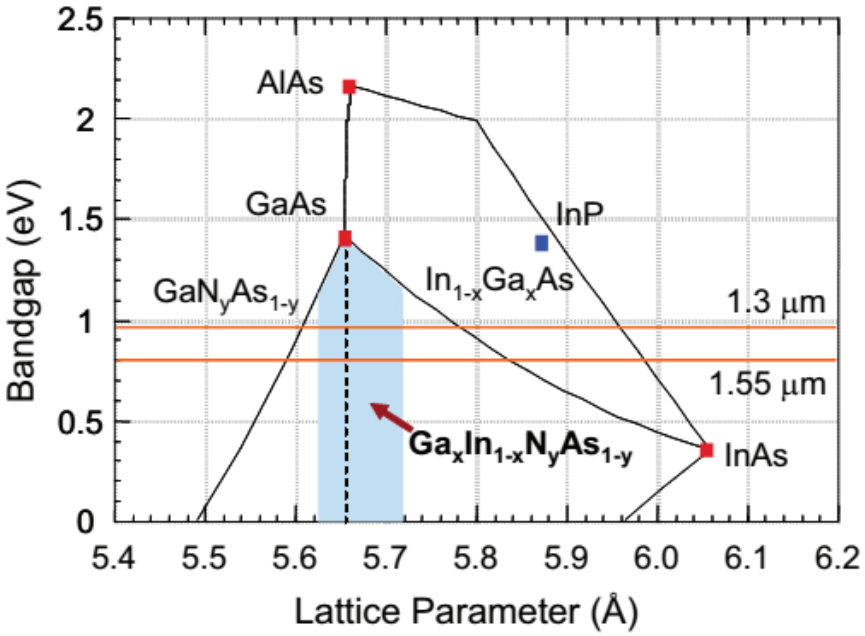

Figure 2.16: Bandgap versus lattice constant for the selected III-V alloys [135].

Majority carrier electron transport is still controversially discussed in the literature and is thought to be strongly influenced by the quaternary composition, resulting in different bandgaps as well as by the post-growth annealing procedures, resulting in different distribution of the alloying elements. Minority carrier transport might be governed by intrinsic structural characteristics of the dilute nitride material systems, namely a chain-like ordering of N in the growth direction. This configuration, which reduces the strain energy of the crystal, might act as a non-radiative recombination centre and/or a carrier trap. Dissolution of this N-ordering by annealing in quaternary material via altering the N-neighbour environment to an In-rich one, results in improved minority carrier properties [136].

The introduction of dilute concentrations of nitrogen into III–V materials is known to cause a large drop in the electron mobility. In addition to the scattering from nitrogen sites and clusters, the conduction band becomes highly non-parabolic, which further affects the transport properties [137]. The causes of this mobility drop appear to be two fold. Firstly, the introduction of nitrogen is known to have a profound effect on the conduction band, manifesting most obviously in the large redshift of the energy gap [138]. This phenomenon is well explained by the band anti-

crossing (BAC) model due to Shan et al. [139], which predicts a splitting of the conduction band around a localised nitrogen energy level. Secondly, whilst polar-optical phonon scattering is usually the dominant scattering process at room temperature in polar semiconductors, it has been predicted by Fahy and O'Reilly [140] that it is scattering from nitrogen complexes that will limit the mobility in dilute nitrides.

The addition of nitrogen also has a large impact on the carrier dynamics, often resulting in a considerable increase in shallow traps, which readily capture excitons. A number of mechanisms have been proposed to explain the creation of shallow traps, which gives rise to localised states. Many of these are associated with deposition problems, such as well width fluctuations and compositional inhomogeneities, caused by the large miscibility gap associated with the incorporation of nitrogen. However, some of these growth issues are not intrinsic to dilute nitrides and advances in deposition technology have shown that these associated problems can be significantly reduced [141].

In order to obtain GaInNAs based devices operating at 1.3 μm, it is essential to incorporate a substantial amount of either Nitrogen (N) or Indium (In) in QW materials. However the optical quality and performance might be degraded. Thus, roughly 30% of Indium is required by keeping the Nitrogen amount low. Incorporation of Indium into GaAs will increase the strain by lowering the conduction band (C_B) and increasing the valence band (V_B). By incorporating Nitrogen into GaInAs, the tensile strain will be increased by lowering both the C_B and V_B since the C_B falls more expeditiously because of the high effective mass. This incorporation is a difficult task to achieve, as integrating tiny fractions of nitrogen in GaInAs results in a rapid reduction in the fundamental bandgap energy and lattice match to the GaAs (Fig.2.16). It elevates huge bowing in the energy which alters the optical properties of the materials for variations in the bandgap energy profile.

The effect of Nitrogen on the bandgap appears to be seen entirely in the conduction band. In order to amend the performance of such devices, it is convenient to increase the fraction of Indium in the sample, so the quantity of nitrogen composition is reduced. Unfortunately, as explained before, this solution leads to an incremented strain between the GaInNAs quantum wells and GaAs barrier, which can lead to an incremented number of misfit dislocations. W. Li [146-147] proposed a solution for this quandary by utilising a strain compensated GaInNAs/GaNAs quantum well structure. The GaNAs barrier can a result in reduction of the barrier potential. The GaNAs layers can act as a source of nitrogen, significantly reducing Nitrogen out-diffusion from the well. Finally, the presence of tensile strain in GaNAs barriers could balance the highly compressive strain for least defects in GaInNAs/GaNAs as compared to GaInNAs/GaAs.

It has been discovered also that an excess flux of Antimony (Sb) introduced in the growth process enhances the optical properties of GaInNAs/GaAs, where Sb acts in a surfactant-like manner [148], lowering surface free energy and supressing surface diffusion, thus preventing 3D growth, island formation, and phase separation [149]. All these advantages are visible in the PL spectrum of the GaInNAs(Sb), which enhances with increasing Sb flux as shown in Fig.2.17. All these characteristics make GaInNAs(Sb) more attractive and perhaps more competitive than the novel GaInNAs material. A further research on other III-V semiconductor compounds with Antimony added have been done, such as GaNAsSb [150-151], which has been also used as a barrier for long wavelength GaInNAs:Sb based MQWs [152-153], with an Indium incorporation of 46% [154]. However, in the GaNAsSb material system, antimony (Sb) atoms are used to counter-balance the tensile strain, instead of the indium atoms. Nevertheless, the presence of Sb atoms promotes the incorporation of N atoms and decreases the nitrogen-related defects [155].

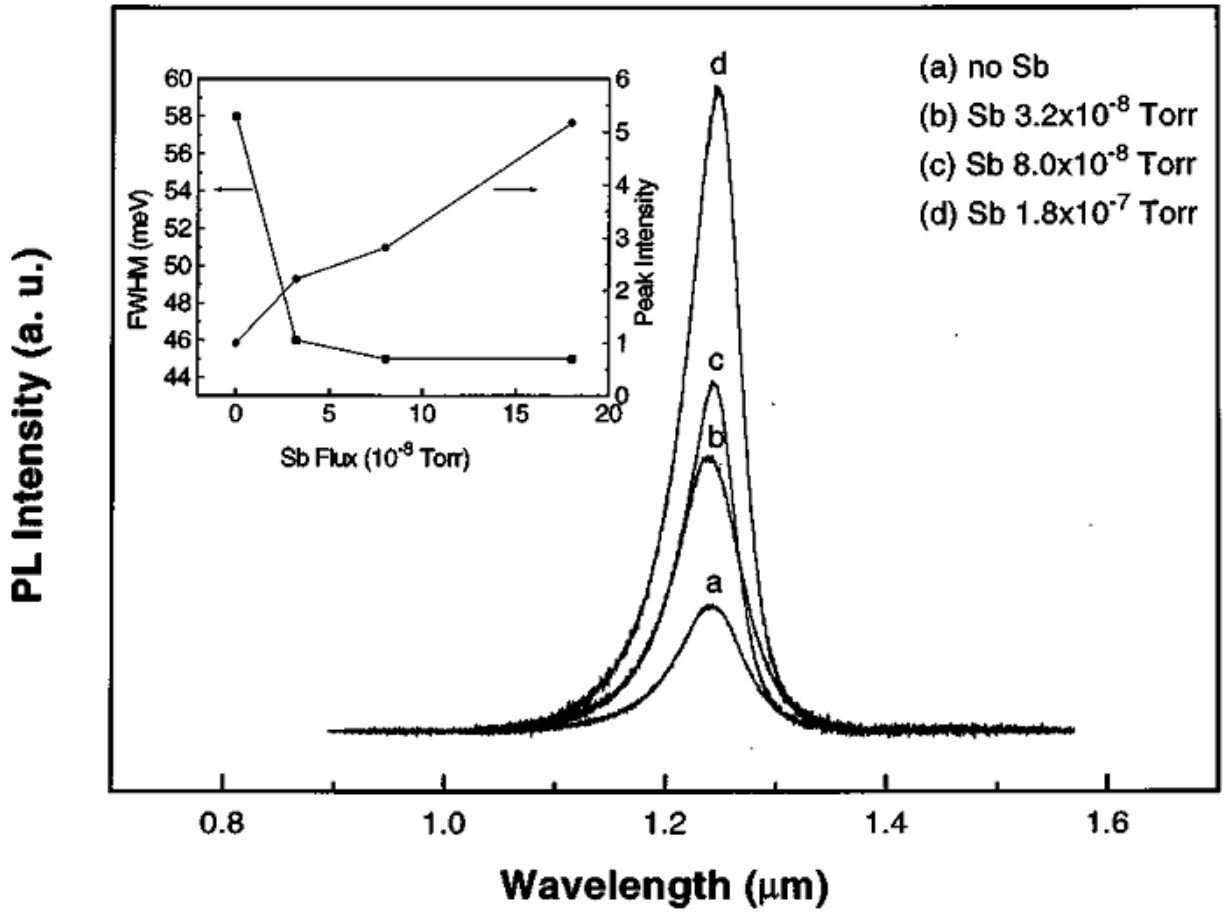

Figure 2.17: 300K PL of various GaInNAs:Sb/GaAs QW samples at different Antimony, Sb beam fluxes [156]

2.11.1 Effects of Nitrogen in GaInNAs

The most common and useful compound semiconductors in optoelectronics are the III-V materials, made from the elements from the Group III (Ga, In, Al) and the Group V (As, P, Sb, N) in the periodic table. GaInNAs/GaAs QW based devices were originally proposed as replacements for GaInAs/InP QW based devices, due to their reduced temperature sensitivity[157].

The most interesting material in the dilute nitride family is gallium indium nitride arsenide (GaInNAs). The first quaternary $Ga_xIn_{1-x}N_yAs_{1-y}$ alloy was first proposed by M. Kondow [160] in 1995. Since then, it has been the subject of much research and development. The composition of GaInNAs enables it to be fairly closely lattice matched to GaAs and to have a direct band gap in the range of telecommunications wavelengths (1.25–1.65 μm), as per required

in many network applications. By incorporating a small percentage of nitrogen, significant changes occur in the band structure as compared to GaAs. These include an increase in the electron effective mass [161], nonlinear pressure dependence of the bandgap [162], a large redshift of the bandgap [139, 145], the addition of N-induced formation of new bands, and a strong line width broadening of all the transitions [163]. There are many models used to understand the unusual behaviour observed in dilute nitride alloys. One of the models was based on the assumption that the GaInNAs emission energy was decreasing linearly with increasing nitrogen content [164], varying this shift from 100 meV to 160 meV [165] per 1% of incorporated nitrogen.

Another similar approach was the virtual crystal approximation (VCA) for GaInNAs. According to this approach, a non-linear bowing parameter [166], varying between 14 meV [130] to 22meV [167], was introduced to explain the non-linear behaviour of the material`s bandgap in the presence of nitrogen. This model was disproved by later experiments that revealed a clear reduction of the bowing parameter with increasing nitrogen content [168]. Furthermore, these models ignore the effects on the bandgap induced by strain and quantum confinement in the sample. It is considered reliable with QW containing structures. The other band structure theory used to describe the electronic structure was based on an experimentally observed band-anti-crossing (BAC) effect. This model has been extensively used in this thesis.

The key to understanding the unusual properties of the GaInNAs alloys is the large difference in size and electronegativity of the Arsenic (As) and Nitrogen (N) atoms [145, 169]. The covalent radius and electronegativity of N are 0.65 Å and 3.04, respectively compared to those of 1.15 Å and 2.18 for As. A large difference in the atomic size causes deformation of the crystal lattice and the larger electronegativity of nitrogen leads to an increased charge transfer from the neighbouring Ga atoms to the N site. These cause a large composition-dependent bandgap bowing parameter. The energy gap of a ternary material can be derived with an optical bowing parameter:

$$E_g(A_xB_{1-x}C) = xE_g(AC) + (1-x)E_g(BC) - bx(1-x) \quad \ldots\ldots (2.30)$$

This equation describes the energy gap variation as a function of the alloy composition x, where $E_g(AC)$ and $E_g(BC)$ are the energy gaps of the constituents AC and BC of a ternary alloy $A_xB_{1-x}C$ respectively, and b is the optical bowing parameter. The optical bowing parameter of conventional semiconductor alloys is composition independent and small (b~0.477eV in GaInAs) [169]. U. Tisch *et. al.* [170] has suggested an empirical double exponential composition dependence of the bowing parameter. According to their model, the bowing parameter reaches 40 eV for dilute compositions of 0.1 %, and decreases strongly with increasing nitrogen molar fraction reaching a constant value of 7.5 eV for x > 8 % [170]. An increase of the effective mass in the GaInNAs alloys compared to GaInAs has also been predicted by different theories [171].

2.11.2 Band Anti-Crossing Model

A number of theoretical approaches have been applied to explain the optical bowing in dilute nitride alloys [172]. A band anti-crossing (BAC) model has been highly successful in describing a wide variety of experimentally observed phenomena such as band edge energies, their variation upon annealing, the band gap bowing parameter, pressure dependence of the band gap, and an enhancement of electron effective mass, the electronic structure, and explaining the properties of III–V dilute nitrides as well as other mismatched alloys. It allows calculation of the strength of the optical transitions in bulk materials [142-143], and the transition energies between electronic states in QWs. The first BAC model was proposed by Shan et al. [139, 161] which describe the electronic structure of GaInNAs alloys in terms of the interaction between the elongated conduction-band state with localized nitrogen impurity states, resulting in a splitting of the conduction band to the E_- and E_+ bands, and a reduction of the fundamental bandgap. The E_+ transition is blue-shifted and the E_- transition is red-shifted from the nitrogen resonant level with increasing nitrogen concentration. When the extended state in the conduction band and the

nitrogen localized state are empowered with the energies of E_M and E_N, respectively, the approximate solutions of the coupling between the two states are established from the two-state-like eigenvalue as [139]:

$$H_{BAC(y)} = \begin{pmatrix} E_M & V_{NM} \\ V_{NM} & E_N \end{pmatrix} \quad \ldots\ldots (2.31)$$

Under the assumption of low nitrogen concentrations in the group V sub-lattice sites [90]:

$$V_{NM} = C_{NM}\sqrt{y} \quad \ldots\ldots (2.32)$$

where C_{MN} is the coupling parameter that illustrates the combination between conduction bands and valence bands of extended heavy hole (HH) states, light hole (LH) states, and spin-orbit split-off (SO) states [173], and y is the nitrogen concentration in the III–V-N alloy. The symmetry of the lattice break due to the presence of Nitrogen which generates a highly localised impurity-like-state in the host materials conduction band then leads to a mixing of the electronic states and subsequent formation of the E_+ and E_- bands. Mathematically, by solving the eigenvalue for Eq.2.31, it is evident that the BAC model predicts the splitting of the conduction band into two sub-bands, where the formula for the lower E_+ and upper E_- sub-band is given by [139, 173]:

$$E_{\pm} = \frac{E_N + E_M \pm \sqrt{(E_N - E_M)^2 + 4C_{NM}^2 y}}{2} \quad \ldots\ldots (2.33)$$

where E_M and E_N are the energies of the GaInAs matrix conduction band edge and of the N level relative to the top of the valence band [139]. This equation clearly indicates that the lower sub-band E_- shifts downwards with increasing nitrogen concentration. This is responsible for the decrease in the band gap, hence the emission energy. R. Potter [10] developed a different theoretical model, based on parabolic bands and the BAC model for the splitting of the conduction band. A schematic of the band structure for bulk GaInNAs with the E_{MN} and $E_{\pm}$ levels is shown in Fig.2.18.

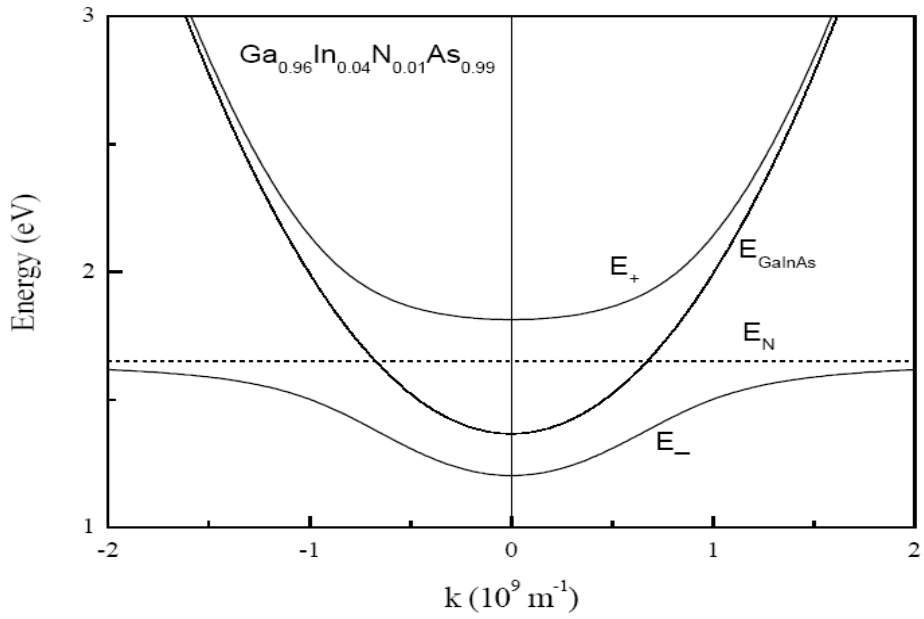

Figure 2.18: Dispersion relation for the conduction band structure of $Ga_{0.96}In_{0.04}N_{0.01}As_{0.99}$ near the Γ- point (k = 0) calculated with the BAC model. A parabolic approximation for the conduction band of GaInAs was used [174].

In most semiconductors, the electron effective mass is observed to decrease with decreasing bandgap. However, for cases when the bandgap is decreased by adding a small amount of nitrogen, we can conclude that the effective mass will decrease with the nitrogen fraction. The value of the electron effective mass has been obtained by using indirect measurements based upon quantum confinement [175]. This BAC model will be used in chapter 3 to estimate the composition of Indium and Nitrogen of the GaInNAs material to achieve the bandgap equivalent to 1.3μm wavelength.

2.12 Summary

An overview of various material systems for semiconductor photodetector performance have been discussed. The materials could be either lattice-matched with GaAs, as in the case of the dilute nitrides, or metamorphic, as in the case of either InGaAs or Silicon. The semiconductor physics principles such as lattice constant, diode junction, impact ionisation and

tunnelling photocurrent have been presented. The next chapter will discuss about the device design and modelling of the structure for vertical cavity enhanced photodetector.

References

1. A.L. Schawlow, C.H. Townes, Phys. Rev. 112, 1940 (1958)
2. M.I. Nathan, W.P. Dumke, G. Burns, F.H. Dill, G. Laser, Appl. Phys. Lett. 1, 62 (1962)
3. P. Bhattacharya, Semiconductor optoelectronic devices, Prentice-Hall, New Jersey (1994)
4. J. Allison, Electronic engineering semiconductors and devices, McGraw-Hill, London (1990)
5. H. Teichmann, Semiconductors, Butter Worths, London (1964)
6. J. Singh, Semiconductor Devices: An introduction, McGraw-Hill, London (1994)
7. M. Hayne, A. Usher, J.J. Harris, V.V. Moshchalkov, and C.T. Foxon, Phys. Rev. B, 57, 14813 (1998).
8. S.M. Sze, Physics of semiconductor devices, 2nd ed., J. Wiley, NY (1981)
9. J.S. Harris, M. Wistey, V. Gambin, W. Ha, T. Gugov, H. Yuen, S. Bank, SNRC Workshop, Stanford, CA December (2001)
10. R.J. Potter, PhD thesis, University of Essex (2002)
11. G.C. Osbourn, J. Vac. Sci. Techn. 21, 459 (1982)
12. E.P. O'Reilly, Semic. Sci. Techn. 4, 121 (1989)
13. E. Yablonovitch, E.O. Kane, J. Lightwave Techn. 6, 1292 (1988)
14. S.L. Chuang, Physics of optoelectronic devices, J. Wiley, NY (1995)
15. J.F. Liu, J. Michel, W. Giziewicz, D. Pan, K. Wada, D.D. Cannon, S. Jongthammanurak, D.T. Danielson, L.C. Kimerling, J. Chen, F.O. Ilday, F.C. Kartner, J. Yasaitis, Appl. Phys.Lett., 87, 103501 (2005)
16. N.C. Harris, J.T. Baehr, A.E.J. Lim, T.Y. Liow, G.D. Lo, M. Hochberg, IEEE J. Lighw. Technol., 31, 23 (2013)
17. D. Feng, S.R. Liao, P. Dong, N.N. Feng, H. Liang, D.W. Zheng, C.C. Kung, J. Fong, R. Shafiha, J. Cunningham, A.V. Krishnamoorthy, M. Asghari, Appl. Phys. Lett., 95, 261105 (2009)
18. M. Beals, J. Michel, J.F. Liu, D.H. Ahn, D. Sparacin, R. Sun, C.Y. Hong, L.C. Kimerling, A. Pomerene, D. Carothers, J. Beattie, A. Kopa, A. Apsel, M.S. Rasra, D.M. Gill, S.S. Patel, K.Y. Tu, Y.K. Chen, A.E. White, Proc. SPIE., 6898, 689804 (2008)
19. A. Chatterjee, P. Mongkolkachit, B. Bhuva, A. Verma, IEEE Photon. Technol. Lett., 15, 1663 (2003)
20. P.C. Eng, S. Song and B. Ping, Nanophotonics, 4, 277 (2015)
21. M.W. Geis, S.J. Spector, M.E. Grein, J.U. Yoon, D.M. Lennon, T.M. Lyszczarz, Opt. Express, 17, 5193 (2009).
22. R.R. Grote, K. Padmaraju, K. Bergman, IEEE Photon. Technol. Lett., 25, 67 (2013)
23. T. Baehr-Jones, M. Hochberg, A. Scherer, Opt. Express, 16, 1659 (2008)
24. H. Chen, X. Luo, A.W. Poon, Appl. Phys. Lett., 95, 171111 (2009)
25. M.K. Lee, C.H. Chu, Y.H. Wang, Opt. Lett., 26, 160 (2001)
26. M. Casalino, L. Sirleto, M. Iodice, N. Saflti, M. Gioffe, I. Rendina, G. Coppola, Appl. Phys. Lett., 96, 241112 (2010)
27. S. Zhu, G.Q. Lo, D.L. Kwong, Appl. Phys. Lett., 93, 071108 (2008)
28. S. Zhu, G.Q. Lo, D.L. Kwong, IEEE Photon. Technol. Lett., 20, 1396 (2008)
29. T. Tanabe, K. Nishiguchi, E. Kuramochi, M. Notomi, Opt. Express, 17, 22505 (2009)
30. H. Chen, A.W. Poon, Appl. Phys. Lett., 96, 191106 (2010)
31. K. Kikuchi, IEEE Elec.Lett., 34, 123 (1998)
32. K. Kikuchi, IEEE Elec. Lett., 34, 1354 (1998)
33. R. Salem, T.E. Murphy, Opt.Lett., 29, 1524 (2004)
34. P. Norton, Opto-electron. Rev., 10, 159 (2002)
35. A. Rogalski, Prog. Quant. Electron., 27, 59 (2003)

36. H.L. Koppens, T. Mueller, Ph. Avouris, A.C. Ferrari, M.S. Vitiello, M. Polini, Nat. Nanotechnology, 9, 780 (2014)
37. X.T. Gan, R.J. Shiue, Y.D. Gao, I. Meric, T.F. Heinz, K. Shepard, J. Hone, S. Assefa, D. Englund, Nat. Photon., 7, 883 (2013)
38. A. Pospischil, M. Humer, M.M. Furchi, D. Backmann, R. Guider, T. Fromherz, T. Mueller, Nat. Photon., 7, 892 (2013)
39. X.M. Wang, Z. Cheng, K. Xu, H.K. Tsang, J. Xu, Nat. Photon., 7, 888 (2013)
40. F.N. Xia, T. Mueller, Y.M. Lin, A.V. Garcia, P. Nat., Nanotechnol., 4, 839 (2009)
41. G. Konstantatos, M. Badioli, L. Gaudreau, J. Osmond, M. Bernechea, F.P.G.D. Arquer, F. Gatti, F.H.L. Koppens, Nat. Nanotechol., 7, 363 (2012)
42. F. Wang, G. Dukovic, L.E. Brus, T.F. Heinz, Science, 308, 838 (2005)
43. L. Prechtel, L. Song, S. Manus, D. Schuh, W. Wegscheider, A.W. Holleitner, Nano Lett., 11, 269 (2011)
44. St-Antoine, D. Menard, R. Martel, Nano Lett., 11, 609 (2011)
45. Lucent Technologies News, "AllWave(TM) fiber from Bell Labs squeezes out water for more spectrum" (1998)
46. A.M. Glass, D.J. Di Giovanni, T.Strasser, A.J. Stentz, R.E. Slusher, A.E. White, A.R. Kortan, B.J. Eggleton, Bell Labs Technical Journal, 168 (2000)
47. J.M. Senior, Optical fiber communications. Principle and practice, 2nd ed., Prentice Hall, NY (1992)
48. X. Zheng, Doctor of Philosophy: The University of Texas at Austin, (2004)
49. J.J. Goedbloed and J. Joosten, Electron. Lett., 14, 363 (1976)
50. O.I. Dosunmu, D.D. Cannon, M.K. Emsley, L.C. Kimerling, and M.S. Unlu, IEEE Photon. Technol. Lett., 1, 175 (2005)
51. N. E. J. Hunt, E. F. Schubert, and G. J. Zydzik, Appl. Phys. Lett., 3, 391 (1993)
52. B.M. Onat et al., IEEE Photon. Technol. Lett., 5, 707 (1998)
53. A. Ramam, G.K. Chowdhury, and S. J. Chua, Appl. Phys. Lett., 86, 17 (2005)
54. C. Li, Q. Yang, H. Ou, and Q. Wang, IEEE Electron. Compon. Technol. Conf., 1486 (2000)
55. M. Gokkavas et al., IEEE Photonics Technol. Lett., 12, 1349 (2001)
56. M.S. Unlu, M.K. Emsley, O.I. Dosunmu, P. Muller, and Y. Leblebici, Journal of Vacuum Science and Technology A: Vacuum, Surfaces and Films, 3, 781 (2004)
57. K. Kishino et al., IEEE J. Quantum Electron, 8, 2025 (1991)
58. M.S. Unlu and S. Strite, J. Appl. Phys., 2, 607 (1995)
59. V. Gambin, Ph.D. thesis, Stanford University, (2002)
60. N. Bouadma and J. Semo, Journal of Ligthwave Technology, 12, 742 (1994).
61. A. Salvador, F. Huang, B. Sverdlov, A.E. Botchkarev and H. Morkoç, 30, 1527 (1994).
62. K. Yang, A. L. Gutierrez-Aitken, X. Zhang, G. I. Haddad, and P. Bhattacharya, Journal of Ligthwave Technology, 14, 1831 (1996).
63. T. G. Andersson, Z. G. Chen, V. D. Kulakovskii, Applied Physics letters, 51, 752 (1987).
64. J. Bardeen, W. H. Brattain, Physical Review, 74, 230 (1948).
65. R. N. Hall, G. E. Fenner, J. D. Kingsley, Physical Review Letters, 9, 366 (1962)
66. T. Asano, M. Suemitsu, K. Hashimoto, M.D. Zoysa, T. Shibahara, T. Tsutsumi and S. Noda. Science Advances , 2, 12 (2016)
67. T. Soga, Nanostructured Materials for Solar Energy Conversion, Elsevier, (2006).
68. E. D. Palik, Handbook of Optical Constants of Solids, Academic Press, (1985)
69. D. C. Johnson, I. M. Ballard, K. W. J. Barnham, Conference Record of the 2006 IEEE 4th World Conference on Photovoltaic Energy Conversion, 26 (2007).
70. T. P. Lee and T. Li, in Optical Fiber Telecommunications edited by S. E. Miller and A. G. Chynoweth, Eds. San Diego: Academic Press, (1979)
71. K. Hess, Solid State Electronics, 31, 319 (1988).
72. Y. Sun, PhD theses. University of Essex (2008).
73. R.A. Smith, Semiconductor 2nd Ed., Cambridge University Press, (1978).
74. J.A. Van Vechten, and T.K. Bergstresser, Phys. Rev. B, 1, 3351 (1970).
75. T. Mattila, S.H. Wei, and A. Zunger, Phys. Rev. B, 60, 11245 (1999).
76. A. Lindsay and E.P. O'Reilly, Soli. Stat. Commun., 112, 443 (1999).

77. R. F. Pierret, Advanced Semiconductor Fundamentals, modular series on solid state devices, Vol. 4, Prentice Hall, (2002).
78. J. Nelson, The Physics of Solar Cells, Imperial College Press, (2003).
79. S.M. Sze, "Physics of Semiconductor Devices", 3rd Edition. John Wiley & Sons (2007)
80. E.A. Saleh and M.C. Teich, Fundamental of Photonics, John Wiley&Sons, (1991).
81. J.M. Senior, Optical Fiber Communications: Principles and Practice, 2nd Edition, Prentice Hall, (1992)
82. K.W.J. Barnham and C. Duggan, J. Appl. Phys., 67, 3490 (1990).
83. Y. P. Varshni," Physica (Utrecht) 34, 149 (1967).
84. J. Piprek, "Optoelectronic devices", Springer-Verlag, 217 (2005).
85. J. Piprek, "Semiconductor optoelectronic devices: Introduction to physics and simulation", Academic press, 171 (2003).
86. J. Bowers and Jr. C. A. Burrus,Journal of Lightwave Technology, 5 (1987)
87. M.J.N. Sibley, Optical Communications, Macmillan Education Ltd, (1990).
88. B. Royall. PhD Thesis, University of Essex, (2011).
89. B. K. Ridley, Quantum Processes in Semiconductors, Oxford University Press, New York, (1982)
90. S.L. Chuang, and K. Hess J. Appl. Phys., 59, 2885 (1986).
91. S.L. Chuang, and K. Hess, "Tunnelling assisted impact ionization for a superlattice", J.Appl. Phys., 61, 1510 (1987).
92. R. Rehm, H. Schneider, M. Walther, P. Koidl, and G. Weimann, Appl. Phys. Lett., 82, 2907 (2003).
93. B.K. Ridley, J. Phys. C, 16, 3373 (1983).
94. G. Juska, and K. Arlauskas, Phys. Status Solidi A, 59, 389 (1980).
95. K. Tanioka, J. Yamazaki, K. Shidara, K. Taketoshi, T. Kawamura, S. Ishioka, and Y. Takasaki, IEEE J. Selected Topics in Electron Device Letters, 8, 392 (1987).
96. K. Tsuji, Y. Takasaki, T. Hirai, and K. Taketoshi, J. Non-Crystalline Solids, 114, 94 (1989).
97. G.A. Baraff, Phys. Rev., 128, 2507 (1962).
98. Y. Zhang. A. Mascarenhas, H.P. Xin , and C.W. Tu, Phys. Rev. B, 61, 7479 (2000).
99. M.G. Burt, J. Phys. C: Solid State Phys., 18, L477 (1985).
100. S. McKenzie, and M.G. Burt, J. Phys. C: Solid State Phys., 19, 1959 (1986).
101. J. Marsland, Solid state Electron, 30, 125 (1987).
102. H. Shichijo, and K. Hess, Phys. Rev. B, 23, 4197 (1981).
103. M. Hostut, and N. Balkan, Tr. J. Of Physics, 23, 799 (1999).
104. B.F. Levine, K.K. Choi, C.G. Bethea, J. Walker, and R.J. Malik, Appl. Phys. Lett., 51, 934 (1987)
105. A. Reznik, S.D. Baranovskii, O. Rubel, K. Jandieri, S. Kasap, Y.Ohkawa, M. Kubota, K. Tanioka and J. A. Rowlands, Journal of Non-Crystalline Solids, 354, 2691 (2008).
106. S. Kasap, J.B. Frey, G. Belev, O. Tousignant, H. Mani, L. Laperriere, A. Reznik, and J. A. Rowlands, Phys. Status Solidi B, 246, 1794 (2009).
107. S. Dong, N. Li, S. Chen, X. Liu, and W. Lu, J. Appl. Phys., 111, 034504 (2012).
108. E. Gaubas, J. Vaitkus, and K.M. Smith, Nucl. Instrum.Methods Phys. Res. A, 460, 35 (2001).
109. J.Y. Andersson, J. Appl. Phys., 78, 6298 (1995).
110. S.M. Sze, Semiconductor Devices: Physics and Technology, John Wiley and Sons, New York, (1985)
111. P.M. Solomon, T.W. Hickmott, H. Morkoç, R. Fischer, Appl. Phys. Lett. 42, 821 (1983)
112. T.W. Hickmott, P.M. Solomon, R. Fischer, H. Morkoç, J. Appl. Phys. 57 (1985).
113. E. Pelve, F. Beltram, C.G. Bethea, B.F. Levine, V.O. Shen, S.J. Hsieh, R.R. Abbot, J. Appl. Phys. 66, 5656 (1989).
114. M.E. Daniels, P.J. Bishop, K.O. Jensen, B.K. Ridley, D.A. Ritchie, M. Grimshaw, E.H. Linfield, G.A.C. Jones, G.W. Smith, J. Appl.Phys. 74, 5606 (1993)
115. M.E. Daniels, P.J. Bishop, B.K. Ridley, D.A. Ritchie, M. Grimshaw, E.H. Linfield, G.A.C. Jones, Semiconductor Science and Technology, 9 (1994)
116. P.J. Bishop, M.E. Daniels, B.K. Ridley, J.S. Roberts, G. Hill, Semiconductor Science and Technology, 11, 873 (1996).
117. I. Hase, H. Kawai, K. Kaneko, N. Watanebe, J. Appl. Phys. 59, 3792 (1986).
118. M.E. Daniels, P.J. Bishop, B.K. Ridley, Semiconductor Science and Technology, 12, 375 (1997).
119. P.J. Bishop, M.E. Daniels, B.K. Ridley, Semiconductor Science and Technology, 13, 482 (1998).

120. L. Esaki, Physical Review, 2, 603 (1958)
121. L. L. Chang, L. Esaki, and R. Tsu, Appl. Phys. Lett. 24, 593 (1974)
122. F. Capasso and R.A. Kiehl, Journal of Applied Physics 58, 1366 (1985)
123. F. Capasso, K. Mohammed and A.Y. Cho, IEEE Journal of Quantum Electronics, No.9, (1986).
124. L.L. Chang, L. Esaki, and R. Tsu, App. Phy. Lett., 24, 593 (1974)
125. M. A. Fox, D. A. B. Miller, G. Livescu, J. E. Cunningham, and W. Y. Jan. IEEE J. Quantum Electron, 27, 2281 (1991).
126. U. Prechtel, Ch. Zeller, G. Abstreiter, and K. Ploog, Gallium Arsenide and Related Compounds, Inst. Phys.Conf., 5, 339 (1984).
127. C. H. Kuan , D. C. Tsui, K. K. Choi, P. G. Newman, and W. H. Chang, Appl. Phys. Lett., 63, 2091 (1993).
128. J. F. Geisz, and D. J. Friedman, Semiconductor Science and Technology, 17, 769 (2002).
129. S.M Ramey and R. Khaoie, IEEE Transaction on Electron Devices, 50, 1179 (2003).
130. M. Weyers, M. Sato, and H. Ando, Jpn. J. Appl. Phys., 31, 853 (1992).
131. C. Skierbiszewski, P. Perlin, P. Wisniewski, T. Suski, J. F. Geisz, K. Hingerl, W. Jantsch, D. E. Mars, & W. Walukiewicz, Phys. Rev. B, 65, 035207 (2001).
132. M. Kondow, T. Kitatani, S. Nakatsuka, M. C. Larson, K. Nakahara, Y. Yazawa, M. Okai, & K. Uomi, IEEE J. Select. Topics Quantum Electron, 3, 719 (1997).
133. A. Wagner, C. Ellmers, F. Hohnsdorf, J. Koch, C. Agert, S. Leu, M. Hofmann, W. Stolz, & W. W. Ruhle, Appl. Phys. Lett., 76, 271, (2000).
134. J. F. Geisz, D. J. Friedman, J. M. Olson, S. R. Kutz, & B. M. Keyes, J. Cryst. Growth, 195, 401 (1998).
135. J.S. Harris, M. Wistey, V. Gambin, W. Ha, T. Gugov, H. Yuen, S. Bank, SNRC Workshop, Stanford, California, (2001).
136. K. Volz, W. Stolz, J. Teubert, P.J. Klar, W. Heimbrodt, F. Dimroth,C. Baur, and A.W. Bett, Dilute III-V Nitride Semiconductors and Material Systems, edited by A. Erol, Springer-Verlag Berlin Heidelberg, 369 (2008).
137. S.M.P. Vaughan and B.K. Ridley, Dilute III-V Nitride Semiconductors and Material Systems, edited by A. Erol, Springer-Verlag Berlin Heidelberg, 255 (2008).
138. M. Weyers, M. Sato, H. Ando, Jpn. J. Appl. Phys. 31, L853, (1992).
139. W. Shan, W. Walukiewiez, J.W. Ager, E.E. Haller, J.F. Geisz, D.J. Friedman, J.M. Olson and S.R. Kurtz, Phys. Rev. Lett., 82, 1221 (1999).
140. S. Fahy, E.P. O'Reilly, Appl. Phys. Lett. 83, 3731 (2003).
141. S. Mazzucato and R.J. Potter, Dilute III-V Nitride Semiconductors and Material Systems, edited by A. Erol, Springer-Verlag Berlin Heidelberg, 181 (2008).
142. P.N. Hai, W.M. Chen, I.A. Buyanova, H.P. Xin, and C.W. Tu, Appl. Phys. Lett., 77, 1843 (2000).
143. P. Perlin, S.G. Subramanya, D.E. Mars, J. Kruger, N.A. Shapiro, H. Siegle, and E.R. Weber, Appl. Phys. Lett., 73, 3703 (1998).
144. J.D. Perkins, A. Mascarenhas, J.F. Geisz, and D.J. Friedman, Phys. Rev. B, 64, 121301R (2001).
145. T. Kitatani, M. Kondow, K. Nakahara, T. Tanaka, IEICE Trans. Elect. E, 83, 830 (2000).
146. W. Li, T. Youhti, C.S. Peng, J. Konttinen, P. Laukkanen, E.M. Pavelescu, M. Dumitrescu, and M. Pessa, Appl. Phys. Lett., 79, 3386 (2001).
147. W. Li, M. Pessa, T. Ahlgren, and J. Decker, Appl. Phys. Lett., 79, 1094 (2001).
148. X. Yang, M.J. Jurkovic, J.B. Heroux, W.I. Wang, Electronic. Lett. 35, 1082, (1999)
149. X. Yang, J.B. Heroux, M.J. Jurkovic, W.I. Wang, Appl. Phys. Lett. 76, 795 (2000)
150. J.C. Harmand, A. Caliman, E.V.K. Rao, L. Largeau, J. Ramos, R. Teissier, L. Travers, G. Ungaro, B. Theys, I.F.L. Dias, Semicond. Sci. Techn. 17, 778, (2002)
151. T W.K. Loke, S.F. Yoon, Z. Xu , K.H. Tan , T.K. Ng , Y.K. Sim, S. Wicaksono, N. Saadsaoud, D. Decoster, and J. Chazelas, Applied Physics Letters, vol. 93, 081102 (2008)
152. J.S. Harris, R. Kudrawiec, H.B. Yuen, S.R. Bank, H.P Bae, M.A. Wistey, D. Jackrel, E.R. Pickett, T. Sarmiento, L.L. Goddard, V. Lordi and T. Gugov, Development of GaInNAsSb alloys: Growth, band structure, optical properties and applications
153. D.B. Jackrel, S.R. Bank, H. B. Yuen, M.A. Wistey and J. S. Harris, Journal of Applied Physics, 101, 114916, (2007)
154. W. Ha, V. Gambin, M. Wistey, S. Bank, H. Yuen, S. Kim, J.S. Harris, Electr. Lett. 38, 277 (2002)

155. J. C. Harmand, G. Ungaro, L. Largeau, and G. Le Roux, Applied Physics Letters, 77, 2482 (2000).
156. X. Yang, M.J. Jurkovic, J.B. Heroux, W.I. Wang, Appl. Phys. Lett. 75, 178 (1999)
157. T Miyamoto, K. Takeuchi, T. Kageyama, F. Koyama, K. Iga, J.Crystal Growth, 197, 67 (1999)
158. T. Miyamoto, K.Takeuchi, F. Koyama, K. Iga, EEE Photonics Technology Letters, 9, 1448 (1997)
159. T. Kageyama, T. Miyamoto, S. Makino, F. Koyama, K.. Iga, Japanese journal of applied physics, 38 (1999)
160. M. Kondow, K. Uomi, A. Niwa, T. Kitatani, S. Watahiki, Y. Yazawa, Jpn. J. Appl. Phys. 13, 1273 (1996)
161. W. Shan, W. Walukiewicz, J.W. Ager III, E.E. Haller, J.F. Geisz, D.J. Friedman, J.M. Olson and S.R. Kurtz, J. Appl. Phys., 86, 2349 (1999).
162. K. Takeuchi, T. Miyamoto, T. Kageyama, F. Koyama and K. Iga, Jpn. J. Appl. Phys., 37, 1603 (1998).
163. M. Hetterich, M.D. Dawson, A.Yu. Egorov, D. Bernklau and H. Riechert, Appl. Phys. Lett., 76, 1030 (2000).
164. H.P. Xin, and C.W. Tu, Appl. Phys. Lett., 72, 2442 (1998).
165. X. Yang, J.B. Heroux, M.J. Jurkovic, and W.I. Wang, J. Vac. Sci. Techn. B, 17, 1144 (1999).
166. M.R. Gokhale, J. Wei, H. Wang, and S.R. Forrest, Appl. Phys. Lett., 74, 1287 (1999).
167. T. Makimoto, H. Saito, T. Nishida, and N. Koyayshi, Appl. Phys. Lett., 70, 2984 (1997).
168. K. Uesugi, I. Suemune, T. Hasegawa, T. Akutagawa, and T. Nakamura, Appl. Phys. Lett., 76, 1285 (2000).
169. I. Vurgaftman, J.R. Meyer and L.R. Ram-Mohan, J. Appl. Phys., 89, 5815 (2001).
170. U. Tisch, E. Finkman, and J. Salzman, Appl. Phys. Lett., 81, 463 (2002).
171. C. Skierbiszewski, P. Perlin. P. Wisniewski, W. Knap, T. Suski, W. Walukiewicz, W. Shan, K.M. Yu, J.W. Ager , E.E. Haller, J.F. Geisz, and J.M. Olson, Appl. Phys. Lett., 76, 2409 (2000).
172. H.M. Khalil. PhD Thesis, University of Essex, (2014).
173. W. Shan, W. Walukiewicz, K.M. Yu, J.W. Ager III, E.E. Haller, J.F. Geisz, D.J. Friedman, J.M. Olson, S.R. Kurtz, H.P. Xin and C.W. Tu, Phys. Stat. Sol., B, 223, 75 (2001).
174. J.C. Phillips, “Bands and bonds in semiconductors”, Academic Press New York (1973)
175. C. Skierbiszewski, Experimental Stduies of GaInNAs Conduction Band Structure, Dilute III-V Nitride Semiconductors and Material Systems, edited by A. Erol, Springer-Verlag Berlin Heidelberg, 123 (2008).

CHAPTER 3

Device Design and Modelling

3.1 Introduction

In this chapter, several design elements of vertical cavity enhanced (VCE) photodetector devices are considered. The VCE photodetector is made by sandwiching an active region of dilute nitride between two epitaxially grown distributed Bragg reflector (DBR) mirrors. The design of the device is mainly focused on the DBR mirrors using the static reflectivity approach, while and the appropriate concentration of dilute nitride (active region) is determined based on BAC model for 1.3μm wavelength application. MATLAB R2015b has been used for all the simulations carried out.

3.2 VCE Photodetector Design Considerations

Most modern photodetectors operate on the basis of the internal photoelectric effect where the photon excited electrons and holes remain within the material while the electrical conductivity of the material changes as a function of the intensity of the incident light. The absorption material should be chosen with a bandgap energy slightly less than the photon energy corresponding to the longest operating wavelength of the system. This will give a sufficiently high absorption coefficient to ensure a good response and yet limit the number of thermally generated carriers in order to attain a low dark current or leakage current. The p-n junction forms the basis of a semiconductor photodetector structure. The photo response of a detector results from the photon generation of electron-hole (e-h) pairs through band to band optical transitions. The photon generated e-h pairs in the depletion layer are subject to the local electric field within the layer. The electron and hole carriers drift in opposite directions. This transport process induces an electric current in the external circuit [1]. The p-i-n photodiode is commonly used as opposed to the original p-n junction structure as the intrinsic region can replace the depletion

width as shown in Fig.3.1. The depletion region contains multiple quantum wells (QWs) which can absorb most of the photons generated carriers that will be swept by the built-in electric field[2].

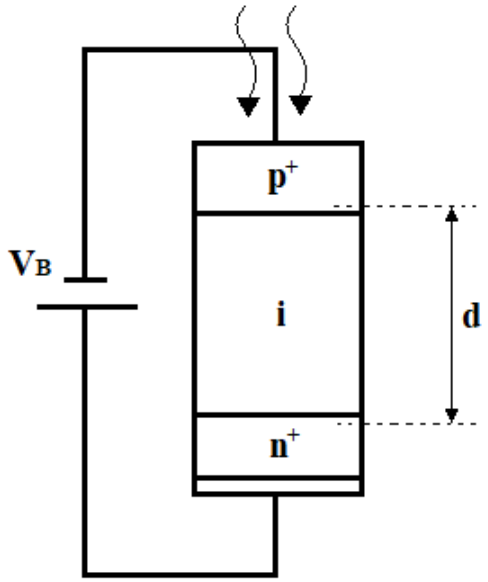

Figure 3.1: Depletion region of p-i-n photodiode

The p-i-n photodetector consist of highly doped *p* and *n* layers and an undoped photon absorption layer in between. In this thesis, the p doped layer is designed to be at the top of the structure to minimise both the transit time of hole carriers and the effect of the absorption distance. The absorption of light and the creation of e-h pairs mostly occur near the top of the absorption layer. The short hole transit distance and following it the time is preferred as the hole mobility is much lower than electron mobility [3]. Most of the hole carriers will be created near the p-layer. By putting the *p*-layer on top of the p-i-n structure, this will give a shorter transit distance as the hole carrier drift towards the *p*-layer. The intrinsic layer is usually more than 1µm, leading to the increase in the carrier transit time. The carrier which has higher velocity (electron) is preferred to traverse across this layer to minimize the carrier transit time. Therefore, it is most preferable for the top-illuminated p-i-n photodetectors to adopt the p-layer on top design.

As described in Chapter 2, the junction capacitance is desired to be low in high speed applications, such as in the detection of fast optical signals in optical communication systems. If the RC time constant is high, it may not respond to fast optical pulses and will result in the loss of information. Because high quantum efficiency values require a long absorption layer thickness, thus high device resistance and long transit times will face a trade-off between the bandwidth and quantum efficiency. The smallest area of mesa structure that will be used in this thesis is 1mm of diameter, therefore the RC delay will be expected to dominate the bandwidth of the output. Hence in this thesis, the thickness of the absorption region will make use of 9 and 20 QWs as different absorption regions forms part of the consideration of the internal gain. GaNAs is used as the material for the barrier layer to reduce the defect in quantum well. The excess flux of Antimony is applied to enhance the optical properties of the GaInNAs. The Nitrogen composition for GaNAs is estimated to be between 2% to 5% subject to the strain of the GaInNAs. A fixed quantum well width at 7nm and a suitable thickness of barrier layer (roughly between 10nm to 15nm) will be used. The use of 7nm QWs width is based on the optimum quantum carrier confinement in most dilute nitride materials [4-6]. The DBR mirrors of the cavity will be developed based on the materials that can be lattice matched with GaAs. To fulfill the requirement of having the DBR mirrors operate for a certain wavelength, the tuneable wavelength selection is proposed in this thesis as this approach has never been reported before neither by simulation or experimentally for VCE photodetectors. The temperature dependence model is going to be applied during the structure design. As for the active region material, GaInNAs will be owing to ability to achieve bandgap of 1.3μm wavelength.

3.3 Design of the VCE Photodetector

Cavity-based photodetectors are still under extensive research and development. The choice of active region and mirror materials should be considered when designing a VCE

photodetector based on GaInNAs for the 1.3 μm window of optical fibre communications. The circular-symmetric mode in vertical cavity devices yields a high coupling efficiency to optical fibres, which is useful for achieving a low noise figure [7]. However, thermal management is one of the most critical issue for the design of vertical cavity devices operating at long wavelength. Excessive Joule heating may also be produced due to the high series resistance of the doped DBR mirrors [8]. The structure of vertical cavity devices requires a well-designed active region in order to provide gain. The narrow signal of a nanometer or less has become the most important feature of vertical cavity devices [9]. The narrow bandwidth allows vertical cavity devices to function as optical filters with gain.

Vertical cavity devices can be operated in reflection mode and transmission mode, depending on the reflectivity from the Distributed Bragg Mirrors (DBR). The two configurations are shown schematically in Fig.3.2. In the reflection mode operation, vertical cavity devices are designed to have a high reflectivity mirror to achieve gain. The signal is injected through the top DBR and collected from the same side through a slightly transparent mirror. With this operation, it is possible to reach much higher values of vertical cavity device gain with acceptable bandwidths [10]. In the transmission mode operation, [11] both mirrors are slightly transparent and the signal is injected from one DBR and is collected from the other DBR [12]. In this thesis, the reflection mode is adopted in the design of the VCE photodetector. The construction of the DBR mirrors and active region composition will be discussed in the remaining sub-topics.

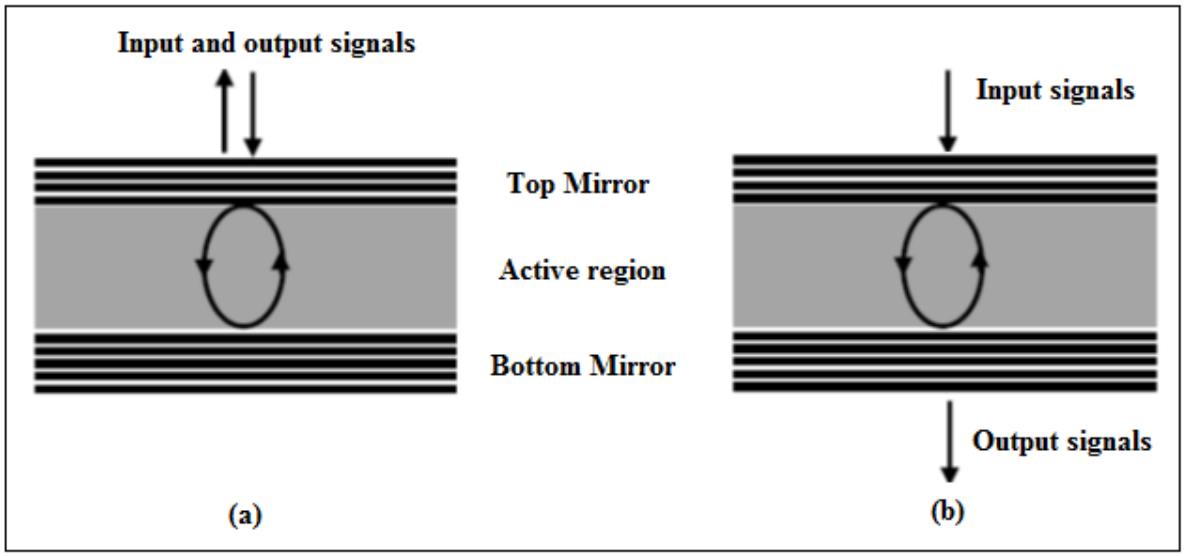

Figure 3.2: Schematic diagram of the operating modes of vertical cavity devices, including (a) reflection mode and (b) transmission mode

3.3.1 Distributed Bragg Mirrors (DBRs) and Transmission Matrix Method

A DBR (multi-layered mirror) consists of alternating periodic quarter-wavelength stacks of high and low refractive index (n_h and n_l) semiconductors, which are used to provide high mirror reflectivity in an optoelectronic device. The Bragg mirrors can be dielectric mirrors based on thin film coating technology as used in laser mirrors, or semiconductor Bragg mirrors based on a lithographic method as used in semiconductor diode lasers. Fig.3.3 shows a dielectric multi-layered Bragg mirror with air index (n_o), high index (n_h), low index (n_l), and substrate index (n_s), respectively. Each layer has quarter wavelength thickness in the material system, and a fraction of the light wave is reflected with π phase shift when light travels from high to low index materials [13].

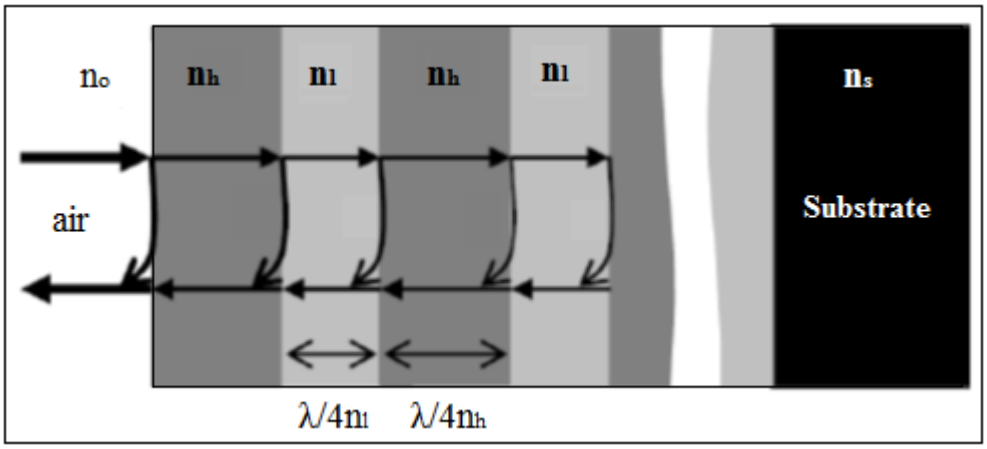

Figure 3.3: Schematic of a dielectric multilayered Bragg mirrors [10].

The reflectivity is proportional to the refractive difference between low and high index layers in the DBR mirror. The large refractive index contrast between the layers can produce high reflectivity mirrors with a wide stop band using a few periods [14]. However, DBR mirrors typically have lower index contrast and thus have a narrower mirror stop band requiring a high number of periods for high reflectivity. Increasing the number periods of DBR layers increases the mirror reflectivity, while increasing the refractive index contrast between the materials in DBRs increases both reflectivity and the bandwidth [15].

Generally, different methods can be used to analyse and design DBRs. However, the design of a DBR based on thin film optics deals with the propagation of light waves through layers [16] was used in this study. This is because thin film layers are able to reflect some wavelengths and transmit others. The transmission matrix approach is used to analyse the reflectance and transmittance of the layers at an interface [17-18], which includes the individual properties of the various layers [19]. This approach involves solving Maxwell's equation at the interfaces of each layer. The electric field *E*, and magnetic field *H*, vectors of the electromagnetic (EM) wave travelling in the positive and in the negative directions of the a^{th} layer can be expressed as [17]:

$$E_a = E_a^+ + E_a^- \quad \ldots\ldots (3.1)$$

$$H_a = \mu_l (E_a^+ + E_a^-) \quad \ldots\ldots (3.2)$$

where E_a and H_a represents the resultant tangential fields at normal incidence. The optical admittance for perpendicular (s-) and for parallel (p-) polarisation can be written as:

$$\mu_a = n_a Y \quad \ldots\ldots (3.3)$$

$$\mu_a = \frac{n_a}{Y} \quad \ldots\ldots (3.4)$$

where n_a is the refractive index of alternate layers and Y is the characteristic optical admittance. By using Snell's law [16],

$$n_{o,a} sin\theta_{o,m} = n_{a,s} sin\theta_{a,s} \quad \ldots\ldots (3.5)$$

the phase change of electromagnetic radiation while travelling through the layer of index n_a can be expressed as [18]:

$$\delta_a = \frac{2\pi n_a d_a cos\theta_a}{\lambda} \quad \ldots\ldots (3.6)$$

where θ_a, λ and d_a are the angle of incidence, the wavelength of the radiation, and the thickness of each quarter wavelength respectively. The thickness of the layer, d_a can be expressed as [16]:

$$d_a = \frac{\lambda_B}{4n_a} \quad \ldots\ldots (3.7)$$

where λ_B and n_a are the Bragg wavelength and layer thickness, respectively. The reflected and transmitted light can be determined by applying the boundary conditions to Maxwell's equation of electromagnetism [20]. The tangential components can be obtained by using Eq.3.1 and Eq.3.2, namely:

$$\begin{pmatrix} E_{a-1} \\ H_{a-1} \end{pmatrix} = \begin{bmatrix} cos\delta_a & isin\dfrac{\delta_a}{\mu_a} \\ i\mu_a sin\delta_a & cos\delta_a \end{bmatrix} \begin{bmatrix} E_a \\ H_a \end{bmatrix} \quad \ldots\ldots (3.8)$$

For a-layers, Eq.3.8 can be written as [17-18]:

$$\begin{pmatrix} E_\circ \\ H_\circ \end{pmatrix} = \prod_{a=1}^{z} M_a \begin{bmatrix} E_z \\ H_z \end{bmatrix} \quad \ldots\ldots (3.9)$$

$$M_a = \begin{bmatrix} cos\delta_a & isin\dfrac{\delta_a}{\mu_a} \\ i\mu_a sin\delta_a & cos\delta_a \end{bmatrix} \quad \ldots\ldots (3.10)$$

$$\left(\frac{E_z}{H_z}\right) = \binom{1}{\mu_s} E_s^+ \quad \ldots\ldots (3.11)$$

where μ_s is the optical admittance of the substrate in the (s-) or (p-) component of polarisation.

$$E_z \binom{1}{Y} = \binom{1}{\mu_s} E_s^+ \quad \ldots\ldots (3.12)$$

$$Y = \frac{H_\circ}{E_\circ} \quad \ldots\ldots (3.13)$$

where *Y* is recognised as the characteristic optical admittance. Therefore, by substituting Eq.3.9, Eq.3.11 and Eq.3.13 into equation Eq.3.8, we obtain:

$$\binom{B}{C} = \prod_{a=1}^{z} M_a \binom{1}{\mu_s} \quad \ldots\ldots (3.14)$$

where *B* and *C* are used to calculate the total characteristic matrices. As a result, the amplitudes of reflectance layers can be expressed respectively as the ratio of reflected to the incident energy [19]:

$$R = \left|\frac{\mu_\circ B - C}{\mu_\circ B + C}\right| \quad \ldots\ldots (3.15)$$

The equations above are used to calculate the reflectivity and phase change using a program that runs in Matlab. The materials selection for the DBR is crucial in order to build a high performance sample. Those materials however are limited by the availability of semiconductors that can be lattice matched to the substrate. It is subject to a trade-off between abrupt (for the highest reflectivity per interface) and graded profiles (for the lowest series resistance in the stack). It is known that the electrical resistance of a DBR is greatly reduced when an intermediate composition layer is inserted in the DBR structure. A graded structure is capable of reducing the height of the potential barrier [21], thus enhancing current flow through the layers. However there is a serious problem for the holes in the *p*-type DBR due to larger effective mass,

resulting in high series resistance in the cavity structures. The large resistance of the DBR seriously affects the device performance. To overcome this issue, the DBR can be doped to improve the electrical conductivity [22]. However a doped DBR introduces excessive free carrier absorption especially in *p*-type DBRs. Alternatively, an intermediate layer may reduce the potential energy barriers for majority carriers and therefore reduces the interface electrical resistance, and the self-heating [23] (a good thermal conductivity is also one of the necessary requirement for materials used to design a VCEP structure). As a whole, *p*-doped DBRs have a significant influence on the relative barrier height and hence reduce series resistance [24]. In this thesis, the adoption of a *p*-doped abrupt DBR is taken into the design consideration by applying high doping to overcome the high resistance in the cavity structures.

3.3.2 Active Region

Generally the epitaxy of dilute III-V nitride materials allows the realisation of semiconductor quantum structures with thin layers (from a few nm to a few tens of nm in dimension) in the cavity. Photons are passed into the active region uniformly through the surface of the confinement layers as the active region is enclosed between two dielectric mirrors of reflectivity R_f and R_b as shown in Fig.3.4. Photons are emitted vertically from the surface of the confinement layers but are confined transversely inside the optical cavity where they undergo multiple reflections all the photons are absorbed in the active region [25].

VCE photodetector designs need to fit a large number of quantum wells (QWs) to achieve possible gain. However, incorporating a large number of QWs makes it hard to achieve uniform photon distribution in the device and the gain in QWs is no longer homogenous [14]. If higher gain is desired, the maximum number of QWs is limited by the speed of the detector and required bandwidth. Accordingly, the amplification process takes place in an active region [26]. The BAC model described in chapter 2 is going to be applied for GaInNAs composition

approximation for active region operating at 1.3μm wavelength and will be discussed in the modelling results section.

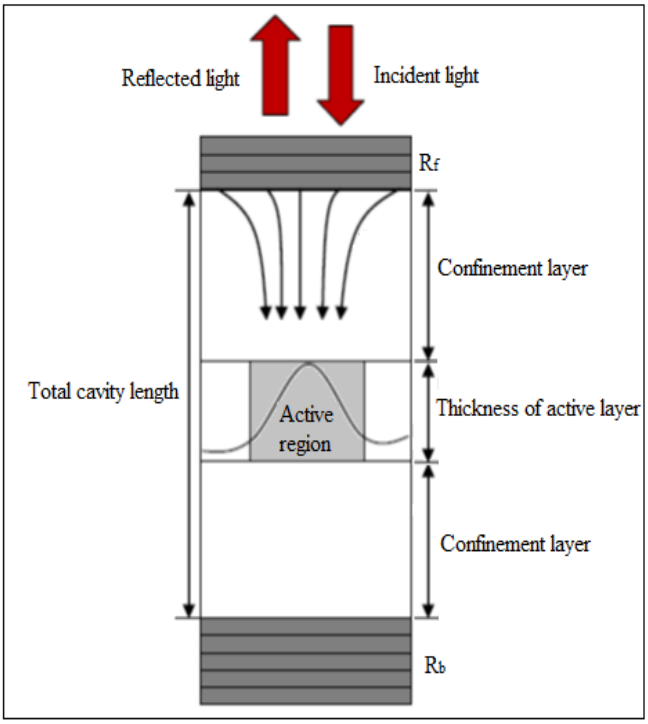

Figure 3.4: Schematic of VCE photodetector

3.4 VCE Modelling Results

The p-i-n junction of the semiconductor device is important for modern electronic applications and in understanding other devices. As mentioned earlier in this chapter, a few factors need to be considered when designing the photodetector device. The theory behind the photodetector and DBR structures explained previously is used as the structure of the design. The BAC model approach is used to estimate the composition of the GaInNAs material. The modelling and calculation involved for both the DBR and the active region output will be made using the Matlab software.

3.4.1 DBR Mirrors Design

Fig.3.5 and Fig.3.6 show the calculated reflectance of top and bottom DBRs as a function of pair of mirrors. As more pairs are added, the stop band becomes smaller with greater interference resonances at the sides. The light is forbidden to propagate in the selected structure within the range of the stop band. The Bragg mirrors for this design contain GaAs/AlGaAs layers as the top mirrors and GaAs/AlAs layers as the bottom mirrors. As shown in the figures, the top mirrors have been calculated with different numbers of layer pairs of 7, 9, 12, 15 and 18-pairs, while the bottom mirrors have 10, 12, 14, 18 and 20-pairs. The resonance wavelength is fixed at 1.3 μm for the DBR materials at 300K, while the reflectivity depends on the number of layer pairs.

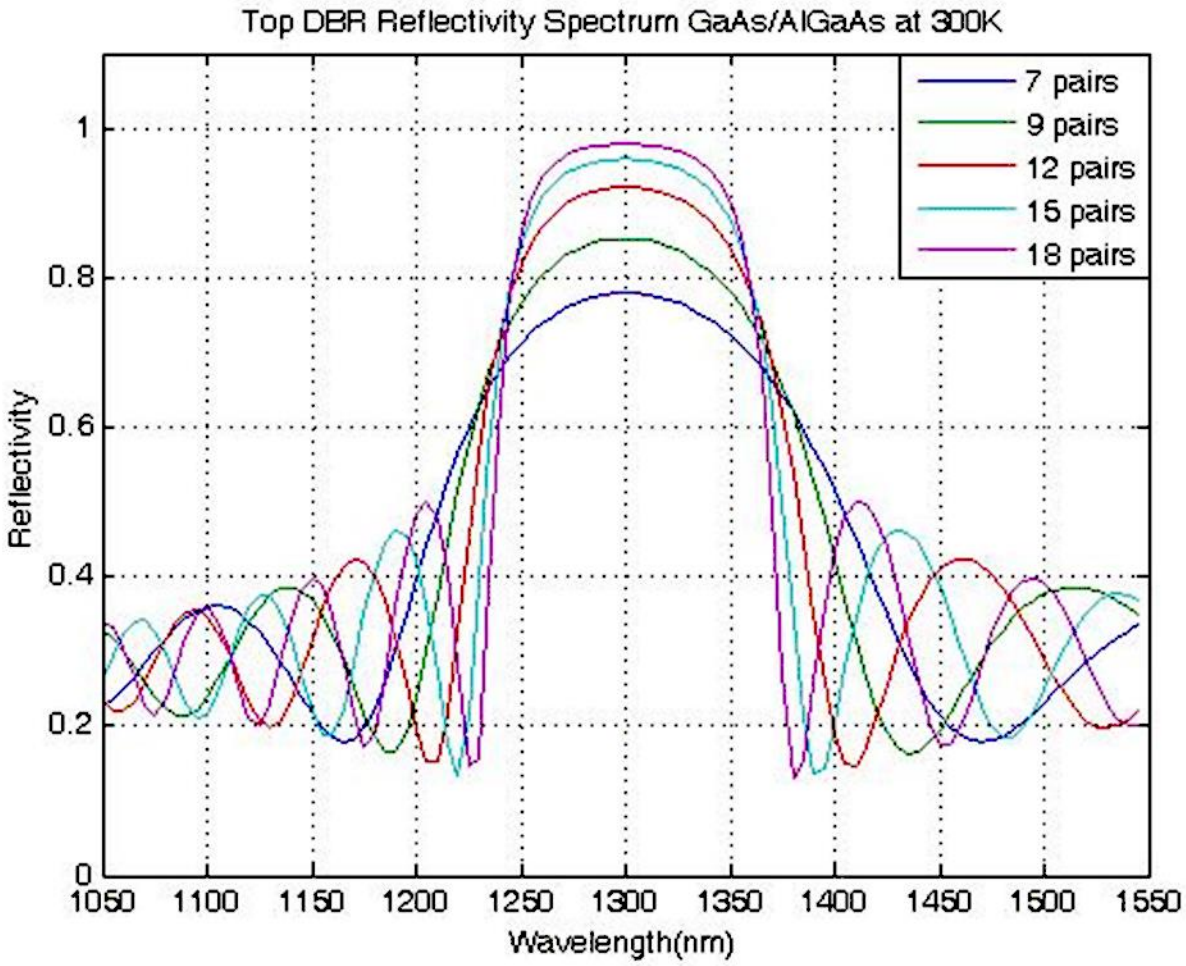

Figure 3.5: Reflectivity spectrum of top DBR at 300K

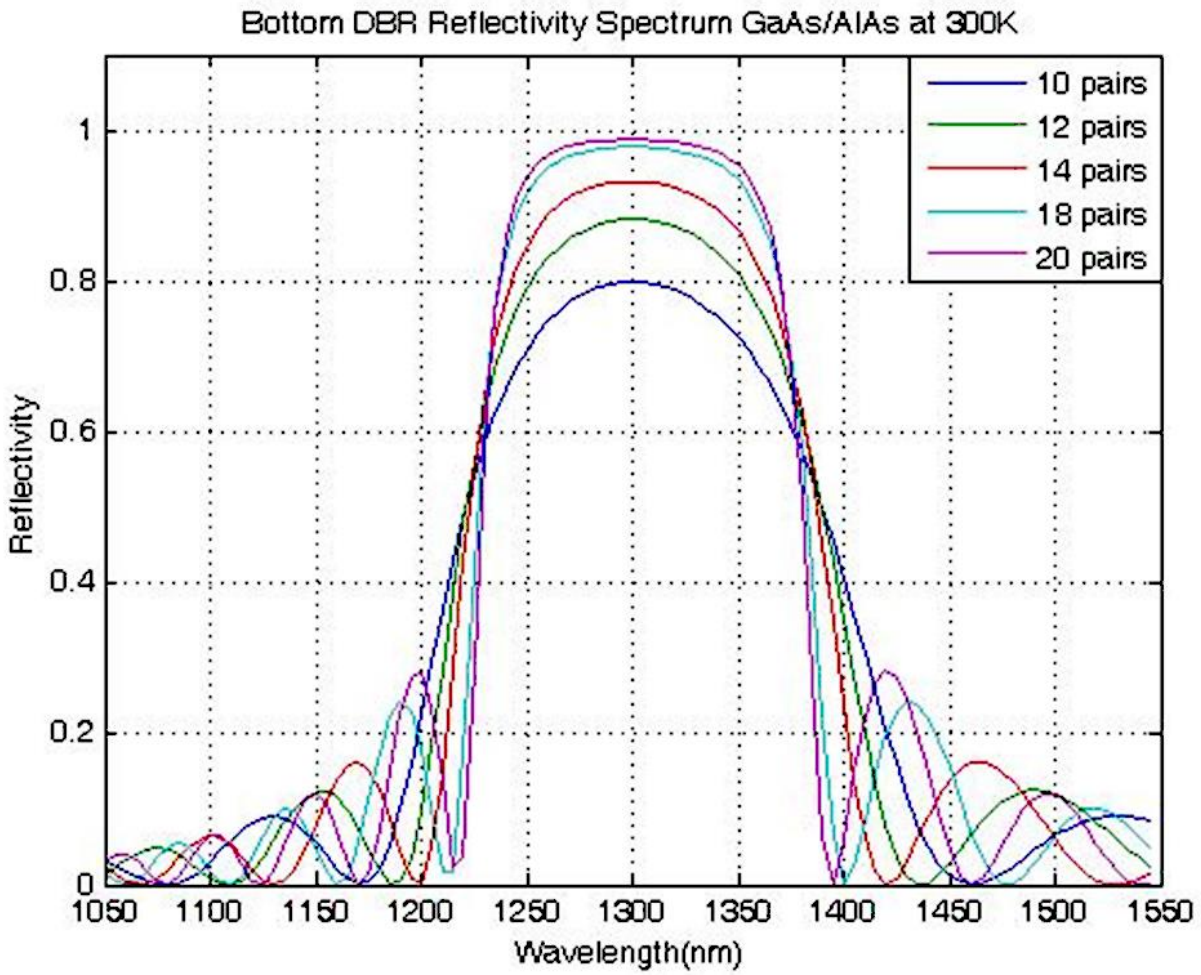

Figure 3.6: Reflectivity spectrum of bottom DBR at 300K

Some useful steps of simulation need to be taken into consideration when designing the structure of the VCE photodetector at 1.3 μm wavelength operation, which relies on the determination of the epitaxial layer contrast, layer thickness and the reflectivity dependence upon wavelength. The refractive index versus Aluminium concentration for $Al_xGa_{1-x}As$ and the influence of the index contrast ratio with top GaAs/ AlGaAs DBR with 12 pairs are given in Fig.3.7 and Fig.3.8. It can be seen that the high index contrast ratio will increase the reflectivity. Thus only a small number of pairs are required to achieve a given reflectivity.

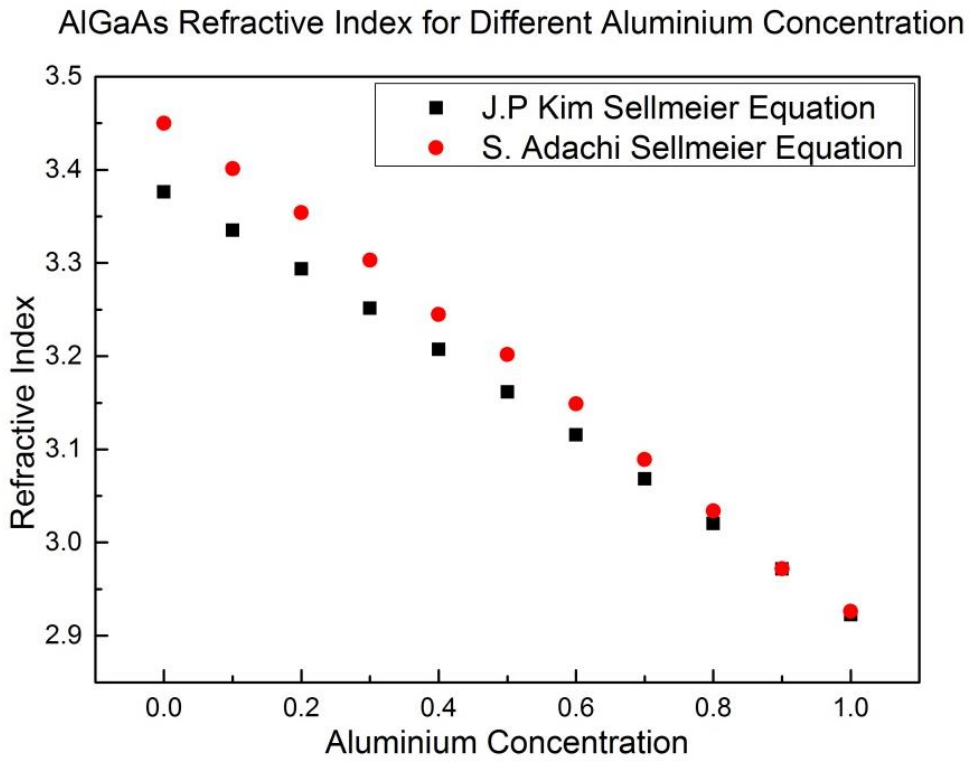

Figure 3.7: Comparison of AlGaAs refractive index value by Kim [32] and Adachi [33] at 300K

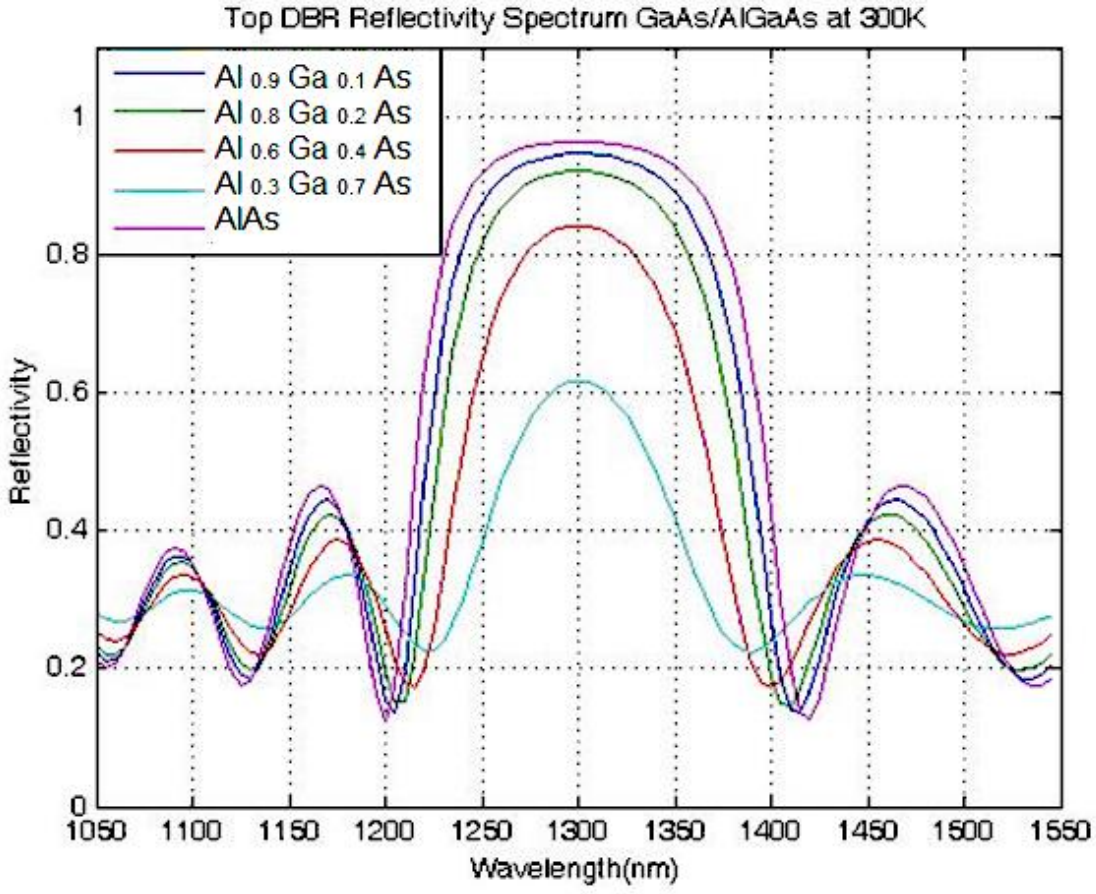

Figure 3.8: Reflectivity spectrum of top DBR for different Aluminium concentration at 300K

The peak reflectivity depends on the number of quarter wavelength layers and the refractive indices of the incident and exit media, as well as the high and low index materials. Increasing the number of periods of the DBR layers increases the mirror reflectivity, while increasing the refractive index contrast between the materials in the DBRs increases both the reflectivity and the bandwidth [15]. Thus, Bragg reflectivities have significant consequence for the amplifier results including gain, amplifier bandwidth, noise figure and saturation output power.

In this thesis, multiple wavelength detection is considered when designing the devices. As stated earlier, the changes of refractive index will affect the reflectivity and bandwidth. Hence, the temperature dependent refractive index of the DBR materials is considered as the temperature variation that will affect the refractive index. The most often-used model for the wavelength-dependent refractive index is the empirical Sellmeier equation. Although it is very convenient and simple to use, it is valid only at room temperature. When devices are operated at either elevated or reduced temperatures, the traditional models could become inaccurate. Several material systems have been reported to show the same effects of temperature on their refractive index [27-31], but the best modified Sellmeier equation for $Al_xGa_{1-x}As$ temperature dependence is found to be developed by Kim [32] which can be written as:

$$n(x,\lambda,T) = \left[10.906 - 2.92x + \frac{097501}{\lambda^2 + R_{l,h}} - 0.002467(1.41x + 1)\lambda^2\right]^{\frac{1}{2}} \quad \ldots..(3.16)$$

$$+ \left[(T - 26°C) \times (2.04 - 0.3x) \times \frac{10^{-4}}{°C}\right]$$

$$R_l = (0.52886 - 0.735x)^2 \text{ for x } \leq 0.36 \quad \ldots..(3.17)$$

$$R_h = (0.30386 - 0.105x)^2 \text{ for x } \geq 0.36 \quad \ldots..(3.18)$$

where λ is a wavelength in μm, T is temperature in Celsius and x is Aluminium concentration. Fig.3.7 shows the different Aluminium concentration of refractive index at 300K between Kim [32] and Adachi [33]. The value obtained by Kim was relatively lower when the Aluminium

concentration was zero. Kim had reported that the value was slightly different because the operating wavelength and temperature have been changed. In Eq.3.16, Kim had included the changes of refractive index for Aluminium concentration before and after 36% of Aluminium concentration as the behaviour of AlGaAs will change for that range. The validation of Eq.3.16 is compared with experimental data obtained by Kawai [34] which gave only small differences between them and it was due to the absorption coefficient of $Al_xGa_{1-x}As$ that was included in the experiment by Kawai. The refractive index values for wavelength and temperature dependence used in this project are shown in Fig.3.9 and Fig.3.10. It can be seen that the refractive index varies almost linearly with temperature and wavelength. Bearing in mind that the current flowing towards the active region via a large number of DBR layers will encounter a high electrical resistance which leads to problems with self-heating [35], therefore, the composition of the DBR mirrors should be chosen to avoid absorption of the reflection in the case of optical excitation of the active region. Using low reflectivity mirrors allows operation below threshold [26]. The alternate combination of GaAs and AlAs layers is used for the top and bottom DBR to achieve optimum reflectivity with lower resistance.

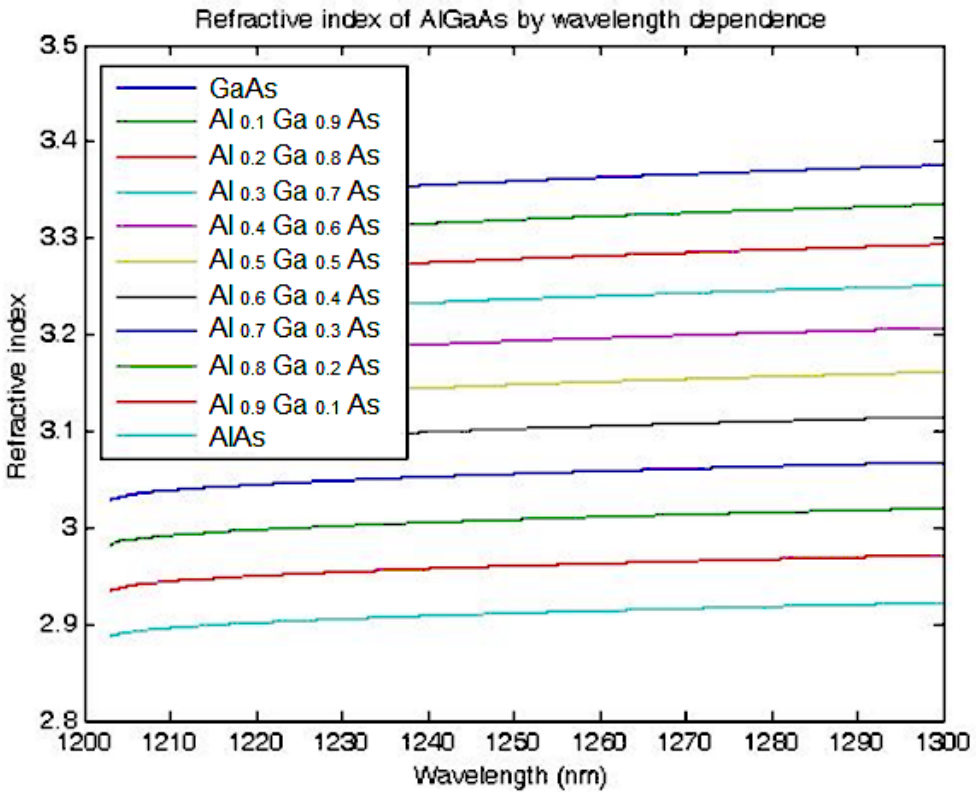

Figure 3.9: Refractive index of wavelength dependence for AlGaAs

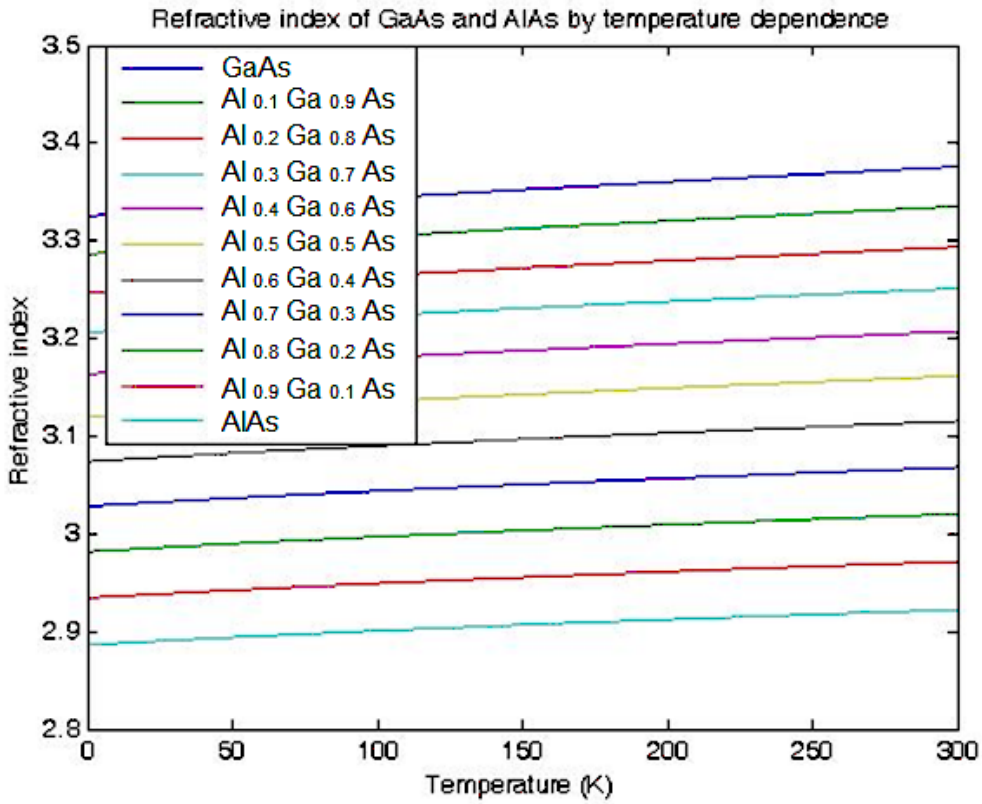

Figure 3.10: Refractive index of temperature dependence for AlGaAs

3.4.2 Active Region Design

The resonance cavity wavelength in this thesis depends on the energy absorption in the active region. The absorbed energy in the active region is calculated based on the BAC model as explained in chapter 2. The active region is based on dilute nitride material, GaInNAs which has been designed to achieve 1.3μm wavelength at a temperature of 300 K. As discussed before, the proposed structure is expected to detect at multiple wavelengths, while reflectivity of the DBR is to be aligned with the peak gain at the active region. Therefore, the active region composition in this thesis is calculated and designed according to the temperature dependence of the designed DBR.

To achieve the resonance wavelength at 1.3 μm using $Ga_{1-x}In_xN_yAs_{1-y}$ material, it is important to look at the composition of Indium and Nitrogen. The composition of these two materials will give the appropriate energy bandgap hence the desired resonance cavity wavelength. Potter [36] had summarised the potential composition of Indium and Nitrogen to obtain the energy bandgap that is equivalent to 1.3 μm wavelength. There are two main strategies to achieving 1.3 μm emission from GaInNAs; high Indium (typically 30 to 40 %) with low nitrogen (typically less than 1.5 %) or lower Indium (less than 30 %) with higher Nitrogen (greater than 1.5 %) fractions. Higher Indium fractions result in increased compressive strain. This reduces the critical thickness and hence imposes an upper limit on the well width. As a result, the increase in the emission wavelength that is achieved by increasing the Indium is partially offset due to increased quantum confinement and the slight increase in bandgap directly imposed by the compressive strain. These effects can be reduced with the addition of Nitrogen, which compensates for the compressive strain. However, it is well established that increasing the Nitrogen concentration decreases the material's optical quality [36].

Therefore, a few previous researches which provide the parameter of E_M, C_{MN} and E_N have been reviewed [37-50], to use in the BAC model to obtain the energy bandgap equivalent to

1.3 µm wavelength. Based on the researches on 1.3µm application, the calculation of C_{MN} and E_N using the BAC model for $Ga_{1-x}In_xN_yAs_{1-y}$ are widely used from the following equation,

$$C_{NM} = 2.3(1-x) + 1.9x - 4.2x(1-x)\ [51] \quad \ldots\ldots (3.19)$$

$$E_N = 1.7 + 3.89y\ [52] \quad \ldots\ldots (3.20)$$

where x is the fraction of Indium and y is the fraction of Nitrogen. E_M, the energy bandgap value of GaInAs is the crucial parameter that will provide the temperature dependence of $Ga_{1-x}In_xN_yAs_{1-y}$. In this thesis, there are three methods that have been adopted to estimate the E_M parameter based on temperature dependence. The first method is using the equation given by Paul et. al. [49],

$$E_{GaInAs}(x,T) = 0.42 + 0.625x - \left\{\left[\frac{5.8}{(T+300)} - \frac{4.19}{(T+271)}\right] \times 10^{-4} \times T^2 x\right\} \quad \ldots\ldots (3.21)$$

$$- \left[\frac{4.19 \times 10^{-4}}{(T+271)}\right] T^2 + 0.475x^2$$

where T is the temperature and x is the Gallium fraction. The second method is by using the Varshni's equation [42] as stated in Eq.2.11 and Vegard's law with the ternary alloy and the bowing parameter given by Vurgaftman et. al. [53],

$$E_{In_xGa_{1-x}As} = x.E_{InAs} + (1-x).E_{GaAs} - x.(1-x)0.477 \quad \ldots\ldots (3.22)$$

where x is the Indium fraction. The third method is by using Eq.3.22 as per in the second method for InGaAs bandgap energy. But, the energy bandgap for GaAs and InAs are based on the 4-parameter equation used by Passler [45] as the following,

$$E_g(T) = E_o(T=0) - \frac{\alpha\Theta}{2}\left[\sqrt[p]{1 + \left(\frac{2T}{\Theta}\right)^p} - 1\right] \quad \ldots\ldots (3.23)$$

where α is the limiting slope of bandgap shift at high temperature, Θ is a constant closely related with average phonon temperature, and p is Passler fitting parameter. All the parameters used in the Varshni and 4-parameter equations are listed in Table.3.1.

Table 3.1: Parameters used in the Varshni and 4-parameters equations [50, 53]

Material	E_o (eV)	$\alpha_{Varshni}$ (meV/K)	$\beta_{Varshni}$ (K)	$\alpha_{Passler}$ (meV/K)	Θ (K)	p
GaAs	1.519	0.5405	204	0.472	230	2.44
InAs	0.417	0.276	93	0.281	143	2.10

The results of the energy bandgap value from all three methods are then compared with the experimentally derived values obtained at Istanbul University by the Nano-Optoelectronics Research Group. The group has been working on dilute nitride composition to achieve an application wavelength of 1.3 μm [54, 55]. The group uses Varshni's equation to relate the energy bandgap temperature dependence with the parameters derived from photoluminescence (PL) experimental results. The β parameter in Varshni's equation used in their calculation is based on the Debye temperature for $Ga_{0.68}In_{0.32}N_yAs_{1-y}$ and can be obtained as [50],

$$\beta_{Ga_{1-x}In_xN_yAs_{1-y}} = xy(\beta_{InN}) + x(1-y)(\beta_{InAs}) + (1-x)y(\beta_{GaN}) + (1-x)(1-y)(\beta_{GaAs}) \quad \ldots\ldots (3.24)$$

where x is the Indium fraction, y is the Nitrogen fraction and the β value is as in Table.3.2.

Table 3.2: Debye temperature of several binary compounds [50].

Compound	GaAs	InAs	GaN	InN
Debye temperature (K)	360	262	870	700

The output obtained by all methods show promising results for achieving a wavelength of 1.3μm as shown in Fig.3.11, Fig.3.12 and Table.3.4. As can be seen in Table.3.4, both sample's results provided by the Istanbul group are producing the possibility of 1.5% Nitrogen concentration needed to be used to achieve a response at 1.3μm wavelength. The three methods used in this thesis give a deviation of ±10nm when compared to the PL results from the Istanbul group for 1.2% and 1.7% of Nitrogen concentration at 300K. It shows that the active region methods used

in this thesis have the capability to attain bandgap energy at 1.3μm by using a 1.5% Nitrogen concentration. The first method will be applied into the resonance cavity calculation following the value of bandgap obtained at 1.3μm for 300K compared to other methods.

Table 3.3: Varshni parameter obtained from Nano-Optoelectronics Research Group.

Sample	E_o **(eV)**	α_{Varshni} **(meV/K)**
$Ga_{0.68}In_{0.32}N_{0.012}As_{0.988}$ (*p*-type)	1.044	0.4242
$Ga_{0.68}In_{0.32}N_{0.017}As_{0.983}$ (*p*-type)	0.996	0.3938

Table 3.4: The summary of GaInNAs bandgap at 300K

Sample / Method	**Bandgap energy by calculation**	**Wavelength by calculation**	**Wavelength by PL**
$Ga_{0.68}In_{0.32}N_{0.012}As_{0.988}$ (p-type)	0.9838 eV	1262 nm	1260 nm
Method 1 (Paul et. al.)	0.9548 eV	1300 nm	-
Method 2 (Varshni)	0.9474 eV	1310 nm	-
Method 3 (Passler)	0.9490 eV	1308 nm	-
$Ga_{0.68}In_{0.32}N_{0.017}As_{0.983}$ (p-type)	0.9404 eV	1320 nm	1326 nm

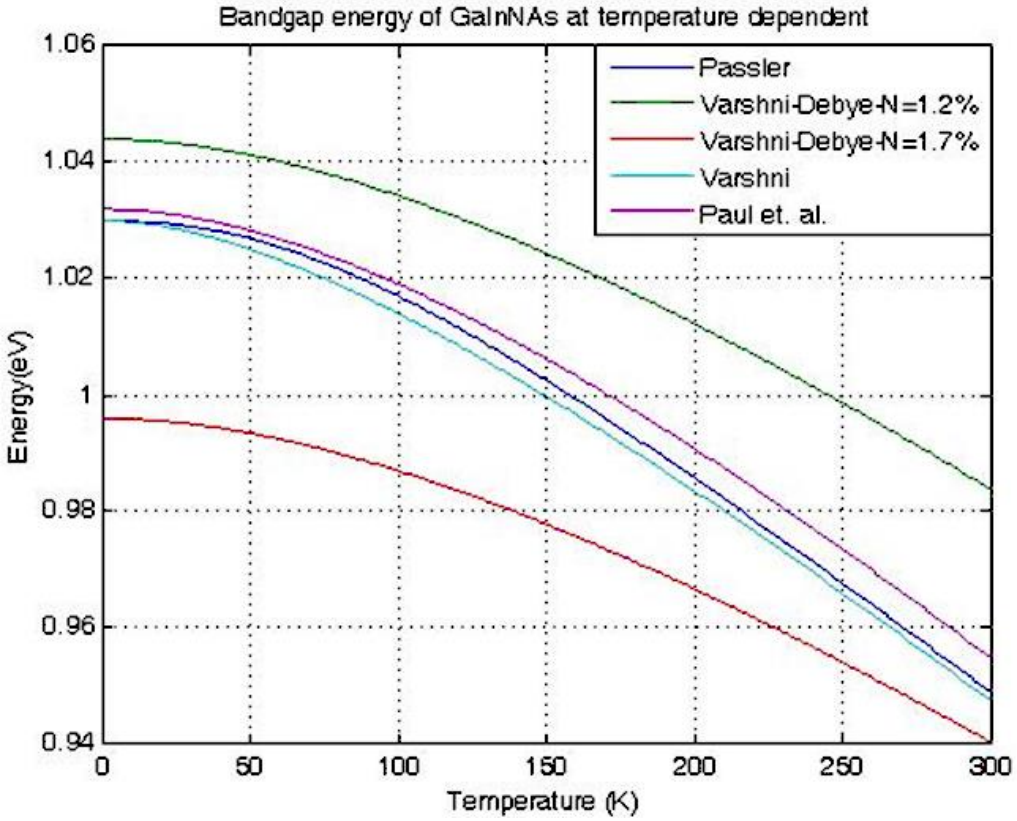

Figure 3.11: Temperature dependence of GaInNAs energy bandgap

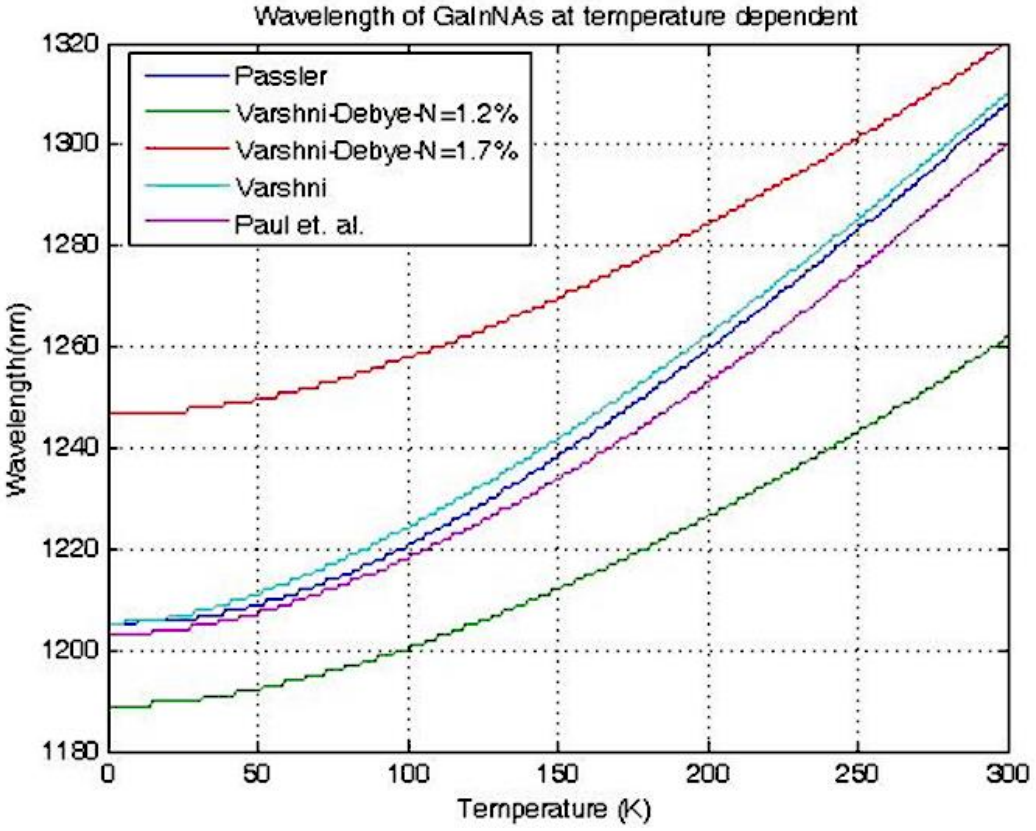

Figure 3.12: Temperature dependence of GaInNAs wavelength

3.4.3 Structure Design Output

The wavelength of the resonance cavity is obtained using the method one for the active region calculation, as well as after taking into account, the optimum reflectivity from the DBR mirror pairs. It can be seen in Fig.3.13, the cavity wavelength is found to be too narrow at 1.3µm with a full width half maximum (FWHM) of 5nm. The resulting reflectivity reached almost 99% within the band stop ranging from between 1225nm up to 1375nm.

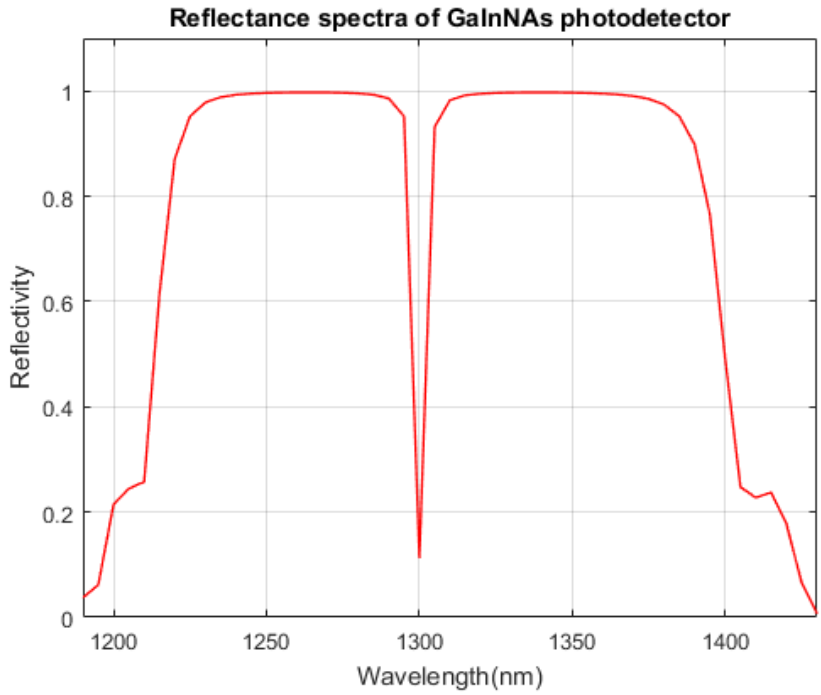

Figure 3.13: Resonance cavity of $Ga_{0.68}In_{0.32}N_{0.015}As_{0.985}$ for 1.3µm wavelength at 300K

To further ensure that the design will be showing temperature dependent characteristics, another four temperature value is used to see the differences on the resonance cavity wavelength as shown in Fig.3.14. When the temperature changed, both the wavelength as well as the reflectivity of the resonance cavity varied. The wavelength selectivity varied from 1295nm at 280K up to 1310nm at 320K. The average change rate is theoretically expected to be 0.375nm/K from 280K to 320K. When the number of top DBR pairs at 300K were decreased, the result shows that the reflectivity is reduced and the cavity windows are widely stretched as depicted in

Fig.3.15. Following the results, this work will be making use of 10 pairs of top DBR and 15 pairs of bottom DBR in the design.

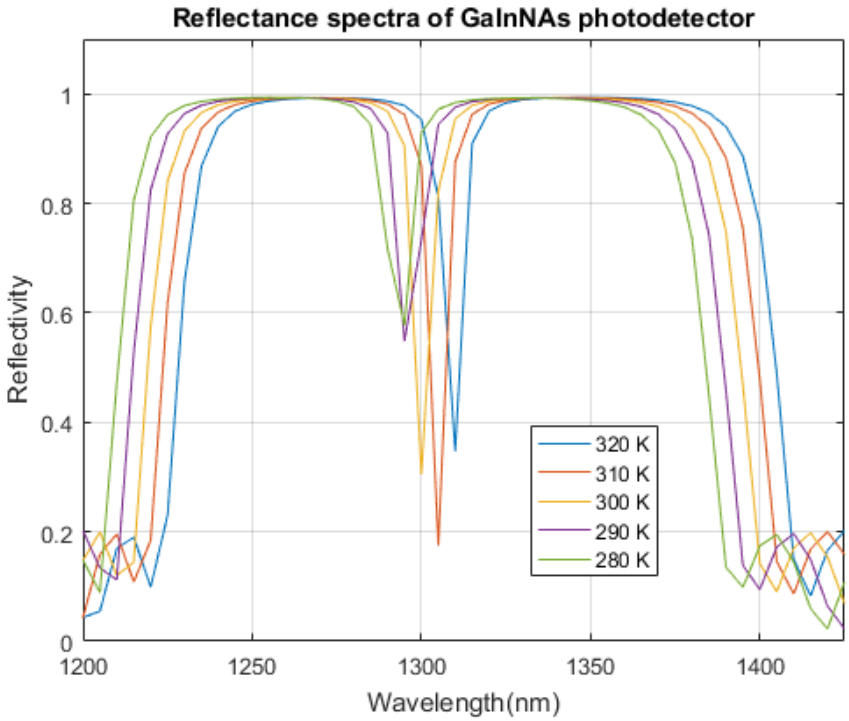

Figure 3.14: Temperature dependent of $Ga_{0.68}In_{0.32}N_{0.015}As_{0.985}$ resonance cavity

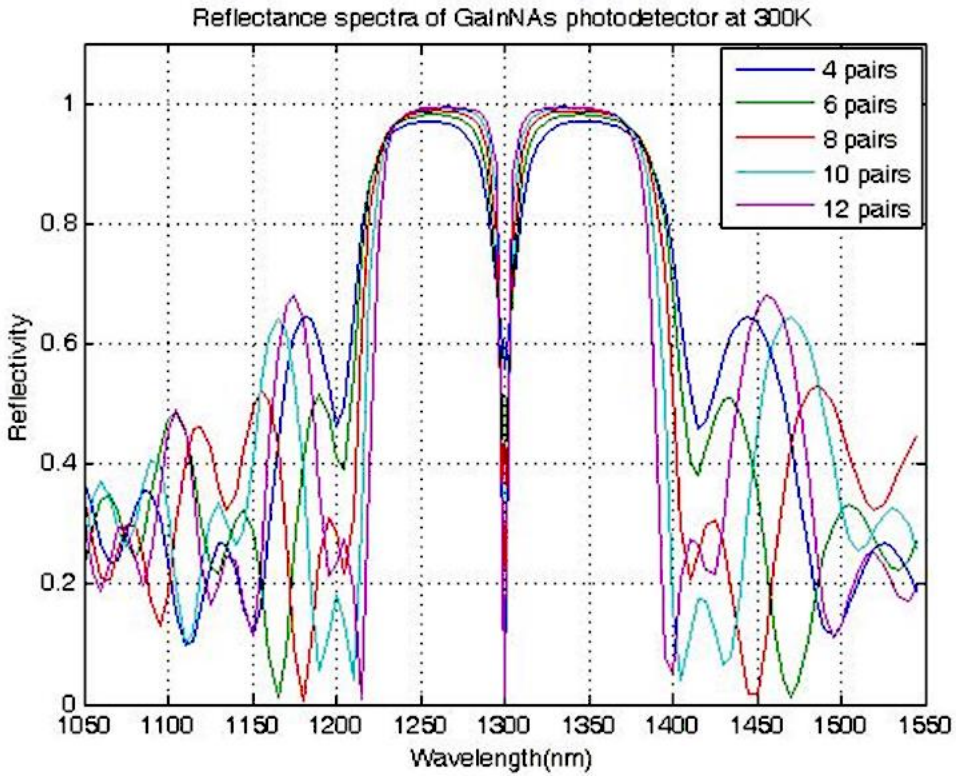

Figure 3.15: Resonance cavity of $Ga_{0.68}In_{0.32}N_{0.015}As_{0.985}$ for different top DBR pairs at 300K

The refractive index of the DBR is really important because it will specify the possible thickness of each DBR layer calculated in this thesis. Fig.3.16 shows that the obtained output cavity at a fixed refractive index value displayed no change in the wavelength cavity at different temperatures. Because of this, the change in the layer thickness for GaAs, $Al_{0.8}Ga_{0.2}As$ and AlAs due to temperature is investigated by using Eq.3.7. As shown in Fig.3.17, the thickness rate shift from 300K to 0K for GaAs, $Al_{0.8}Ga_{0.2}As$ and AlAs are 0.019nm/K, 0.022nm/K and 0.023nm/K respectively. Even though the differences are small in value, they affect the wavelength of the cavity output. It can be observed that the rate of change of both the DBR and the active region is not same. The thickness value of DBR at 300K is taken as the standard reference to grow the structural layers of the sample.

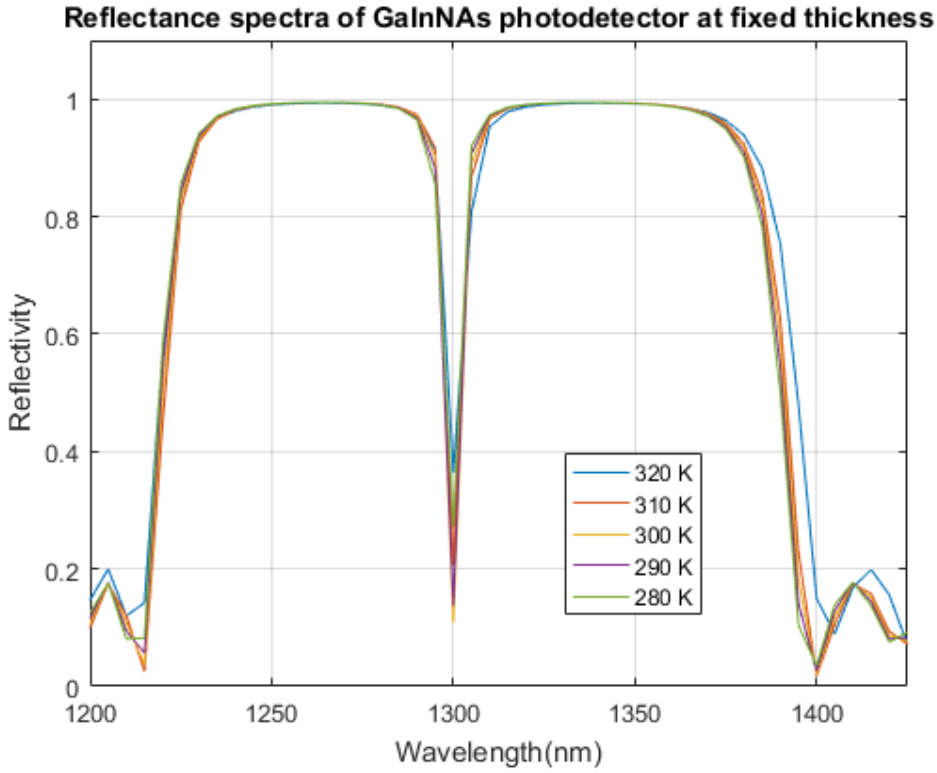

Figure 3.16: Temperature dependence of $Ga_{0.68}In_{0.32}N_{0.015}As_{0.985}$ resonance cavity at fixed thickness of DBR mirrors

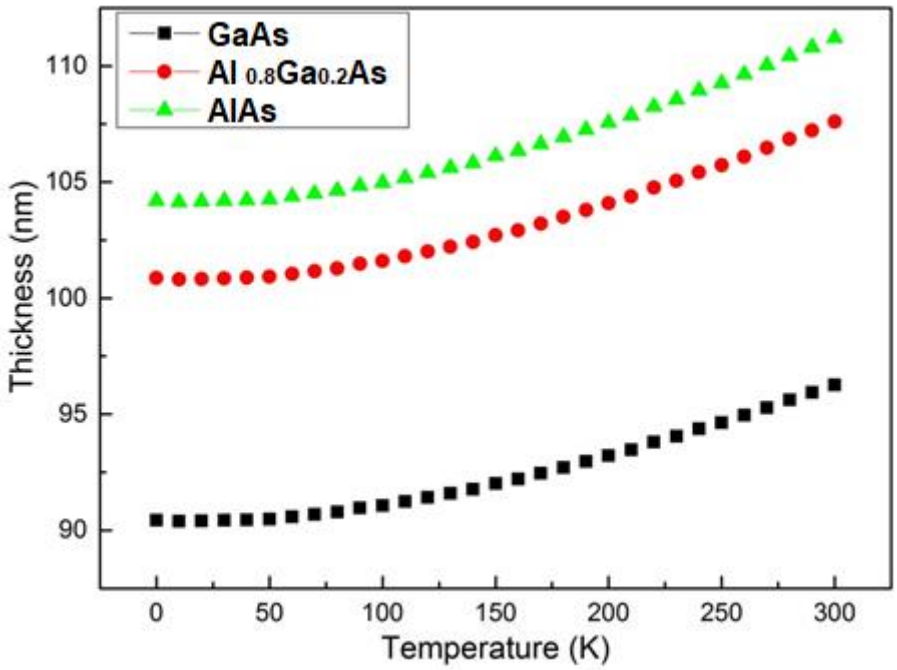

Figure 3.17: Temperature dependence of GaAs, $Al_{0.8}Ga_{0.2}As$ and AlAs layer thicknesses

The proposed structure, shown in Table.3.5, contains 9 layers of 7 nm-thick $Ga_{0.68}In_{0.32}N_{0.015}As_{0.985}$ quantum wells separated by 13.5 nm GaNAs barriers. The active region is enclosed between 95 nm-thick cladding layers C-doped ($p^+ = 5 \times 10^{18}$ cm^{-3}) on the top side and 70 nm of Si-doped ($n^+ = 3 \times 10^{18}$ cm^{-3}) on the bottom side. The structure is sandwiched between two DBRs. The top DBR has 10 pairs of GaAs/AlAs quarter-wave stacks and provides a reflectivity in excess of 98.14% at 1.3 μm. On the other side, the bottom DBR has 15 pairs of AlAs/GaAs quarter-wave stacks giving around 99.21% reflectivity. This is higher than the top DBR, thus it will allow light emission from the top surface. The 98.01 nm thick GaAs capping layer is used to protect the AlAs layer from oxidation. The second design contains 20 QWs. The structure is adjusted according to the layer thicknesses to achieve the cavity of 1.3μm with the same doping concentration maintained. The top DBR pairs and both DBR layer thicknesses are changed as shown in Table 3.6. The barrier and n^+ doped layer thicknesses are reduced to 12nm and 60nm respectively. The reflectance spectrum of 20QWs structure is the same as for the 9 QW design as shown in Fig.3.13.

Table 3.5: Structural layers diagram of 9 QWs VCE photodetector.

Notes	Doping	Repeats	Material	Thickness (nm)
p^+ Doped GaAs / AlAs DBR	Be = 5 x 10^{18} cm^{-3}	**10**	GaAs	**99.2**
			AlAs	**115.15**
p^+ Doped	Be = 5 x 10^{18} cm^{-3}	1	GaAs	95
Graded layer	Undoped	1	GaAs	10
Barrier	Undoped	**9**	GaNAs	**13.5**
Intrinsic			$Ga_{0.68}In_{0.32}N_{0.015}As_{0.985}$	7
Barrier	Undoped	1	GaNAs	**13.5**
Graded layer	Undoped	1	GaAs	10
n^+ Doped	Si = 3.1 x 10^{18} cm^{-3}	1	GaAs	**70**
n^+ Doped GaAs / AlAs DBR	Si = 3 x 10^{18} cm^{-3}	15	AlAs	**113.54**
			GaAs	**98.01**
n^+ Doped Substrate	Si = 3 x 10^{18} cm^{-3}	1	GaAs	350000

Table 3.6: Structural layers diagram of 20QWs VCE photodetector.

Notes	Doping	Repeats	Material	Thickness (nm)
p^+ Doped GaAs / AlAs DBR	Be = 5 x 10^{18} cm^{-3}	**11**	GaAs	**98.38**
			AlAs	**113.57**
p^+ Doped	Be = 5 x 10^{18} cm^{-3}	1	GaAs	95
Graded layer	Undoped	1	GaAs	10
Barrier	Undoped	**20**	GaNAs	**12**
Intrinsic			$Ga_{0.68}In_{0.32}N_{0.015}As_{0.985}$	7
Barrier	Undoped	1	GaNAs	**12**
Graded layer	Undoped	1	GaAs	10
n^+ Doped	Si = 3.1 x 10^{18} cm^{-3}	1	GaAs	**60**
n^+ Doped GaAs / AlAs DBR	Si = 3 x 10^{18} cm^{-3}	15	AlAs	**114.67**
			GaAs	**98.95**
n^+ Doped Substrate	Si = 3 x 10^{18} cm^{-3}	1	GaAs	350000

The samples structure shown in Table 3.5 and Table 3.6 are grown at Optoelectronics Research Centre, Tampere University of Technology in Finland using Molecular Beam Epitaxy (MBE) and will be discussed in the next chapter.

3.5 Summary

The resonance cavity structures based photodetector have been designed using two different number of quantum wells. The structures is designed using the transfer matrix method, while the bandgap energy of the active region is calculated based on the Band-Anti Crossing model. The structures adopted the strategy of placing the p–doped layer on top in order to minimise both the hole carriers transit time and the absorption distance. Both DBR mirrors are

doped and have been arranged in graded structure form to enhance the current flow through the layers. The temperature dependence parameter of the material in use have been taken into account to provide the tunable wavelength application. The growth technique and fabrication process of the designed sample will be explained in the next chapter.

References

1. S.M. Sze, Physics of Semiconductor Device, 255 (1982).
2. V. Lordi, PhD Thesis, Stanford University, (2004).
3. H.M. Khalil. PhD Thesis, University of Essex, (2014).
4. I. Li and E. Herbert, Semiconductor Quantum Well Intermixing: Material Properties and Optoelectronic Applications (Optoelectronic Properties of Semiconductors and Superlattices, Overseas Publishers Association, (2000).
5. B.R. Nay, Physics of Quantum well Devices, Kluwer Academic Publishers, (2000)
6. A. Erol, Dilute III-V Nitride Semiconductors and material System: Physics and Technology, Springer Heidelberg New York, (2008)
7. E.S. Bjorlin thesis on "Long wavelength vertical cavity semiconductor optical amplifier," (2002).
8. J. Piprek, Optoelectronic devices, Springer-Verlag, 217, (2005).
9. F. Koyama, S. Kubota, and K. Iga, Elect. Lett., 27, 1093 (1991).
10. E.S. Bjorlin, A. Dahl, J. Piprek, P. Abraham, Y.-J Chiu, J.E. Bowers, Phot. Technol. Lett., 13, 1271 (2001).
11. H.A. Macleod, "Thin-Film Optical Filters", Adam Hilger Ltd., (1986).
12. G.D. Cole, S. Björlin,C.S. Wang, N.C. MacDonald, and J.E. Bowers, IEEE Photo. Tech. Letts., 17, 2526 (2005).
13. T.E. Sale, "Vertical Cavity Surface Emitting Lasers", Research Studies Press, (1995).
14. C. Wilmsen, H. Temkin and L.A. Goldren, "Vertical cavity surface emitting laser: Design, fabrication, characterization, and applications", Cambridge studies in modern optics, (2001).
15. J. Piprek, Semiconductor optoelectronic devices: Introduction to physics and simulation, Academic press, 171 (2003).
16. H.M. Liddell, "Computer-Aided Techniques for the Design of Multilayer Filter", Adam Hilger Ltd, (1980).
17. H.A. Macleod, "Thin-film optical filters", Adam Hilger Ltd., (1986).
18. D.M. Berreman, Opt. Eng., 25, 933 (1986).
19. L.A. Colder and S.W. Corzine, "Diode lasers and photonic integrated circuits", Wiley, (1995).
20. M. Born, E. Wolf, "Principles of optics", Pergamon Oxford, (1970).
21. K. Kurihara, T. Numai, I. Ogura, A. Yasuda, M. Sugimoto, and K. Kasahara, J. Appl. Phys., 73, 21 (1993).
22. 52 K. Tai, L. Yang, Y.H. Wang, J.D. Wynn, and A.Y. Cho, Appl. Phys. Lett., 56, 2496 (1990).
23. 53 M.G. Peters, B.J. Thibeault, D.B. Young, A.C. Gossard, and L.A. Coldren, J. Vac. Sci. Technol., 12, 3075 (1994).
24. 54 B. Weigl, M. Grabherr, C. Jung, R. Jager, G. Reiner, R. Michalzik, D. Sowada, and K.J. Ebeling, IEEE J. Sel. Topics Quant. Elect., 3, 409 (1997).
25. S.F. Yu, "Analysis and design of vertical cavity surface emitting lasers", Wiley series in lasers and applications, (2003).
26. F.A.I. Chaqmaqchee, PhD theses. University of Essex (2012).
27. M. V. Hobden and J. Earner, Phys. Lett. 22, 243 (1966).
28. N. P. Barnes and M. S. Piltch, J. Opt. Soc. Am. 67, 628 (1977).
29. D. H. Jundt, Opt. Lett. 22, 1553 (1997).
30. A. Bruner, D. Eger, M. B. Oron, P. Blau, and M. Katz, Opt. Lett. 23, 194 (2003).
31. H. Y. Shen, X. L. Meng, G. Zhang, J. J. Qin, W. Liu, L. Zhu, C. H. Huang, L. X. Huang, and M. Wei, Appl. Opt. 43, 955 (2004).

32. J.P. Kim and A.M. Sarangan, Optics Letters, 5, 536 (2007)
33. S. Adachi, Journal of Applied Physics, , R1 (1985)
34. H. Kawai, S. Imanaga, K. Kaneko, and N. Watanabe, J.Appl. Phys. 61, 328 (1986).
35. J. Gustavsson, Â. Haglund, P. Westbergh, K. Szczerba, B. Kögel and A. Larsson, Optoelect. and commun. SPIE Newsroom, (2010).
36. R.J. Potter, PhD theses. University of Essex (2002).
37. C. Skierbiszewski, P. Perlin. P. Wisniewski, W. Knap, T. Suski, W. Walukiewicz, W. Shan, K.M. Yu, J.W. Ager , E.E. Haller, J.F. Geisz, and J.M. Olson, Appl. Phys. Lett., 76, 2409 (2000).
38. W. Shan, W. Walukiewicz, K.M. Yu, J.W. Ager III, E.E. Haller, J.F. Geisz, D.J. Friedman, J.M. Olson, S.R. Kurtz, H.P. Xin and C.W. Tu, , Phys. Stat. Sol., B, 223, 75 (2001).
39. M. Hetterich, A. Grau, A. Yu. Egorov and H. Riechert, Journal of Applied Physics 94, 18110 (2003)
40. I. Vurgaftman and J. R. Meyer, Journal of Applied Physics 94, 3675 (2003)
41. Skierbiszewski C, Semicond Sci Technol, 17, 803 (2002)
42. Y. P. Varshni, Physica (Utrecht) 34, 149 (1967).
43. Skierbiszewski C, Semicond Sci Technol, 17, 803 (2002)
44. S. Shirakata, M. Kondow and T. Kitatani, Applied Physics Letters, 1, 54 (2001)
45. R. Pa¨ssler, Phys. Status Solidi B 200, 155 (1997)
46. R. Kudrawiec, Journal of Applied Physics 101, 023522, (2007)
47. P. Seoung-Hwan, Journal of the Korean Physical Society, 4, 1085 (2004)
48. P.J. Klar, H. Gruning, W. Heimbrodt, J. Koch, W. Stolz, P.M.A. Vicente, A.M. Kamal Saadi, A. Lindsay and E.P. O'Reilly, Phys. Stat. Sol. (b), 223, 163 (2001).
49. S. Paul, J. B. Roy, and P. K. Basu, J. Appl. Phys. 69, 827 (1991)
50. R. Passler, Phys. Stat. Sol. B, 216, 975 (1999).
51. P. Seoung-Hwan, Journal of the Korean Physical Society, 4, 1085 (2004)
52. P.J. Klar, H. Gruning, W. Heimbrodt, J. Koch, W. Stolz, P.M.A. Vicente, A.M. Kamal Saadi, A. Lindsay and E.P. O'Reilly, Phys. Stat. Sol. (b), 223, 163 (2001).
53. I. Vurgaftman, J.R. Meyer and L.R. Ram-Mohan, J. Appl. Phys., 89, 5815 (2001).
54. F. Sarcan, O. Donmez, M. Gunes, A. Erol, M. C. Arikan, J. Puustinen and M. Guina, Nanoscale Research Letters, 7, 529, (2012)
55. F. Sarcan, O. Donmez, A. Erol, M. Gunes, M. C. Arikan, J. Puustinen and M. Guina, Applied Physics Letters 103, 082121 (2013)

CHAPTER 4

Experimental Techniques

4.1 Introduction

This chapter covers all experimental techniques employed in the work presented in the thesis including details about the experimental set ups, practical procedures and some theoretical background on the techniques being used. This chapter begins with a review of the growth techniques of the dilute nitride material system followed by a discussion on the material preparation and device fabrication. The remainder of this chapter is then devoted to optical and electrical characterisation techniques used during this work.

4.2. Growth Techniques

The study of dilute nitrides has benefited from the advances made in the growth technology. The ability to precisely control the layer thickness, dopant, composition and impurity concentration has resulted in vast improvements in the crystalline quality of the dilute nitride materials, as well as improve their optical and electronic performance and enable the fundamental study of their unusual properties. The samples studied in this thesis were all grown on GaAs substrates using a VG V80 Molecular Beam Epitaxy (MBE) system by Tampere University of Technology in Finland.

4.2.1 Molecular Beam Epitaxy

Molecular Beam Epitaxy (MBE) was initially developed by J.R. Arthur [1] and A.Y. Cho[2] in the late 1960s for growth of GaAs and GaAs-$Al_xGa_{1-x}As$ heterostructures. MBE is essentially a vacuum deposition process utilising an ultra-high ($<10^{-10}$ Torr) vacuum (UHV) and thermal beams of atoms or molecules. In a high-vacuum condition, the constituent elements of a semiconductor are deposited in the form of ‘molecular beams’ onto a heated crystalline substrate

to form thin epitaxial layers. A schematic of a typical MBE system is shown in Fig.4.1. Neutral thermal atomic and molecular beams are created in heated Knudsen cells (K-cell) and diffused into a reaction chamber that is kept at a vacuum pressure of 10^{-7}-10^{-10} Torr.

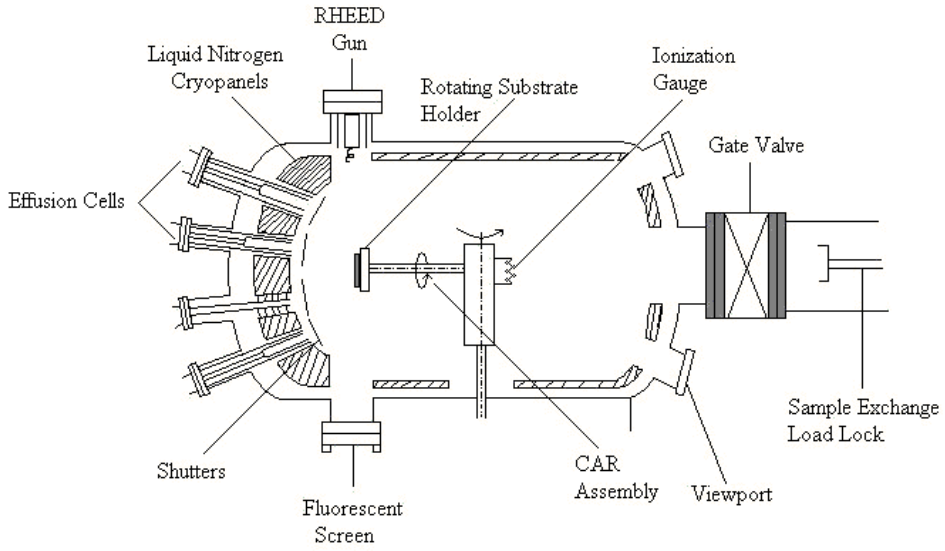

Figure 4.1: A schematic of a typical MBE system

The constituents are independently heated until they achieve enough kinetic energy to effuse from the orifices into the chamber by thermo-ionic emission. To start and stop the beams, simple mechanical shutters are used. When shutters in front of the Knudsen cells are opened, the molecules then migrate in a UHV environment and impinge on a hot substrate, where the equivalent pressure of the molecular beam is low (~10^{-6} Torr), thus the atoms or molecules do not experience compliant motion and interact to form a single crystal [3]. The sticking coefficient determines the probability of the material being deposited on the wafer surface. For GaInNAs, Group III elements coefficient is nearly unity and depends on the growth temperature. Meanwhile for Group V elements it is composition dependent and its value is influenced by the presence of other Group V elements on the wafer [4-5]. In order to grow a sufficiently clean epilayer and satisfy the required growth rate (~1μm/h for III-V type semiconductors), the background pressure in the chamber is reduced to 10^{-11}~10^{-12} Torr. The substrate is kept at a temperature of about 400-700ºC (or lower if possible) to minimize the diffusion of the deposited

atoms and is usually rotated during growth to obtain improved uniformity of composition, thickness and doping. M. Kondow [6] presented a complete review of the growth of GaInNAs using the MBE and more specific introduction of MBE [7-10] growth method can be found in the literature.

With MBE, high quality layers and very abrupt interfaces can be grown. In addition, this technique allows precise control of layer thickness, composition and dopants [11], along with in-situ monitoring such as Reflection High-Energy Electron Diffraction (RHEED) and even the possibility of 3D structure growth using masks.

RHEED is one of the most useful tools for in-situ monitoring of the growth which gives information about substrate cleanliness and proper growth conditions [12, 13]. In RHEED, a high energy (typically 5-50keV) electron beam generated by a RHEED gun is directed towards the sample surface at a grazing angle of less than 5^o (under such conditions the electrons just penetrate a few atomic layers into the crystal, and consequently the RHEED pattern represents the surface symmetry and not the bulk crystal). The electrons are diffracted by the crystal structure of the sample and a surface-sensitive diffraction pattern is then imaged on a phosphor screen mounted opposite to the electron gun [14].

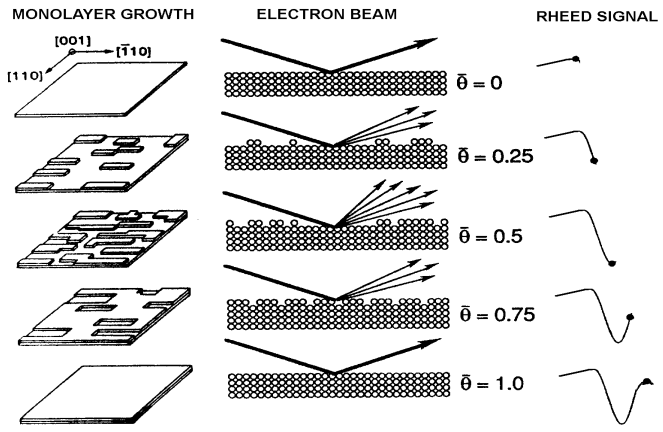

Figure 4.2: First-order growth model in relation to the RHEED intensity oscillations, where $\overline{\theta}$ indicates the number of monolayer grown [15].

The intensity of the RHEED pattern oscillates as the sample is grown layer by layer with time, and the period of the oscillation corresponds to the time needed to grow a monolayer as can be seen in Figure 4.2. The magnitude of the oscillations dampens because as the growth progresses, the coverage statically distributes over more and more layers, eventually a constant surface roughness is yielded. The RHEED pattern can give fundamental information about the surface geometry and chemistry, for example: sharp streaks indicate a smooth surface, while spotty patterns indicate a rough surface [16]. Table 4.1 gives the typical growth parameters used by the Optoelectronics Research Centre (ORC) Tampere University of Technology, where the doping level, the layer compositions, and the layer thickness are targeted according to the design.

Table 4.1: Growth parameters used for the samples grown in Tampere University of Technology

Elements	Growth Temperature	As/III Beam Equivalent Pressures (BEP) ratio	Growth rate
n-AlGaAs(AlAs)/GaAs DBR and staircase grading layers	600 ˚C	40-60	0.248-1.348 μm/h
GaAs (GaNAs) layers in the active region	580 ˚C	17-29	0.248 μm/h
GaInNAs(GaInNAsSb) QWs	340 ˚C	16	0.371 μm/h
p-AlGaAs(AlAs)/GaAs top DBR and p-type staircase grading layers	600 ˚C	40-60	0.248-1.348 μm/h

4.3 Sample Preparation and Device Fabrication

Device fabrication of dilute nitrides samples was performed in a class J-10000 clean room facility at the University of Essex to avoid contamination. To prepare the samples for optical and electrical characterisation, a range of fabrication techniques were used including; cleaving, optical lithography, wet etching, and vacuum deposition.

Samples for optical characterization such as photoluminescence were simply cleaved from the wafer, usually 2×2 mm^2 and mounted on copper pads using crystal bond wax, while samples for electrical characterization such as current-voltage (I-V) and photoconductivity (PC)

require the deposition and diffusion of metallic contacts on the sample. The device fabrication techniques such as optical lithography, etching and metallization are described in the following section. In this thesis, the samples were fabricated as shown in Fig.4.3 with multiple diameters as illustrated in Figure 4.4

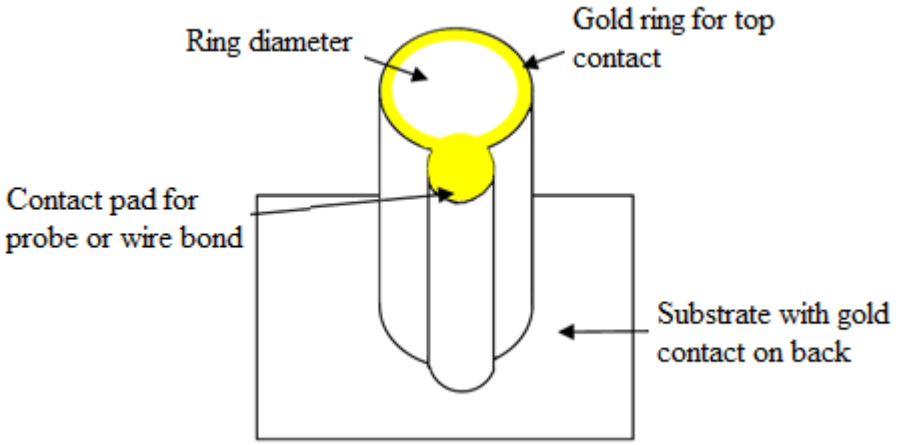

Figure 4.3: A diagram of the photodiodes created in this project

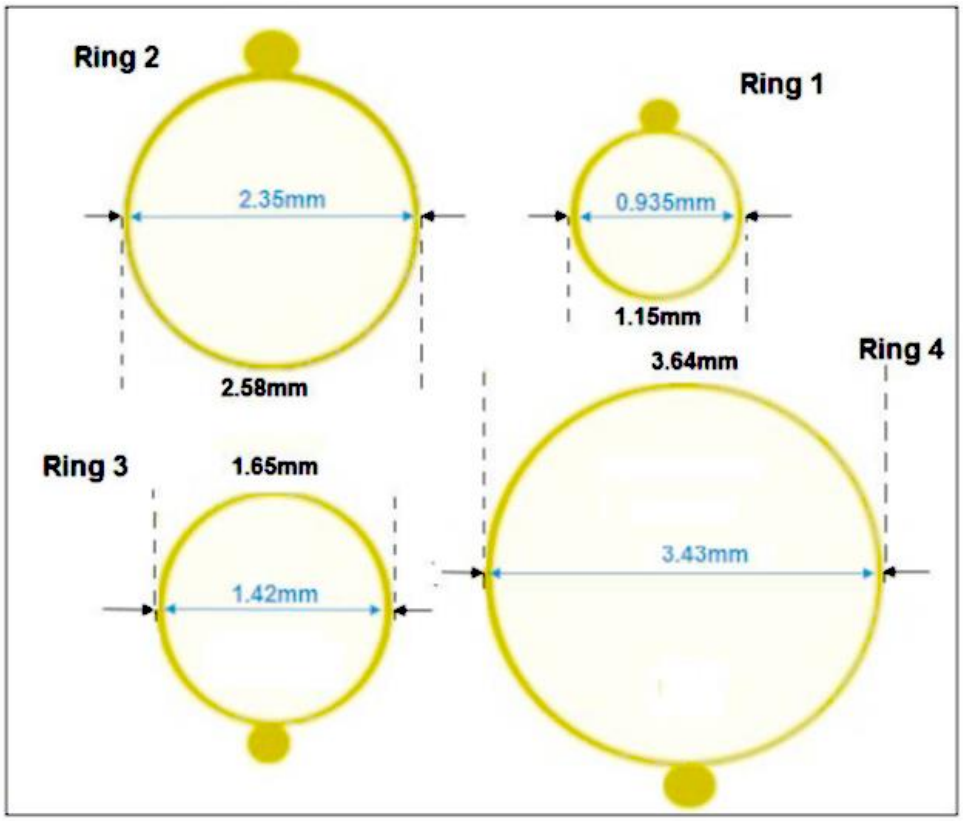

Figure 4.4: Diameter variation of masking

4.3.1 Cleaving

Cleaving is the first step of the device fabrication. All the wafers used for this work were grown on semi-insulating (SI) GaAs (100) substrates. The wafer was cleaved into the desirable sizes using a sharp tungsten carbide scriber. The small scratch was done on the edge of the wafer (top epilayer side) parallel or perpendicular to the major flat. A small nick was made on the edge of the wafer. Cleaving was done by applying a little careful pressure to the backside of the wafer over the scratched side as illustrated in Fig.4.5. Because most semiconductors are anisotropic in their physical properties, they can be cleaved most easily between certain planes. The applied force cracks the semiconductor in a straight line, and in this way the sample can be cut to the required shape.

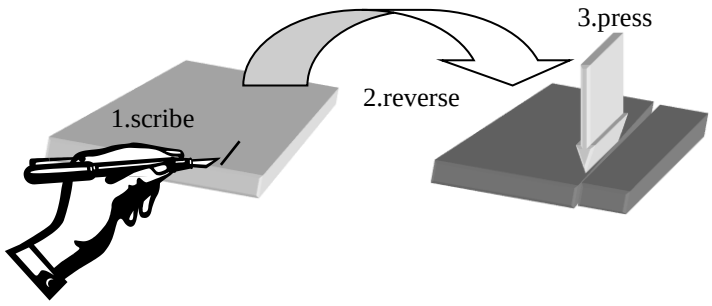

Figure 4.5: Cleaving processes.

4.3.2 Cleaning and Mounting

Cleaning is of importance if fabrication is to be successful. It is the first step and aimed towards the removal of any undesired materials, such as ions and metal impurities, dust, grease and thin oxide film on the surface prior to processing. To avoid poor device electrical characterization such as non-Ohmic contacts which are caused by dirt on the sample surface. The rinsing water used is purified de-ionised water, which has been purified by removing the ionised salts from the solution. Typically, the process of purifying is to replace hydrogen ions with cation impurities and hydroxyl ions with anion impurities (ion-exchange) [17]. In the case that

contact adhesion to the semiconductor is poor, it is believed to be due to residual oxides or photoresist on the surface. Thus, the typical contaminants must be removed prior to photoresist coating. Table 4.2 illustrates the cleaning methods.

Table 4.2: Cleaning methods to remove various substances

	To remove	**Method**	**Time**
1	Wax	Acetone	30 s
2	Photoresist (OCG BPRS150)	Acetone	Fast
3	After metallisation (photoresist)	Acetone	30 min
4	Oxide	HCl (1:3)	15s
5	Developer(OCG PLSI)	Rinsing	-
6	Etching (terminating)	Rinsing	-
7	Recycle ceramic	Acetone	Hours
8	Finger print	Acetone Methanol Rinsing	1-2 min

The initial cleaning processes are described as below:

1. The wafer slice was soaked in acetone and baked on the hot plate for 1 minute at a temperature of 100°C and then in ethanol for 2 minutes to remove any grease (such as fingerprints), wax or dust from surface. It is noted that acetone is flammable and ethanol is toxic by skin adsorption so careful attention must be paid to avoid any hazards.
2. Rinsed under running de-ionised (DI) water for 1 minute and dried with zero grade nitrogen gas.
3. The wafer was mounted on a glass cover slip using melted crystal bond wax at 150ºC on a hot plate.
4. To remove the surface oxidation layer, the sample was immersed in an ammonia solution 1:10=NH_3: DI water for 15 to 20 seconds 3 times, rinsed thoroughly in flowing water after each immersion, and finally blown dry with zero grade nitrogen gas.

4.3.3 Photolithography

Photolithography is the most common lithography technique performed in semiconductor technology to transfer a geometric pattern from a mask to the surface of a wafer. Photolithography involves three major processes; i) application of photo-resist (spin coating), (ii) exposure and (iii) development. The processes of photolithography are as below:

1. The sample is soft-baked on a hot plate for 30 seconds at a temperature of 100°C to remove any water vapour on the sample surface. The sample was placed on the Dynapert photoresist spinner (PR514E), and a few drops of positive photoresist (making sure that the entire surface was coated by it) are applied onto the sample using a resist dispenser. To produce a thin and uniform layer, the spin coater runs at 3000 to 6000 rpm for 15-30 seconds by changing the voltage of the power supply giving a film approximately 1μm thick. In order to make the photoresist film thinner (for better resolution) and to remove some of the coating solvent from the photoresist, it is soft-baked at 90°C for 1 minute. Temperature rises from the bottom of the wafer and penetrates into the wafer and evaporates the coating solvent on the surface. The thickness of the photoresist is decreased by 25-30 % due to it being soft-baked.

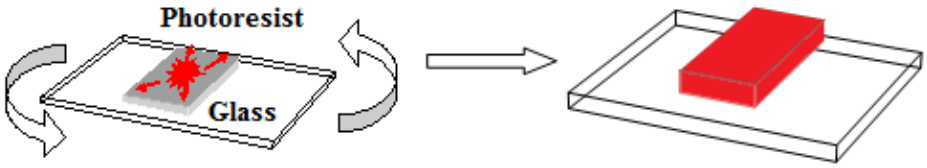

Figure 4.6 (a): Spin coating process.

2. The sample is then inserted onto the vacuum chunk of a Dynapert MAS 12 mask aligner system along with appropriate contact mask (ring mesa). Once the mask had been accurately aligned with the pattern on the wafer's surface, the photoresist is exposed through the pattern on the mask with a high intensity ultraviolet light for 12 seconds.

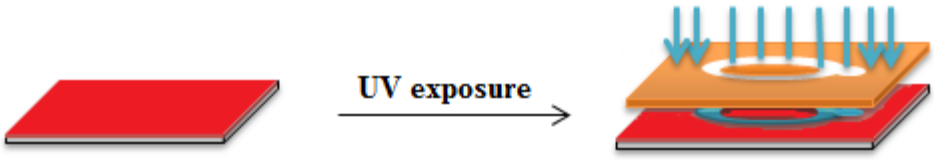

Figure 4.6 (b): Masking and UV exposure process.

3. The pattern is then developed by removing the exposed photoresist via immersion of the sample in a mixture of Sodium Hydroxide: water (approximately 1%) for 30-60 seconds. Once the photoresist was developed and dried with nitrogen gas, it was checked under an optical microscope to assess the quality of the development process.

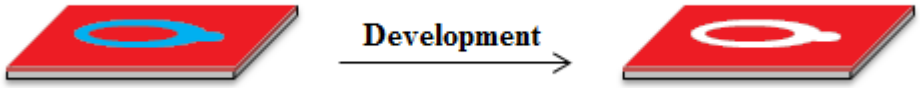

Figure 4.6 (c): Pattern development process.

4.3.4 Metallization

The metallization technique was used to form Ohmic contacts on the sample's surface. The steps in metallization are described below:

1. The sample is immersed 3 times into the acidic solution of HCl:H_2O (1:2) for 20 seconds and then rinsed in DI water and dried using zero grade nitrogen to remove oxidation which is likely to increase contact resistance.
2. The sample was put into an Edwards E306 vacuum coating unit and evacuated with nitrogen trap diffusion pump (10^{-7} mbar). High vacuum is essential to lower the melting points of the metals.
3. Before evaporating metals, the sample was exposed to UV light to soften the remaining photoresist and help to get a successful lift-off.
4. Prepare the metal composition to form the electrical contacts on the sample. The amount of each metal depends on the planned contact thickness and composition for which Au

(5cm) and Ti (1cm) are used. But first Au and Ti are cleaned by putting them in acetone and soft-baked for 1 minute followed by a rinse them in DI water and dried using zero grade nitrogen.

5. Both the sample and the metals are loaded into the vacuum coater (evaporator). The removal of oxide is necessary to ensure the contacts are Ohmic. Empty the evaporator, outgas the metals and filaments against the shutter and melt the metals, which will evaporate and deposit on the sample surface.
6. After finishing the deposition of the contacts (the process takes about 2 hours), the sample was removed from the evaporator, and the excess metal was rinsed away with acetone (lift-off process). Later, the sample is removed from the cover slip by melting the wax on the hot plate. Then the sample was immersed in acetone to remove the remaining wax followed by a rinse with DI water and dried with nitrogen.

Figure 4.6 (d): Top contact evaporation and lift-off metals

7. The samples are then remounted on a cover slip with the substrate facing up. Before evaporating the metals, the photoresist coated samples are exposed to blanket UV light and the sample clip of the vacuum chamber is placed directly upon the middle of the sample. Step 4-6 are repeated. Both top and bottom contacts resistances are checked to test the evaporation process.

Figure 4.6 (e): Bottom contact evaporation and lift-off metals

4.3.5 Etching

Etching in microfabrication refers to removal of unwanted areas of a wafer. There are two major types of etching: dry etching and wet etching. The chemical-reaction-limited wet etching was employed for etching geometric shapes for GaInNAs/GaAs based structures throughout this work. The samples are etched using wet etching solution for which different options were available, depending upon the required etch rate as summarised in Table 4.3.

Table 4.3: Etchants used and relative characteristics

Etchant	Ratio	Etch rate
Citric acid (50g of citric acid in 100ml of DI water): H_2O_2	3:1	500nm/min
Citric acid (50g of citric acid in 100ml of DI water): H_2O_2	1:1	60nm/min
Citric acid (50g of citric acid in 100ml of DI water): H_2O_2	10:1	200nm/min
H_2SO_4 : H_2O_2 : DI water	1:8:80	500nm/min

Before etching, an etch mask was loaded along with the photoresist coated sample into the mask aligner. After developing the sample, a hard-bake at 150ºC for 5-10 minutes was applied to improve the adhesion of the resist to the sample. A step height analyser (Tencor Alpha step 100) is used to measure the photoresist thickness (and the contacts if already present) and monitor the etch depth. The machine consists of a stylus with a microscopic diamond tip, which scans across the surface whilst measuring the vertical movement. This first measurement provides the offset to be considered during the etching process. The material is etched by immersing the sample in the etchant solution for the pre-calculated time, rinsed with DI water, and dried with N_2 gas after each etching run. The etching process is monitored with the surface profiling machine, repeating this procedure until the required depth is reached. When the desired etch depth is reached, the sample is cleaned using acetone and rinsed in DI water and dried with N_2 gas to remove the photoresist and the final etch depth is measured. Finally the sample was mounted onto an Au pad-coated ceramic header using conductive epoxy.

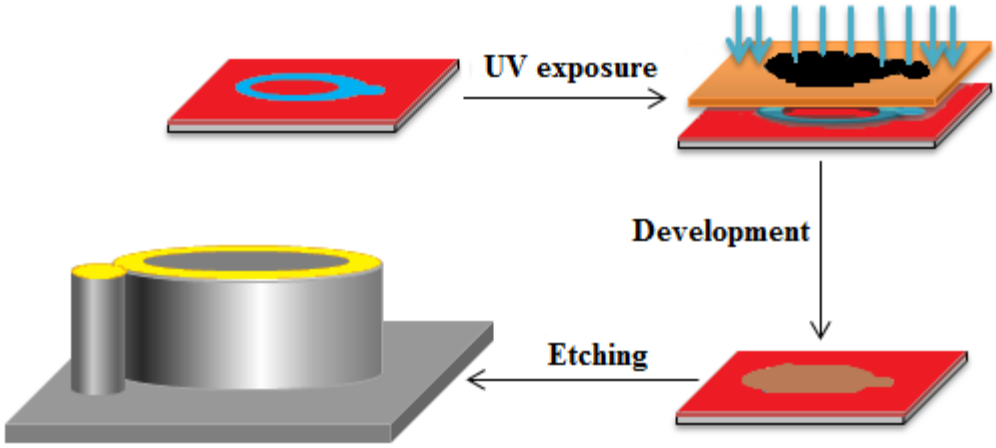

Figure 4.6 (f): Etching process exaggerated to show device structure.

4.3.6 Wire Bonding

The I-V characteristic of the sample after etching is checked. Then, the contacts of the device can be connected to the gold bond pad on the ceramic header by Au wires using a ball-type wire-bonder (Kulicke & Soffa Wirebonder 4524) as the final process step. The bond condition is optimized by adjusting temperature, ball size, pressure, duration and strength of the ultrasonic power. The sample needs to be tested again after wire bonding by measuring the resistance between the gold pads connected to contacts to confirm that the contacts show the Ohmic (linear) I-V behaviour.

4.4 Photoluminescence

The standard technique for the optical characterisation of semiconductor materials and devices is photoluminescence (PL). PL spectroscopy is a contactless, non-destructive and sensitive technique for investigation of optical properties of semiconductors. Since no electrical contacts are required, high-resistivity materials can be investigated without any sample preparation. It is a unique technique which provides information about the impurity levels, defect and recombination process either radiative or non-radiative transitions, present in the semiconductors. The radiative transition in a semiconductor strongly depends upon the material

quality, growth conditions and density of impurities so the technique allows the purity and crystalline quality of semiconductors to be assessed. When light of sufficient energy is incident on a material, photons are absorbed and excess electron-hole pairs are created [18]. Eventually, these excitation energies will relax and electrons return to the ground state via both the radiative and the non-radiative processes. If radiative relaxation occurs, the emitted light is called PL. This spontaneous emission of light can be collected and analysed to characterize a variety of material parameters. The PL spectrum records the various transitions, which can be used to determine the electronic energy levels. The PL intensity gives a measure of relative rates of radiative and non-radiative processes. Variation of the PL spectrum such as peak position, peak intensity and linewidth with external parameters like temperature and excitation power can be used to obtain information on band offsets, help to further identify underlying electronic states and bands, and explore impurity and defects within the material [19-22]. The most important electronic transitions observed in the semiconductors are illustrated in Fig.4.7.

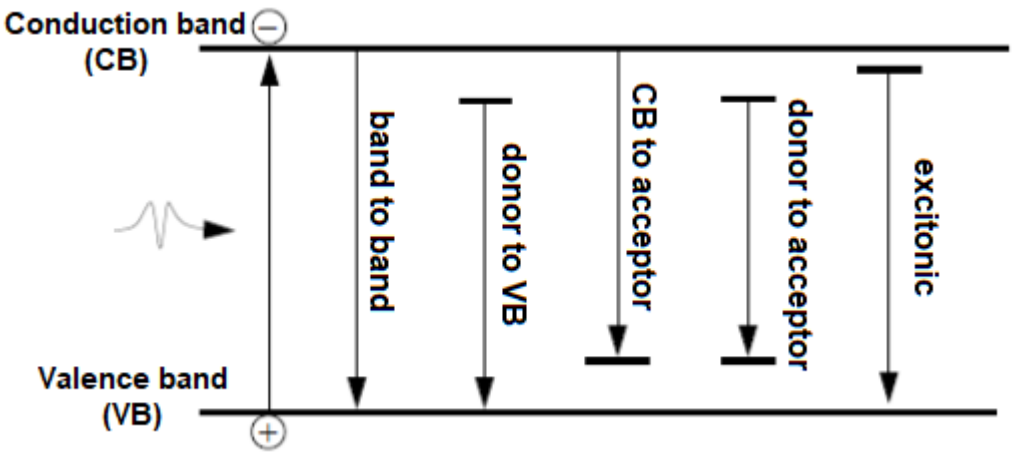

Figure 4.7: Possible radiative recombination in semiconductors.

Among all these transitions, the most common and desirable is the band-to-band, which occurs between the bottom states of the conduction band and the top states of the valence band. This energy difference is usually called the energy bandgap [23]. One of the primary aims of the PL technique is to determine this energy. Bandgap determination is particularly useful when

working with new compound semiconductors or structures. It can also be used to reveal impurity levels, recombination mechanisms, and material quality [17]. In 2D systems, such as in the presence of quantum wells, the used excitation light energy can be high enough to excite the electrons to states higher than the fundamental one (illustration of e_1-h_1 shown in Fig.4.8).

The spectral content of the PL is able to reveal all the low-energy optical transitions. Although it is not possible to identify directly the non-radiative traps from a single PL spectrum, their signature is however evident in several types of PL measurements. The temperature dependence of the PL intensity can be used to identify defect, trap or impurity activation energies. In fact, in a perfect semiconductor, the PL spectrum should not change in amplitude as the temperature varies. However, the associated thermal energy makes the lattice vibrations increase with increase in temperature and this perturbs the free path of the photo-generated carriers. This phenomenon contributes to the total carrier scattering and alters the behaviour of the defects present in the crystal. In the case of QW structures, these perturbations lead to an enhancement of the probability for the confined carriers to escape from the well. This consequence leads to a reduction of the PL spectrum intensity and an enlargement of the corresponding linewidth.

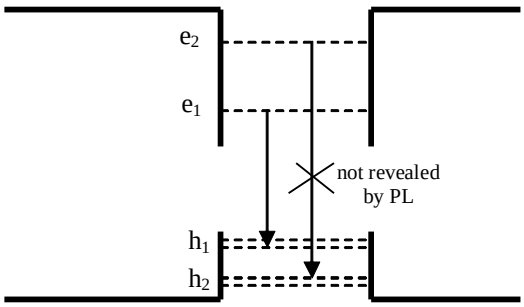

Figure 4.8: Lower and higher transitions in a QW. PL spectroscopy is able to detect just the lower transitions

Temperature changes also affect the material bandgap due to lattice spacing expanding when the amplitude of the atomic vibrations increases. An increased interatomic spacing

decreases the potential seen by the electrons in the material, which in turn reduces the size of the energy bandgap. The same effect can be obtained by direct modulation of the interatomic distance, such as by applying an external pressure or by engineering design to control the strain in the material. PL emission from high-quality QW samples is generally characterised by symmetric Gaussian-shaped peaks where energy bandgap varies according to temperature following the empirical Varshni equation as explained in chapter 2 [24].

The PL experimental setup is shown in Fig.4.9. In the PL measurements, either 488 nm line of an Argon-ion laser or 532 nm line of Nd-YAG laser modulated with an optical chopper is used to excite the samples, generating hot electrons and holes in the conduction and valence bands, respectively. These excitation energies were chosen to be greater than the bandgap energies of all of the investigated samples in this thesis.

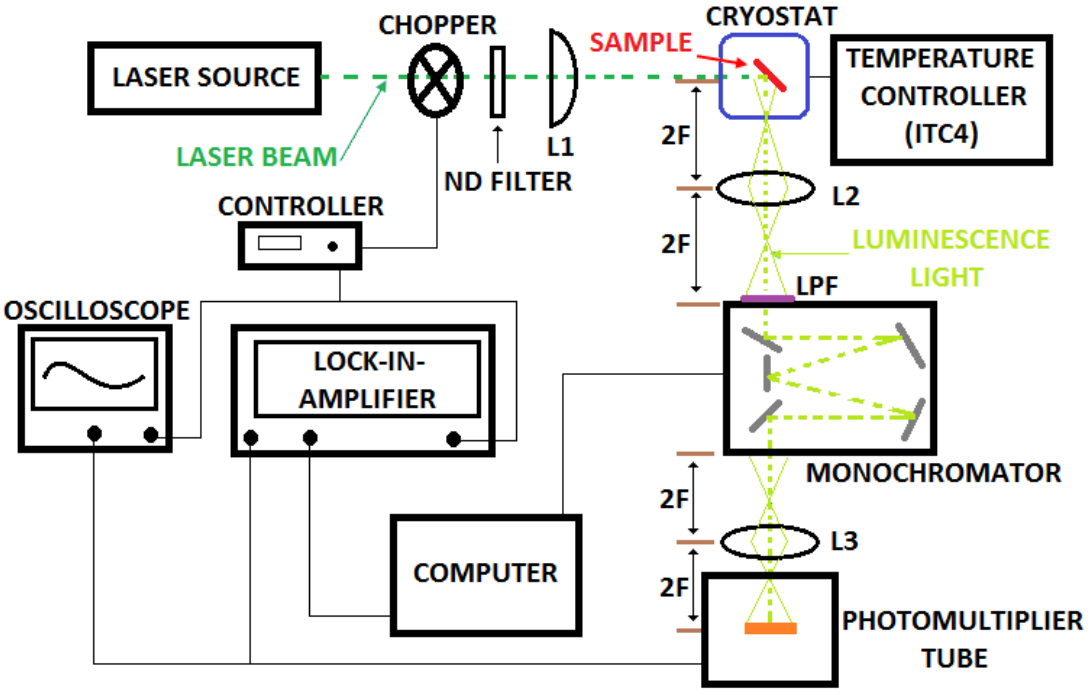

Figure 4.9: The experimental setup for the photoluminescence measurement.

The laser beam is directed using plano-convex optical lens, L1 (F=10cm) to focus the light onto the sample. The investigated samples are placed in a variable temperature liquid-bath Helium cryostat (Oxford instrument, Variox cryostat), using an Oxford Intelligent Temperature

Controller (ITC 4) to allow the sample temperature to be controlled from 15-300 K. The sample temperatures are measured using a temperature sensor installed in the cryostat, which is positioned on the heat exchanger a distance away from the sample. Since the sensor reaches the target temperature prior to the sample, a suitable time interval is necessary between setting the temperature and taking a measurement.

The sample's emission is collected and focused onto the entrance slits of a 1/3 cm high resolution monochromator (Bentham, TMc) using a bi-convex lens, L2 (F=5cm). The monochromator is controlled by a stepping motor (Bentham, SMD3B/IEEE) with a resolution of 0.2A°/step and is able to sweep the appropriate wavelength range. The dispersed luminescence from the monochromator is detected using a liquid nitrogen cooled InP/InGaAs photomultiplier (Hamamatsu, R5509-72), with high sensitivity and nearly flat spectral response across the optical range from 400-1600 nm. In order to protect the photomultiplier and minimise optical noise, a suitable long-pass filter is placed in front of the entrance slit of the monochromator, to remove the majority of the scattered laser light. In addition to the long-pass filter, the experiment was performed in low ambient light conditions, with black curtains placed around the most sensitive part of the equipment to avoid any stray light detection. In order to minimise the noise, a pin-hole was placed before the cryostat to block most of the divergent spontaneous emission light.

The sample was usually orientated at about 70-80° to the incident laser beam, so that the reflected beam in the cryostat could leave the cryostat through the optical window. The intensity of the PL signals should be maximized by slightly adjusting the optical alignment of the lens, L3 and the phase parameter and sensitivity of the lock-in amplifier (Stanford research system, SR830). The amplitude of the electrical signal from the photomultiplier is amplified using a lock-in amplifier, which is triggered synchronically with Bentham 218F Variable Frequency Optical Chopper at frequency of 1 kHz. This procedure is monitored by an oscilloscope (Tektronix TDS 1002, 60MHz) connected to the lock-in amplifier. Finally, the amplified PL

signals from the LIA are recorded on a computer by an interface GPIB cable, triggered by the monochromator stepping motor with a data acquisition via a LabVIEW program.

4.5 Photoconductivity

The photoconductivity (PC) technique is a tool to investigate the changes in the electrical conductivity of a semiconductor when the incident radiation illuminates the sample with appropriate energy. When light illuminates a semiconductor, the photons with the right energy are absorbed by the material. If the photon energy is greater than the band gap of the semiconductor, electron-hole pairs are then created which is called intrinsic photoconductivity. When the photon energy is smaller than the bandgap, only one type of carrier may be generated via ionisation of dopants or impurity levels to band edge transitions. This phenomenon is called extrinsic photoconductivity. In general, the creation of excess carriers leads to an increase in conductivity and the conductivity increase due to excess carriers, which is basically defined to be photoconductivity given by:

$$\Delta\sigma = e(\Delta n u_n + \Delta p u_p) \quad \text{.....(4.1)}$$

where Δn and Δp are the concentration of photo-generated excess electrons and holes, and μ_n and μ_p are the corresponding mobilities. The total conductivity of the material under illumination is then given by the sum of $\Delta\sigma$ and the electrical conductivity of the sample with no illumination, σ_0;

$$\sigma = \Delta\sigma + \sigma_0 \qquad \text{……(4.2)}$$

It is possible to determine the dark conductivity using current- voltage (I-V) measurements. However if the material is high resistivity, the dark conductivity is so low that it can be assumed $\sigma \approx \Delta\sigma$.

In general, photoconductivity is a complex process, which involves photo-generation and recombination of charge carriers and their transport processes. It provides a wide range of information about the physical properties of the investigated material such as density and levels of impurities, the width of the band gap, the life time of the charge carriers, etc. In this thesis, the techniques to measure the PC can be divided into two: (a) spectral photocurrent and (b) transient photoconductivity.

4.5.1 Spectral Photocurrent Measurement

The spectral photocurrent measurement is a deeper analysis of photoconductivity by the device. It is a particularly important experimental method for a photodetector to obtain quantum efficiency. The experimental set-up for spectral response is shown in Fig.4.10.

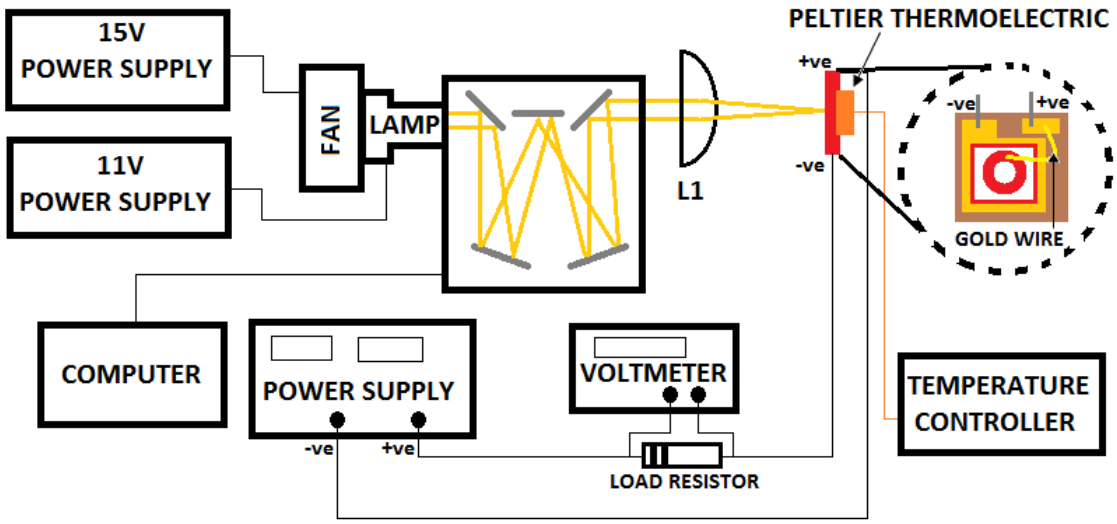

Figure 4.10: The experimental setup for the p-i-n samples spectral photocurrent measurement.

The Bentham IL1 Illuminator (quartz halogen lamp with a spectral range of 350nm to 2.5µm) is used as the light source and is attached to the entrance slit of the monochromator. The Farnell Instrument Stabilised Power Supply (LT30-2) of 11V is connected to the lamp while 15V from a Griffin Low Tension variable voltage supply unit is connected to the fan for cooling purposes. The alignment of the samples is carried out by reducing both slits of the monochromator step by step to 1mm until dispersed light covers the samples. The dispersed light

from the monochromator was then defocused using a plano-convex lens, L1 onto the samples to achieve uniform illumination that fell within the device area. The excitation intensity was then measured and calibrated by using a Coherent power meter and Anritsu Wiltron Optical Handy power meter (ML9002A). During the setup, the environment is set in very low ambient light conditions. A black box is used to cover the dispersed light from the monochromator to prevent any stray light detection from affecting the samples. The procedure for the p-i-n spectral photocurrent used the Thurlby Thandar (PL310) power supply as a bias voltage and a Keithley 177 Microvolt DMM to measure the voltage drop across the load resistor (~50Ω). The PC spectrum was obtained from the photocurrent flowing across the series resistor and induced by a constant DC voltage applied to the circuit.

The setup for the DBR samples is relatively different compared to the one for the p-i-n samples. As depicted in Figure 4.11, the light source is a National Instruments Tunable Laser (NI-PXI-1033) powering up to 7mW which provides wavelengths from 1265nm up to 1350nm. The light source is attenuated by a JD Optics variable optical attenuator (5500L) and 10% coupled into an Agilent 8163A Lightwave Multimeter for incident power measurement and 90% to the samples.

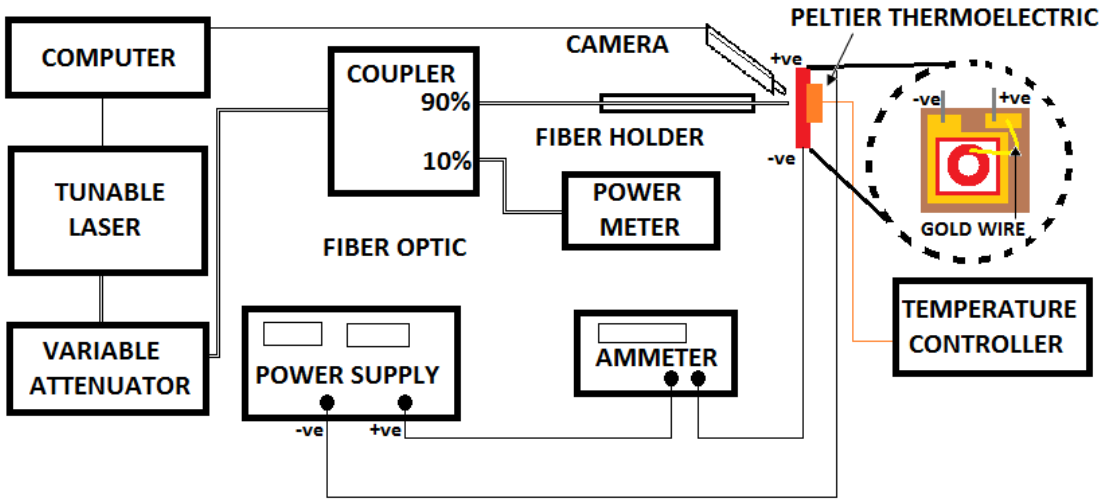

Figure 4.11: The experimental setup for the DBR samples spectral photocurrent measurement.

The Thurlby Thandar (PL310) power supply is used as a bias voltage and Keithley 480 picoammeter is used to measure the current in the samples. The picoammeter is used for DBR samples instead of the load resistor method due to its persistence and responsivity compared to a voltmeter especially during the alignment process. Furthermore, a shortest possible cable connection (less than 0.01Ω) is used to connect all the equipments to reduce circuit resistance and the applied voltage is limited to less than -3V to avoid breaking the diode junction within the device.

The alignment process for the DBR samples is pretty delicate because it needs to be done with the help of a camera to make sure that device is perpendicularly close to the fibre without touching the surface. The alignment process comprises of X, Y, Z (3 Dimension) rotating movement for the sample and fibre holder. The alignment is adjusted precisely until the maximum value of the photocurrent is obtained. The spectral photocurrent measurement in this thesis is made using a Peltier thermoelectric device to vary the temperature. The temperature is taken around 300K and is controlled by using an ILX Lightwave LDC-3724B temperature controller. The data for this experiment has been recorded manually by sweeping the wavelength of the light source and measuring the voltage dropped on the load resistor and the photocurrent for each wavelength is taken.

4.5.2 Transient Photoconductivity Measurement

The transient photoconductivity (TPC) technique investigates the response time of a semiconductor device under illumination. A pulsed laser light with a short pulse duration and slow repetition rate is employed to generate the electron-hole pairs. The pulse duration must be short enough to avoid any steady-state situation so that no recombination or diffusion occurs. When the sample is biased, the photo-generated carriers move towards the contacts (electrons to the anode, holes to the cathode), generating the PC signal. After a very short pulse, the exciting

radiation is turned off and the conductivity decreases exponentially to its dark value [25]. This decay is the result of several decay mechanisms in the recombination process, each one characterised by a different time constant. In the presence of QWs, many different processes must be taken into account to characterise the TPC decay, as discussed in detail by Ridley [26]. This method is most useful when the pulse duration is shorter than the fastest trapping rate while the repetition rate is slower than the slowest trapping rate in the device.

Measuring the TPC signal is possible by considering the photocurrent flowing between two electrical Ohmic contacts diffused into the sample. After the very short pulse width, the exciting radiation is turned off, and the conductivity decreases exponentially to its dark value. The setup for the TPC measurement is shown in Fig.4.12.

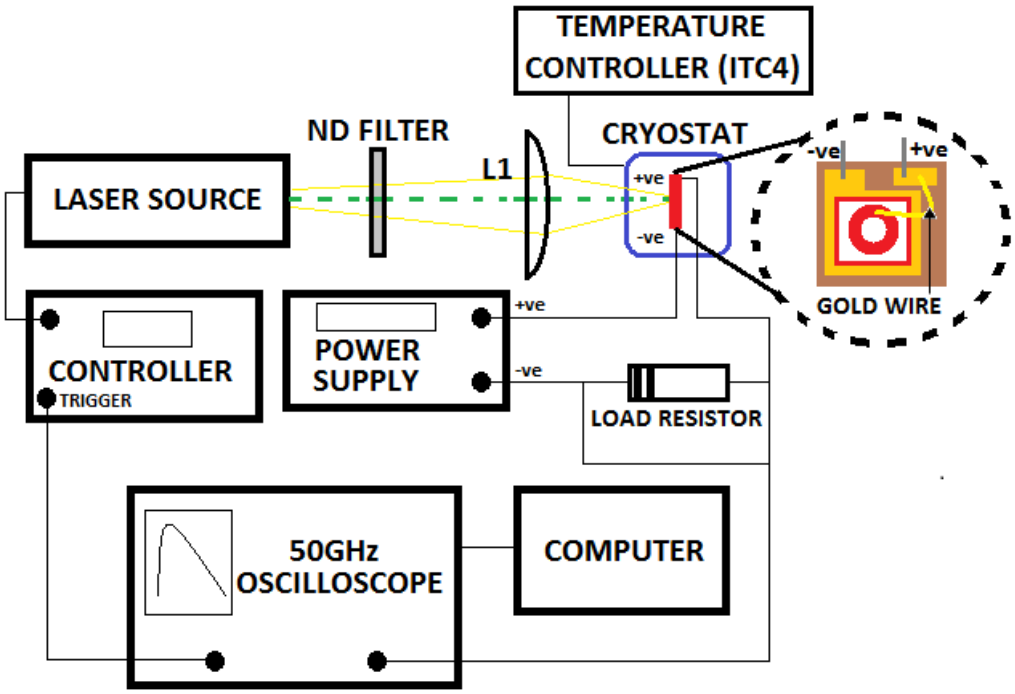

Figure 4.12: The experimental setup for the TPC measurement.

TPC is studied using a Q-switched, Neodymium-doped yttrium lithium fluoride (Nd:YLF) emitting 500ps pulses at 1047nm wavelength with 1kHz repetition rate. These pulses are directed to the sample through a plano-convex lens, L1 to focus and obtain maximum irradiation. The laser incident intensity is varied using a series of neutral density filters. The

samples are placed in the Helium cryostat and are then connected in series with a load resistor (~50Ω) and the Thurlby Thandar (PL310) power supply as bias voltage. In this thesis, TPC is performed between room temperature and T=50 K. A DC power supply is used to bias the samples between 0 V and -6 V, and the voltage drop across the load resistor is used as the input to a 50 GHz digital oscilloscope (Hewlett Packard 54750A), from which the output signal is recorded with a data acquisition of LabVIEW program and then analysed.

4.6 Current-Voltage Measurement

Current-Voltage (I-V) measurements are commonly used to determine device electrical characteristics such as conductivity, resistance, drift velocity and contact quality of the fabricated device. At high temperatures, the conductivity of the semiconductor materials is intrinsic as a result of the excitation of the electrons from the valence band to the conduction band. However, at low temperatures, the conductivity is due to presence of the impurities and depends on the majority impurity type either *n*-type (electron carriers) or *p*-type (hole carriers) [27].

In this thesis, the I-V measurement is mainly focused at operation around room temperature only. The dark current measurement is carried out as the sample diode characteristic need to be investigated right away after fabrication. But before that, the contacts need to be tested for Ohmic behaviour as poor contacts can result to either completely blockage to the flow of current or limiting the current resulting in incorrect measurements. A wealth of information on the quality of the junction can be obtained from the dark I-V. Most importantly is the amount of leakage current across the junction, which is influenced by the recombination currents and tunnelling or thermionic behaviour. The analysis of dark current density plots shows the amount of dark current density generated by the device as well as revealing the nature of the dominant dark current density component. While, the light I-V characteristics of a photodetector determines device absorption efficiency and possible gain under different operating conditions

(temperature or light intensities). Measurements of the I-V characteristics are made by replacing the ammeter/voltmeter and power supply connection of the device terminals to the Keithley 236 source measure unit. A chosen range of voltages from negative bias to positive bias are swapped across the sample and at the same time measuring the resulting current.

4.7 Reflectivity Measurement

Reflectivity measurement is carried out to investigate the reflectance cavity of the DBR mirrors. The measurement process is similar to the photocurrent measurement for DBR samples but an optical circulator is used instead of a coupler to observe the reflected light from the DBR mirrors. The optical circulator used in this work is a three-port optical device designed such that light entering any port exits from the next port. This means that if light enters from port 1, then it will be emitted from port 2. Some of the emitted light is reflected back to the circulator through a bi-directional single fibre. However, the reflected light does not come out of port 1 but instead exits from port 3. An optical circulator is adopted in this method because of their high isolation of the input and reflected optical powers and their low insertion loss. Optical circulators are non-reciprocal optics, which means that changes in the properties of light passing through the device are not reversed when the light passes through in the opposite direction.

Therefore, in the application of the reflectivity measurement as depicted in Fig4.13, the laser light will enter port 1 and emitted from port 2 towards the DBR samples. The reflected light from DBR samples will pass through in the opposite direction from the same port 2. The reflected light will exit from port 3 and converted to electrical data by an oscilloscope. The reflectivity measurement is conducted by sweeping the laser light according to the wavelength and reflected light from the sample will be shown on the oscilloscope where the data will be recorded manually. The wavelength is restricted between 1265nm and 1350nm due to laser limited operation.

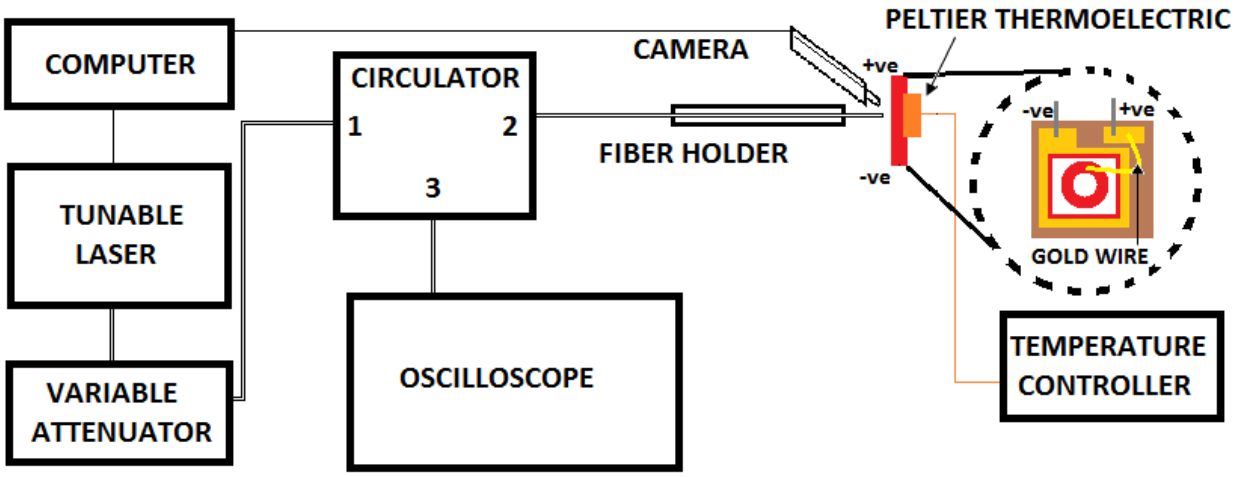

Figure 4.13: The experimental setup for the reflectivity measurement.

4.8 Summary

The techniques and processes used in the experimental work done in this thesis have been presented. The samples used, grown by Molecular Beam Epitaxy system and fabricated in a ring mesa structure, where optically characterised (PL and reflectivity measurements) to investigate the growth quality. The electrical characterisation such as photoconductivity and I-V measurement is conducted to investigate the performance of the device as photodetector. The results of both optical and electrical characterisation will be discussed in the next chapter.

References

1. J.R. Arthur, J. Appl. Phys., 39, 4032 (1968).
2. A.Y. Cho, J. Vac. Sci. Tech., 8, S31, (1971).
3. R.F.C. Farrow, Noyes publications, (1995).
4. A. Rutz, V. Liverini, R. Grange, M. Haiml, S. Schön, and U. Keller, J. of Cryst. Grow. 301, 570, (2007).
5. S. R. Bank, PhD thesis (2006).
6. M. Kondow, T. Kitatani, Semic. Sci. Techn. 17, 746, (2002)
7. J.C. Bean, North Holland, Amsterdam, 1, 237 (1977).
8. B.R. Palping, Molecular Beam Epitaxy, Pergamon, Oxford, (1980)
9. E.H.C. Parker, The technology and physics of Molecular Beam Epitaxy, Plenum Press, NY (1985)
10. L.L. Chang, K. Ploog, Molecular Beam Epitaxy and heterostructures, NATO ASI Series 87 (1985)
11. K. Ploog, Springer-Verlag, 3, 73, (1980)
12. J.M. Van Hove, C.S. Lent, P.R. Pukite, and P.I. Cohen, J. Vac. Sci. Technol., B1, 741, (1983).
13. P.K. Larsen, P.J. Dobson, “Reflection high-energy electron diffraction and reflection electron imaging of surfaces”, Plenum, (1988).
14. W. Braun, Springer-Verlag Berlin, 2 (1999).
15. J.H. Neave, B.A. Joyce, P.J. Dobson, and N. Norton, Appl. Phys., A31 (1983).

16. M. Hanini, “Dilute nitride semiconductors”, Elsevier Ltd., (2005).
17. J.Y. Wah. PhD Thesis, University of Essex, (2003).
18. S.A. Lyon, Journal of Luminescence 35, 121, (1986).
19. H.B. Bebb, and E.W. Williams, Academic, New York, 8, 262 (1972).
20. J.R. Botha, and W.R. Leitch, “Thermally activated carrier escape mechanisms from $In_xGa_{1-x}As/GaAs$ quantum wells”, Phys. Rev. B, 50, 18147 (1994).
21. H.D. Sun, M.D. Dawson, M. Othman, J.C.L. Yong, J.M. Rorison, P. Gilet, L. Grenouillet, and A. Million, Appl. Phys. Lett., 82, 376 (2003).
22. S.R. Bank, M.A. Wistey, H.B. Yuen, V. Lordi, V.F. Gambin, and J.S. Harris, J. of Vac. Sci. & Tech. B23, 1320 (2005)
23. R.A. Stradling and P.C. Klipstein, Photoluminescence Characterization, in Growth and Characterization of Semiconductors, ed. IOP Publishing Ltd., (1990).
24. Y.P. Varshni, Physica E34, 149 (1967).
25. B.K. Ridley, Phys. Rev. B41, 12190 (1990)
26. B.K. Ridley, Quantum processes in semiconductors, 3rd ed., Clarendon Press, Oxford (1993)
27. G.K. White, “Experimental techniques in low-temperature physics”, Oxford University press, (1968).

CHAPTER 5

Results and Discussions

5.1 Introduction

Dilute nitride research has ignited considerable interest from fundamental physics to industrial applications since the late 90's, as confirmed by the huge number of publications available [1-4]. Interest in this material started from the discovery that the addition of small amounts of nitrogen to GaAs and GaInAs will lead to a relatively large redshift in the band gap. This led to research in quaternary material systems based on GaInNAs quantum well (QW), due to their physical properties and their potential applications in long-wavelength optoelectronic devices [5-6]. Dilute nitride based semiconductors can be used in photodetector and laser applications due to the possibility to independently tune the bandgap and lattice constant, by adjusting the material composition. This allows a wider and improved coverage of the near-IR up to 2500 nm. The bandgap energy of grown structures are confirmed by looking at the optical characteristics such as photoluminescence. However, it is really difficult to create a GaInNAs photodetector with high efficiency, as the addition of Nitrogen can lead to the formation of imperfections and dislocations. Moreover, carrier mobility and lifetime are reduced [7] resulting in short diffusion lengths which reduce the efficiency of the GaInNAs's device performance [8]. However, the addition of quantum wells to the intrinsic region of a p-i-n GaInNAs/GaAs or GaInNAs/GaNAs can enhance the functionality of the optoelectronics devices [9-10], because it allows the photo-response to be increased to longer wavelengths as photons with energy lower than the bulk bandgap can still be absorbed in the wells creating electron-hole (e-h) pairs. These carriers can then escape thermally from the wells if enough phonons are present and can then contribute to the photocurrent of the device [11-12].

Because of the rapid ongoing growth of high speed broadband telecommunication and data communication links, the design, fabrication and characterisation of fast transmitters and

receivers are becoming increasingly important. A GaInNAs p-i-n Multi Quantum Well (MQW) and a Vertical Cavity Enhanced (VCE) GaInNAs MQW photodetectors have been studied by measuring the photocurrent, quantum efficiency, selectivity, and response time at room temperature operation. The response time parameter, which is essential for optical modulation and high-speed communication, can be measured by means of ultrafast techniques such as transient photoconductivity (TPC) [13-16]. The performance of these devices for various QW and structure configurations was investigated. At room temperature, thermal escape allows the carriers to leave the quantum wells and causes a space charge potential [11].

5.2 Samples Structure

There are three existing samples and two new samples used to investigate the performance of photodetectors in this thesis. Out of the three existing samples, two of them consists of the GaInNAs/GaAs p-i-n structure without DBR mirrors while the other one has the DBR mirrors. Both of the two new samples consists of GaInNAs/GaNAs p-i-n structure with DBR mirrors. The new samples used GaNAs as the QW barrier compared to the existing samples that has GaAs as the QW barrier. The intrinsic region without DBR samples consists of 10 and 20 undoped GaInNAs QWs while the one with DBRs have 9 undoped GaInNAs QWs. The intrinsic region for the new samples consists of 9 and 20 undoped GaInNAs/GaNAs QWs. All the samples are grown at Tampere University of Technology in Finland by a VG-Semicon-V80 MBE system on a highly n-doped (100)-oriented GaAs substrate. The sample coded ‘AsN’ indicates the sample without the DBR and those coded with ‘G’ indicates the sample with the DBR. Most of the samples used in this thesis are fabricated in the shape of a mesa-structure, with top circular aperture as described in chapter 4 except for the DBR sample with 9 QW of GaInNAs/GaAs. However, due to the high dark current consideration and device capacitance

value at bigger diameters, all the measurement were carried out for the smallest diameter of 1 mm only.

5.2.1 p-i-n GaInNaAs/GaAs MQW

The existing p-i-n $Ga_{0.952}In_{0.048}N_{0.016}As_{0.984}$ QW sample coded as AsN3134 has 10 undoped QWs and AsN3138 has 20 undoped QWs with thickness of 10 nm. Both samples have an AlGaAs window layer (Be-doped 2×10^{18} cm-3) above the intrinsic region to reduce surface recombination of photo-generated electrons in the emitter. n^+ and p^+ type doping were provided by Silicon and Beryllium solid sources respectively. The samples were grown on a highly doped, n^+-type GaAs substrate. The details on the structures are shown in Table 5.1 and Table 5.2. Two 10nm undoped GaAs graded layers were initially grown at the top and bottom of the intrinsic region, sandwiched between a top GaAs and AlGaAs layer consisting of a 600 nm emitter p-doped GaAs barrier with Be = $2x10^{18}cm^{-3}$ followed by 40 nm p-doped AlGaAs with Be = $2x10^{18}cm^{-3}$ and GaAs top layer with Be = $4x10^{18}cm^{-3}$, and a base contact consisted of 1900nm n-doped GaAs with Si = $2x10^{17}cm^{-3}$ and 20nm n^+-doped GaAs with Si = $2x10^{18}cm^{-3}$ and n^+GaAs as a substrate. Both samples have a compressive strain of 0.0019.

Table 5.1: Structural layers of sample AsN3134

Notes	Repeats	Material	Thickness (nm)
Be doped (p+ = 4 x 10^{18} cm^{-3})	1	GaAs	200
Be doped (p = 2 x 10^{18} cm^{-3})	1	AlGaAs	40
Be doped (p = 2 x 10^{18} cm^{-3})	1	GaAs	600
Undoped	1	GaAs	10
Undoped (barrier)	1	GaAs	10
Intrinsic	10	$Ga_{0.952}In_{0.048}N_{0.016}As_{0.984}$	10
Undoped (barrier)		GaAs	10
Undoped	1	GaAs	10
Si doped (n = 5 x 10^{17} cm^{-3})	1	GaAs	1900
Si doped (n+ = 2 x 10^{18} cm^{-3})	1	GaAs	20
n+ GaAs substrate			

Table 5.2: Structural layers of sample AsN3138

Notes	Repeats	Material	Thickness (nm)
Be doped (p+ = 4 x 10^{18} cm^{-3})	1	GaAs	200
Be doped (p = 2 x 10^{18} cm^{-3})	1	AlGaAs	40
Be doped (p = 2 x 10^{18} cm^{-3})	1	GaAs	600
Undoped	1	GaAs	10
Undoped (barrier)	1	GaAs	10
Intrinsic	20	$Ga_{0.952}In_{0.048}N_{0.016}As_{0.984}$	10
Undoped (barrier)		GaAs	10
Undoped	1	GaAs	10
Si doped (n = 5 x 10^{17} cm^{-3})	1	GaAs	1900
Si doped (n+ = 2 x 10^{18} cm^{-3})	1	GaAs	20
n+ GaAs substrate			

5.2.2 VCE GaInNAs/GaAs MQW

The existing VCE sample structure coded G0428 was initially designed for electrically pumped reflection mode for VCSOA/VCSEL operation. The device was fabricated at the University of Glasgow, Scotland. Fig.5.1 shows the designed structure of the 10μm window aperture with its layer thicknesses and doping concentrations listed in Table 5.3. The sample consists of an active region embedded within compositional p-n graded layers lying between the top and bottom DBRs. The active region has nine $Ga_{0.65}In_{0.35}N_{0.02}As_{0.98}$ QWs of 7 nm thickness separated by 20 nm GaAs barriers. The QWs were grouped together in three sets of three wells each, positioned on the standing wave peaks of the 3/2λ cavity. The top mirror consists of 21-pairs of undoped $Al_{0.8}Ga_{0.2}As$/GaAs DBR designed for a centre wavelength near 1.3μm. The bottom mirrors have 24-pairs of n-doped $Al_{0.98}Ga_{0.02}As$/GaAs DBR with a higher reflectivity of over 99.9%. A compositional graded p-type layer is formed between the top DBR and p-doped layer for the best effect and gives strong current confinement. The 961nm thickness of the mesa-structure sample was fabricated by applying fast dry etch down to the bottom DBR layers with a top circular diameter of 62μm. The diameters of the top DBR mirrors were kept as small as 10μm or 15μm respectively to avoid thermal problems due to the high current densities. In order to minimize the optical losses caused by inter valence band absorption in p-type doped material,

undoped mirrors without graded interfaces and adjustable doped layers have been considered [129]. The sample has compressive strain of 0.0205. The strain is slightly higher than previous samples due to the increment of Nitrogen composition from 1.6% to 2%.

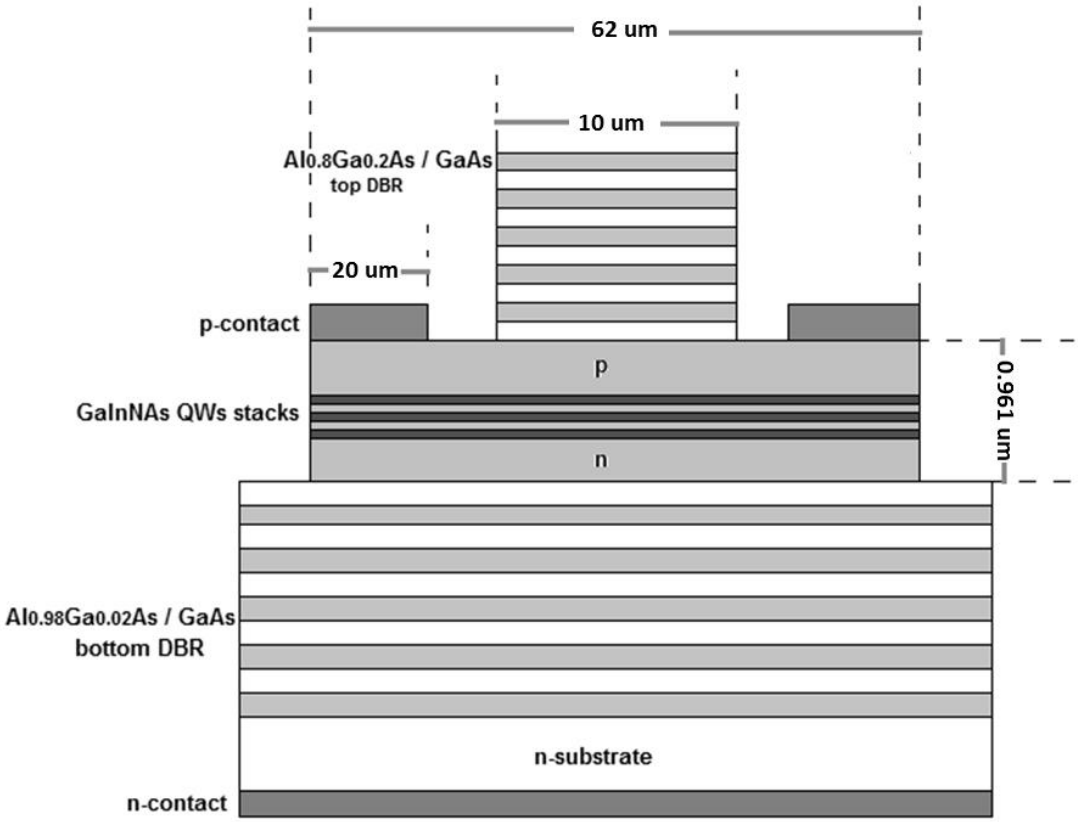

Figure 5.1: VCE GaInNAs/GaAs structure

Table 5.3: Structural layers of sample G0428

Notes	Repeats	Material	Thickness (nm)
Undoped GaAs / $Al_{0.8}Ga_{0.2}As$ DBR	21	GaAs	95.28
		$Al_{0.8}Ga_{0.2}As$	107.12
	1	GaAs	73.82
Be doped (p = 5 x 10^{18} cm^{-3})	1	$Al_{0.2}Ga_{0.8}As$	2
Be doped (p = 5 x 10^{18} cm^{-3})	1	$Al_{0.4}Ga_{0.6}As$	2
Be doped (p = 5 x 10^{18} cm^{-3})	1	$Al_{0.6}Ga_{0.4}As$	2
Be doped (p = 5 x 10^{18} cm^{-3})	1	$Al_{0.8}Ga_{0.2}As$	2
Be doped (p = 5 x 10^{18} cm^{-3})	1	$Al_{0.98}Ga_{0.12}As$	2
Be doped (p = 5 x 10^{18} cm^{-3})	1	$Al_{0.98}Ga_{0.02}As$	2
Be doped (p = 5 x 10^{18} cm^{-3})	1	$Al_{0.8}Ga_{0.2}As$	2
Be doped (p = 5 x 10^{18} cm^{-3})	1	$Al_{0.6}Ga_{0.4}As$	2
Be doped (p = 5 x 10^{18} cm^{-3})	1	$Al_{0.4}Ga_{0.6}As$	2
Be doped (p = 5 x 10^{18} cm^{-3})	1	$Al_{0.2}Ga_{0.8}As$	2
Be doped (p = 0.5 x 10^{18} cm^{-3})	1	GaAs	181.5
Undoped	1	GaAs	50
Undoped	1	$Ga_{0.65}In_{0.35}N_{0.02}As_{0.98}$	7
Undoped (barrier)	1	GaAs	20
Undoped	1	$Ga_{0.65}In_{0.35}N_{0.02}As_{0.98}$	7
Undoped (barrier)	1	GaAs	20
Undoped	1	$Ga_{0.65}In_{0.35}N_{0.02}As_{0.98}$	7
Undoped (barrier)	1	GaAs	130.65
Undoped	1	$Ga_{0.65}In_{0.35}N_{0.02}As_{0.98}$	7
Undoped (barrier)	1	GaAs	20
Undoped	1	$Ga_{0.65}In_{0.35}N_{0.02}As_{0.98}$	7
Undoped (barrier)	1	GaAs	20
Undoped	1	$Ga_{0.65}In_{0.35}N_{0.02}As_{0.98}$	7
Undoped (barrier)	1	GaAs	130.65
Undoped	1	$Ga_{0.65}In_{0.35}N_{0.02}As_{0.98}$	7
Undoped (barrier)	1	GaAs	20
Undoped	1	$Ga_{0.65}In_{0.35}N_{0.02}As_{0.98}$	7
Undoped (barrier)	1	GaAs	20
Undoped	1	$Ga_{0.65}In_{0.35}N_{0.02}As_{0.98}$	7
Undoped	1	GaAs	70
Si doped (n = 2 x 10^{18} cm^{-3})	1	GaAs	85.85
Si doped (n = 1 x 10^{18} cm^{-3})	1	$Al_{0.2}Ga_{0.8}As$	2
Si doped (n = 1 x 10^{18} cm^{-3})	1	$Al_{0.5}Ga_{0.5}As$	2
Si doped (n = 1 x 10^{18} cm^{-3})	1	$Al_{0.8}Ga_{0.2}As$	2
doped (n ≈ 1 x 10^{18} cm^{-3})	24	$Al_{0.98}Ga_{0.02}As$	111
$Al_{0.8}Ga_{0.2}As$ / GaAs DBR		GaAs	95.28
Highly doped GaAs substrate			350000

5.2.3 VCE GaInNAs/GaNAs MQW

The new VCE GaInNAs/GaNAs as described in Chapter 3 was designed using a transfer-matrix for a vertical cavity enhanced photodetector operation. The new samples uses GaNAs material as barrier layers in order to compensate the strain and increase the crystal quality of the structure because strain increases with increasing N composition in our existing samples. The absorbing layers (GaInNAs QWs) for these samples are grown under Antimony (Sb) flow, used as a surfactant atom to facilitate incorporation of more nitrogen into the GaInAs lattice as well as to obtain a sharp interface for the quantum well and the barrier grown. The sufficiently high $1.1x10^{-8}$ Torr Sb flux has been used to provide surfactant effects to reduce the surface diffusion length. If it is too high, it will degrade the optical quality of the material [18]. The VCE $Ga_{0.733}In_{0.627}N_{0.025}As_{0.975}$ QW sample coded as G1384 has 9 undoped QWs and G1386 has 20 undoped QWs with a thickness of 7nm. The barrier layer for G1384 has 13.5nm of $GaN_{0.035}As_{0.965}$ while 12nm of $GaN_{0.036}As_{0.964}$ barrier thickness is applied for the sample coded G1386. Both the top and bottom DBR for the new samples are doped to improve the electrical conductivity as described in section 3.3.1. The structural layers of the 9 and 20 QWs design are shown in Table 5.4 and Table 5.5.

Table 5.4: Structural layers of sample G1384

Notes	Doping	Repeats	Material	Thickness (nm)
p^+ Doped GaAs/AlAs DBR	Be = 5 x 10^{18} cm^{-3}	10	GaAs	99.2
	Be = 3.1 x 10^{18} cm^{-3}		AlAs	115.15
p^+ Doped	Be = 5 x 10^{18} cm^{-3}	1	GaAs	95
	Undoped	1	GaAs	10
Barrier	Undoped	9	$GaN_{0.035}As$	13.5
Intrinsic			$Ga_{0.733}In_{0.267}N_{0.025}As_{0.975}$	7
Barrier	Undoped	1	$GaN_{0.035}As$	13.5
	Undoped	1	GaAs	10
n^+ Doped	Si = 3.1 x 10^{18} cm^{-3}	1	GaAs	70
n^+ Doped GaAs/AlAs DBR	Si = 1.5 x 10^{18} cm^{-3}	15	AlAs	113.54
	Si = 7 x 10^{18} cm^{-3}		GaAs	98.01
n^+ Doped	Si = 7 x 10^{18} cm^{-3}	1	GaAs	200
Highly doped GaAs substrate				350000

Table 5.5: Structural layers of sample G1386

Notes	Doping	Repeats	Material	Thickness (nm)
p^+ Doped GaAs/AlAs DBR	Be = 5 x 10^{18} cm^{-3}	11	GaAs	99.2
	Be = 3.1 x 10^{18} cm^{-3}		AlAs	115.15
p^+ Doped	Be = 5 x 10^{18} cm^{-3}	1	GaAs	95
	Undoped	1	GaAs	10
Barrier	Undoped	20	$GaN_{0.036}As$	12
Intrinsic			$Ga_{0.733}In_{0.267}N_{0.025}As_{0.975}$	7
Barrier	Undoped	1	$GaN_{0.036}As$	12
	Undoped	1	GaAs	10
n^+ Doped	Si = 3.1 x 10^{18} cm^{-3}	1	GaAs	60
n^+ Doped GaAs/AlAs DBR	Si = 1.4 x 10^{18} cm^{-3}	15	AlAs	113.54
	Si = 7 x 10^{18} cm^{-3}		GaAs	98.01
n^+ Doped	Si = 7 x 10^{18} cm^{-3}	1	GaAs	200
Highly doped GaAs substrate				350000

During the growth process, some changes needed to be made to overcome the dislocation problem on the structures, such as on the composition of the Indium and Nitrogen, the doping concentration of doped layer, and the doping concentration of the DBR. Due to growth constraint, the top and bottom DBR thickness layer had to be made the same for both the 9 and 20 QWs samples. Hence, the cavity resonant of 20 QWs sample is slightly different from the designed structure in chapter 3. This will be discussed in the next sub-topic. Even though the Nitrogen composition for the new samples is 2.5%, the strain for the new samples is lower than the previous VCE sample with a value of 0.0173. This shows that the GaNAs barrier is able to compensate the strain in the QW due to the high percentage of Nitrogen. A summary of the samples used in this thesis is shown in Table 5.6.

Table 5.6: List of samples investigated in this thesis with Indium and Nitrogen composition

Sample	Structure	Well width	Number of QW	Indium composition (%)	Nitrogen composition (%)	Strain value
AsN3134	p-i-n	10	10	4.8	1.6	0.0019
Asn3138	p-i-n	10	20	4.8	1.6	0.0019
G0428	p-i-n (DBR)	7	9	35	2	0.0205
G1384	p-i-n (DBR)	7	9	26.7	2.5	0.0173
G1386	p-i-n (DBR)	7	20	26.7	2.5	0.0173

5.3 p-i-n GaInNAs/GaAs MQW

Achieving high responsivity is one of the key challenges in GaAs-based dilute nitride photodetector research. Normally the reported outcomes of the GaAs-based dilute nitride photodetectors can be categorized into either based on QW absorption layers [17-19] or based on bulk absorption layers [20-26]. Even though photodetectors based on a bulk dilute nitride absorption layer exhibit higher responsivity compared to QW based devices, they suffer from reduced absorption at wavelengths longer than 1μm. While such QW devices enable the utilization of highly strained dilute nitride layers and thus offer absorption of up to 1.6μm, their responsivity is generally low [18-19] (typically less than 0.5A/W) due to the thin QW photon-absorption layer. However, these responsivity values are still much lower compared to those of commercial InGaAs photodetectors, with typical responsivity of up to ~0.9A/W. In this section, significant improvement in the responsivity of GaInNAs based p-i-n photodetectors near 1.1μm wavelength is demonstrated. This improvement is achieved by manipulating the number of QWs to allow for higher absorption and electron-hole recombination in the intrinsic region.

In order to check the optical quality and confirm the expected bandgap, photoluminescence measurement is carried out on the samples. The results of the PL measurements are shown in Fig.5.2 for AsN3134 and Fig.5.3 for AsN3138. The peak wavelengths show very good agreement with the e_1-h_h transition energies (effective band gap) in the GaAs and GaInNAs QWs materials, which were calculated using the band-anti crossing model as explained in section 2.11.2. It can be seen from Fig.5.2 and Fig.5.3, that for lower temperatures, there is a very distinct tail extending from the low energy side of the wells PL emission to beyond 1300 nm. This tail indicates strong carrier localisation within the sample where electrons become trapped in states below the conduction band and recombine radiatively in GaInNAs alloys with lower indium content [27-29].

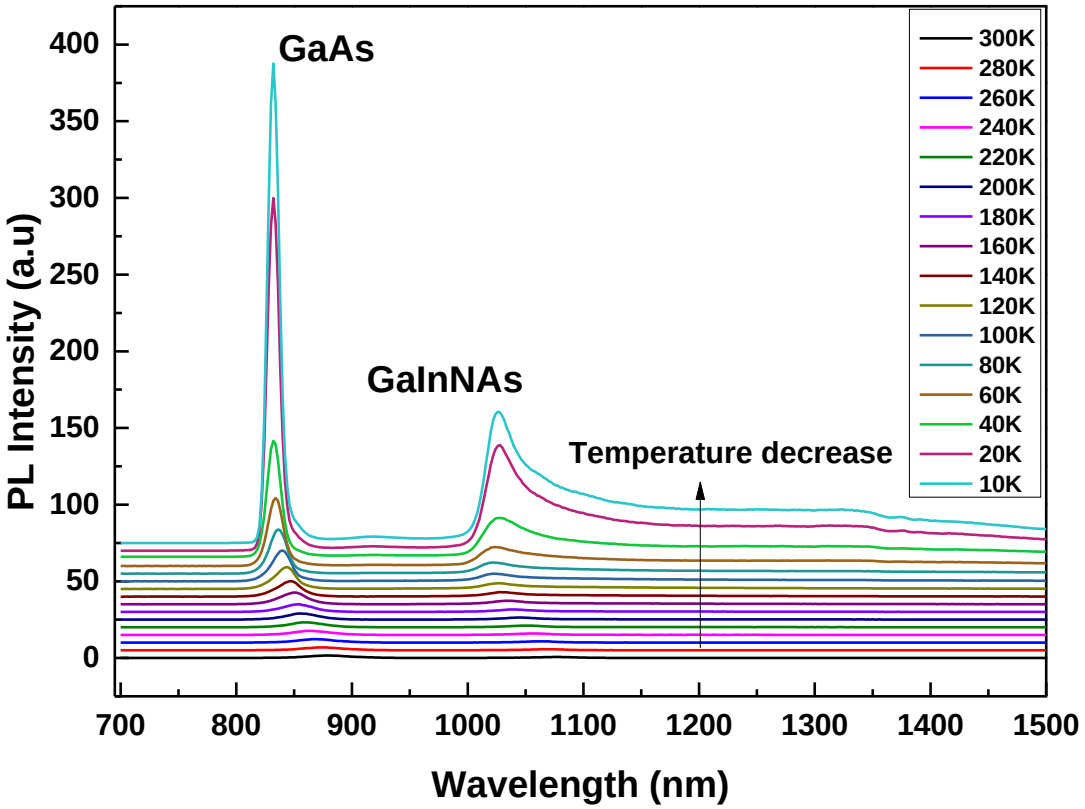

Figure: 5.2: The photoluminescence of AsN3134 (10QWs) sample as a function of temperature.

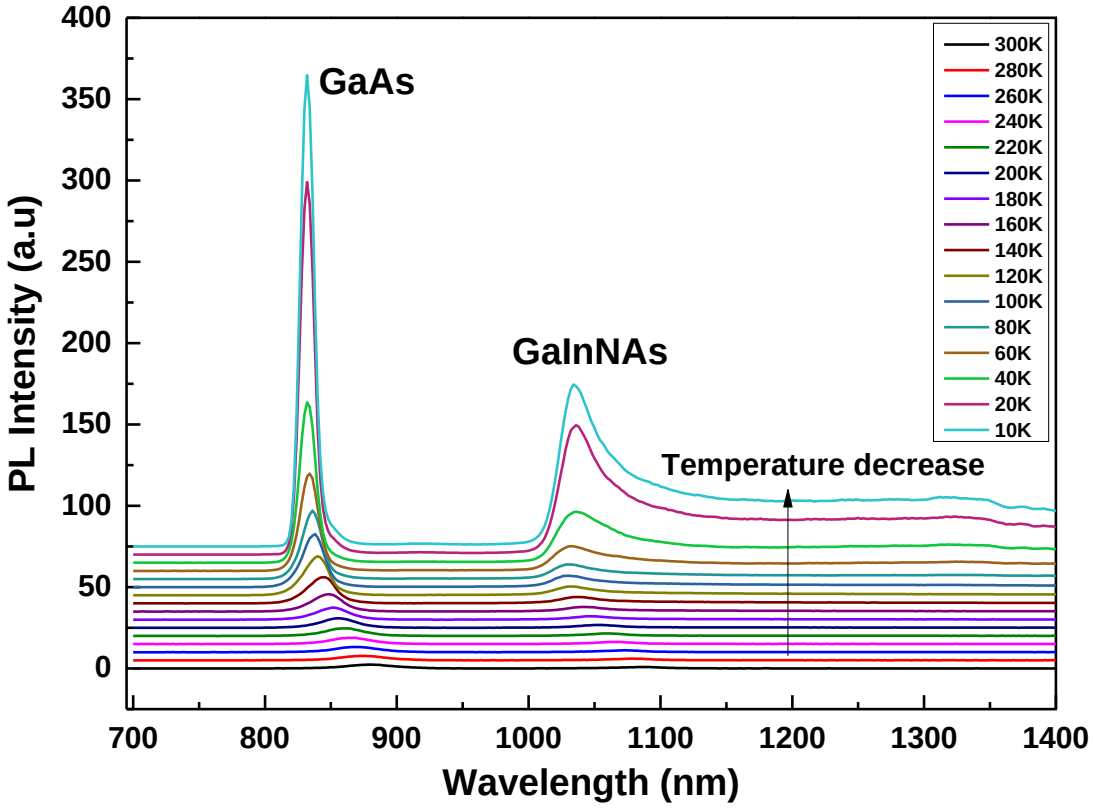

Figure: 5.3: The photoluminescence of AsN3138 (20QWs) sample as a function of temperature.

The AsN3134 (10 QWs) and AsN3138 (20 QWs) samples have PL peaks at λ=1076 nm and 1086 nm respectively at 300K compared to the calculated value of λ=1087 nm as depicted in Fig.5.4. The small difference in PL peak wavelengths between these two structures may be due to the power of the plasma source being slightly higher to grow for the wider intrinsic region of AsN3138. As a result, in AsN3138, the nitrogen content is slightly elevated giving rise to a reduced bandgap.

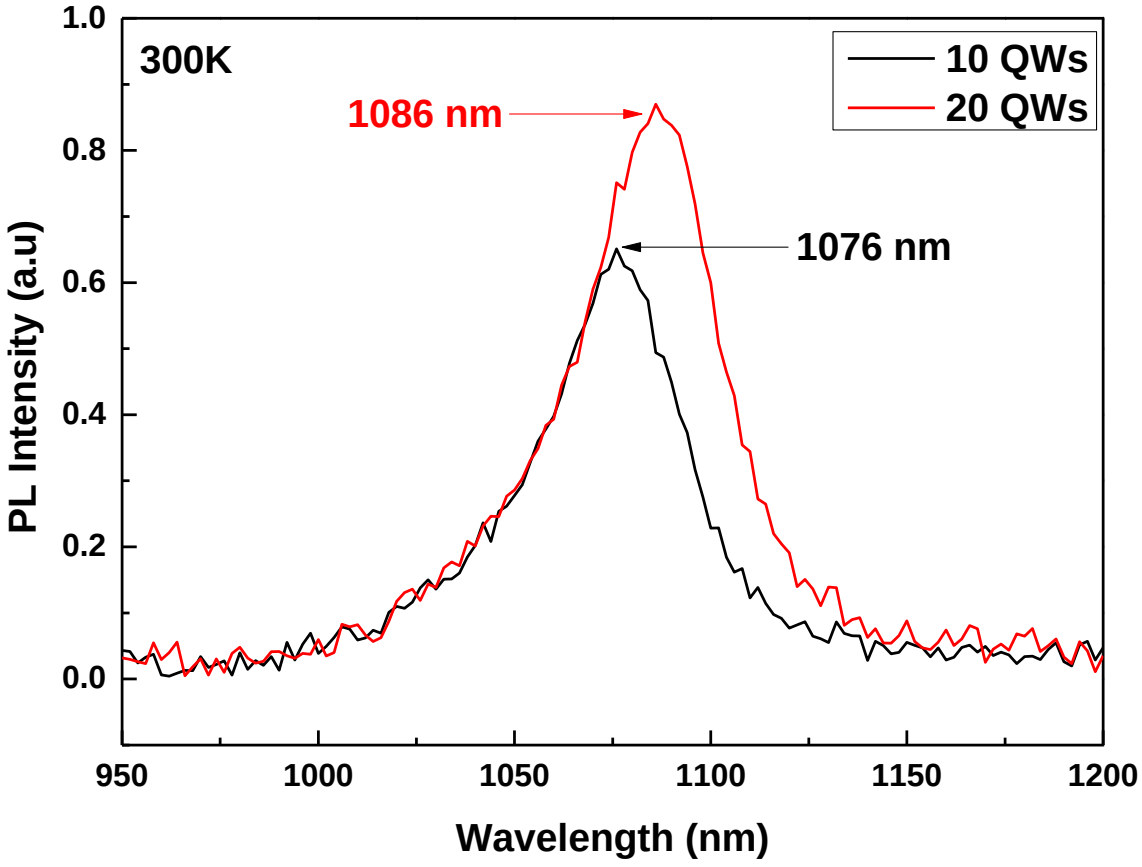

Figure 5.4: The photoluminescence of the quantum well photodetector measured at room temperature.

The energy at which the PL peak occurs is plotted in Fig.5.5. The PL peak energy blue shifts as the temperature drops between T=300K to T=100K, but then red shifts between T=100K and T=50 K before blue shifting again as the temperature is decreased from T=50 K towards liquid helium temperatures creating a clear "S-shape" which is commonly reported for dilute nitride material [30-31].

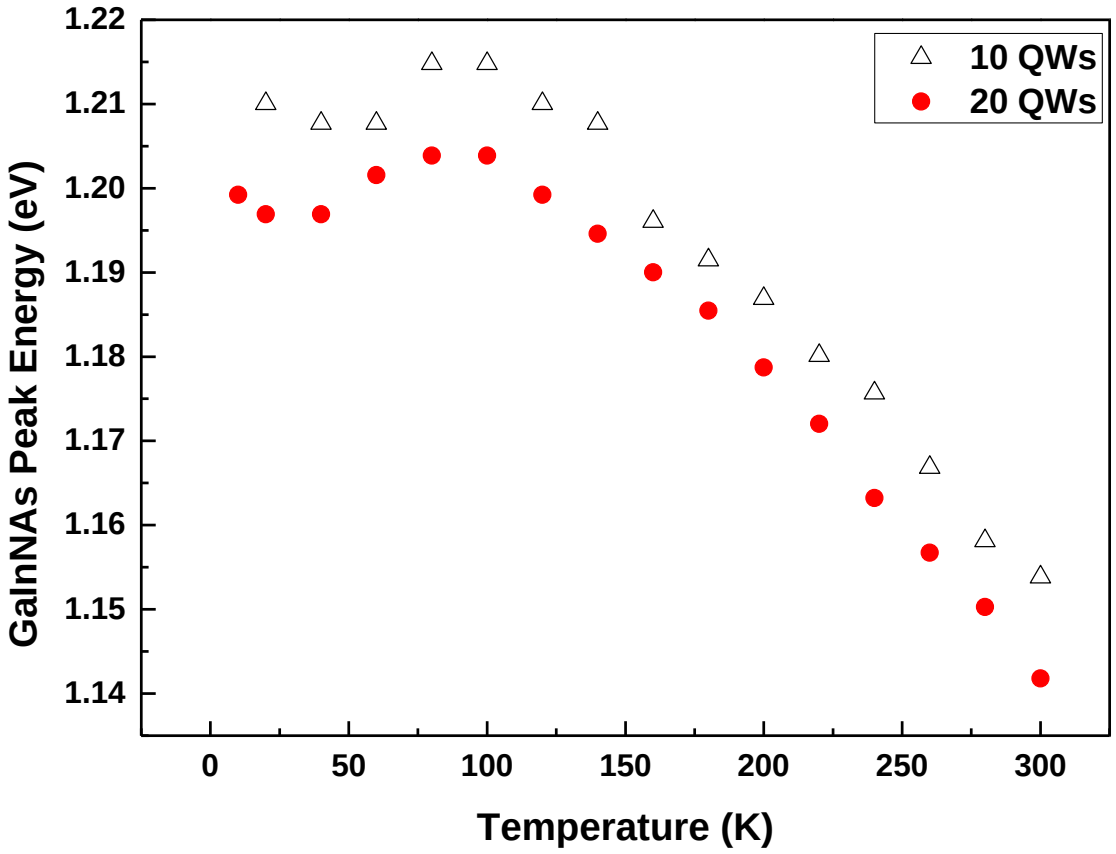

Figure 5.5: The S-shape PL shift of AsN3134 (10 QWs) and AsN3138 (20QWs).

The origin of this S-shape is due to the large number of defects, impurities and structural compositions near the conduction band causing excitons to become localised. As the temperature rises between T=10 K and T=50 K, the localised excitons increasingly overcome low potential barriers and become trapped in the low energy levels of the density of states. When they recombine in these low energy states, they cause a red shift to the PL peak. After the temperature increases from T=50K the extra thermal energy allows for more localised excitons to become de-trapped, and therefore reverses the effect of the red shift in the bandgap. At T=100K, there is enough thermal energy present that all excitons are delocalised such that the temperature dependence will then be dominated by standard band gap shrinkage.

The peak intensity of AsN3134 and AsN3138 are plotted in Fig.5.6 showing clearly a very large increase in intensity as the temperature is reduced. As the temperature drops from T=300K to T=50K, the intensity steadily increases due to the escape probability of electrons

decreasing, resulting in more carriers recombining in the wells. Between T=50K to T=20K, the PL intensity increases dramatically due to the thermal escape time of holes dropping rapidly and approaching that of the recombination time. Finally, at T=20K the thermal escape times of both carriers would have become long enough such that carrier sweep out is dominated by either recombination or tunnelling that further changes in temperature have little effect on the PL intensity [32]. Furthermore, the behaviour is due to the effect of a phonon scattering mechanism increasing with temperature. This causes a non-radiative band to band transition which lead to the PL amplitude to decrease with increasing temperature.

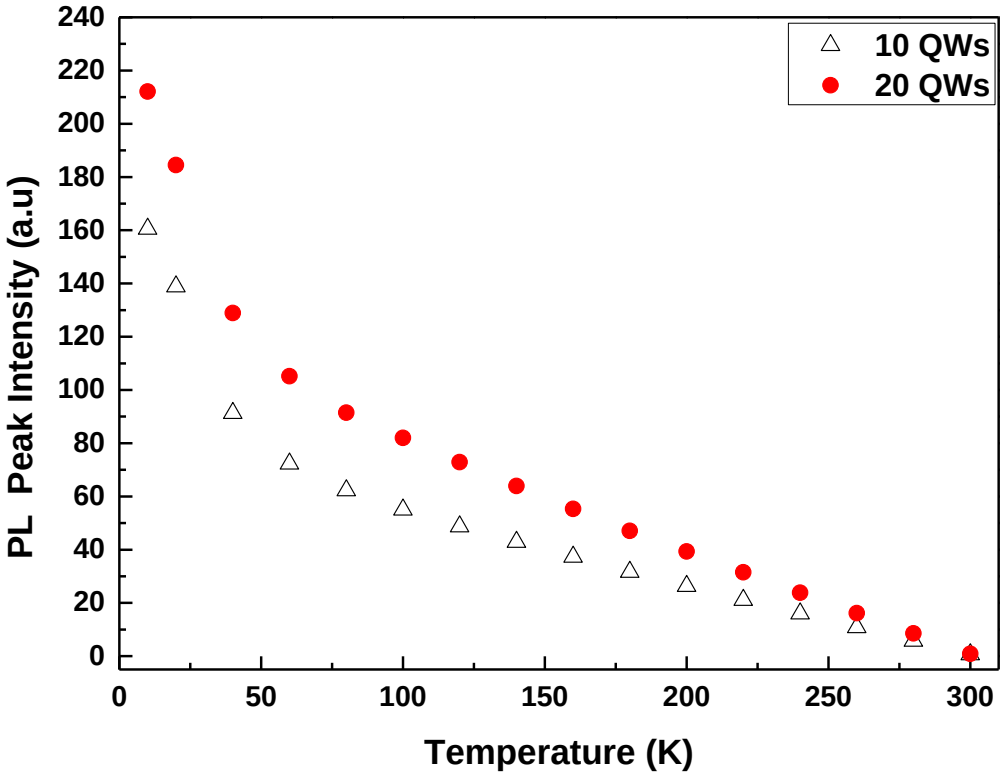

Figure 5.6: The PL intensity versus temperature for AsN3134 and AsN3138.

The photocurrent measurements were carried out using a quartz halogen lamp as the light source in conjunction with a monochromator as described in section 4.5.1. The responsivity is calculated (after taking into account 30% incident power reflection) for both samples according to the intensity of the light at different wavelengths and biasing. The photocurrent value taken into the calculation has been deducted with leakage current to obtain the responsivity value. The

300K responsivity for both samples with wavelength dependence obtained at V=0V and V= -5V are shown in Fig.5.7. The photodetectors show absorption between the wavelengths of 900nm to 1100nm where the maximum peak occurred at 1000nm for AsN3134 and 1010nm for AsN3138.

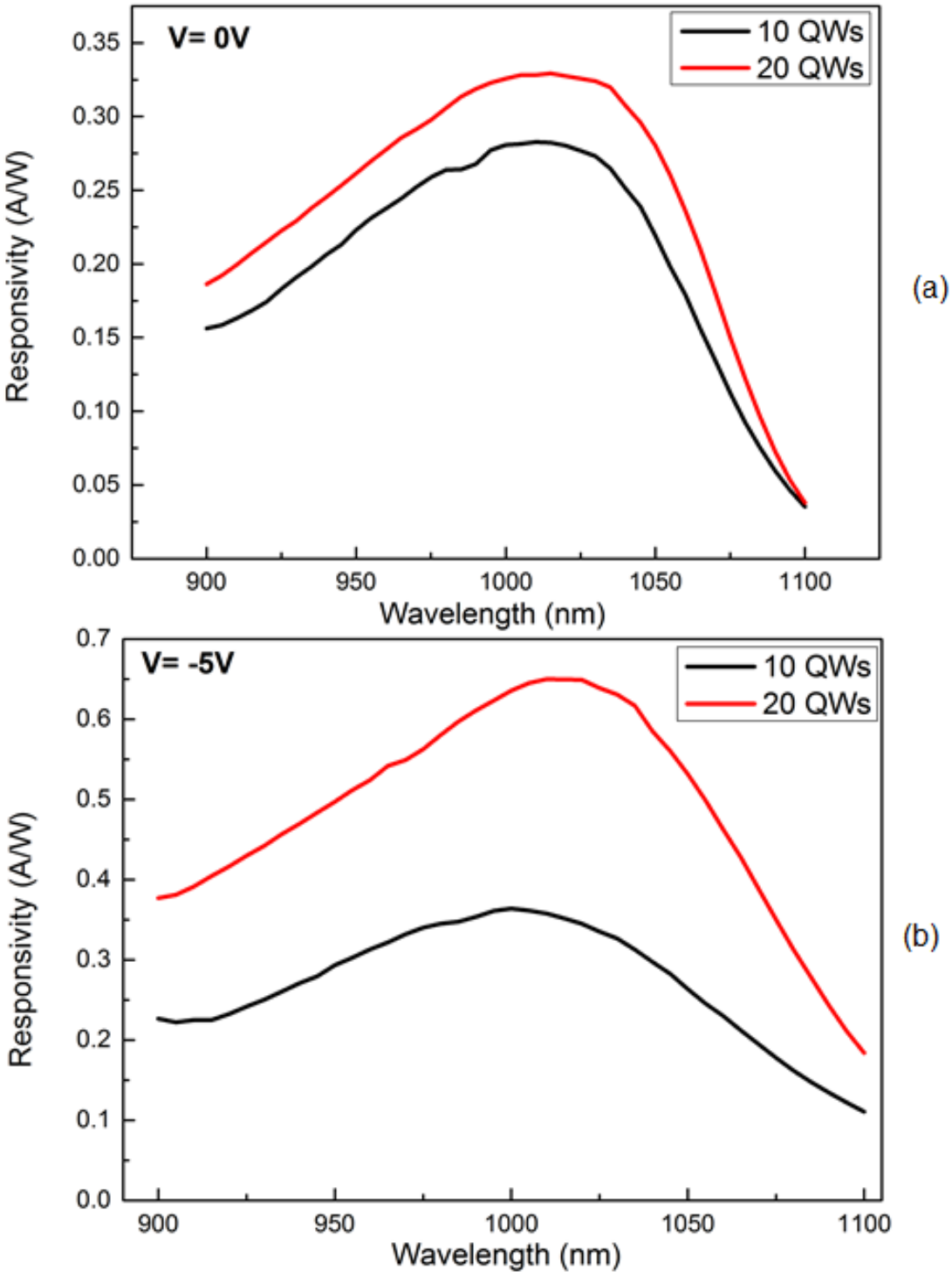

Figure 5.7: Responsivity for AsN3134 and AsN3138 (a) 0V and (b) -5V

It is interesting to note that for these samples, the quantum wells show a clear contribution to the photocurrent which requires both electrons and holes to cross the depletion region, yet the p-type layers contribution is almost zero suggesting that electrons cannot cross the intrinsic region. If no recombination and fast field dependent transport occurs for electrons in the barriers, the probability of a carrier generated in the well closest to the n-type region contributing to the photocurrent is assumed to be equivalent to its escape probability from the quantum well.

Electrons generated in the p-type region will have to cross all wells before they can contribute to the photocurrent. Should the chance of an electron being captured in each well be close to unity, electrons generated on the p-type side would have to thermally escape from all of the quantum wells in the intrinsic region as shown in Fig.5.8. Therefore, the probability of an electron generated in the wells to get away from the n-type region to contribute to the photocurrent would be the same as the escape probability from the quantum well efficiency.

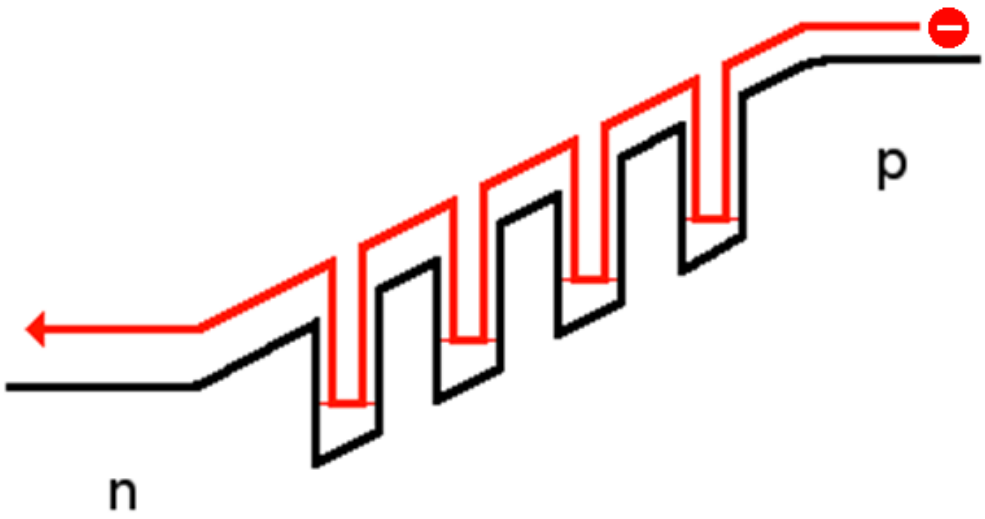

Figure 5.8: A Diagram illustrating a minority electron in the p-type region being captured, and then having to escape from each well in the device.

To reach higher short circuit currents and efficiencies, the escape probability from the wells needs to be increased. One way of improving this is to increase the electric field across the wells. Increasing the field will improve the escape probability by lowering the barrier height as well as increasing the lifetimes of the carriers confined in the wells by spatially separating the electrons and holes. In order to assess the increase in electric field required to reach the maximum escape probability, the photocurrent measurements were repeated under higher applied bias and are shown in Fig.5.7(b). It is clear that by applying bias, the escape probability can be increased leading to a large increase in the quantum efficiency, with reverse biases of -5V leading to responsivity values of 0.37A/W for AsN3134 and 0.65A/W for AsN3138 respectively. This suggests that at this level of reverse bias escape probabilities of unity are achieved. With this level of bias, the full potential of the wells with their contribution is seen being more than double the level achieved without bias as observed for sample AsN3138.

The I-V measurements were carried out for both samples in the dark and under illumination condition. As shown in Fig.5.9, the dark current density is relatively low with -472.8nAcm^{-2} for AsN3134 and -22.6nAcm^{-2} for AsN3138 at -6V reverse bias respectively. However, there is an increment for AsN3134 current density at bias -4V. This is due to thermal energy enabling the carriers to overcome the quantum barrier and escape from one well to another as favoured by the electric field in reverse bias which contribute to more leakage current. Another factor could be due to the higher internal resistance of the AsN3138 sample compared to AsN3134 sample. More QWs number equals to a longer intrinsic depletion length, and hence a higher resistance which affects the carriers passing through them.

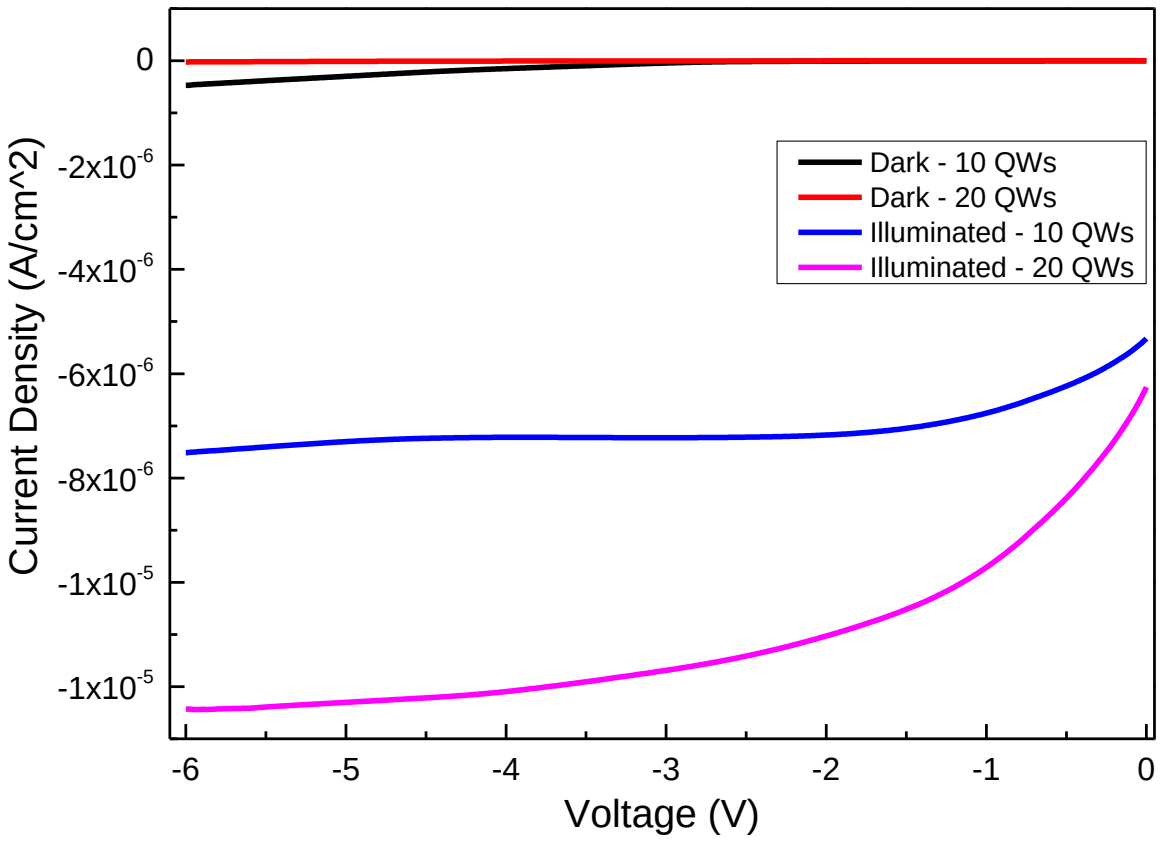

Figure 5.9: I-V measurements for AsN3134 and AsN3138

As illustrated in Fig.5.10(a), the electric field for AsN3134 has already reached 400kV/cm compared to 120kV/cm of AsN3138 at the reverse bias of 4V. Under illumination at peak wavelength, the AsN3138 sample produces higher current density compared to the AsN3134 sample due to the wider depletion region in the AsN3138 sample which allows for more absorption. The band profile becomes flat when the voltage is increased thus removing the possibility of re-trapping or charge accumulation as shown in Fig.5.10.

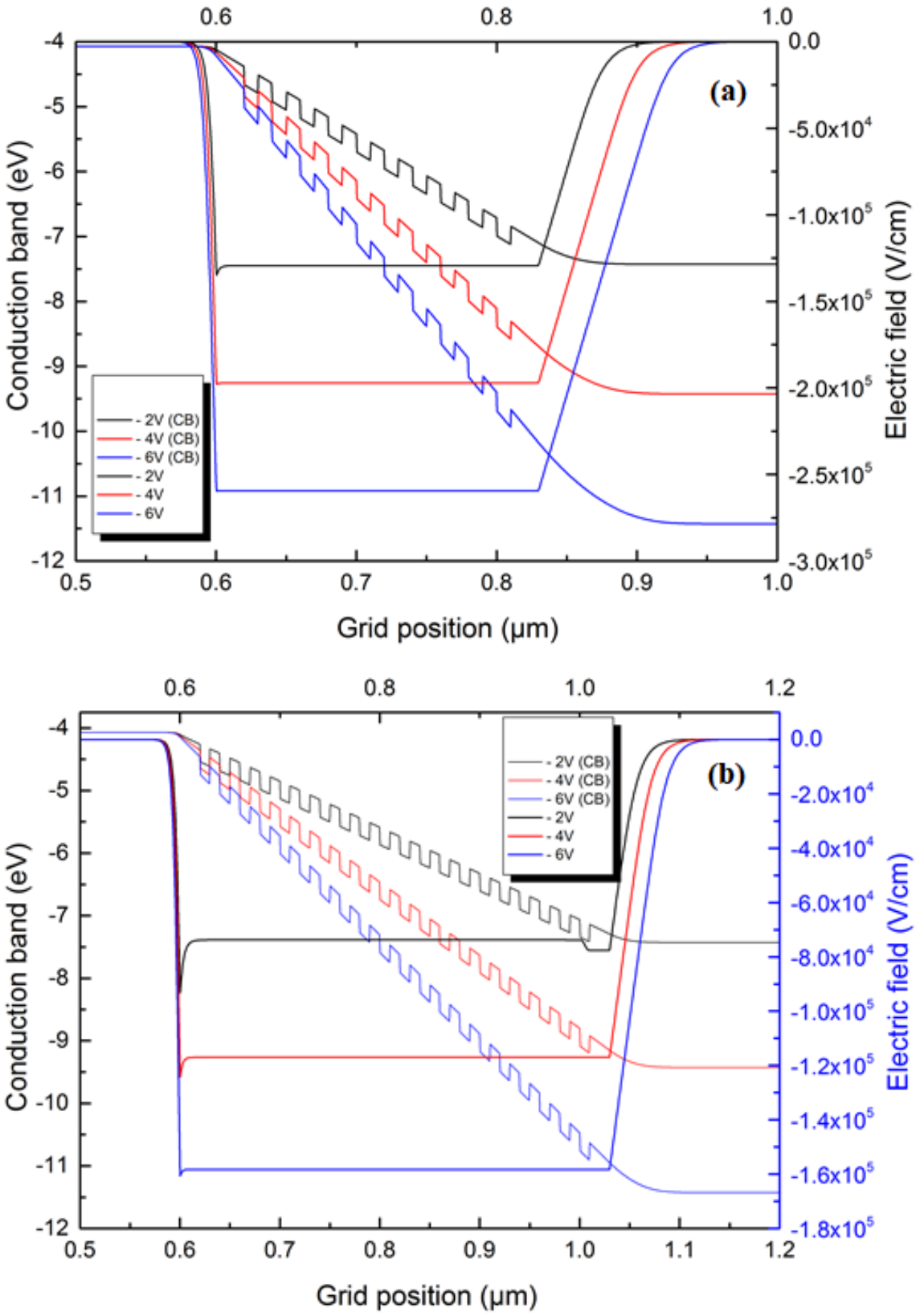

Figure 5.10: Band diagram and electric field for (a) AsN3134 and (b) AsN3138

As can be seen from Fig.5.7(b) and Fig5.9, the responsivity and current density for AsN3138 are double that of the AsN3134 which reflects the doubled number of QW of AsN3138

compared to AsN3134. The quantum efficiencies (QE) for both devices with bias dependence are shown in Fig5.11. It can be seen that maximum efficiency is reached at a bias of -6V due to saturation for both samples. The maximum QE was found to be 80.3% for AsN3138 and 46% for AsN3134 with the 80.3% being the highest value ever reported for a GaInNAs QW photodetector operating near 1.0μm wavelength.

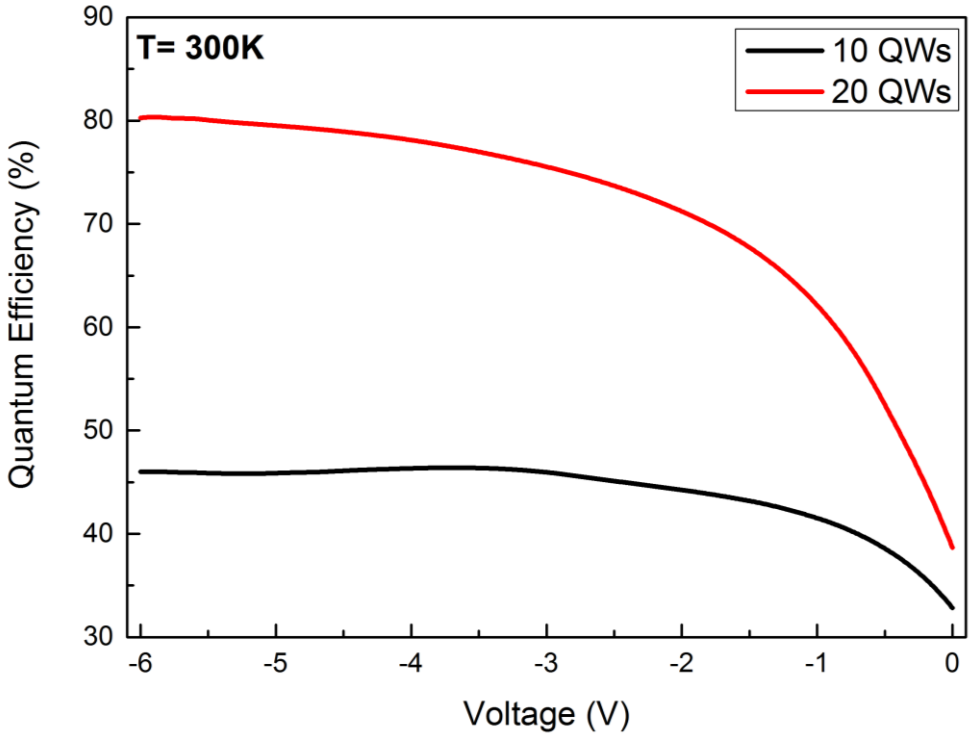

Figure 5.11: Quantum efficiency for AsN3134 and AsN3138 at 300K

Another key parameter to be investigated when dealing with photodetectors is the response time. This parameter, which is essential for optical modulation and high-speed communication, can be measured by means of ultrafast techniques such as transient photoconductivity (TPC) [33]. The detection of optical information requires conversion of an optical signal to electrical signal, which can then be processed by electronic devices such as photodetectors which are used along with lasers. As an additional comparative studies, the temporal response characteristic of a dilute nitride based (GaInNAs/GaAs) p-i-n MQW devices have been demonstrated in this thesis for operation near the 1.0μm wavelength region. The temperature dependence of the transient photoconductivity at different bias voltages and

excitation intensity studies are carried out to investigate the photodetector speed by measuring its response time. The "response time" term represents the period of time taken for the generated photocurrent to rise after optical excitation on the detector. The current will take a finite time to reach a steady-state value once the photodetector is turned on, before decaying back to its initial zero level [34]. Hence, the term "rise time", τ_{rise} is used to describe the detector's speed of response to light excitation and can be measured between the 10% and 90% point of the peak amplitude output on the rising edge of the pulse

Response time in a photodetector is attributed to the rise and decay time of the photo-generated carriers within the detector. The p-i-n photocurrent decays exponentially with a time constant determined by several factors [35-36]. One of them is the transit time of the photo-generated carriers across the depletion region. Increasing this width allows for more photons to be absorbed therefore increasing the quantum efficiency, but the response time slows down as carrier transit becomes longer. The second factor is the diffusion time of the photo-generated carriers outside the depletion region towards the electrical contacts. Finally the RC time constant associated with the device itself and the external circuit will be the main factor of detector performance if a bigger diameter is employed. The larger area of the detector will affect the capacitance hence increasing the rise time. Nevertheless, if the area is smaller, the transit time of the carrier to travel across the depletion region will limit the high frequency response of the detector due to the saturated drift velocity of the slower carrier. In a poor quality material, carrier traps and defects can also play an important role in the determination of the detector bandwidth[37]. The temporal response for a few photodetectors based on dilute nitrides has been demonstrated previously. For example, Han *et.al.* demonstrated a rise time for a 160μm diameter cavity photodetector based on GaInNAs at 1.55μm of not less than 800ps at -3V operation using a 35ps pulse YAG laser [17]. Tan *et.al.* reported a rise time of 17.4ps at -8V using a Ti:Sapphire 260 fs Kerr-lens mode-locked laser. Their device is a GaNAsSb *p-i-n* structure with 10μm of

diameter operating in the wavelength range 1.1-1.38µm [22]. Khalil *et.al.* reported a 1mm diameter GaInNAs *p-i-n* photodetector with a rise time of 2-4 ns using a 100ps pulse Nd:YAG laser. Their device operated in the range of 0.885-1.127µm with an excellent detectivity and low NEP at a temperature of T=100K [16, 38]. In this thesis, the transient photoconductivity measurements were carried out as a function of temperature with high-speed coaxial cable connections as mentioned in section 4.5.2. The TPC response measurements of AsN3134 and Asn3138 where the saturation occurred at T=300K for a range of applied voltages are plotted in Fig.5.12.

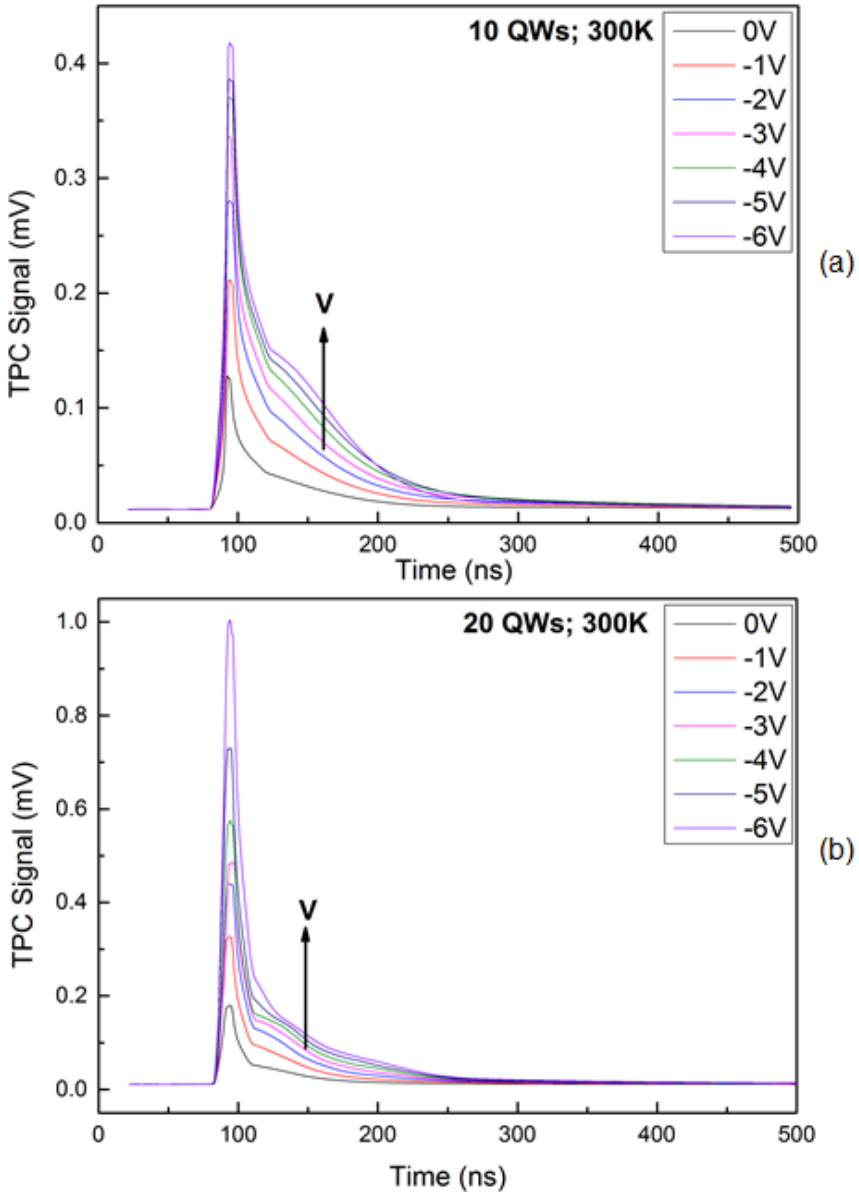

Figure 5.12: TPC response for different applied biases for (a) AsN3134 and (b) AsN3138.

The graphs show that the TPC signal increases with increasing applied bias and increasing number of QWs. The variation of the TPC peak amplitude with applied voltage is depicted in Fig.5.13(a). The values are proportional at low reverse bias while at high bias voltages, internal gain can be observed. The plot of the first derivative of the I-V curve *versus* the applied voltage clearly shows the dependency of current on the bias voltage as depicted in Fig.5.13(b).

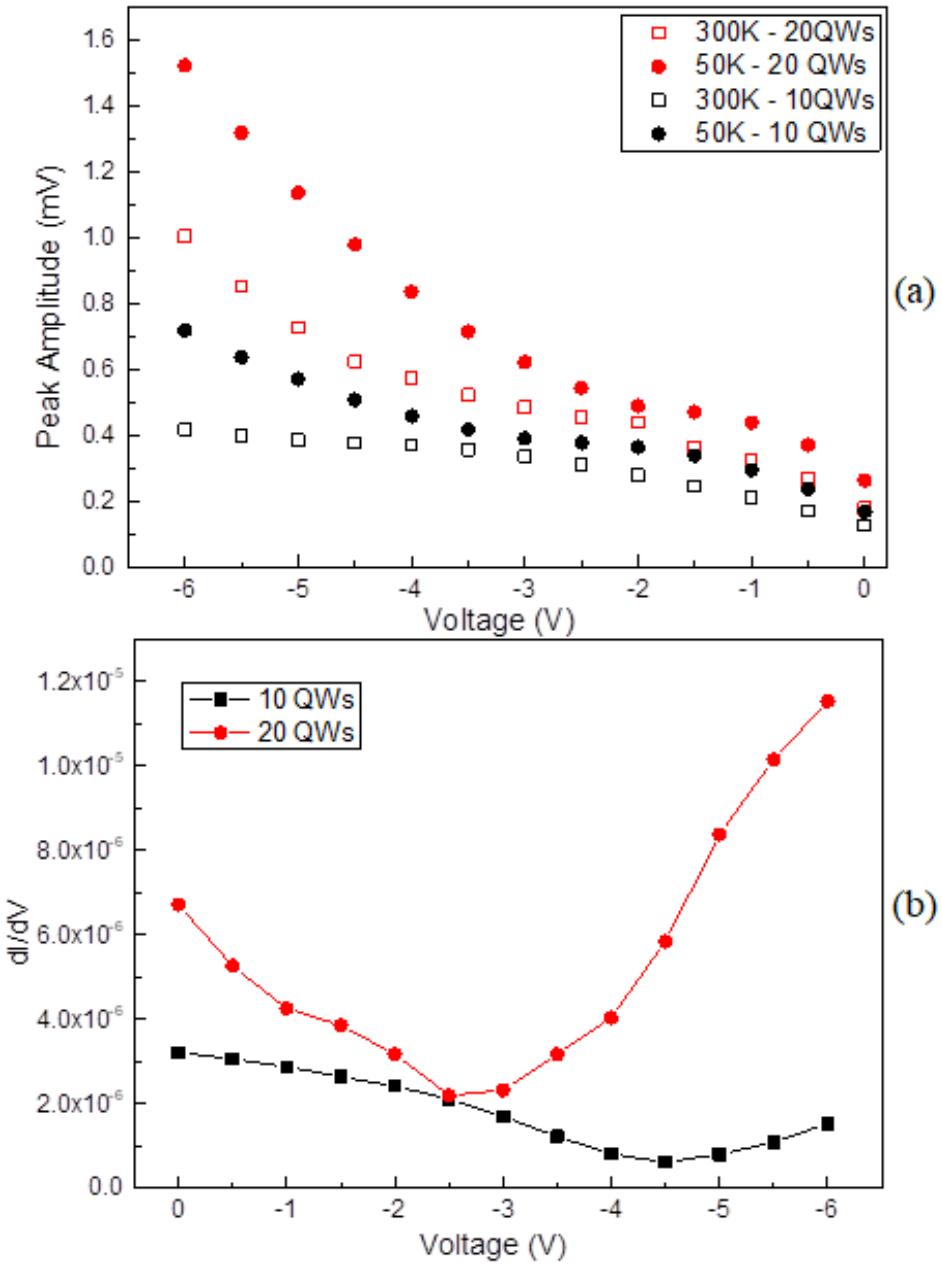

Figure 5.13: TPC peak amplitude as a function of applied voltage (b) Current-voltage derivative *versus* bias voltage at 300K.

The gradient has sub-linear dependence on the photocurrent. Hot carrier effects reduces mobility at high electric fields [39-40]. At V≥-4.5V (AsN3138) and V≥-5.5V (AsN3134), it surpasses its value on the low bias region with the ensuing carrier multiplication through valence band electron impact ionisation [41]. The variation of the TPC peak amplitude as a function of temperature has also been studied and is illustrated in Fig.5.14, showing an exponential increase in the peak amplitude with decrease in temperature. Recombination during the excitation is thought to be irrelevant as steady-state conditions do not occur due to the short pulse-width of the excitation, therefore the photocurrent decays to its initial dark value when the laser is turned off. The decay behaviour generally will be affected by the transit time of the carrier to pass the depletion region and the area of the detector. The response decay time, V(t), is clearly defined by two exponential curves as depicted in Fig.5.15, one corresponding to a fast, and the other to a slow decay process with time constants τ_1 and τ_2 respectively as:

$$V(t) = Ae^{-t/\tau_1} + Be^{-t/\tau_2} + V_0 \qquad (6.1)$$

where *A* and *B* are proportionality constants and V_0 is the voltage offset.

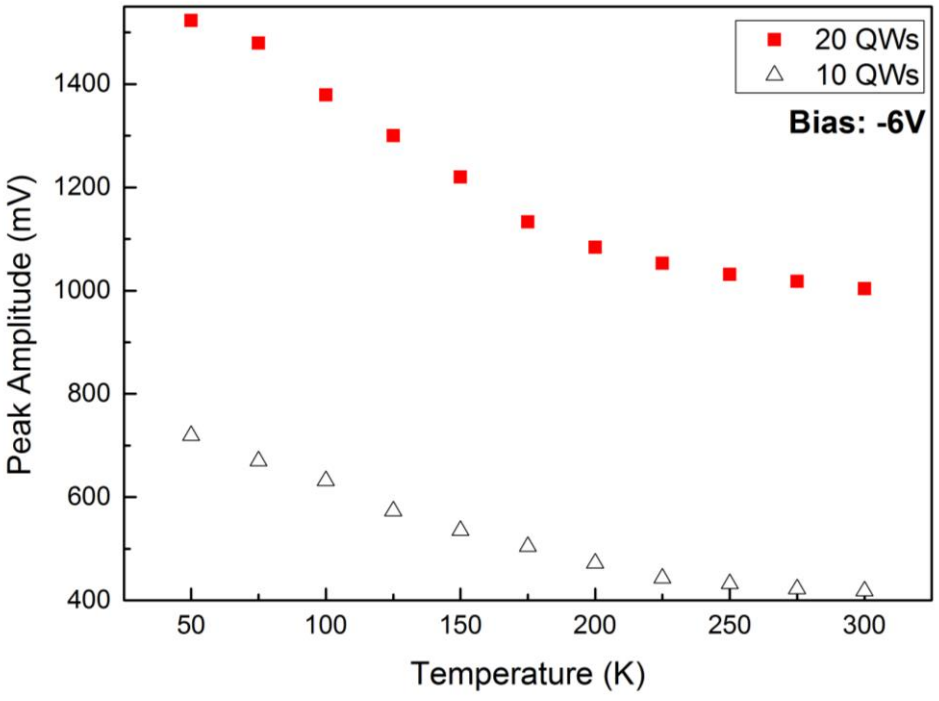

Figure 5.14: Temperature variation of TPC peak amplitude.

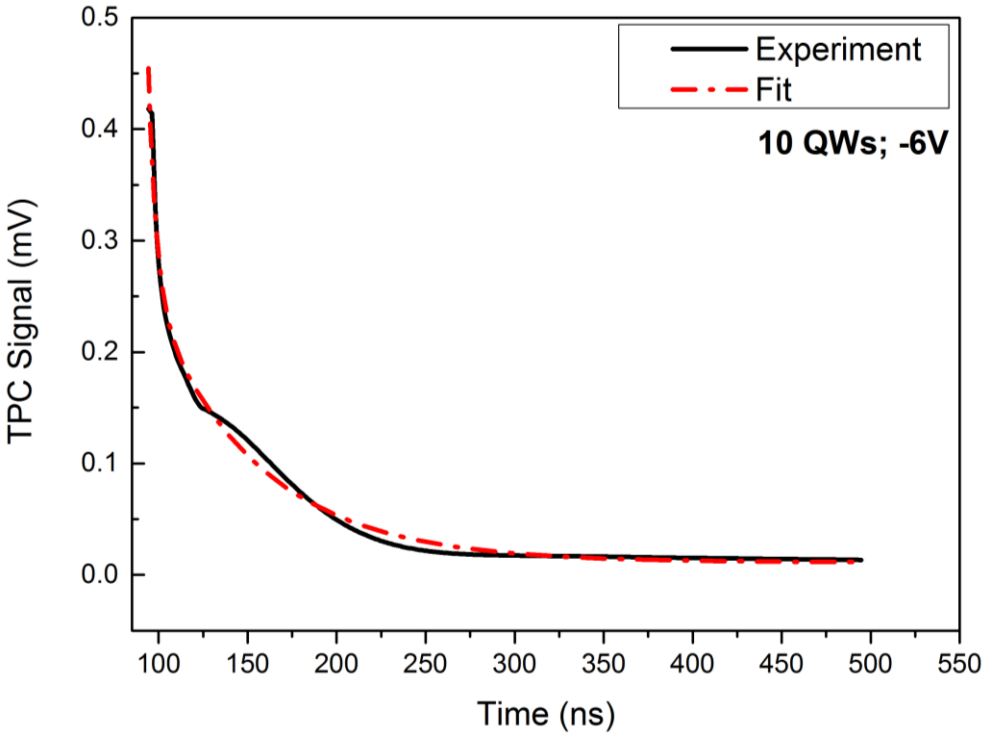

Figure 5.15: The experimental and theoretical fit of the TPC signal at T=300 K for AsN3134.

The overall fast component of the TPC decay due to the band-to-band recombination process [42] has a time constant $\tau_1 \approx$ 5ns for Asn3134 ($\tau_1 \approx$ 7ns for Asn3138), which agrees with the presented value for the GaInNAs based *p-i-n* photodetector by Khalil [43]. This is followed by a comparatively slower decay time constant $\tau_2 \approx$ 62.39ns for AsN3134 ($\tau_2 \approx$ 80.26ns for AsN3138) at T=300K, which can be associated with the existence of traps in the quantum wells [44]. This behaviour can be explained in terms of more electrons being released by deeper traps with increasing thermal energy, thus contributing to the photoconductivity. The rise time, τ_{rise} and the decay times (τ_1 and τ_2), are small at low temperature and increase with the temperature as depicted in Fig.5.16. The rise time is 4.77ns for AsN3134 and 10.3ns for AsN3138 at T=300K, while at 50K, the rise time decreases to 3.62ns for AsN3134 and 7.73ns for AsN3138. According to Eq.2.25, the wider the intrinsic region, the lower the response time. In this case, a higher QW number in the intrinsic region will create high resistance and traps in quantum wells which will reduce the response time. There is no significant variation of bias dependence is on the rise time.

However the decay times are observed to increase by about 1.1ns (AsN3134) and 0.8ns (AsN3138) when the applied bias is increased from 0V to -6V.

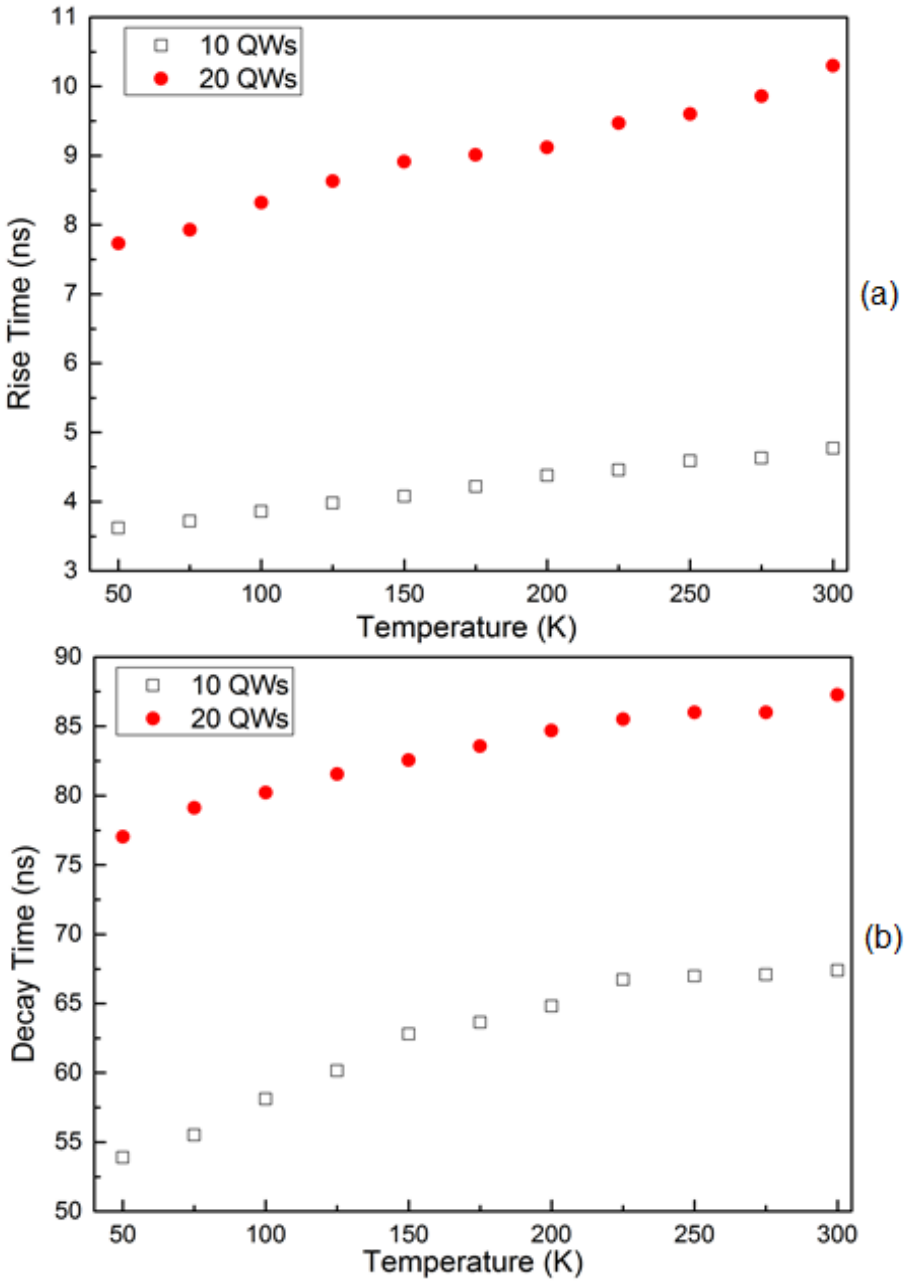

Figure 5.16: The (a) rise time and (b) decay time of temperature dependence at reverse bias of 6V.

The initial peak amplitude versus the laser intensity is depicted in Fig.5.17. It is clear that the TPC amplitude saturates as the excess carrier density increases after the linear increase at low excitation intensity. This happens as a result of sub-band, well-filling, and transparency effects in

addition to the dependence of mobility on carrier density [45]. Band filling occurs when the laser intensity creates enough excess carriers to fill all the available states in the conduction band [46], without these states having enough time to empty themselves *via* carrier recombination or phonon emission.

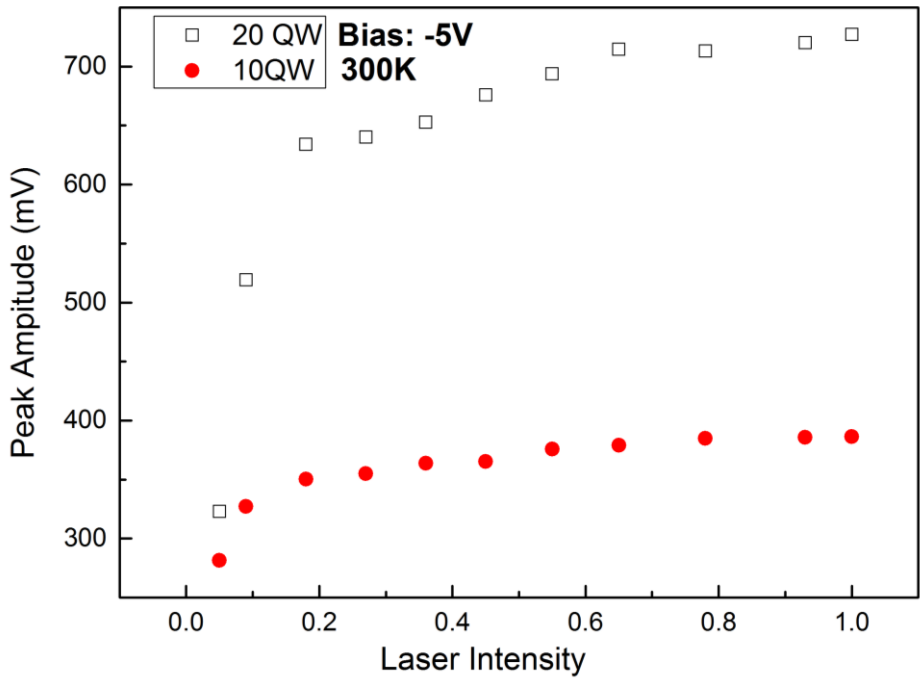

Figure 5.17: TPC peak amplitude as a function of incident laser intensity at a reverse bias of 5V

There are basically three limiting factors to the speed of a photodetector: diffusion of carriers, drift transit time in the depletion region, and capacitance of the depletion region. The slowest of the three processes is the diffusion of carriers due to the high-electric field from outside the depletion region. To minimize this slow effect, carriers should be generated near, or in the depletion region. The second process, transit time, is the time required for the carriers to drift across the depletion region and get swept out of the device. Lastly, the capacitance of the device will determine its RC time constant where R is the load resistance. To maximize a photodiode response, the transit time is typically designed to be comparable to the RC time constant. The output voltage across the load resistor is:

$$V_{out} = V_0\left(1 - e^{-t/RC}\right) \tag{6.2}$$

As the rise time signal can be measured between the 10% point and the 90% point of the peak amplitude output, the V_{out}/V_0 is equal to:

$$0.1 = 1 - e^{-t_1/RC} \qquad 0.9 = 1 - e^{-t_2/RC} \tag{6.3}$$

$$0.9 = e^{-t_1/RC} \qquad 0.1 = e^{-t_2/RC} \tag{6.4}$$

$$\ln(0.9) = -t_1/RC \qquad \ln(0.1) = -t_2/RC \tag{6.5}$$

$$t_1 = -RC(\ln 9 - \ln 10) \qquad t_2 = -RC(\ln 1 - \ln 10) \tag{6.6}$$

$$t_2 - t_1 = -RC(-\ln 10) + RC(\ln 9 - \ln 10) \tag{6.7}$$

Then finally:

$$t_2 - t_1 = (\ln 9)RC \tag{6.8}$$

The rise time for a p-i-n photodiode is given by

$$\tau_{rise} = t_2 - t_1 = (\ln 9)(\tau_{tr} + \tau_{RC}) \tag{6.9}$$

where τ_{RC} is the RC time constant and τ_{tr} is the transit time as described in section 2.7. The relatively large (about 1mm) diameter of the sample, implies that the RC time dominates the photodiode response time. The measured rise time, τ_{rise} is applied into Eq.6.9 and (τ_{RC} + τ_{tr}) is replaced into Eq.2.48 resulting in a bandwidth, which can be expressed as:

$$\Delta f = \frac{1}{2\pi(\tau_{rise}/\ln 9)} \tag{6.10}$$

At 300K, the bandwidth of AsN3134 is calculated to be 73.3MHz and 33.95MHz for AsN3138. It shows that the bandwidth of the photodetector will reduce when using a wider absorption region. In order to determine the sensitivity of a photodetector, the peak detectivity (D^*) is determined to characterize the performance of the photodetector. The detectivity is the reciprocal of the noise-equivalent power (NEP) corresponding to the signal power that gives a signal–to-noise ratio (SNR) equal to 1 with a 1Hz output bandwidth. These are expressed as [38, 47-48]:

$$NEP = \frac{\sqrt{4egI_0\Delta f}}{R_{NEP}} \qquad (6.11)$$

$$D^* = \frac{\sqrt{A\Delta f}}{NEP} \qquad (6.12)$$

where R_{NEP} is the responsivity, $g = L/x$ is the optical gain, $L = v_{th}\tau_{sc}$ is the mean free path, x is the superlattice length, v_{th} is the thermal velocity, τ_{sc} is the scattering time, I_o is the current flowing across the device, $A = \pi r^2$ is the photodetector area, and Δf is the bandwidth. The thermal velocity and scattering time are determined using the following equation:

$$v_{th} = \frac{\sqrt{3k_BT}}{m^*} \qquad (6.13)$$

$$\tau_{sc} = m^*\mu/e \qquad (6.14)$$

where T is temperature, k_B is Boltzman constant, m is effective mass and μ is carrier mobility. The temperature dependence of the mobility parameter is found from the measurement done by Sun [49] and Sarcan *et. al.* [50-51] for the nearest value of Nitrogen composition of GaInNAs used in this thesis. The resulting D* and NEP of a GaInNAs/GaAs MQW p–i–n photodetector at different temperatures are shown in Fig.5.18. At room temperature, the D* of the 10 QW photodetector is $4.89\times10^{10}\,cm\sqrt{Hz}/W$ and $7.12\times10^{10}\,cm\sqrt{Hz}/W$ for the 20 QW photodetector respectively. The 10 QW's NEP is $5.85\times10^{-11}W/\sqrt{Hz}$ while for the 20 QW, it is $4.02\times10^{-11}W/\sqrt{Hz}$ indicative of a sensitive photodetector with high quality and low-noise which is comparable with $\sim10^{10}\,cm\sqrt{Hz}/W$ of commercial polycrystalline mid-infrared photodetectors and resonant cavity enhanced mid-infrared photodetector on a silicon platform [52]. The performance of the p-i-n photodetector of GaInNAs is much better if the operation is being made at low temperature, however, it would be costly as it needs an expensive cooling system to cool down the detector to 50K.

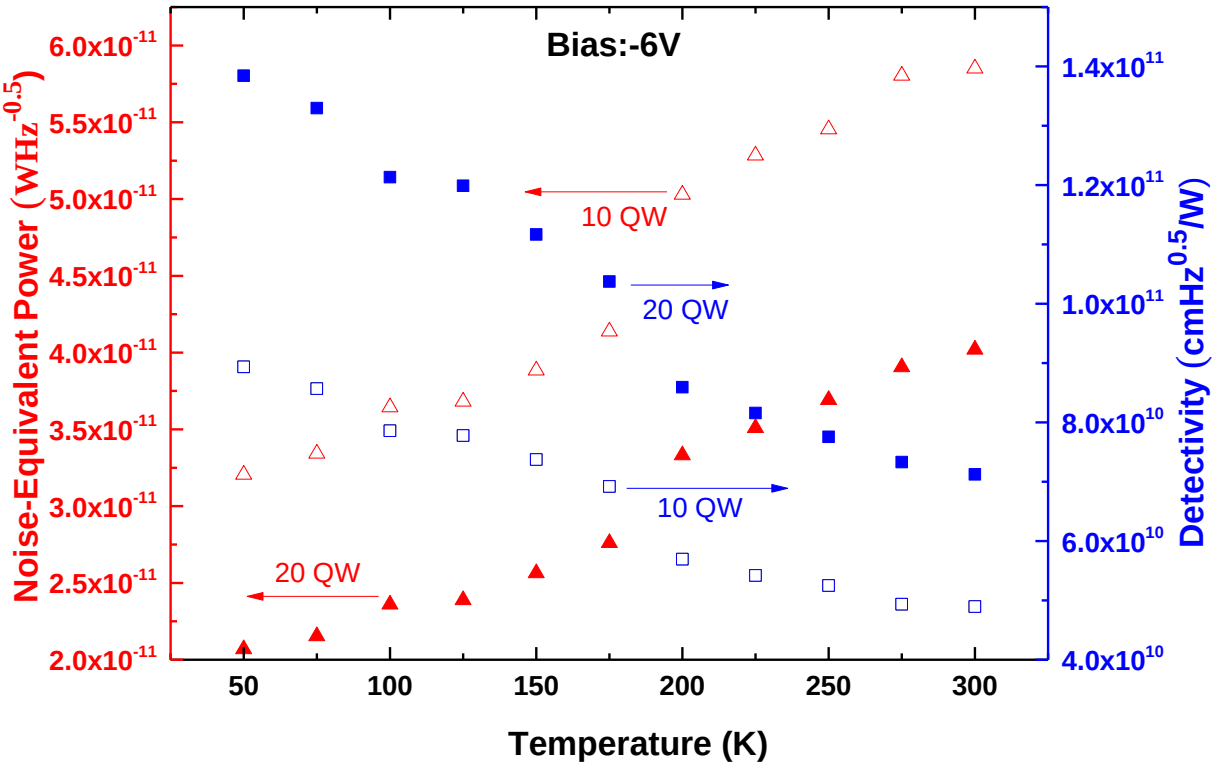

Figure 5.18: NEP and detectivity as a function of temperature at reverse bias of 6V

5.3.1 Summary

The photodetector based on p-i-n dilute nitride for 1.0μm of wavelength application has been demonstrated between two different numbers of QW. The quantum efficiency for the 20 QW sample is doubled compared to the 10 QW sample, however, more number of QW creates a higher internal resistance. Thus, the response time of the 20 QW sample is much slower than the 10 QW sample. This affects the bandwidth performance where the bandwidth of the 20 QW sample is lower than half of the 10 QW sample. However, the 20 QW sample provides lower NEP and better detectivity compared to the 10 QW sample. This indicates that in the selection of an absorption region thickness, there is trade-off option in terms of efficiency, speed, bandwidth, NEP and detectivity. Both photodetector can be operated in the range of wavelength from 950nm up to 1100nm which means that the samples can be used for deep-space communication system [72], as a receiver for 10GB/s OM3 fibre [73], data centre applications [74-75], optical time-domain

reflectometer receiver [76], and the laser interferometer gravitational-wave observatory (LIGO) detector [77-79].

5.4 VCE GaInNAs/GaAs MQW

In the previous section, a wide range of wavelength photodetector with different absorption region thickness has been demonstrated. The most recent application of the photodetector makes use of its fast response and high selectivity especially in optical communication systems. Resonant vertical-cavity enhanced (RVCE) photodetectors (PDs) have created much interest for applications in the 1.3 and 1.55 μm windows of optical communication systems due to their inherent features such as narrow spectral linewidth, ease of coupling, and their potential use as high speed devices with high quantum efficiency and wavelength-selectivity [53-54]. They consist of multiple quantum wells making up the absorbing region, sandwiched by two Distributed Bragg Reflector (DBR) mirror stacks [55], where the high efficiencies can be obtained when light that misses the first pass will be reflected back by the high-reflectivity mirrors and absorbed into the absorption region [82]. In this section, a novel dilute nitride based VCE photodetector, which consists of 21 pairs of undoped $Al_{0.8}Ga_{0.2}As/GaAs$ and 24 pairs of n-doped $Al_{0.98}Ga_{0.02}As/GaAs$ with reflectivity of over 99.9 %, and nine $Ga_{0.65}In_{0.35}N_{0.02}As_{0.98}$ QWs of 7 nm thickness separated by 20 nm GaAs barriers, is investigated.The sample fabrication process has been described in section 5.2.2.

Photoluminescence measurements are performed on the sample to investigate the optical characteristic before the fabrication process. Two cavity peaks are observed within the DBR stop band with λ_1=1.285μm and λ_2=1.22μm at T=300K. The first peak is explained in terms of transitions of photo excited electrons from the localized states below the conduction to the valence band where the holes have a broad momentum distribution [56]. The appearance of the second peak can be related to another cavity mode due to fluctuation of nitrogen in the

$Ga_{0.65}In_{0.35}N_{0.02}As_{0.098}$/GaAs quantum wells during the growth to compensate for the strain in the GaAs. However, both observed peaks of resonant cavity seem to not exactly overlap with the 1.180μm gain peak of the quantum wells region at T=300K. Additionally, the full width at half maximum (FWHM) of the PL signal compared to the cavity structure is quite broad as shown in Fig.5.19(a). The high density of defect centres such as arsenic-antisites, gallium vacancies and arsenic interstitial-gallium vacancies associated with high nitrogen content and quantum well fluctuation in the MQW structure might be the cause of the broad emission in the absorption region [49].

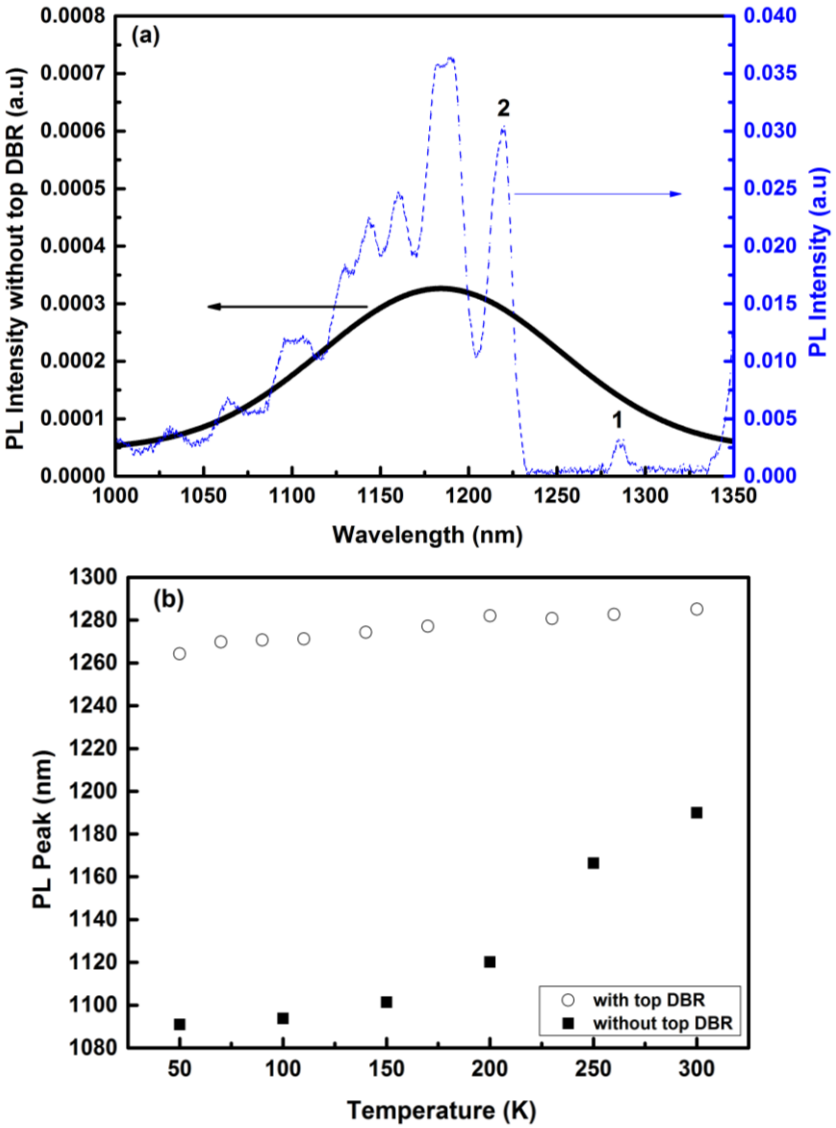

Figure 5.19: (a) 300K photoluminescence with top DBR (dash) and photoluminescence without top DBR (solid) and (b) temperature dependence of PL peak with and without top DBR of the studied structure.

The photocurrent response as a function of wavelength at T=300K is measured in the wavelength range between 1265 nm and 1302 nm. The spectrum photocurrent under incident power of 10 µW at zero and 1V reverse bias with a 5 µm window is shown in Fig.5.20(a). It can be seen that the sample responds very well to the increase in applied bias due to the electron hole pair generation by the incident photons that are swept away from the quantum wells. The effect of resonant cavity is clear, where the maximum photocurrent density of 0.16 A/cm^2 is recorded under 1V reverse bias, at the resonance wavelength of 1286 nm.

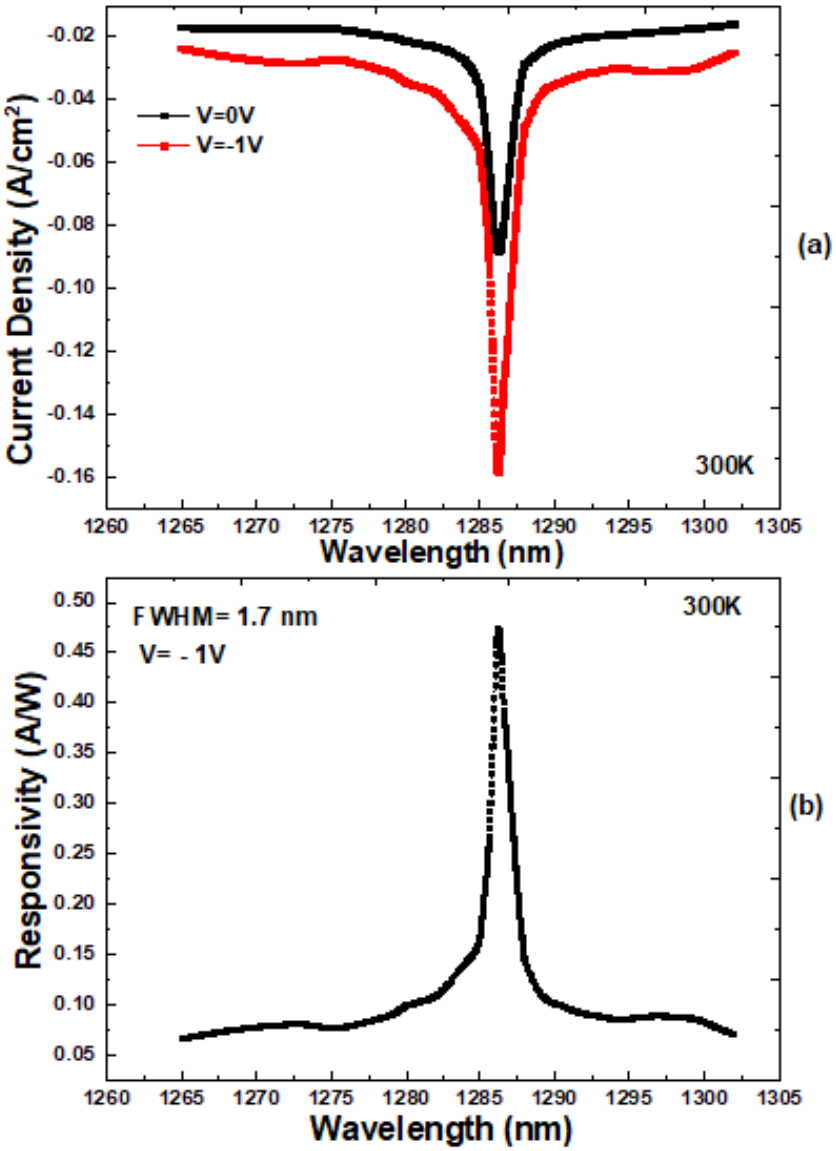

Figure 5.20 (a): Experimental current density spectrum of 0V and -1.0V at T = 300 K with 10 µW incident light power. (b) Responsivity spectrum at - 1.0 V.

The responsivity increases linearly with the bandwidth of the cavity resonance and abruptly tends to zero when the incident photon wavelength exceeds the wavelength of the device cavity. The maximum FHWM of responsivity spectrum is observed to be 1.7 nm under 10μW incident power at -1 V bias and peak responsivity of 0.47 A/W as shown in Fig.5.20(b). The narrow FWHM is likely to be due to both the superior quality and high number of DBR pairs for this sample compared to the ones reported in the literature [17, 57-58, 82].

The current-voltage (I-V) characteristics for both dark and under illumination (between 10μW to 434μW) for another 10μm window diameter sample at T=300K are plotted in Fig.5.21(a). The overall behaviour of I-V characteristics is the same in both samples. The dark current is -1.7nA at -1V and increases to -6.5nA at -2V. The photocurrent results show that the increment of the light power will generate more carriers and increase the photocurrent linearly with the applied bias. Ohmic behaviour occuring at V~0.8V and sub-linear dependence of the photocurrent on the applied bias is observed as expected from the mobility reduction due to the hot carrier effects at high electric fields [39-40, 82]. At -1.5 V bias, the gradual increase of the generated photocurrent is indicative of the behaviour of the avalanche region pattern. The average electric field of 2.4×10^6 V/m is obtained by calculation at -2V bias for the highest optical power of 434μW, more than 10^5 V/m that is typically needed for the inter-band impact ionisation in GaAs [59]. The current and bias voltage dependence relationship is obvious when conductance (dI/dV) versus voltage is plotted as depicted in Fig.5.21(b). The saturation Ohmic region of current at low biases is followed by a reduction of the slope due to the hot carrier effects, before the current increases at -1.5V bias. This could be due to the e-h pairs in the sample being relegated as a band-band process or band-trap process depending on whether the second carrier is initially in the valence band and makes the inter-band transition [41]. In this situation, the kinetic energy of the electron in the conduction band exceeds the threshold energy for impact ionisation thus simulating an electron from the valence band via the Coulomb interaction. This

will cause the electron to be promoted into the conduction band, leaving a hole in the valence band. This process is called carrier multiplication, explaining the behaviour of the carrier conductance (dI/dV) at biases of over -2V in Fig.5.21(b), leading to more electrons being present in the conduction band than the number of holes in the valence band, which may induce electrical instability at high electric fields, with values exceeding that in the low bias region to induce further impact ionisation. As a whole, the sample is considered to have an internal gain of 1.55 at bias voltages of V ≥ -2V with an overall quantum efficiency of 67% [82].

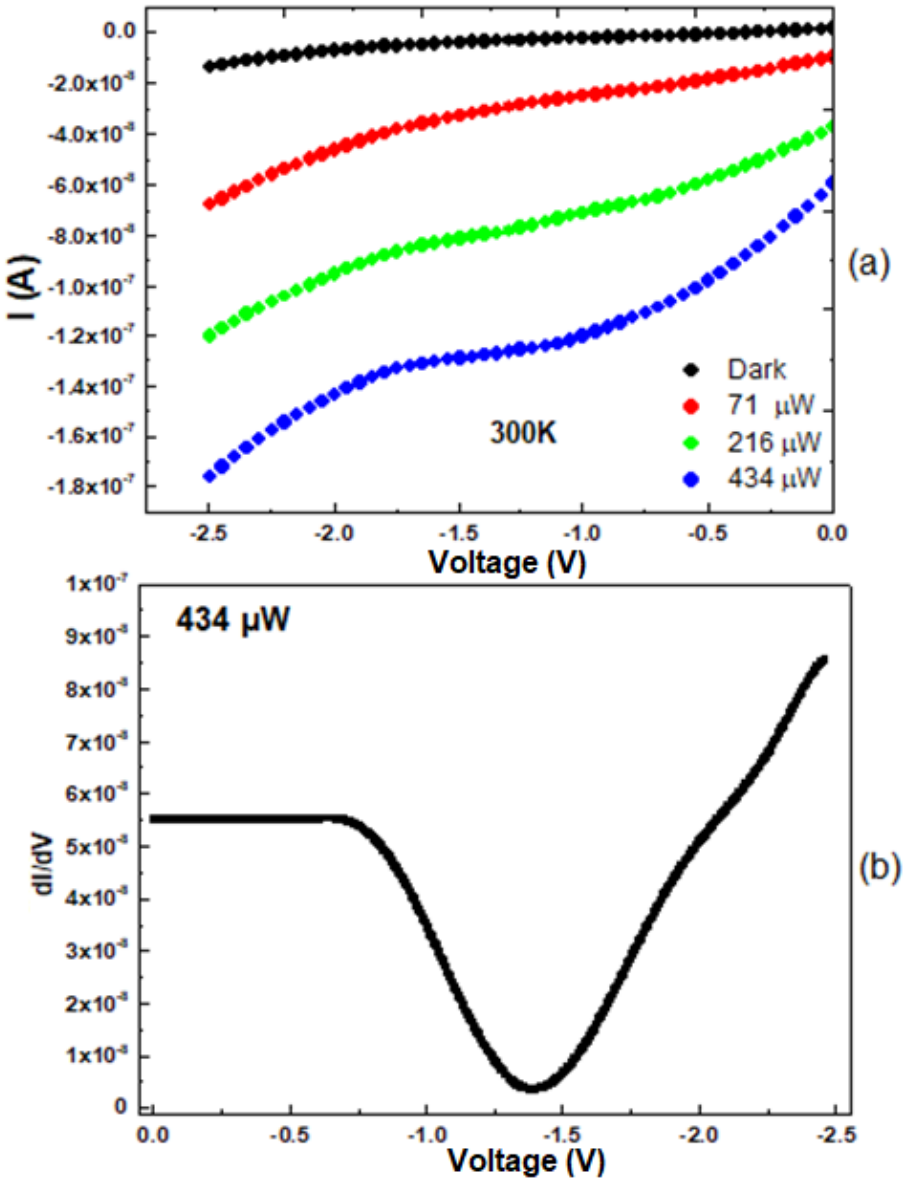

Figure 5.21: (a) The I-V characteristic in darkness and under various incident optical powers (b) conductance-voltage characteristic [82]

The TPC's response measurements where the saturation occurred at T=50K and T=300K for a range of applied voltages are plotted in Fig.5.22. The plots show that the TPC signal increases with increasing applied bias and increasing temperature. Fig.5.23 clearly shows that the temperature dependence increases at the peak amplitude of the TPC signal under -6V constant bias.

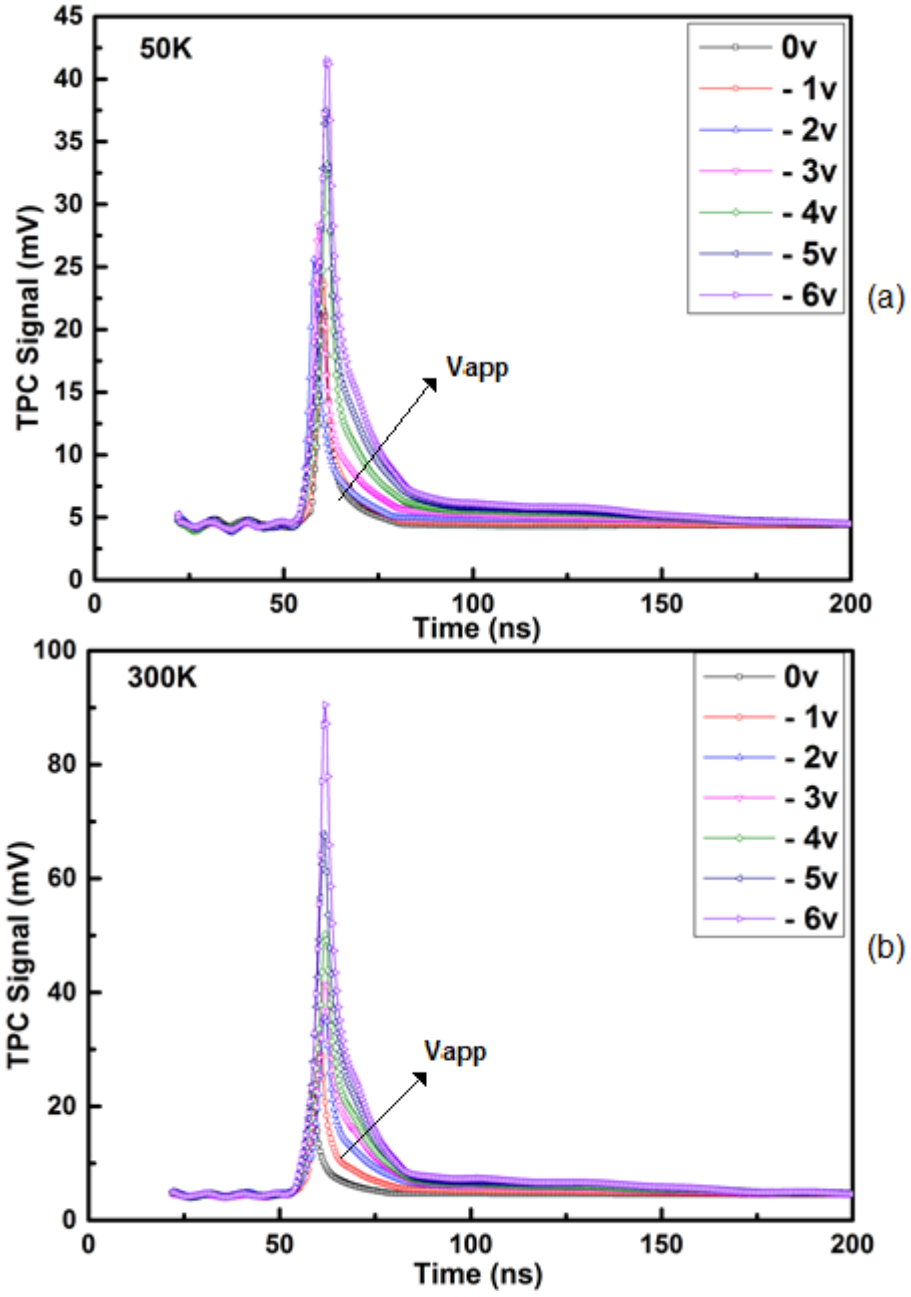

Figure 5.22: Transient photoconductivity response for different applied biases (V_{app}) at (a) T=50K and (b) T=300K.

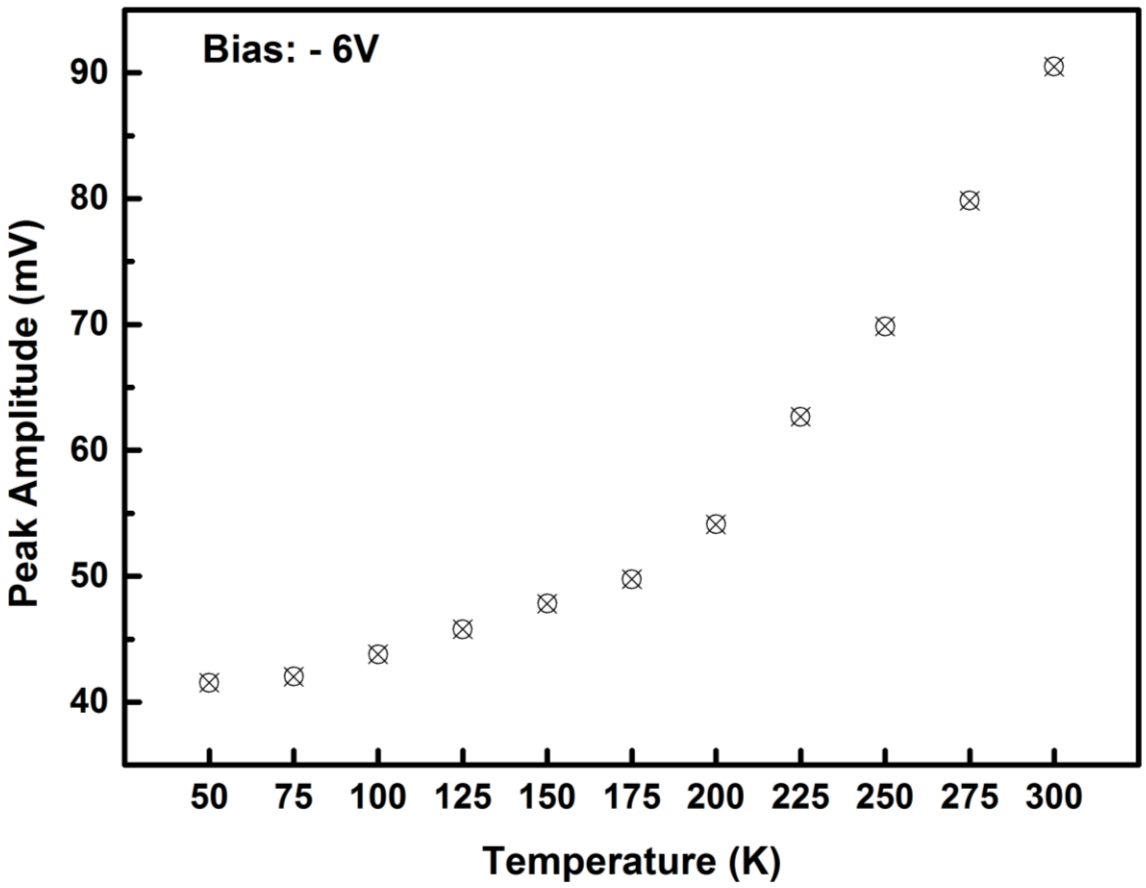

Figure 5.23: Temperature variation of TPC peak amplitude.

TPC peak amplitude between T=50K and T=300K as a function of applied voltage is depicted in Fig.5.24(a). There is an obvious linear dependence at low reverse bias followed by a super-linear dependence for higher bias voltages at T=300K, indicating an internal gain.

The plot of conductance versus applied voltage clearly shows the dependency of current on the bias voltage as depicted in Fig.5.24(b). At T=300K, the gradient represents Ohmic behaviour at low bias and at bias V≥-3V, it surpasses its value in the low bias region via carrier multiplication through the valence band electron impact ionisation. This behaviour is the same as described previously for the I-V measurement on the same structure but with a 15µm window aperture diameter.

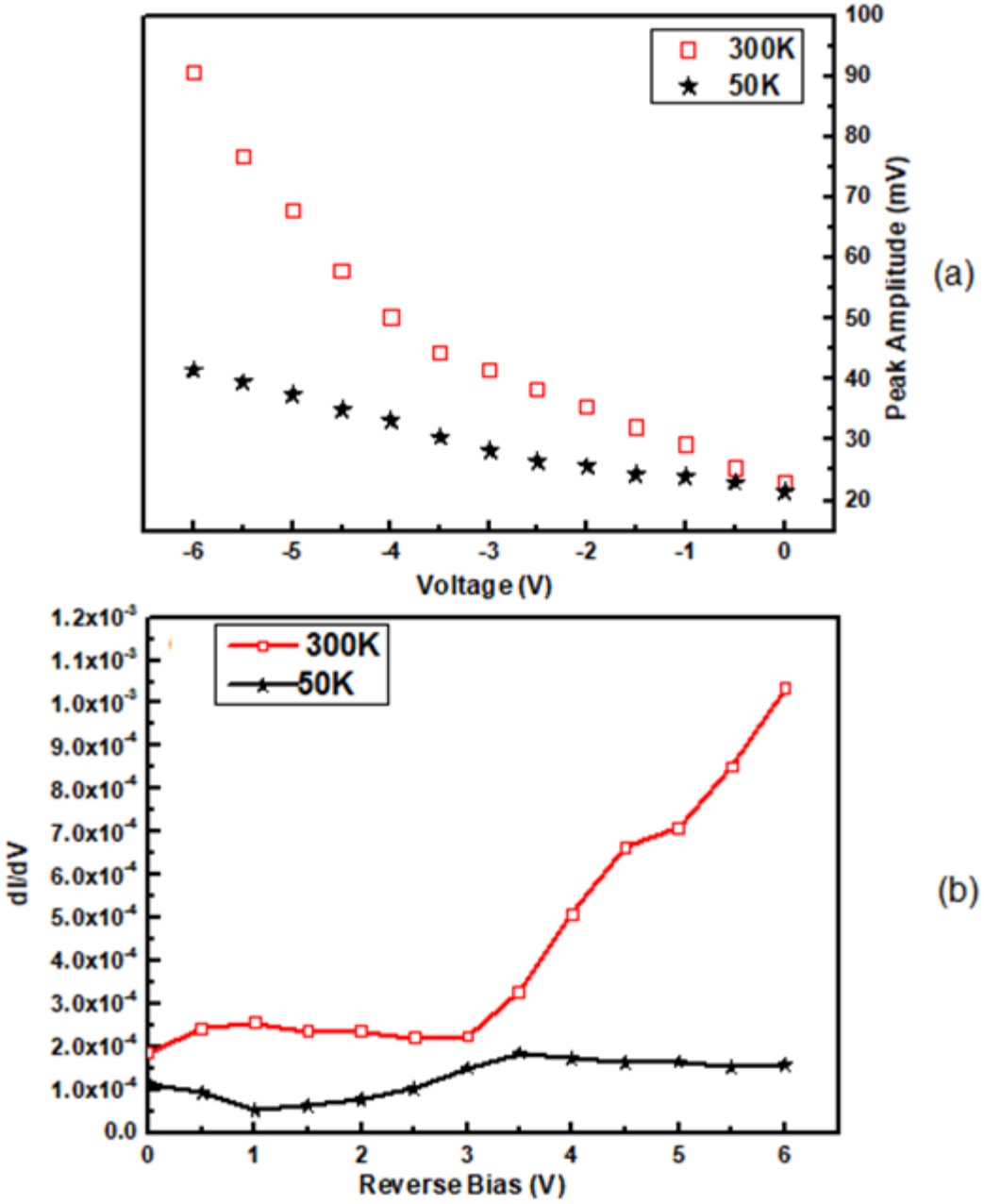

Figure 5.24: (a) TPC peak amplitude as a function of applied voltage (b) derivation of current-voltage characteristic.

In the previous section, the response decay time, V(t), is clearly defined by two exponential curves and for this sample as depicted in Fig.5.25, one corresponding to a fast and the other to a slow decay process as stated in Eq.6.1.

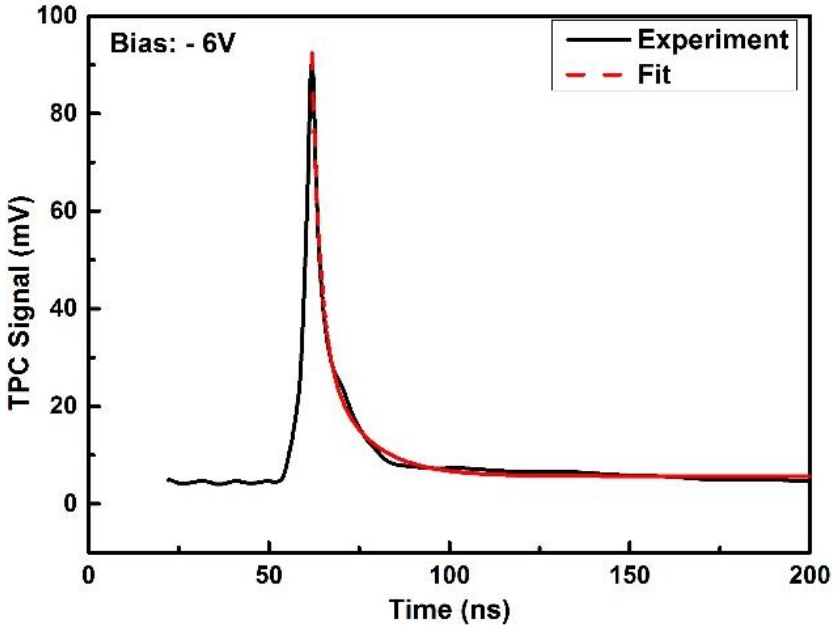

Figure 5.25: The experimental and theoretical fit of the TPC signal at T=300 K.

The overall fast component of the TPC decay has a time constant $\tau_1 \approx$ 3ns, followed by a comparatively slower decay time constant $\tau_2 \approx$ 14ns at T=300K, which can be associated with the existence of traps in the quantum wells. The rise time, τ_{rise} and the decay time (τ_1 and τ_2), are slow at low temperatures and increase with increasing temperature as depicted in Fig.5.26.

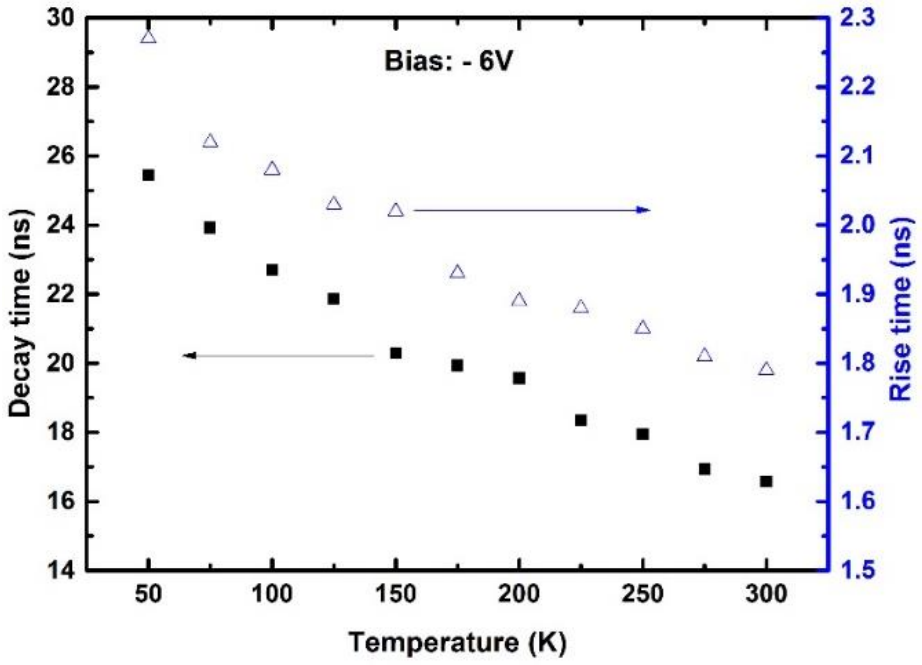

Figure 5.26: The rise time and decay time at temperature dependence of 6V reverse bias

The rise time is 1.79ns at T=300K and increases to 2.27ns at T=50K. In this sample measurement, no significant bias dependence was observed for the rise or decay times. The response time for this sample is expected to perform at a better speed since a smaller diameter (10μm) is used for this TPC measurement. However, the pulse width of the laser that is used in this thesis is just 500ps where it is beyond the transit time for GaInNAs material which is normally lower than 15ps. Hence, the maximum bandwidth of this sample is calculated to be 195MHz at T=300K, limited to the speed of the pulse laser. In this section, a comparison of the two types of laser with different pulse widths has been carried out as shown in Fig.5.27.

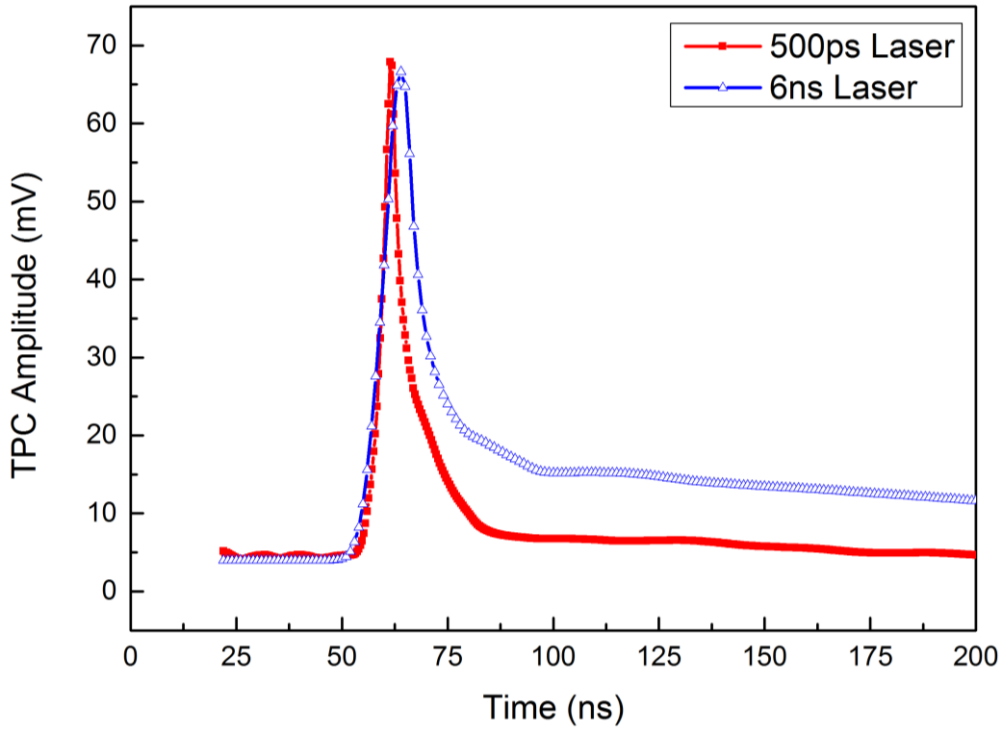

Figure 5.27: TPC measurement at two different speeds of pulse laser

The comparison has been done for the same incident optical power at 300K and the rise time observed from 6ns laser usage is 7.43ns and decay time is 227ns. It shows that the speed of laser is important to get better response of the detector. The initial peak amplitude versus the laser intensity is depicted in Fig.5.28. It is clear that the TPC amplitude linearly increase at low excitation intensity and then saturates as the excess carrier density increases. This happens as a

result of sub-band, well-filling and transparency effects, in addition to the dependence of mobility on carrier density as mentioned previously.

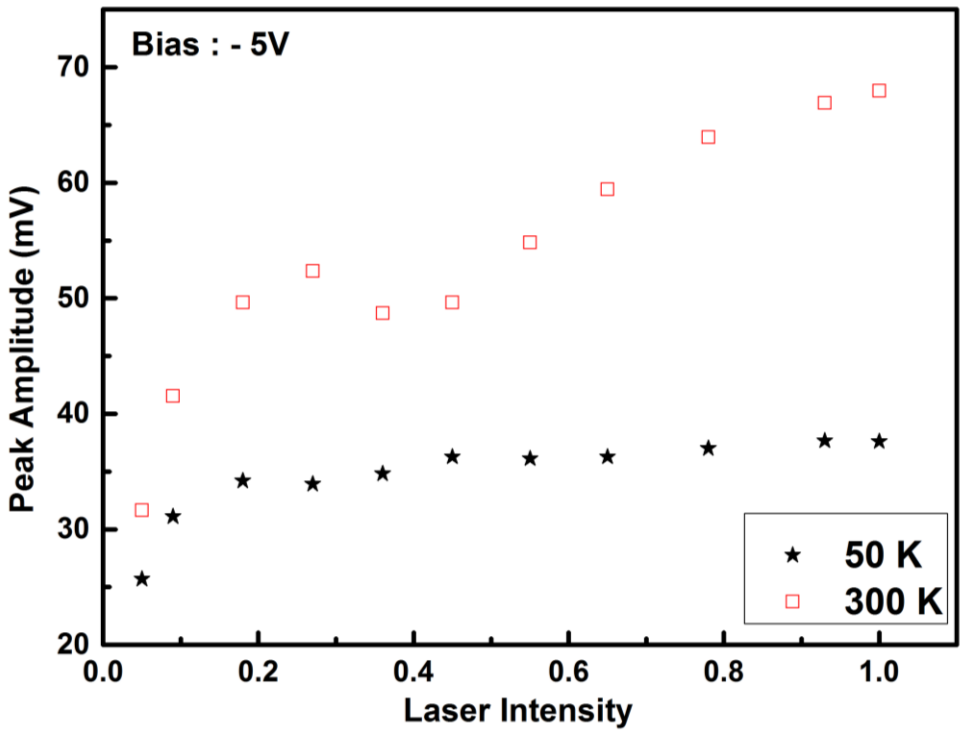

Figure 5.28: TPC peak amplitude as a function of incident laser intensity at a reverse bias of 5V

The behaviour of fast response at T=300K can be explained by the different temperature dependence rate of the cavity resonance and the bandgap of the material of the active layer, i.e., GaInNAs, as shown in Fig.5.19. The temperature induced red-shift of the effective bandgap for the active region was 0.3 nm/K, much higher than for the cavity peak, which shifted at only 0.07 nm/K. Therefore, the cavity peak will show a better absorption peak overlap with increasing temperature i.e. the response time and amplitude improve at higher temperatures, enhancing the performance of the photodetector to display behaviour that is identical to temperature range between 10˚C and 40˚C for a similar device structure [60]. The better performance can be observed as in Fig.5.29 when the absorption peak of the active layer (GaInNAs) and cavity resonance wavelength overlap with each other at room temperature as depicted in Fig.5.19(b). The measured rise time, τ_{rise}, applied into Eq.6.10, results in a bandwidth, Δf =195MHz at T=300K.

The resulting *D** and NEP of the GaInNAs/GaAs MQW photodetector at different temperatures are shown in Fig.5.29. The maximum *D** of the photodetector is $2.28\times10^{10}\,cm\sqrt{Hz}/W$ while the minimum NEP is $2.45\times10^{-11}W/\sqrt{Hz}$, revealing the low-noise, high performance, and high sensitivity photodetector characteristics at T=300K, comparable to the $\sim10^{10}\,cm\sqrt{Hz}/W$ of commercial polycrystalline mid-infrared photodetectors and resonant cavity enhanced mid-infrared photodetector on a silicon platform [52]. These results reveal that incorporation temperature modulation can enhance the performance of samples that incorporate a vertical cavity structure in case of mismatch between the DBR cavity resonance wavelength and the absorption peak of the active layer.

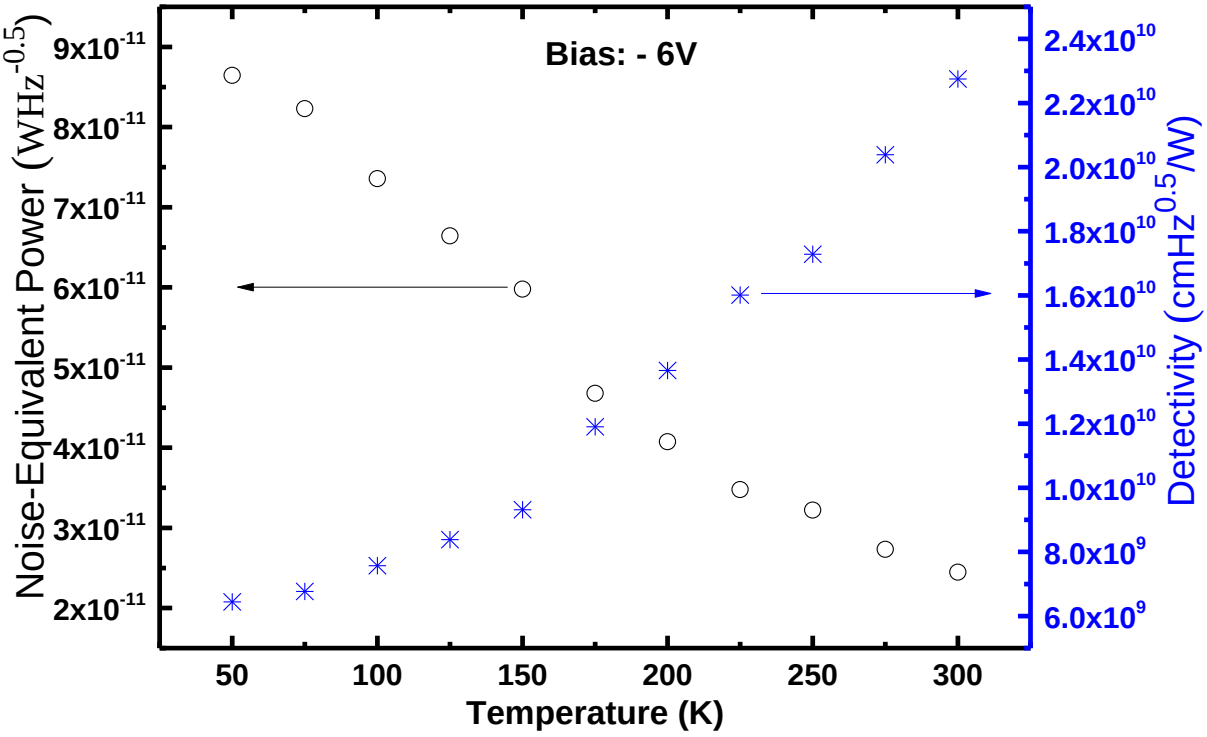

Figure 5.29: NEP and detectivity as a function of temperature at reverse bias of 6V

5.4.1 Summary

A vertical cavity enhanced photodetector based on a dilute nitride GaInNAs/GaAs multi-quantum-well structure operating at 1.286μm has been demonstrated. PL measurements were performed on structures with and without the top DBR to determine any deviation of the optical

signal between 50K and 300K. The deviation of the PL signal between those structures was attributed to the nitrogen-related high density of defects and imperfections in the crystal structure. The two observed cavity peaks display alternative operation modes due to strain and fluctuations in the well width and nitrogen incorporation. The sample has 0.47A/W responsivity (without internal gain). The FWHM of 1.7nm shows excellent wavelength selectivity for incident optical power of 10μW at the resonance wavelength. The internal gain of 1.55 observed at bias voltages of V ≥ -2V is associated with the inter-band impact ionisation. The photocurrent rise time of 2.27ns at T=50K was observed to decrease to 1.79ns at room temperature. The TPC decay showed two components with an initial time constant of ~3ns followed by a slow decay with a time constant of ~14ns, which increased at lower temperature. The corresponding bandwidth of 195MHz and detectivity of $2.28\times10^{10} cm\sqrt{Hz}/W$ with NEP of $2.45\times10^{-11} W/\sqrt{Hz}$ indicates a better performance of photodetector characteristics compared to a previously discussed p-i-n photodetector even at room temperature operation.

5.5 VCE GaInNAs/GaNAs MQW

The performance of a VCE photodetector based GaInNAs with an internal gain of 1.55 at room temperature operation has been demonstrated previously. In this section, the improvement of material and structure has been made in order to obtain better results within room temperature operation. GaInNAs material with Antimony flux has been proposed to improve the optical quality and GaNAs material used as the barrier layer to compensate the strain of the dilute nitride QW. The structures of the samples described in section 5.2.3, are grown by Molecular Beam Epitaxy (MBE) on an n-doped (100)-oriented GaAs substrate and have been fabricated in the shape of a mesa-structure, with a top circular aperture of 1 mm diameter.

PL and reflectivity measurements are performed to investigate the optical quality and cavity resonance for each sample. The peak wavelength of PL and the reflectivity resonant cavity

wavelength at 300K are quite close to each other as depicted in Fig.5.30. The PL peak for the 9 QW is 1299.7nm while the reflectivity peak was observed at 1300nm. The measured reflectivity for the 20 QW structure was observed at 1324nm while the PL peak found to be at 1324.6nm.

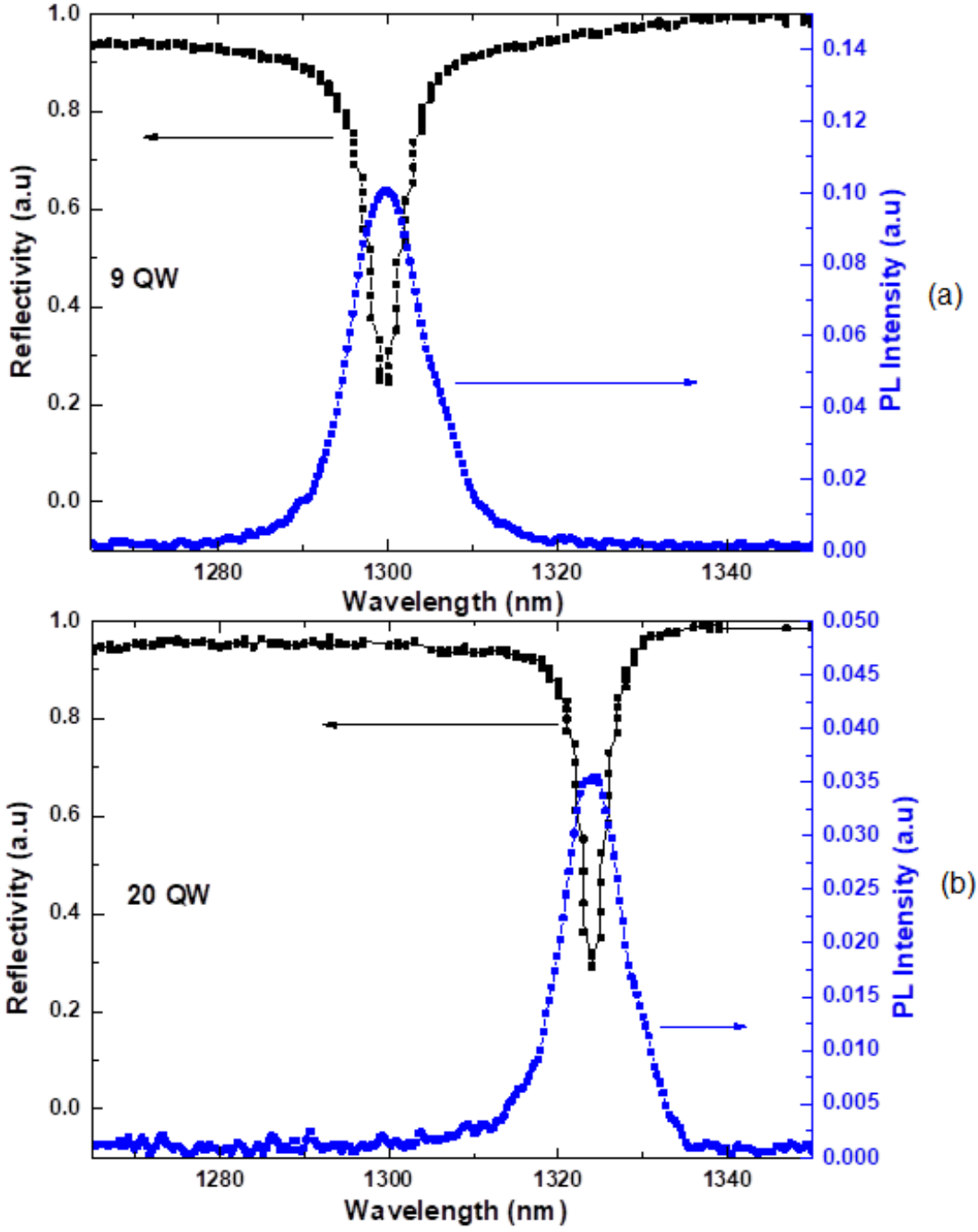

Figure 5.30: Room temperature photoluminescence (blue) and reflectivity (black) (a) 9QWs (b) 20QWs

The peak wavelength of the PL and the measured resonant cavity wavelength are both taken from 1265nm to 1350nm on a quarter of a two inches wafer piece. According

to the reflectance and PL results, an excellent wavelength selectivity is observed to be less than 5nm for both samples. The reason for the narrower FWHM compared to the values reported in the literature [17, 57-58] is likely to be due to the superior quality of the DBR pairs as discussed in the previous section. The temperature dependence of the PL has been carried out for both samples as shown in Fig.5.31.

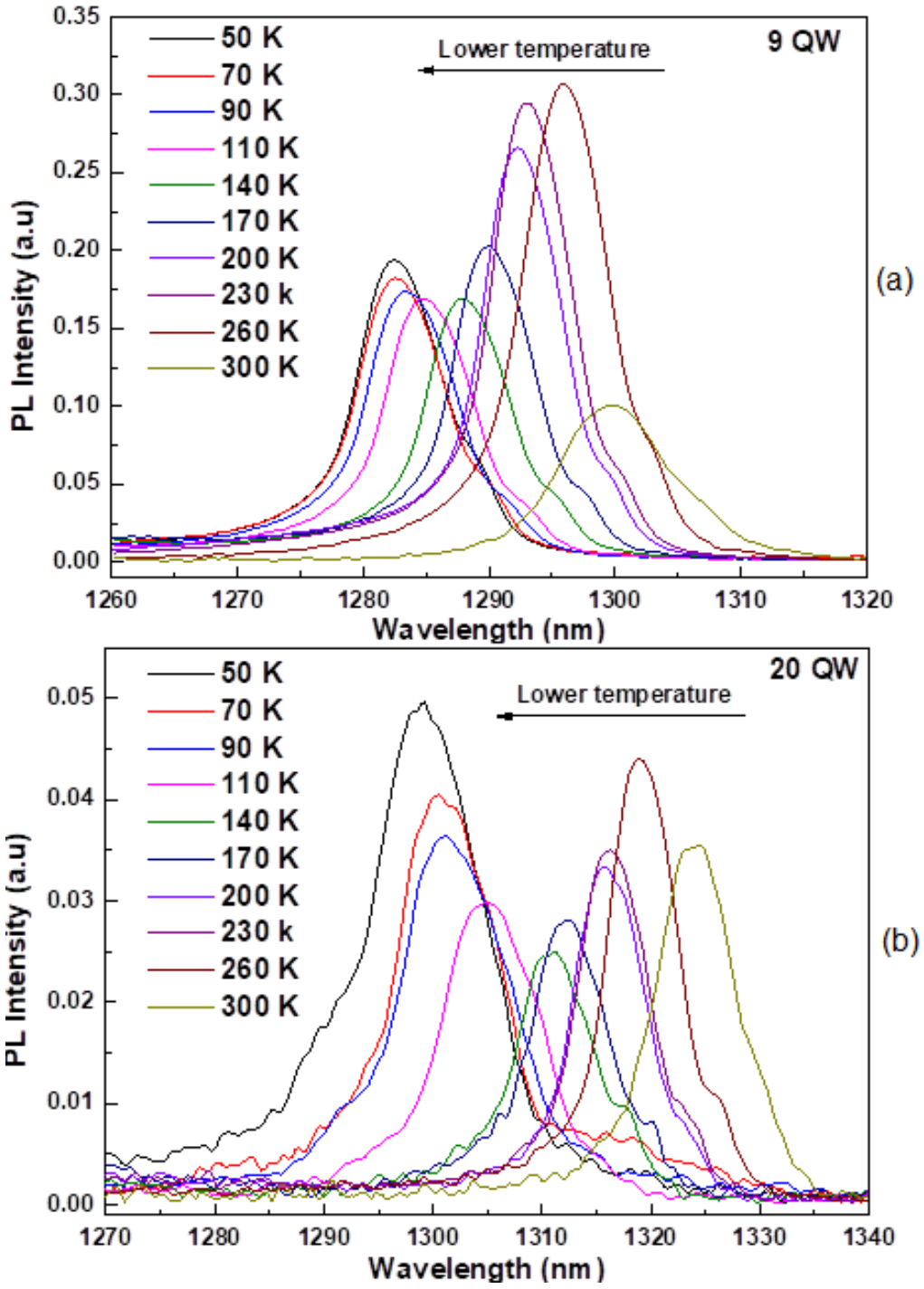

Figure 5.31: Temperature dependence of PL for (a) 9QWs (b) 20QWs

The bandgap energy of both samples increases with decreasing temperature but not as much as the normal PL temperature dependence behaviour. There is no significant relationship observed between both the peak amplitude of the PL and the temperature dependence. This could be due to the cavity reflectance of the DBR mirror structure on top of both samples that obstructs the actual emission of the GaInNas quantum well material. The temperature dependence characterisation of both samples without the top DBR mirror are performed in order to investigate the effective bandgap of active region as depicted in Fig.5.32

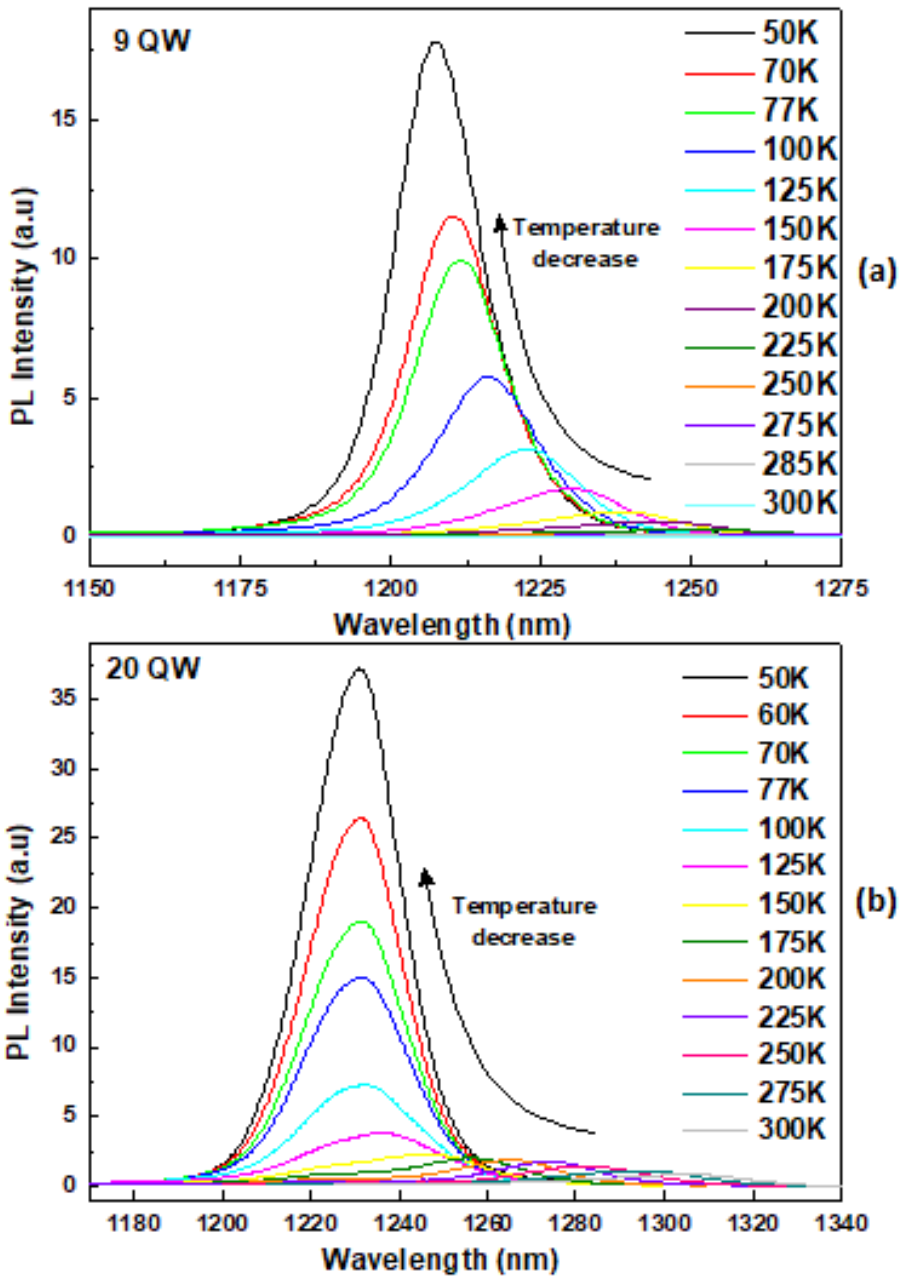

Figure 5.32: Temperature dependence of PL without top DBR for (a) 9QWs (b) 20QWs

Both samples without top DBR mirrors clearly show a very large increase in intensity as the temperature is reduced, as shown in Fig.5.33. This behaviour is due to the effect of the phonon scattering mechanism of the GaInNas, increasing with temperature, and causing a non-radiative band to band transition which leads to the PL amplitude to decrease with increasing temperature. The same pattern was observed for the other samples as discussed in section 5.3.

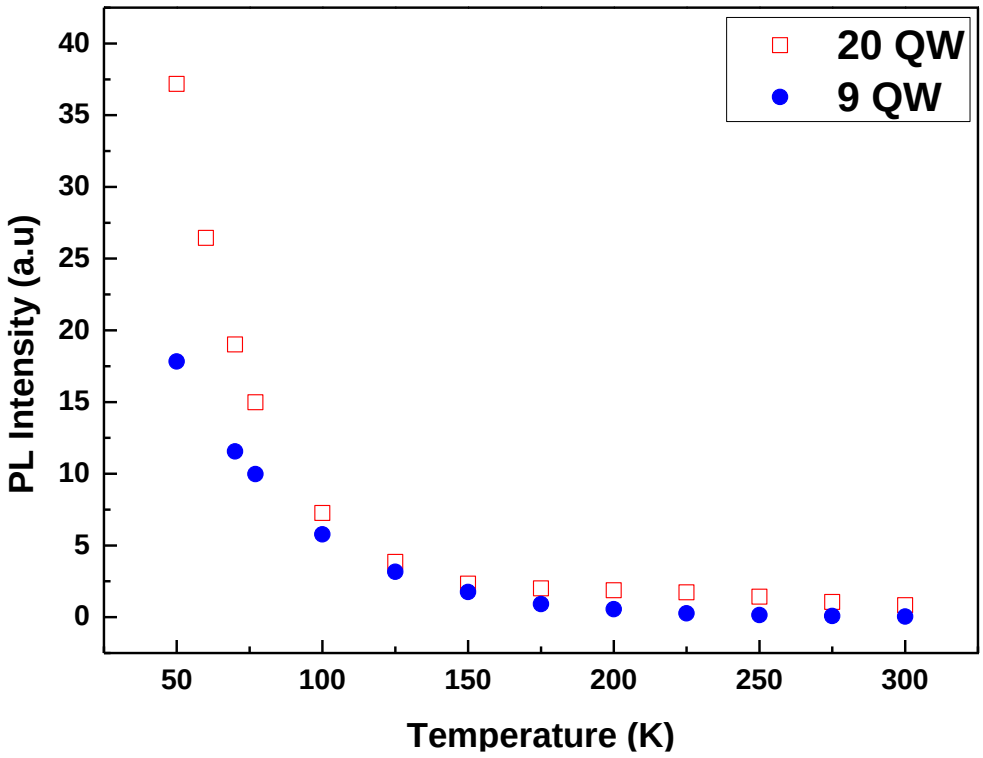

Figure 5.33: The PL intensity versus temperature for 9 QWs and 20 QWs

Due to the growth constraint as mentioned in section 5.2.3, there could be a mismatch problem between the absorption peak of the active region (GaInNAs) and the cavity resonance peak. The relationship of the bandgap energy between both peaks is shown in Fig.5.34. As temperature increases, the resonance of both the active region and the cavity are redshifted. However, the active region redshifts at a higher rate. The temperature-induced redshift rate of the effective bandgap of the GaInNAs QW layer is determined to be 0.298nm/K for the 9 QW sample and 0.242nm/K for the 20 QW sample while the cavity resonance shifts at the rate of 0.068nm/K for 9 QW sample and 0.072nm/K for 20 QW sample. These behaviours indicate that

both samples are best operated near room temperature as active layer and cavity resonance retaliate with each other.

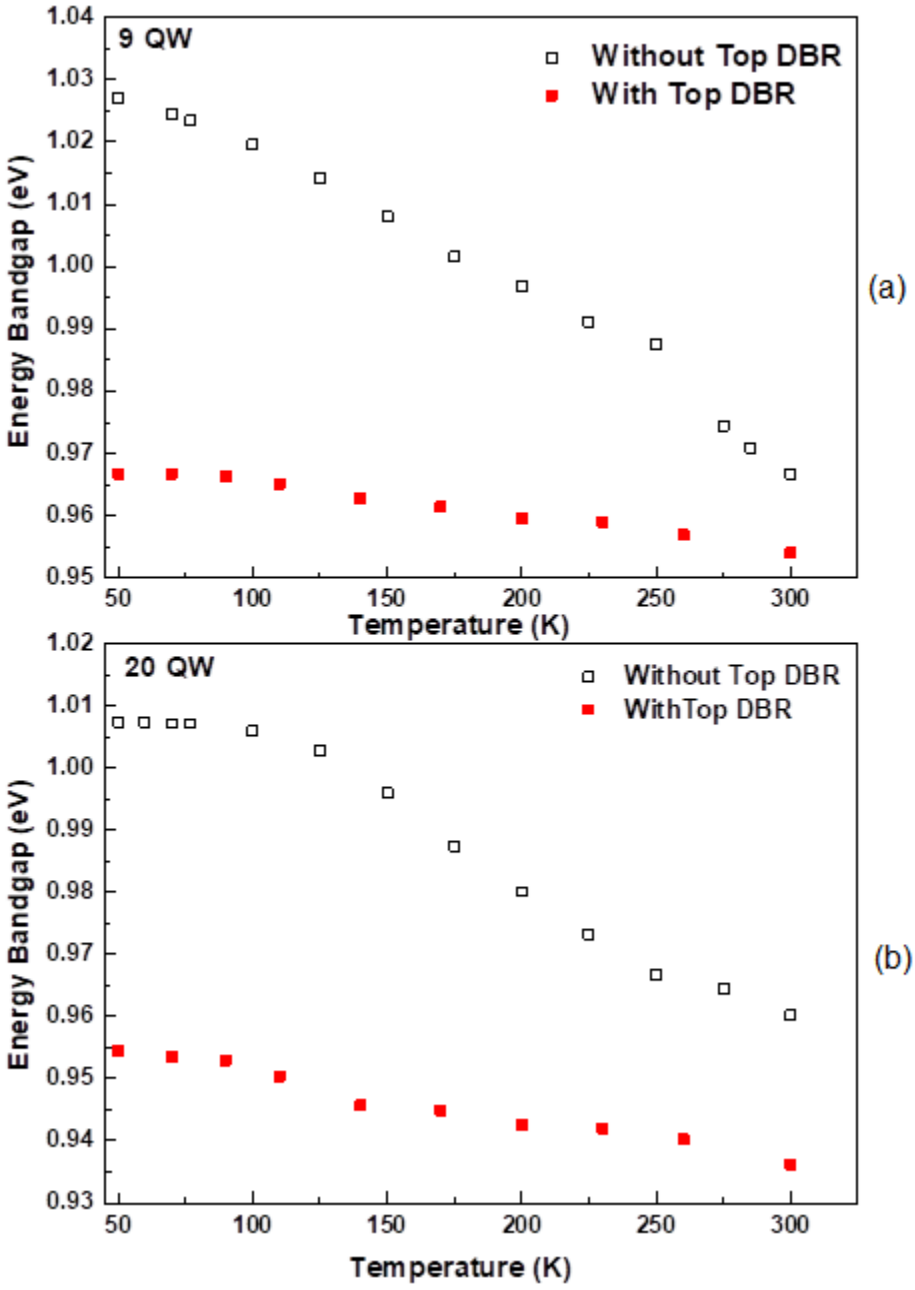

Figure 5.34: Temperature dependence of PL peak with top DBR (red) and without top DBR (black) for (a) 9QWs (b) 20QWs

The 9 QW sample shows better overlap between both the active region and the cavity resonance compared to the 20 QW sample at room temperature. The mismatch between both peaks is 15.09nm for the 9 QW sample and 33.23nm for the 20 QW sample. The observed PL

peaks for both samples arises from both the GaNAs (at the higher energy side) and the GaInNAs QW layer (at the lower energy side) and can be seen clearly by using Gaussian fits to the experimental data as shown in Fig. 5.35.

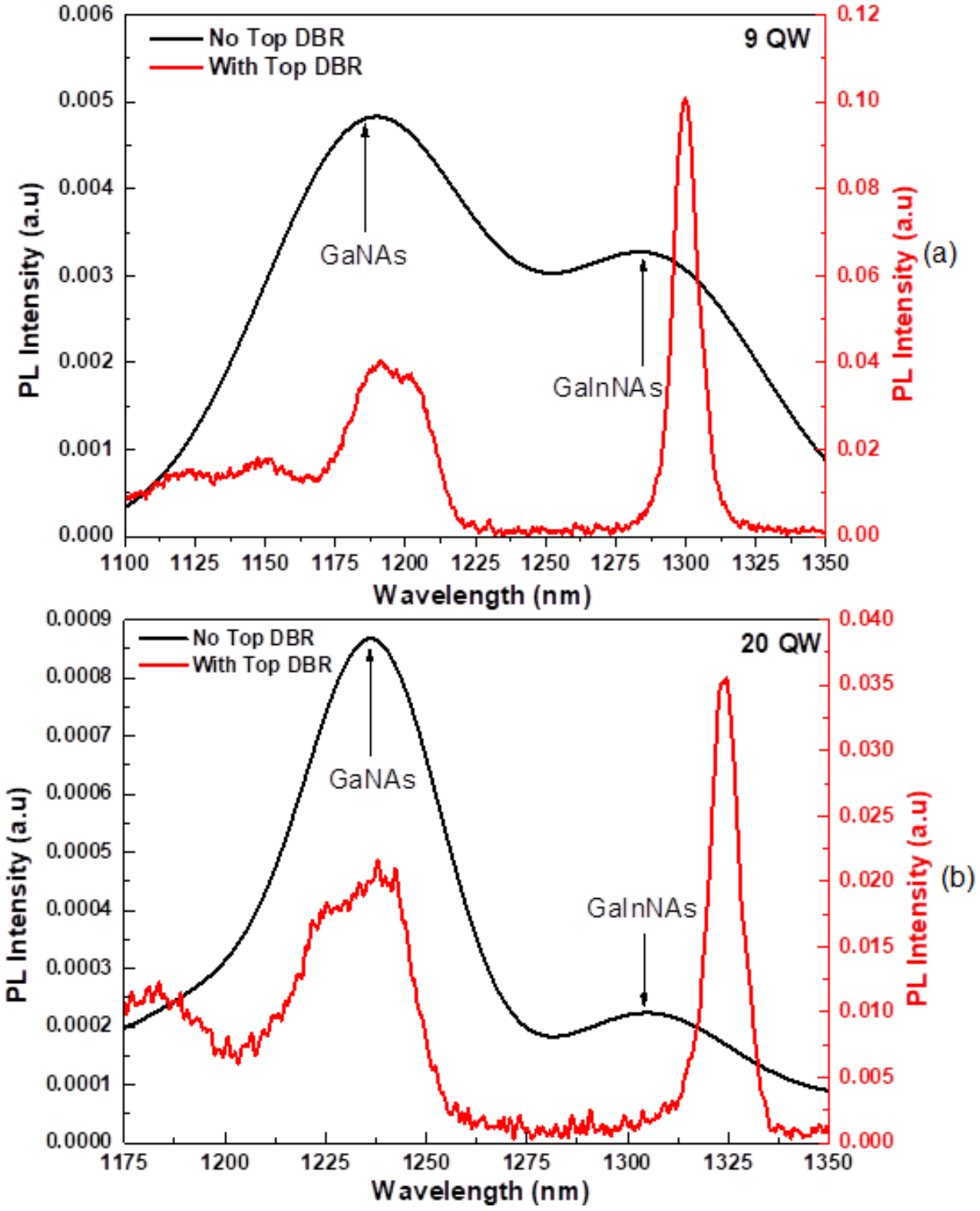

Figure 5.35: 300K PL with top DBR (red) and without top DBR (black) for (a) 9QWs and (b) 20QWs

It can seen from Fig.5.35 that the bandgaps of GaNAs and GaInNAs are close to one other. The calculated well barrier energy for the 9 QW sample is 64.62meV and is 42.38meV for the 20 QW sample. This proves that both samples are going to experience a weak confinement of electron in the GaInNAs QWs. It means that the performance of the 20 QW sample is expected to be lower than that of the 9 QW sample due to QW confinement and the aforementioned mismatch problem.

The photocurrent was measured with temperature dependence as a function of wavelength by using a tuneable laser with a wavelength, λ range between 1.285μm and 1.335μm. Incident light was coupled into an optical fibre and aligned onto the optical window of the photodetector with the help of an infrared camera. The micro-cavity resonance effect is clear even when it is recorded under very low reverse bias of -0.2V for the 9 QW sample and -0.15V for the 20 QW sample. The spectral responsivity of both samples under 116μW incident power is obtained from the spectral photocurrent measurements and plotted in Fig.5.36. The pattern of the responsivity of both samples is similar with the modelling results described in chapter 3. The peak responsivity at T=300K is 1.47 A/W at 1.301μm for the 9 QW sample and 0.76 A/W at 1.322μm for the 20 QW sample. The maximum responsivity, (achieved when the cavity resonance is overlapped with the absorption peak of GaInNAs) of 1.74 A/W (1.302μm) is observed at T=310K for the 9 QW sample and 1.13 A/W (1.325μm) for the 20 QW sample at T=315K. The observed enhancement in the responsivity with increasing temperature is due to a better match between the active region of the GaInNAs-based absorption layer and the cavity resonance wavelength of the DBR stack at the expense of the temperature-induced broadening of the FWHM of response of the samples. The FWHM for the 9 QW sample expanded from 4.1nm (T=290K) to 5.9nm (T=320K) and 2.7nm (T=290K) to 5nm (T=320K) for the 20 QW sample. The maximum responsivity of both samples however is significantly larger than 1, possibly due to the presence of an avalanche carrier multiplication effect.

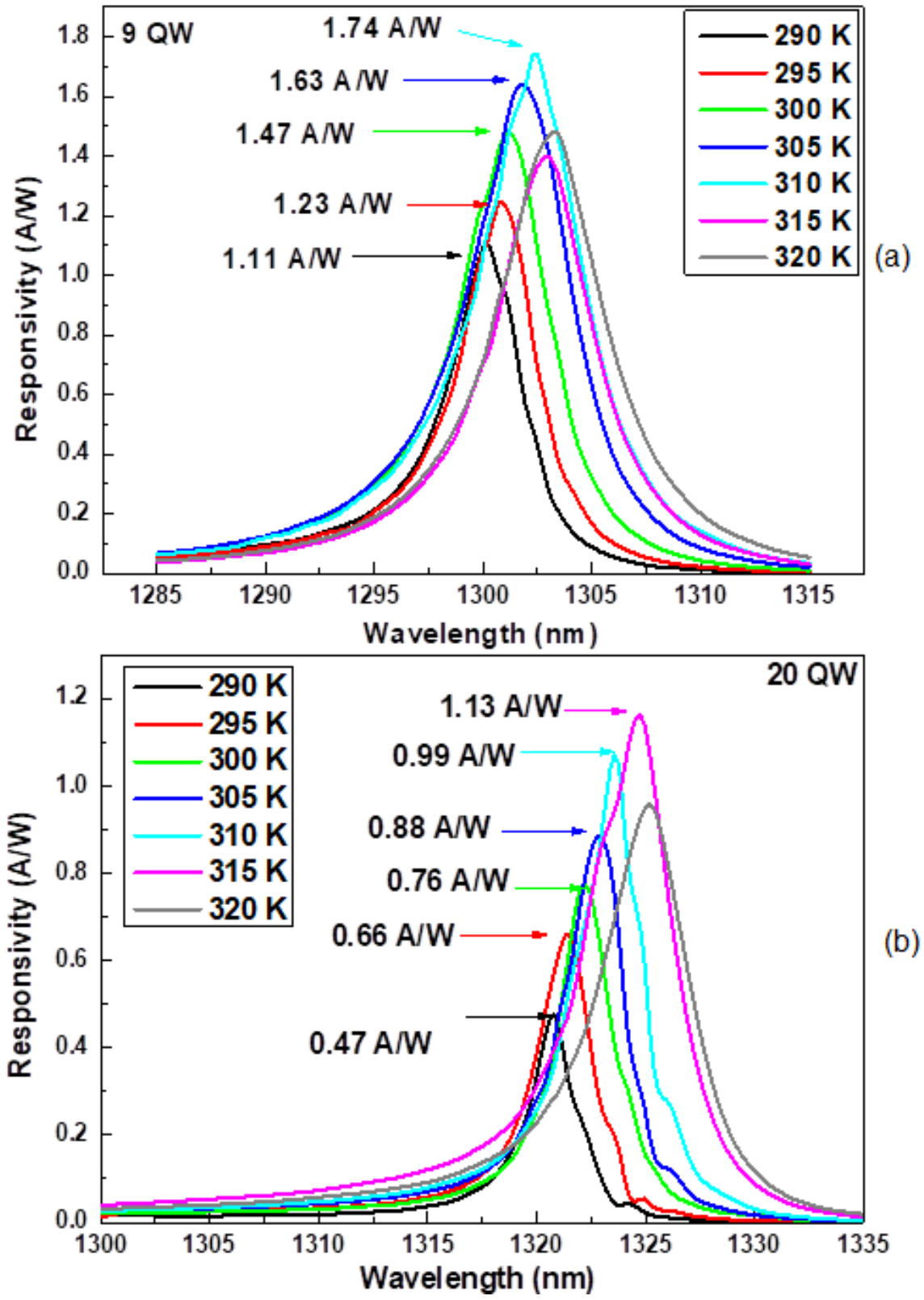

Figure 5.36: Temperature dependence responsivity under light power of 116μW for (a) 9QW at 0.2V and (b) 20QW at 0.15V

The effects of the incident optical power could be explained if the sample is producing gain or reaches the saturation point. It can be seen in Fig.5.37(a), when a reverse bias of -0.1V is applied to the 9 QW sample, the photocurrent slope shows a slightly positive increment that represents a gain behaviour. However, the photocurrent of the 20 QW sample is seen to reach saturation level after 83μW of optical power even at same applied bias as shown in Fig.5.37(b) and will also be different if a higher temperature operation is applied.

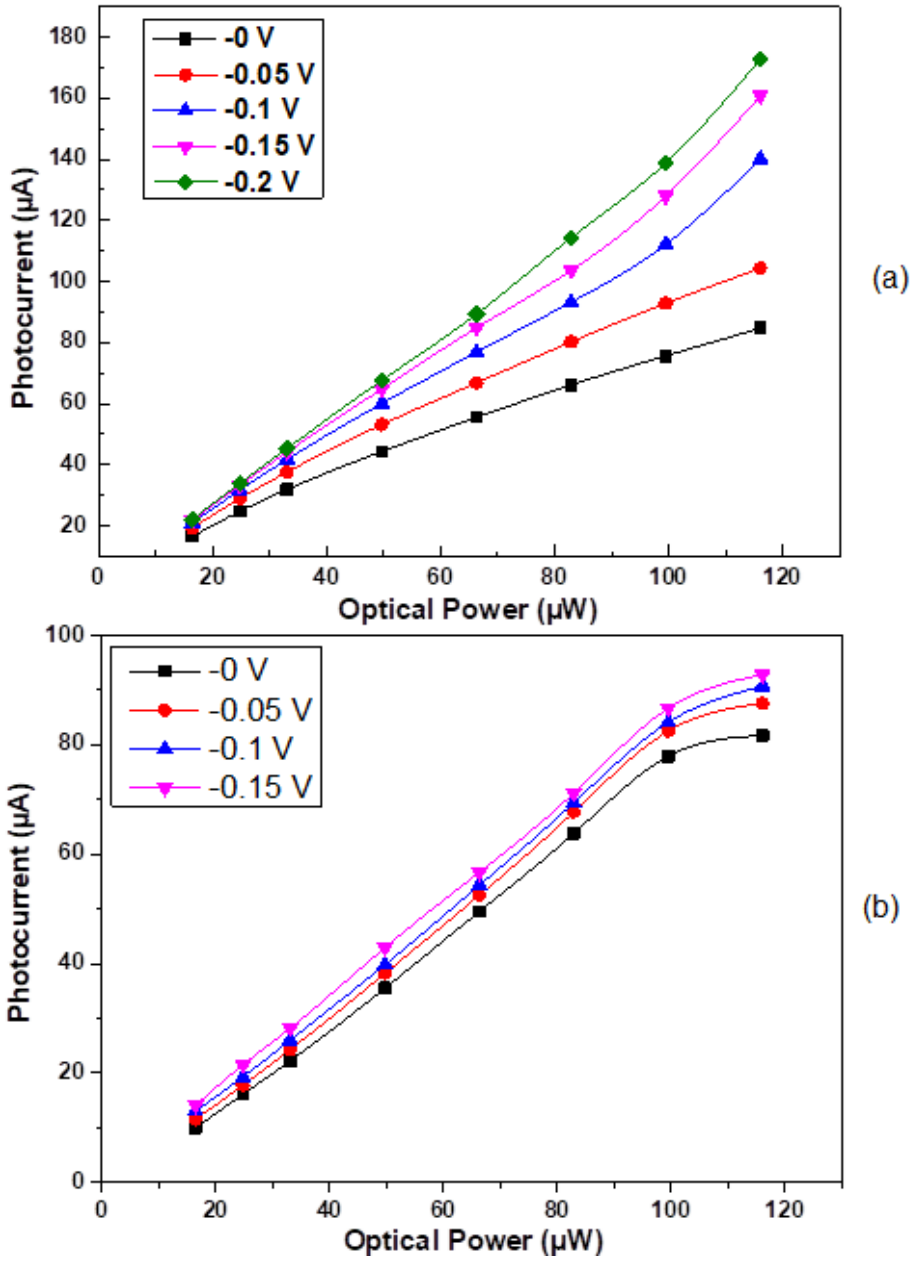

Figure 5.37: Photocurrent of optical power dependence for (a) 9 QWs and (b) 20 QWs

The effects of temperature on the spectral response of the DBRs is calculated using the model proposed by Dudley [61] where the shift in the centre wavelength with temperature ($d\lambda/dT$) can be determined. The calculated result is compared with the experimental result obtained from the photocurrent measurements. The model includes both the thermal effect on the refractive index and the change in thickness of each layer due to the temperature variation using thermal expansion coefficients for each the material. Dudley *et al.* used the modified single effective oscillator (SEO) model proposed by Afromowitz [62]. In this model, the refractive index below the band edge is given by,

$$\boldsymbol{n = \sqrt{\frac{E_d}{E_0} + E_{ph}^2 \frac{E_d}{E_0^3} + \frac{E^4 E_d}{2E_0^3(E_0^2 - E_g^2)} ln\left[\frac{2E_0^2 - E_g^2 - E_{ph}^2}{E_g^2 - E_{ph}^2}\right]}} \qquad (6.15)$$

where E_0 and E_d are the oscillator energy and strength from the SEO model, E_g is the bandgap of the semiconductor and E_{ph} is the photon energy. In order to obtain temperature dependence of the refractive index, the derivative of Eq.6.15 is taken with respect to temperature by considering the shift of the bandgap and the oscillator energies:

$$\boldsymbol{\frac{\partial n}{\partial T} = \frac{\partial n}{\partial E_g} \frac{\partial E_g}{\partial T} + \frac{\partial n}{\partial E_0} \frac{\partial E_0}{\partial T}} \qquad (6.16)$$

Taking into consideration both thermal expansion and temperature induced change in the refractive index, the temperature dependence of the cavity wavelength is expressed as

$$\boldsymbol{\frac{\partial \lambda}{\partial T} = \frac{\left\{n_1 \alpha_1 d_1 + n_2 \alpha_2 d_2 + d_1 \frac{\partial n_1}{\partial T} + d_2 \frac{\partial n_2}{\partial T}\right\}}{\left\{\frac{1}{2} - d_1 \frac{\partial n_1}{\partial \lambda} - d_2 \frac{\partial n_2}{\partial \lambda}\right\}}} \qquad (6.17)$$

where n_1 and n_2 are the refractive index of layers with the thickness d_1 and d_2 respectively, and λ is the designed cavity wavelength of the structure. The parameters used in the calculations are given in Table 5.7. Eq.6.17 is included in the transfer-matrix method (TMM) for calculation of the reflectance spectrum. Fig.5.38 shows the temperature dependence of the calculated and the measured cavity wavelengths. The temperature dependence of the centre wavelength obtained

from the slopes of the measured photocurrent point are 0.11nm/°C for 9 QW and 0.15nm/°C for 20 QW and 0.080 nm/°C respectively.

Table 5.7: Parameters used in the calculations.

	GaAs	AlAs	Reference
n	3.4	2.9	[63]
$\boldsymbol{\alpha}$ **(10^{-6}/°C)**	6.86	4.9	[64]
$\boldsymbol{E_g}$ **(eV)**	1.424	2.16	[65]
$\boldsymbol{E_0}$ **(eV)**	3.65	4.70	[62]
$\boldsymbol{E_d}$ **(eV)**	36.1	33.65	[62]
$\boldsymbol{\partial E_g/\partial T}$**(10^{-4}eV/°C)**	3.9	5.2	[19]
$\boldsymbol{\partial E_O/\partial T}$**(10^{-4}eV/°C)**	5.2	6.9	[66]

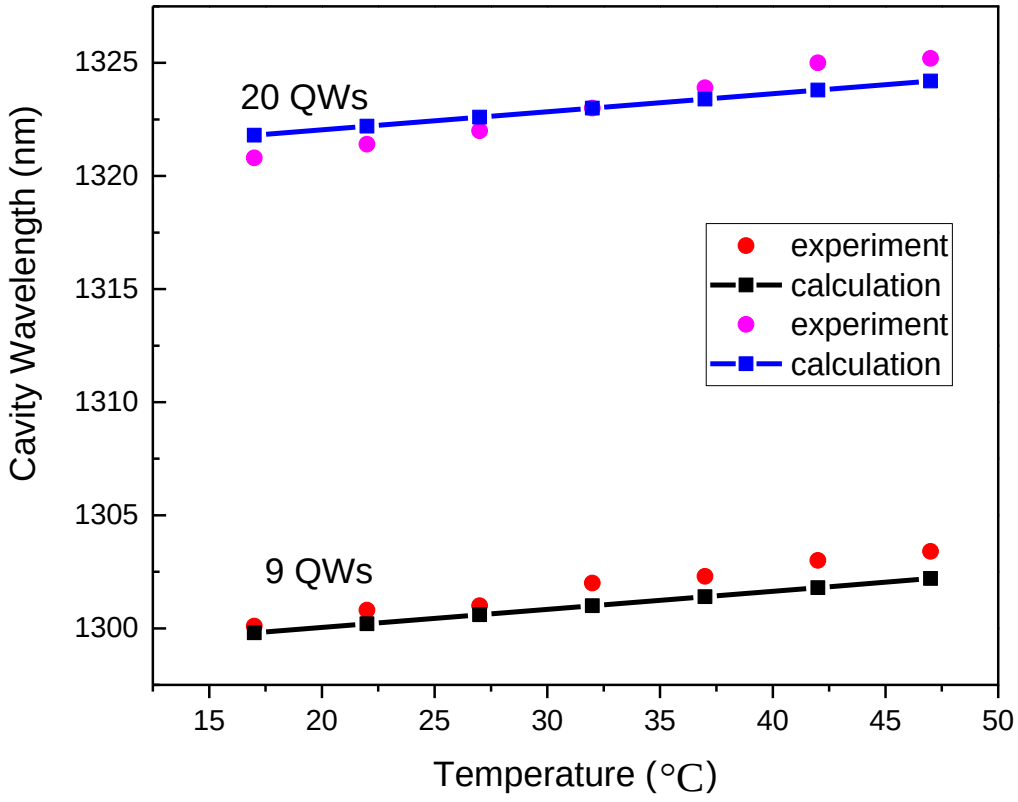

Figure 5.38: Temperature dependence of calculated and measured cavity resonance wavelength of the device.

Fig.5.39 shows the I-V characteristic of both samples in the dark between 290K and 320K. The dark current of both samples are observed to be slightly higher than the previous sample even at room temperature. At T=300K, the dark current of the 9 QW sample is 4.08µA at –0.5 V, increasing to 60.82 µA at –2V, and for the 20 QW sample the dark current is 2.29 µA at

-0.1V, increasing to 138μA at –0.8V. As the bandgaps of GaNAs and GaInNAs are close to one another, this explains the observed high dark current for both samples due to the weak confinement of the electrons in the GaInNAs QWs. As temperature is increased, electrons gain more thermal energy to escape from the QWs *via* thermionic emission over the low conduction band offset of GaNAs barrier layer, giving rise to increase dark current. The dark current of the 9 QW sample is increased from 41.73μA at T=290K to 132μA at T=320K and from 132μA at T=290K to 153μA at T=320K for the 20 QW sample. Due to the doubling of the number of QWs, the leakage current behaviour is also affected as shown in Fig.5.39(b).

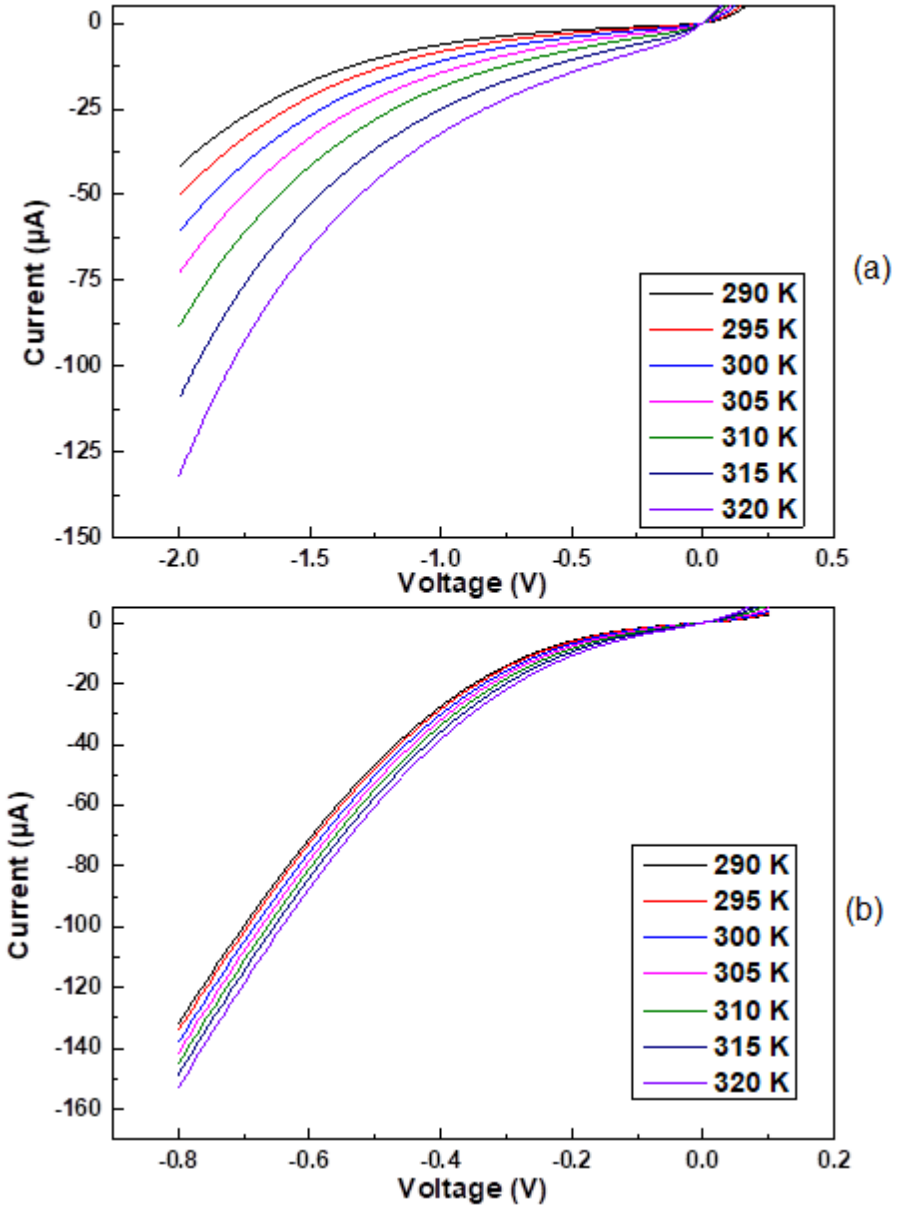

Figure 5.39: Dark I-V characteristic of temperature dependence for (a) 9 QWS and (b) 20QWs

The I-V characteristic of the 9 QW sample at T=300K was measured at incident optical powers from 16µW to 600µW as depicted in Fig.5.40. At low incident optical power, there is an Ohmic behaviour where the photocurrent increases linearly with the applied bias and the photocurrent has a linear dependence on the optical power, and thus on the photo-generated carrier density. At lower biases (less than -0.5V) and under high optical power illumination, there is a massive increase of the photocurrent with bias, followed by a tendency towards current saturation. The current is measured to be 83.47µA at 16µW optical power and increased to 852.85µA at 600µW with a bias of -2V.

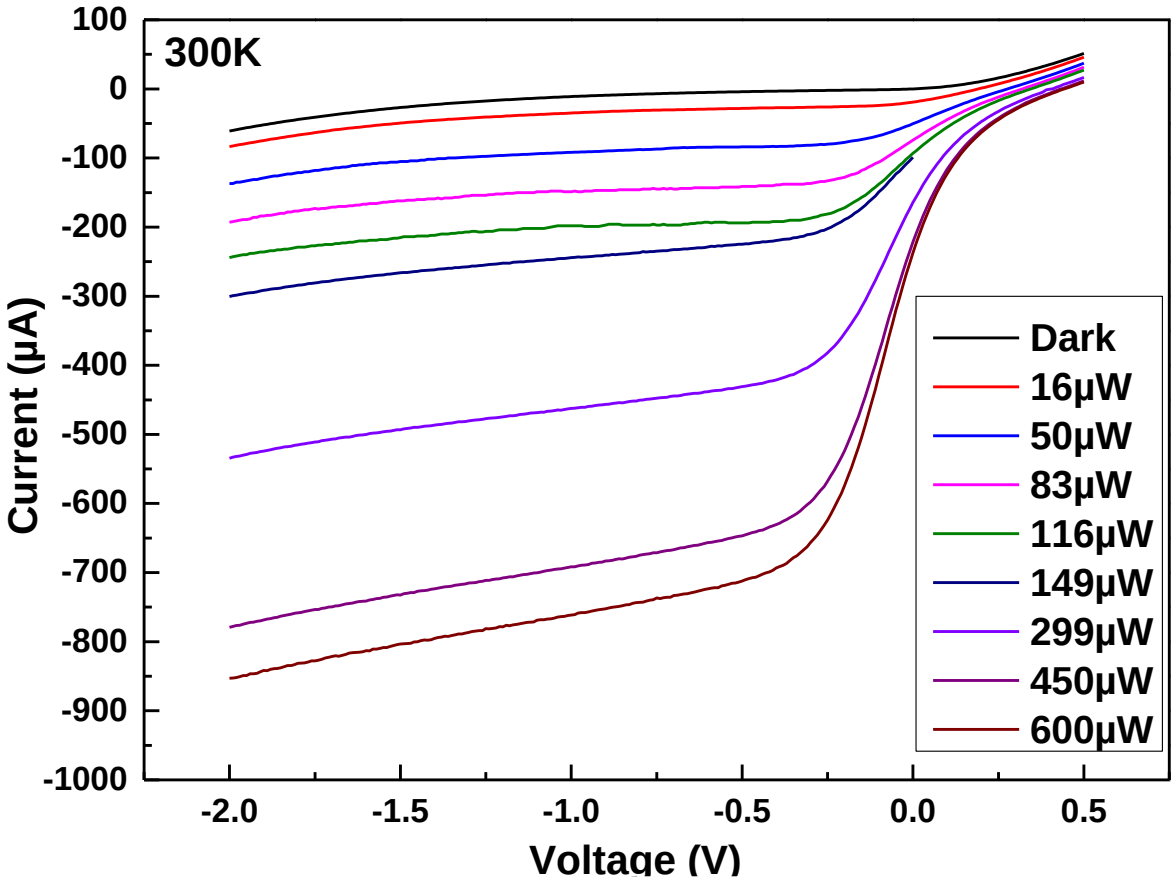

Figure 5.40: I-V characteristic under various incident optical powers for 9QW at T=300K

A high multiplication occurred between 0V and -0.5V. This phenomena exhibits a high carrier multiplication factor at average electric field strengths of less than 100kV/cm. This electric field strength is surprisingly too low to initiate a carrier avalanche process. Normally, the GaAs-based photodetectors only show carrier multiplication at electric field strengths higher

than ~200kV/cm [80-81]. This suggests that the GaInNAs used in this sample has a high impact ionisation coefficient which provides the beginning of a carrier avalanche process at low electric field. The phenomenon could be explained by the existence of mid-gap As antisite defects (As_{Ga}) in the material that has been grown at low temperature. It is known that dilute nitride materials contain As_{Ga} defects [23, 67] when they are grown at low temperature of less than 500^{o}C. In this thesis, the GaInNAs layers in all the samples are grown at 350^{o}C and consequently has the highest concentration of As_{Ga} defects. The As_{Ga} defects helps to initialize the impact ionisation process at a lower electric field. The concentration of the As_{Ga} defects increases in response to the decrease in the growth temperature of the dilute nitride material [67].

Generally, carriers in a p-n junction require an energy of $3E_g/2$ to initiate impact ionisation and thus an avalanche process [68-70]. E_g is the bandgap energy of the material. Mid-gap defects such as As_{Ga} are reported [71] to enhance the impact ionisation process by lowering the energy required in the impact ionisation process. The impact ionisation process assisted by the mid-gap defects only requires energy less than $E_g/2$ [71]. The existence of these mid-gap defects enables a more efficient impact ionisation and carrier multiplication process at a lower electric field by lowering the required energy. This shows that the 9 QW sample contains more As_{Ga} defects and thus have higher carrier multiplication. As can be seen from Fig5.40, the multiplication behaviour occurred between 0V to -0.5V and the current tends to saturate after a bias of -0.5V. An overall of 0.5V is equivalent to 500meV which represents half the bandgap energy of the GaInNAs (around 483meV) and correlate to the As_{Ga} mid-gap defect level.

However, for 20 QW sample, there is no multiplication pattern similar to the 9 QW sample observed, as can be seen in Fig.5.41. This could be due to the mismatch problem which causes the absorption degradation and weak confinement of electron in the QW as previously explained. As can be seen in Fig5.41, the small deviation from the Ohmic behaviour occurred at around V~ -0.1V and a sub-linear dependence of the photocurrent on the applied bias is observed

as expected from the mobility reduction due to the hot carrier effects at high electric fields. At higher biases, there is a tendency towards current saturation followed by a gradual increase of the photocurrent with bias. At applied voltages of more than -0.25V under an optical power of 116μW, the current starts to increase with bias super linearly, indicative of carrier multiplication. At this bias, even after considering a non-uniformly distributed electric field in the depletion region, the maximum electric field strength is less than 100kV/cm owing to the As_{Ga} mid-gap defect level as initiation of a carrier avalanche process at low electric field. Therefore, at biases of V≥-0.25V, the 20 QW sample operates with an internal gain of ~1.1 giving an overall responsivity of ~0.7A/W at T=300K.

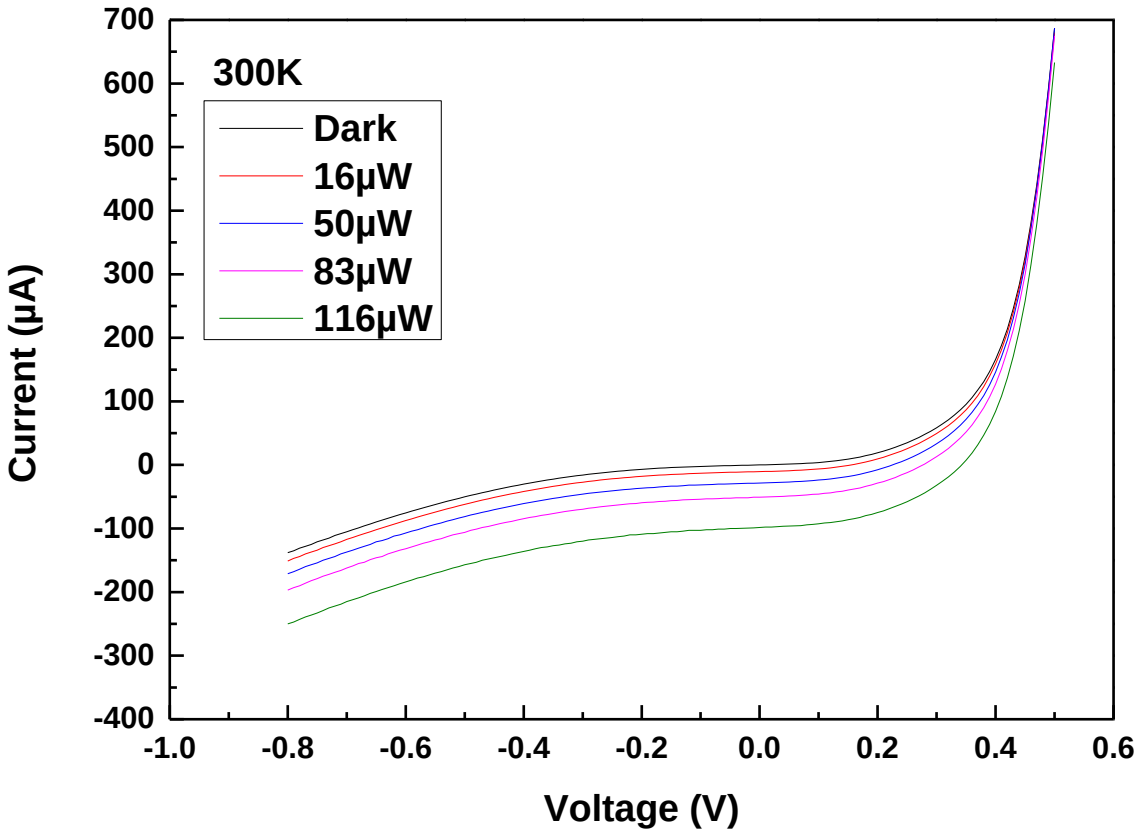

Figure 5.41: I-V characteristic under various incident optical powers for 20QW at T=300K

Both samples are then compared for room temperature operation. The maximum responsivity for the 9 QW sample is observed to be 1.63A/W with an internal gain of 2.45 at an applied bias of -2V under an incident optical power of 149μW as shown in Fig.5.42(a). While the maximum responsivity is found to be 0.96A/W with an internal gain of 1.14 at an applied

bias of -0.8V for the 20 QW sample under an incident optical power of 116μW as shown in Fig.5.42(b).

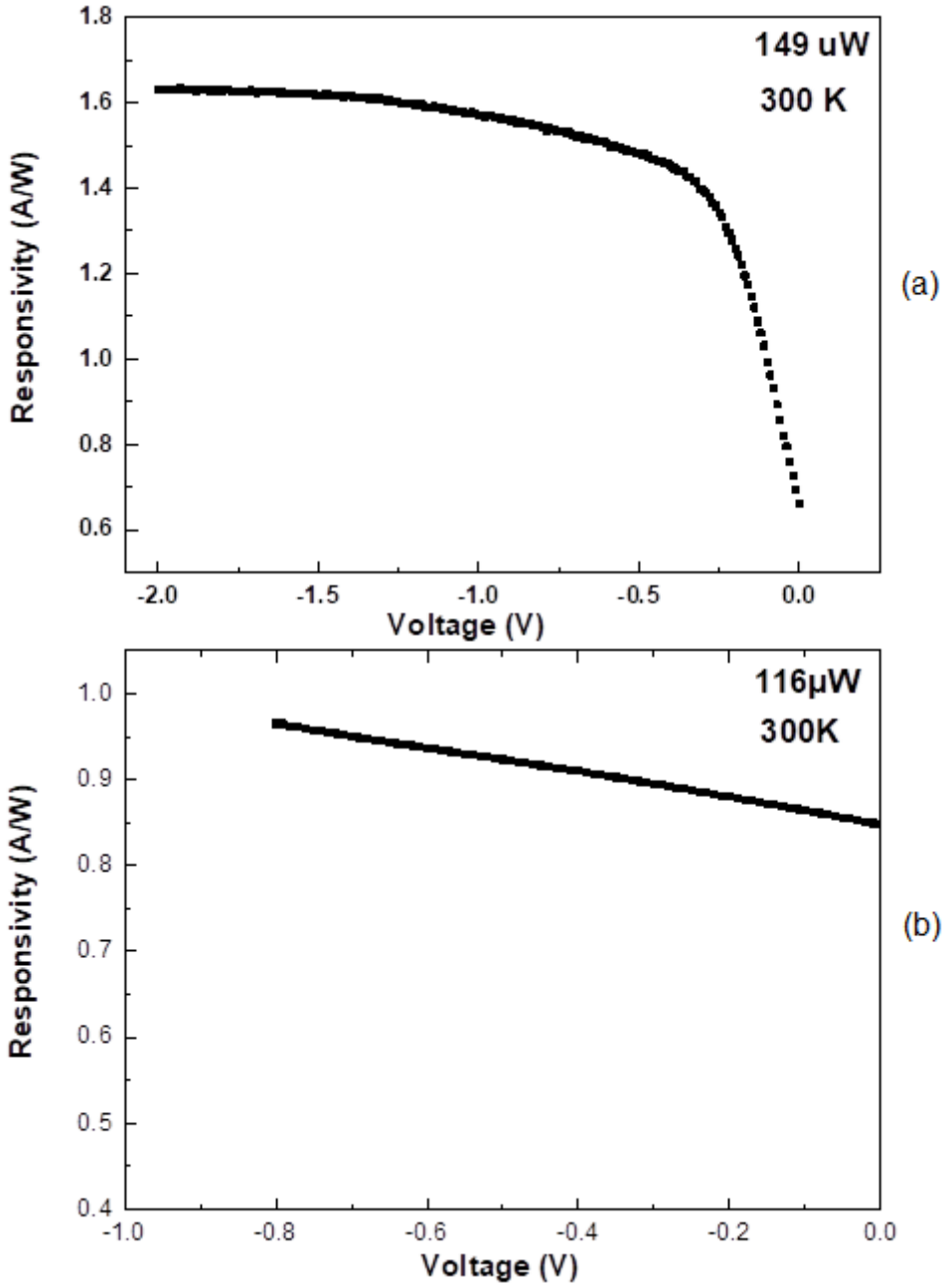

Figure 5.42: 300K bias dependence of responsivity for (a) 9 QWs and (b) 20 QWs

However, under high optical powers, the responsivity of 9 QW sample degrades due to heating problem. Its responsivity is decreased to 1.33A/W under an optical power of 600μW at V=-2V, although the internal gain increases to 3.34, as depicted in Fig5.43. The internal gain seems to reach saturation point above 500μW optical power due to the reduction of the

responsivity. Hence, a proper cooling system is needed if the sample needs to be operated under a high optical power. However, a small range of temperature dependence under constant lower optical power and voltage bias can be the alternative way to improve gain performance as shown in Fig.5.44.

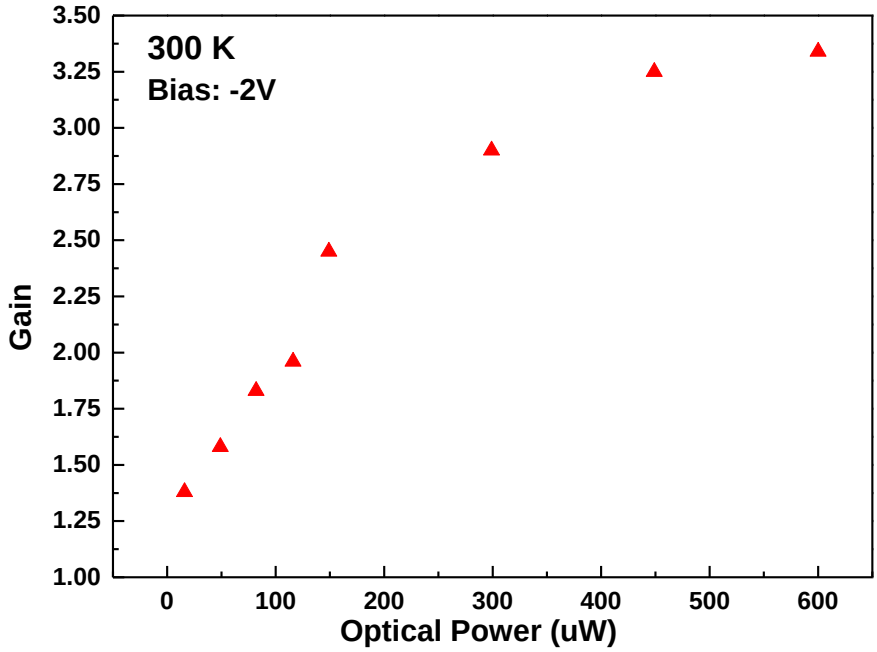

Figure 5.43: An optical power dependence of gain under V=-2V for 9 QWs sample at T=300K

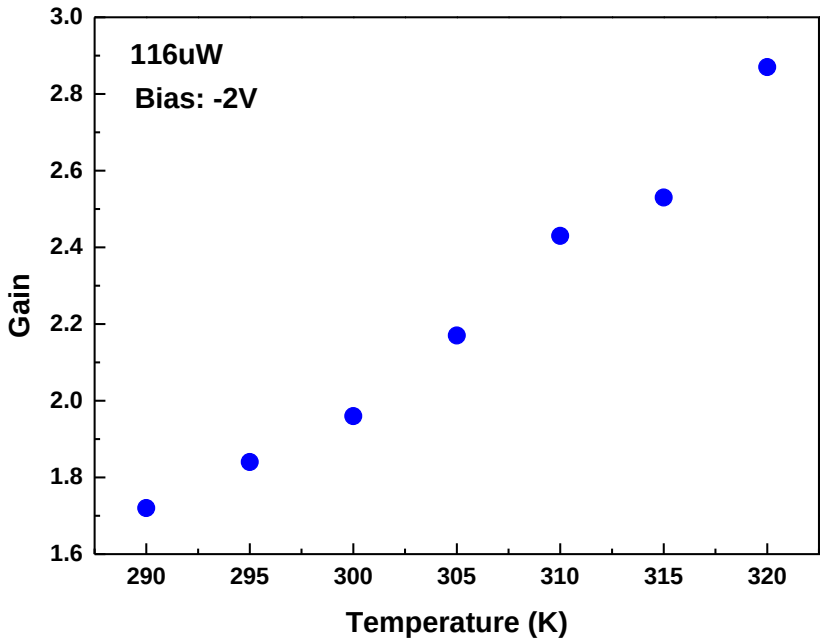

Figure 5.44: Temperature dependence of gain for 9 QWs sample under constant applied bias and optical power.

The TPC response measurements where saturation occurred at 50K and 300K for an applied bias of -6V are plotted in Fig.5.45. These plots show that the peak TPC signal increased with increasing temperature and number of QWs. Fig.5.46 clearly shows the temperature-dependent increase of the peak amplitude of the TPC signal under a -6V constant bias. The 20 QW sample have greater peak amplitude because of the higher absorption in the active layer compared to the 9 QW sample.

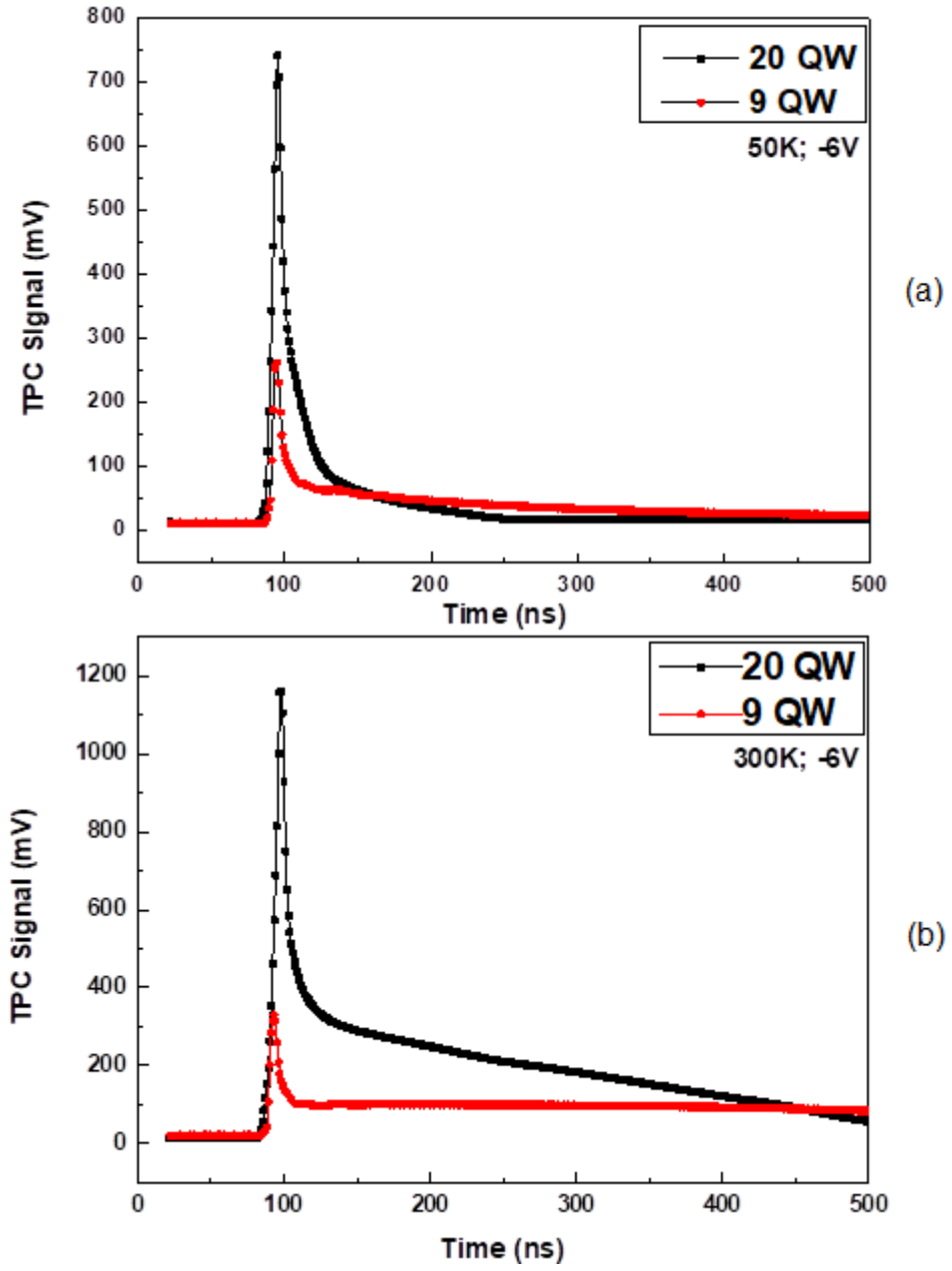

Figure 5.45: Transient photoconductivity response of 9 and 20 QWs at (a) 50K and (b) 300K

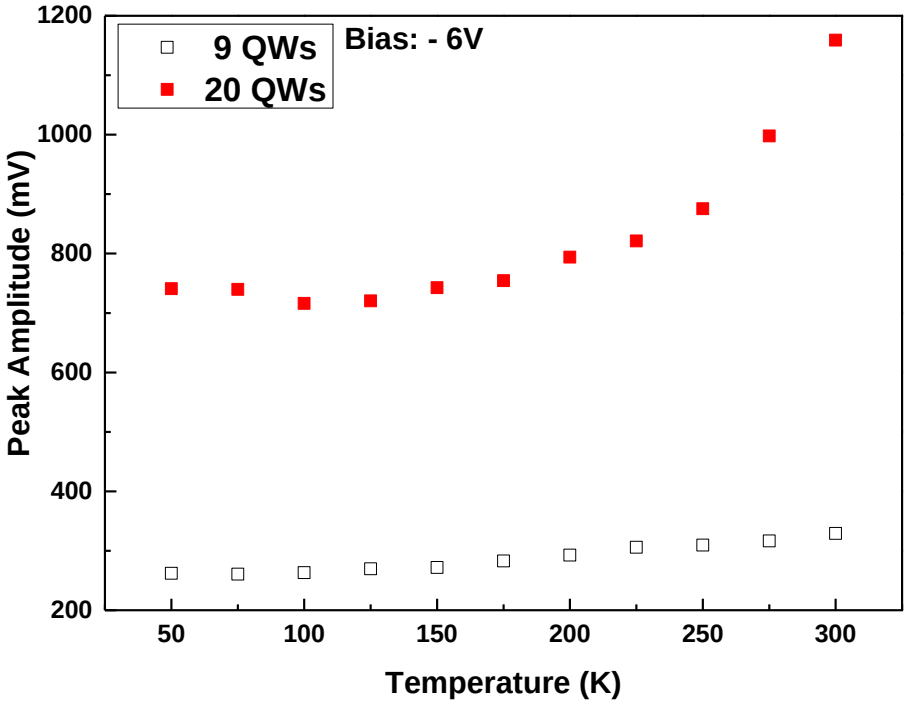

Figure 5.46: Temperature dependent of TPC peak amplitude

The TPC peak amplitude between T=50 K and T=300 K as a function of applied voltage is depicted in Fig.5.47(a). There is a clear linear dependence at low reverse bias followed by a super linear dependence at V≥-3V for both samples indicating internal gain. The electron-hole pairs in the device may be relegated as a band-band process or band-trap process depending on whether the second carrier is initially in the valence band and makes a transition from the valence band to the conduction band, although it might also be initiated at a localized level (trap, donor, acceptor), forming a transition to a band state [49]. In the latter, with the kinetic energy of the electrons in the conduction band exceeds the threshold energy for impact ionisation and can therefore stimulate an electron from the valence band via the Coulomb interaction. This will cause the electron to be knocked into the conduction band leaving a hole in the valence band. The result of this process is called carrier multiplication and explains the refers of the carrier conductance (dI/dV) at -5V for the 9 QW sample and -2V for the 20 QW sample as depicted in Fig.5.47(b). This process leads to two electrons in the conduction band and one hole in the valence band, which may induce electrical instabilities at high electric fields. The threshold

energy for impact ionisation is determined by the size of the forbidden energy gap, energy conservation, momentum conservation, and details of the band structure. The hot electrons will lose most of their energy through the creation of other charge carriers to gain kinetic energy from the field. This behaviour is the same as reported in the previous section on the same DBR structures, but with a different window aperture diameter.

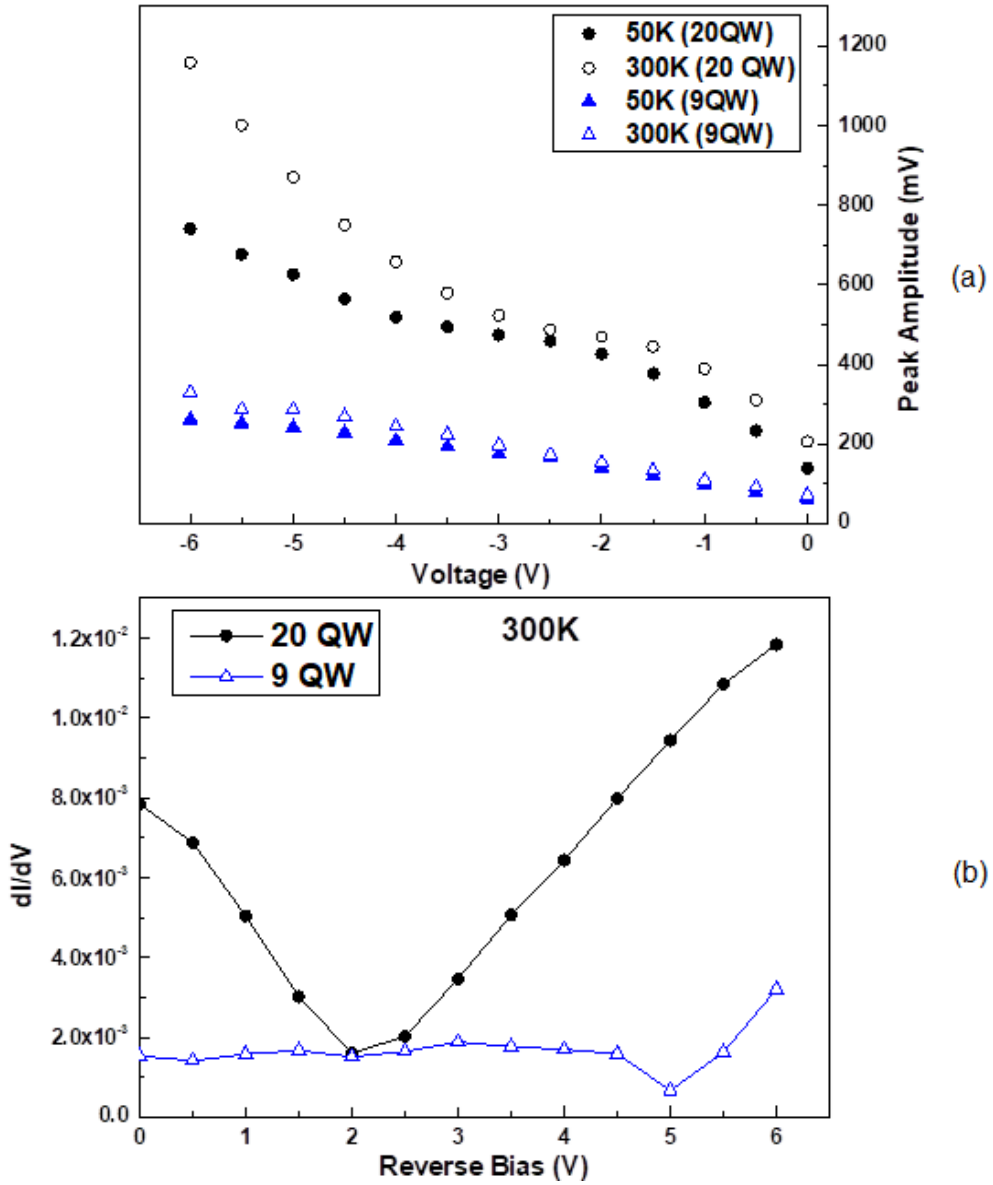

Figure 5.47: (a) TPC peak amplitude as a function of applied voltage (b) Current-voltage derivative *versus* bias voltage.

An overall TPC decay due to the band-to-band recombination process has a fast component with a time constant $\tau_1 \approx 3.5$ns for the 9 QW sample and $\tau_1 \approx 5$ns for the 20 QW

sample. This agrees with the value obtained for the GaInNAs-based photodetector reported in the previous section. The decay time then is followed by a relatively slower decay with time constants $\tau_2 \approx 151.8$ns for the 9 QW and $\tau_2 \approx 505$ns for the 20 QW at 50K that can be associated with the existence of traps in the quantum wells. At room temperature, the decay time for the 9 QW sample only has a fast component time constant of 5ns while the decay time constants observed for the 20 QW sample are $\tau_1 \approx 5$ns and $\tau_2 \approx 34$ns as shown in Fig5.48(a). The TPC rise time is decreased from 3.59ns at T=50K to 2.74ns at T=300K for the 9 QW sample and from 8.8ns at T=50K to 6.4ns at T=300K for the 20 QW sample as depicted in Fig.5.48(b). No significant bias dependence was observed for both the rise and decay times.

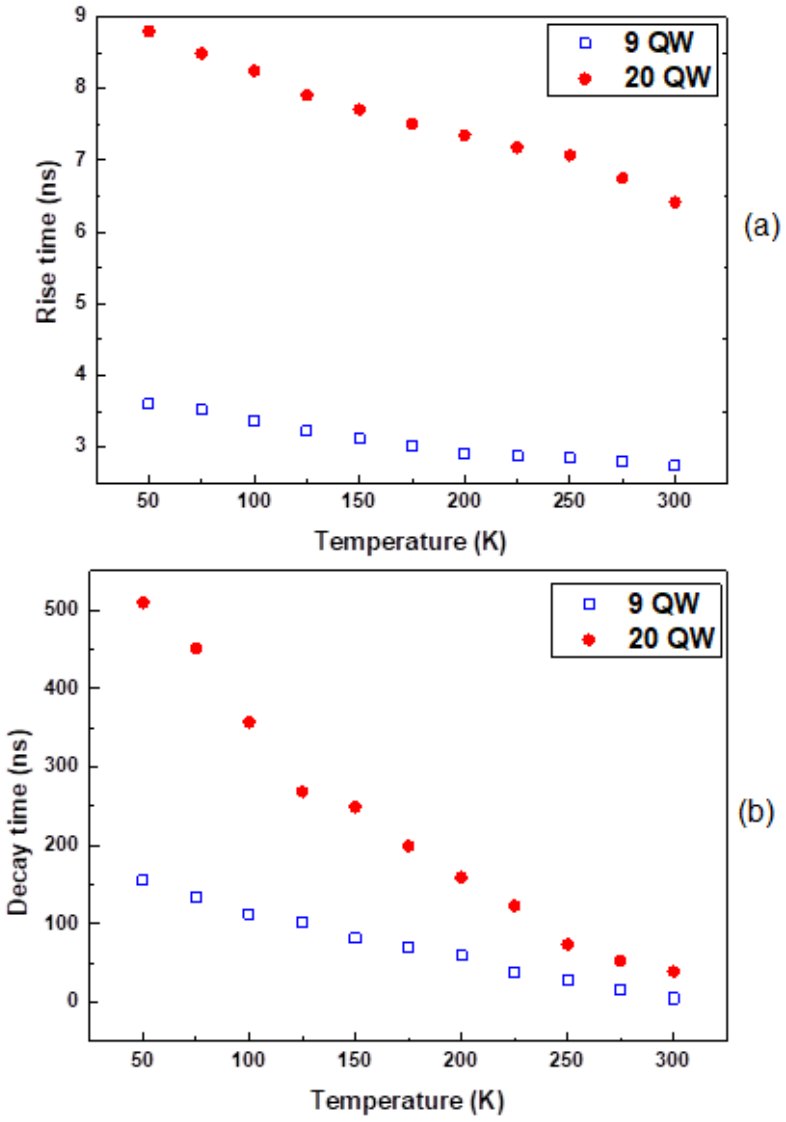

Figure 5.48: Temperature dependent of rise and decay time at reverse bias of 6V

This behaviour can be explained as a form of mismatch between the absorption peak of the sample and the cavity resonance for the designed operating temperature as discussed previously. A higher number of QW in the intrinsic region will increase the resistance and traps in the QW for the 20 QW sample thus affecting its response time, as compared to the 9 QW sample. The room temperature bandwidths of both samples are found to be 128MHz for the 9 QW sample and 55MHz for the 20 QW sample. In Fig.5.49, it is clearly shown that the TPC amplitude saturates as the excess carrier density increases after the linear increase at low excitation intensity. This behaviour can be explained by sub-band, well-filling and transparency effects in addition to the dependence of mobility on carrier density as discussed in the previous section.

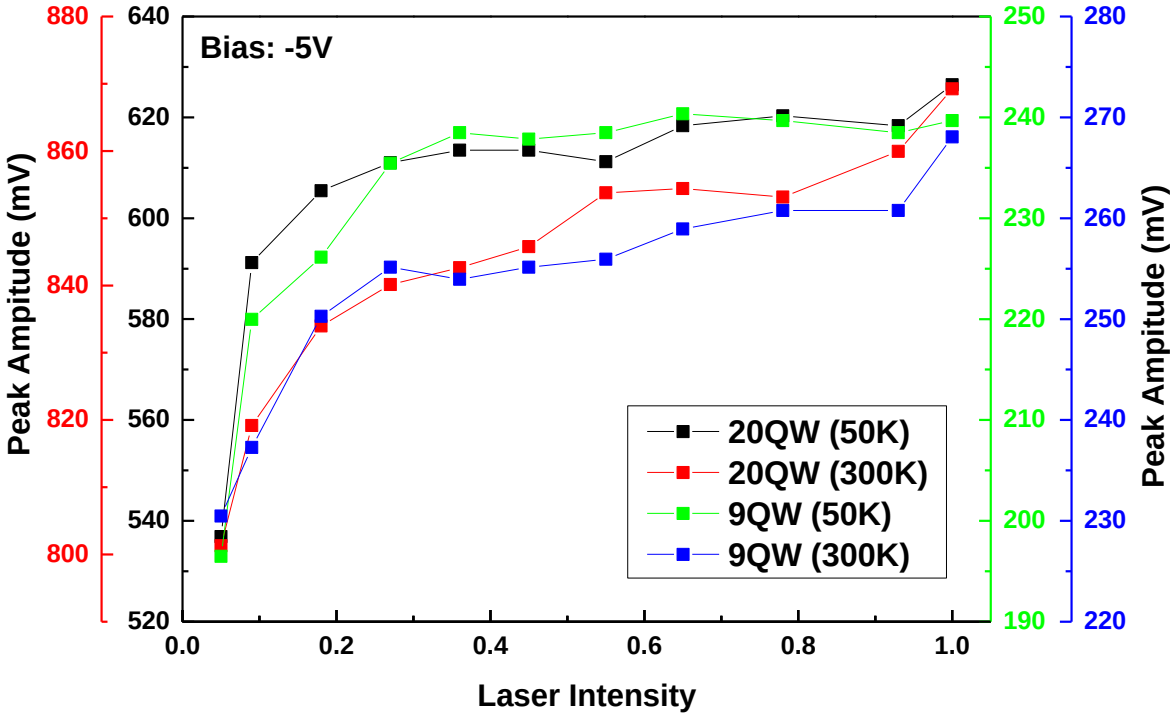

Figure 5.49: TPC peak amplitude as a function of incident laser intensity at a reverse bias of 5V

The resulting *D** and NEP of both samples at the different temperatures are depicted in Fig.5.49. The maximum *D** of the sample of photodetectors are $1.39\times10^{11} cm\sqrt{Hz}/W$ and $3.58\times10^{11} cm\sqrt{Hz}/W$, while the minimum NEP is $2.06\times10^{-11} W/\sqrt{Hz}$ and $8\times10^{-12} W/\sqrt{Hz}$ for the 9 QW and the 20 QW samples respectively. These results are comparable to the performance

of the other previous samples and commercial photodetectors characteristics discussed in this chapter, which revealing a sensitive photodetector with high quality and low-noise at T=300K.

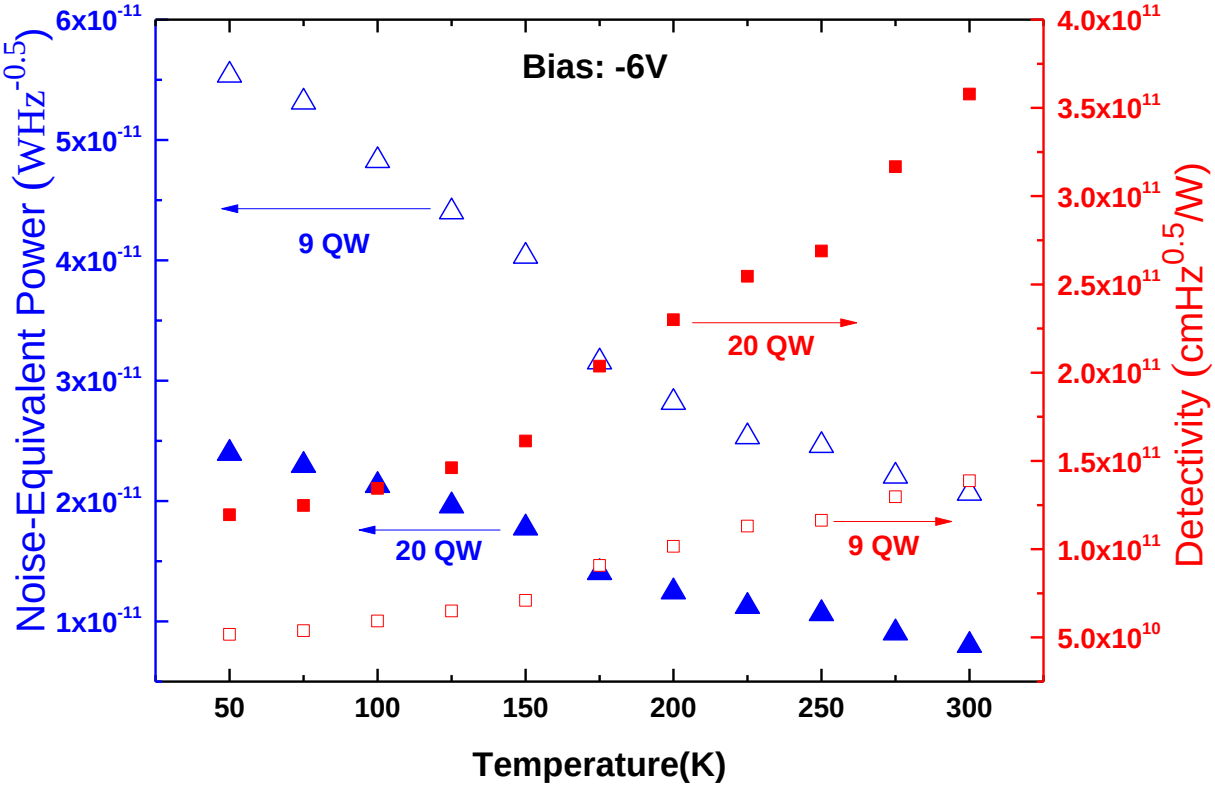

Figure 5.43: NEP and Detectivity as a function of temperature at reverse bias of 6V

5.5.1 Summary

A vertical cavity enhanced photodetector based on a dilute nitride GaInNAs/GaNAs multi- quantum-well structure operating near 1.3μm has been demonstrated for two different numbers of QW. A GaNAs material has been used as the QW barrier layer to compensate the strain in between the GaInNAs QW but will weaken the confinement of electrons in GaInNAs QW. PL measurements were performed on structures with and without top DBR to determine any deviation of the optical signal between 50K and 300K. The 9 QW sample has 1.63A/W of responsivity with an internal gain of 2.45, better than the VCE sample performance in the previous section while the responsivity of the 20 QW sample is 0.96A/W with an internal gain of 1.14 at room temperature operation. The observed internal gain can be related to the As_{Ga} mid-

gap defect level that initiate a carrier avalanche process at low electric field. The lower performance of the 20 QW sample is due to the huge mismatch between the active region peak and the cavity resonant peak. While temperature modulation can be used to enhance the characteristic of both samples, it suffers from responsivity degradation due to heating problem. The response time of the 20 QW sample is much slower than the 10 QW sample as a higher number of QW creates higher internal resistance, affecting the bandwidth performance where bandwidth of the 20 QW sample is lower than half of the 10 QW sample. The 20 QW sample produces a lower NEP and better detectivity compared to the 10 QW sample. This shows that when selecting the thickness of the absorption region, the trade-off option between efficiency, speed, bandwidth, NEP and detectivity need to be taken into account.

References

1. M. Henini, Dilute Nitride Semiconductors, Elsevier Science, Amsterdam (2005)
2. A. Erol, Dilute III-V Nitride Semiconductor and Material Systems, 105 Material Science Springer Series Berlin (2008)
3. P. H. Tram, Y. S. Fatt and L. K. Peng, Fabrication and Characterization of Dilute Nitride Indium Antimonide for Long Wavelength Infrared Applications, Chemistry Research and Applications, Novinka, Singapore (2012)
4. G. Ciatto, Hydrogenated Dilute Nitride Semiconductors: Theory, Properties, and Applications, CRC Press, New York, (2015)
5. M. Kondow, K. Uomi, A. Niwa, T. Kitatani, S. Watahiki, and Y. Yazawa, Jpn. J. Appl. Phys., 35, 1273 (1996).
6. M. Weyers, M. Sato, and H. Ando, Jpn. J. Appl. Phys., 31, L853 (1992).
7. K.W.J. Branham, and G. Duggan, J. App. Phys., 67, 3490 (1990).
8. B. Royal, N. Balkan, S. Mazzucato, H.M. Khalil, M. Hugues, and J.S. Roberts, Phys. Status Solidi B, 248, 1191 (2011).
9. G. Kieblich, A. Wacker, E. Scholl, S.A. Vitusevich, A. E. Belayev, S. V. Danylyuk, A. Forster, N. Klein, and M. Henini,, Phys. Rev. B, 68, 125331 (2003).
10. A.E. Belayev, A. Patane, L. Eaves, P.C. Main, M. Henini, and S.V. Danylyuk, Nanotechnology, 12, 515 (2001).
11. U. Prechtel, C. Zeller, G. Abstreiter, and K. Ploog, Phys. Conf. Ser. 74, 5, 339 (1984).
12. L.L. Chang, L. Esaki, and R. Tsu, App. Phy. Lett., 24, 593 (1974).
13. Z. Djuric, and B. Radjenovic, Solid, State, Electronics, 26, 1143 (1983).
14. B.K. Ridley, and P.J. Bishop, IEEE Proc., 138, 294 (1991).
15. P.J. Bishop, and B.K. Ridley, Semicond. Sci. Technol., 7, 498 (1992).
16. H.M. Khalil S. Mazzucato and N.Balkan, Physica Satus Solidi C, 10, 4 (2013)
17. Q. Han, X. H. Yang, Z. C. Niu, H. Q. Ni, Y. Q. Xu, S. Y. Zhang, Y. Du, L.H. Peng, H. Zhao, C. Z. Tong, R. H. Wu, and Q. M. Wang, Applied Physics Letters, 87, 111105 (2005)
18. H. Luo, J. A. Gupta, and H. C. Liu, Applied Physics Letters, 86, 211121 (2005)
19. E. Luna, M. Hopkinson, J. M. Ulloa, A. Guzman, and E. Munoz, Applied Physics Letters, 83, 3111 (2003)
20. S. Wicaksono, S. F. Yoon, W. K. Loke, K. H. Tan, K. L. Lew, M. Zegaoui, J.P. Vilcot, D. Decoster, and J. Chazelas, Journal of Applied Physics, 102, 044505 (2007)

21. S. Wicaksono, S. F. Yoon, W. K. Loke, K. H. Tan, and B. K. Ng, Journal of Applied Physics, 99, 104502 (2006)
22. K. H. Tan, S. F. Yoon, W. K. Loke, S. Wicaksono, K. L. Lew, A. Stohr, O. Ecin, A. Poloczek, A. Malcoci, and D. Jager, Applied Physics Letters, 90, 183515 (2007)
23. W. K. Loke, S. F. Yoon, K. H. Tan, S. Wicaksono, and W. J. Fan, Journal of Applied Physics, 101, 33122 (2007)
24. W. K. Cheah, W. J. Fan, S. F. Yoon, D. H. Zhang, B. K. Ng, W. K. Loke, R. Liu, and A. T. S. Wee, IEEE Photonics Technology Letters, 17, 1932 (2005)
25. W. K. Loke, S. F. Yoon, S. Wicaksono, and B. K. Ng, Materials Science and Engineering: B, 131, 40 (2006.)
26. J. S. Ng, W. M. Soong, M. J. Steer, M. Hopkinson, J. P. R. David, J. Chamings, S. J. Sweeney, and A. R. Adams, " Journal of Applied Physics, 101, 64506 (2007)
27. S.H. Wei, and A. Zunger, Phys. Rev. Lett., 76, 664 (1996)
28. W. Shan, W. Walukiewiez, and J.W. Ager, Phys. Rev. Lett., 82,1221 (1999)
29. L.H. Li, G. Patriarche, and A. Lemaitre, J. Crys. Grow., 251, 403 (2003)
30. F. Ishikawa, A. Guzman, O. Brandt, Journal of Applied Physics, 104, 113502 (2008)
31. S. Mazzucato, R.J. Potter, A. Erol, Physica E, 17C, 242 (2003)
32. B. Royall, PhD thesis, University of Essex (2011)
33. S. Reynolds, C. Main, D.P. Webb, and S. Grabtchak, J. Appl. Phys., 88, 278 (2000)
34. C.K. Sun, P.K.L. Yu, C.T Chang, and D.J. Albares, IEEE J. Selected Topics in Quantum Electron Devices, 39, 2240 (1992)
35. G. Lukovsky, R.F. Schwarz, and R.B. Emmons, J. Appl. Phys., 35, 622 (1964)
36. G. Lukovsky, and R.B. Emmons, Appl. Opti., 4, 697 (1965)
37. J. M. Senior, “Optical Fiber Communications”, Prentice-Hall, International Series in Optoelectronics. Second Edition (1992)
38. H. M. Khalil, N. Balkan, S. Mazzucato, IEEE, Advanced Semiconductor Devices and Microsystems. (2012).
39. Y. Sun, N. Balkan, J. Appl. Phys. 106, 073704 (2009)
40. E. Ozturk, N.C. Constantinou, A. Straw, N. Balkan, B.K. Ridley, D.A. Ritchie, Semicond. Sci. Technol., 9, 782 (1994)
41. L. Gendron, V. Berger, B. Vinter, E. Costard, M. Carras, A. Nedelcu, P. Bois, Semicond. Sci. Technol. 19, 219 (2004)
42. B. K. Ridley, Phys. Rev. B, 41, 12190 (1990).
43. H.M. Khalil. PhD Thesis, University of Essex, (2014).
44. B.G Streetman, J. Appl. Phys., 37, 3137 (1966).
45. P.J. Bishop, M.E. Daniels, B.K. Ridley, E.G. Scott, and G.I. Davies, Semicond. Sci. Technol., 4, 639 (1989).
46. P.J. Bishop, M.E. Daniels, B.K. Ridley, S.J. Bass, and L.L. Taylor, “Photoconductivity measurement of the electron mobility in an electron-hole plasma”, Semicond. Sci. Technol., 6, 631 (1991).
47. B.F. Levine, J. Appl. Phys., 74, R1 (1993)
48. Y.F.Chen, W.C. Chen, R.W. Chuang, Y.K. Su, and H.L. Tsai, Jpn. J. Appl. Phys., 47, 2982 (2008)
49. Y. Sun, PhD theses. University of Essex (2008).
50. F. Sarcan, O. Donmez, M. Gunes, A. Erol, M. C. Arikan, J. Puustinen and M. Guina, Nanoscale Research Letters, 7, 529 (2012)
51. F. Sarcan, O. Donmez, A. Erol, M. Gunes, M. C. Arikan, J. Puustinen and M. Guina, Applied Physics Letters 103, 082121 (2013)
52. J. Wang, J. Hu, P. Becla, A. M. Agarwal and L. C. Kimerling, Optics Express. 18, 2 (2010)
53. M.S. Ünlü, S. Strite, J. Appl. Phys., 78, 607 (1995)
54. M.K. Emsley, O. Dosunmu, M.S. Ünlü, IEEE Photon. Technol. Lett. 14, 519 (2002)
55. K. Kishino, M.S. Ünlü, J. Cyhi, J. Reed, L. Arsenault, H. Morkoc, IEEE J. Quantum Electron. 21, 2025 (1991)
56. Y. Sun, A. Erol, M. Yilmaz, M. C. Arikan, B. Ulug, A. Ulug, N. Balkan, M. Sopanen, O. Reentilä, M. Mattila, C. Fontaine and A. Arnoult, Optical and Quantum Electronics. 40, 7 (2008)
57. Z. Ruikang, Acta Ohoton. Sin. 31, 303 (2002)
58. J.B. Hereoux, X. Yang, W.I. Wang, Appl. Phys. Lett. 75, 2716 (1999)
59. B.E. Foutz, L.F. Eastman, U.V. Bhapkar, M.S. Shur, Appl. Phys. Lett. 70, 2849 (1997)
60. F. Sarcan, M.S. Nordin, F.Kuruoglu, A.Erol and A.J. Vickers, Superlattices and Microstructures, 102 (2017)
61. J.J. Dudley, D.L. Crawford, J.E. Bowers, IEEE Phot. Technol. Lett. 4, 311 (1992)
62. M.A. Afromowitz, Solid State Commun. 15, 59 (1974)
63. J. Talghader, J.S. Smith, Appl. Phys. Lett. 66,335 (1995)

64. V. Swaminathan, A.T. MacRander, Materials Aspects of Gaas and Inp Based Structures, Prentice Hall, 1991.
65. I. Vurgaftman, J.R. Meyer, L.R. Ram-Mohan, J. Appl. Phys. 89, 5815 (2001)
66. P. Lautenschlager, M. Garriga, S. Logothetidis, M. Cardona, Phys. Rev. B 35, 9174 (1987)
67. W. M. Chen, I. A. Buyanova, C. W. Tu, and H. Yonezu, Physica B: Condensed Matter, 376, 545 (2006)
68. W. Shockley, "Problems related to p-n junctions in silicon," Solid-State Electronics, vol. 2, pp. 35-67, 1961.
69. R. A. Logan, A. G. Chynoweth, and B. G. Cohen, Physical Review, 128, 2518 (1962)
70. R. A. Logan and H. G. White, Journal of Applied Physics, 36, 3945 (1965)
71. L. Partain, D. Day, and R. Powell, Journal of Applied Physics, 74, 335 (1993)
72. H. Memmati, Deep Space Optical Communications, John Wiley & Sons, 337 (2006)
73. Y. Sun, M. E. Ali, K. Balemarthy, R. L. Lingle Jr, S. E. Ralph, and B. E. Lemoff, Technical Digest, OTuE2 (2006)
74. H. Venghaus and N. Grote, Fibre Optic Communication: Key Devices, Springer, 91 (2012)
75. N. Hanzawa, K. Saitoh, T. Sakamoto, T.Matsui, S. Tomita, M. Koshiba, Technical Digest, PDPB8 (2011)
76. A.H. Hartod, An Introduction to Distributed Optical Fibre Sensors, CRC Press (2017)
77. K. Riles, Prog. Part. Nucl. Phys. 68, 1 (2013)
78. C.J. Moore, R.H. Cole and C.P.L. Berry, Class. Quantum Grav. 32, 015014 (2015)
79. B.P. Abbott et al. Phys. Rev. Lett. 116, 131103 (2016)
80. C. Hu, K. A. Anselm, B. G. Streetman, and J. C. Campbell, Applied Physics Letters, 69, 3734 (1996)
81. J. S. Ng, J. P. R. David, G. J. Rees, and J. Allam, Journal of Applied Physics, 91, 5200 (2002)
82. N. Balkan, A. Erol, F. Sarcan, L.F.F. Al-Ghuraibawi & M.S. Nordin., Superlattices and Microstructures, 86, 467 (2015)

CHAPTER 6

Avalanche Photodetector

6.1 Introduction

In Chapter 5, a vertical-cavity-enhanced (VCE) based GaInNAs/GaNAs p-i-n photodiode was demonstrated for 1.3 μm operation. The device exhibited a responsivity of 1.63A/W, an internal gain of 2.45, and a high dark current (~60 μA), at a bias of -2V. In that device, the narrow bandgap GaInNAs layers acted as both the absorption region and part of the multiplication region. In order to achieve adequate gain from the photodiode, a high electric field in the multiplication region is essential. At high electric field, the multiplication and band-to-band tunnelling in these GaInNAs layers are the primary components of the dark current. In order to reduce these dark current components, it is necessary to separate the multiplication and absorption regions and tailor the electric field profile. This leads to a modified avalanche photodiode (APD) structure with multiplication, absorption and charge separation (MACS) regions that is called MACS APD. In long-haul, high-bit-rate fibre optic communication systems, low noise is another critical requirement for the photodetectors in order to improve the detection sensitivity and reduce the number of repeaters and amplifiers during the transmission. The multiplication region of the MACS APD plays an important role in noise performance. By using some low noise materials such as GaAs for the multiplication region and GaInNAs as the absorber, we can obtain APDs operating at 1.3 μm on GaAs substrates with very low noise. In this chapter, the structure of a VCE GaInNAs MACS APD operating at 1.3μm is proposed.

6.2 Avalanche VCE Photodetector (AVCEP)

Avalanche photodetector (APD) is a relatively large reverse bias device. There is a built-in gain in the device due to carrier multiplication in the absorption region. Most of the electric

field drops across the undoped absorption region. The high field across the absorption region helps to drive the photogenerated carriers across the depletion region and thus, reduces the carrier transit time. The avalanche photodiode is usually a heterojunction diode with wide-bandgap P^+ or N^+ window layers and narrow-bandgap undoped absorption layer to make sure that the absorption happens in the absorption region and the carrier diffusion from outside the depletion region is eliminated. However, in narrow bandgap semiconductors, the high electric field causes high tunnelling current which contributes to the dark current at high bias [1]. The carriers escape by tunnelling or thermionic emission, the latter reducing the APD response speed. In order to avoid the excessive dark current at high bias, it is necessary to separate the multiplication and absorption regions and to tailor the profile of the electric field. A modified APD structure with multiplication, absorption and charge separation (MACS) layers is shown in Fig.6.1.

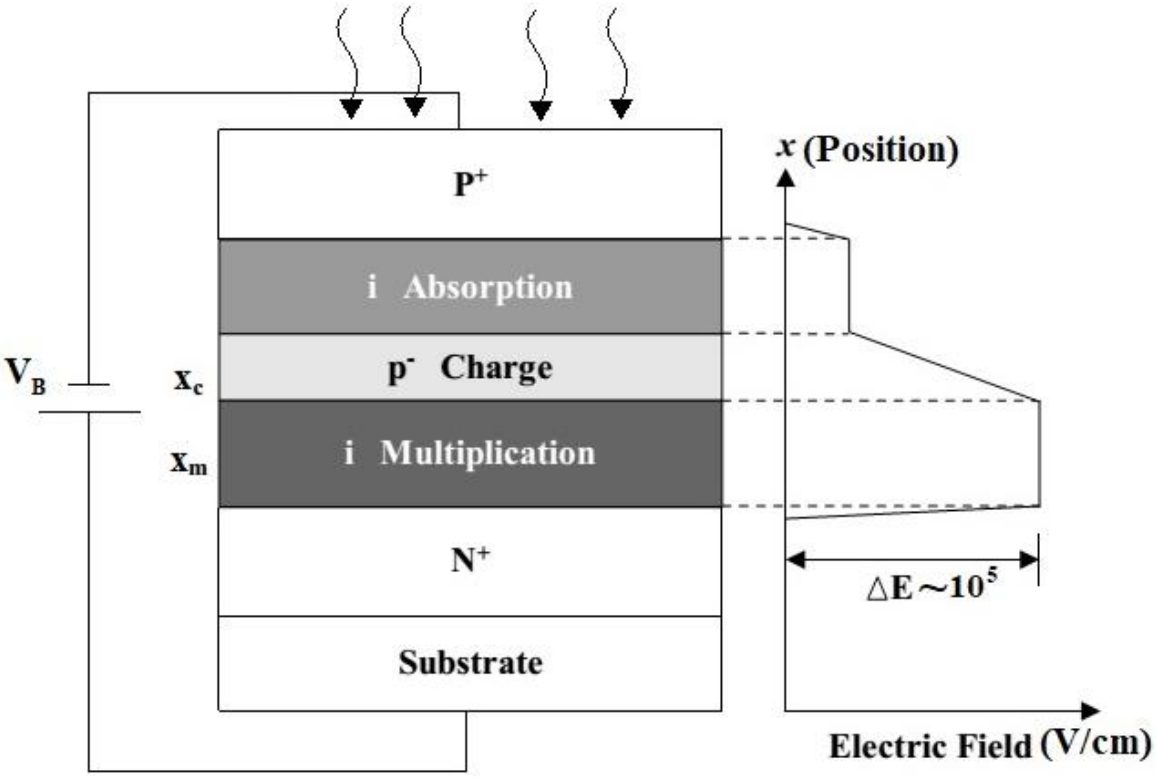

Figure 6.1: The schematic cross-section and electric field of MACS APD

This alloy compositional grading layers are able to reduce the offset of the band-discontinuity, which greatly reduce the carrier trapping effect. In this structure, most of the electric field drops across the undoped wide bandgap multiplication region. The thin lightly p-type doped charge layer ensures a low field in the absorption region. Therefore the tunnelling in the narrow bandgap absorption region is significantly reduced.

A typical gain, *M* for an APD is between 10 to 100. Normally the leakage current or dark current, I_d is negligible at low bias as compared to photocurrent, I_{ph}, as shown in Fig.6.2. Hence the gain, *M* can be determined as [2]:

$$M = \frac{I_{ph} - I_d}{I_{primary}} \qquad (6.1)$$

where $I_{primary}$ is the initial photocurrent due to incident photon. From Fig.6.2, the gain, *M* is 0.1 when the diode has attained punch-through and then increases with the applied voltage. The punch-through voltage is where the charge layer is fully depleted. It can be calculated from the area between the charge and multiplication layer as depicted in Fig.6.1.

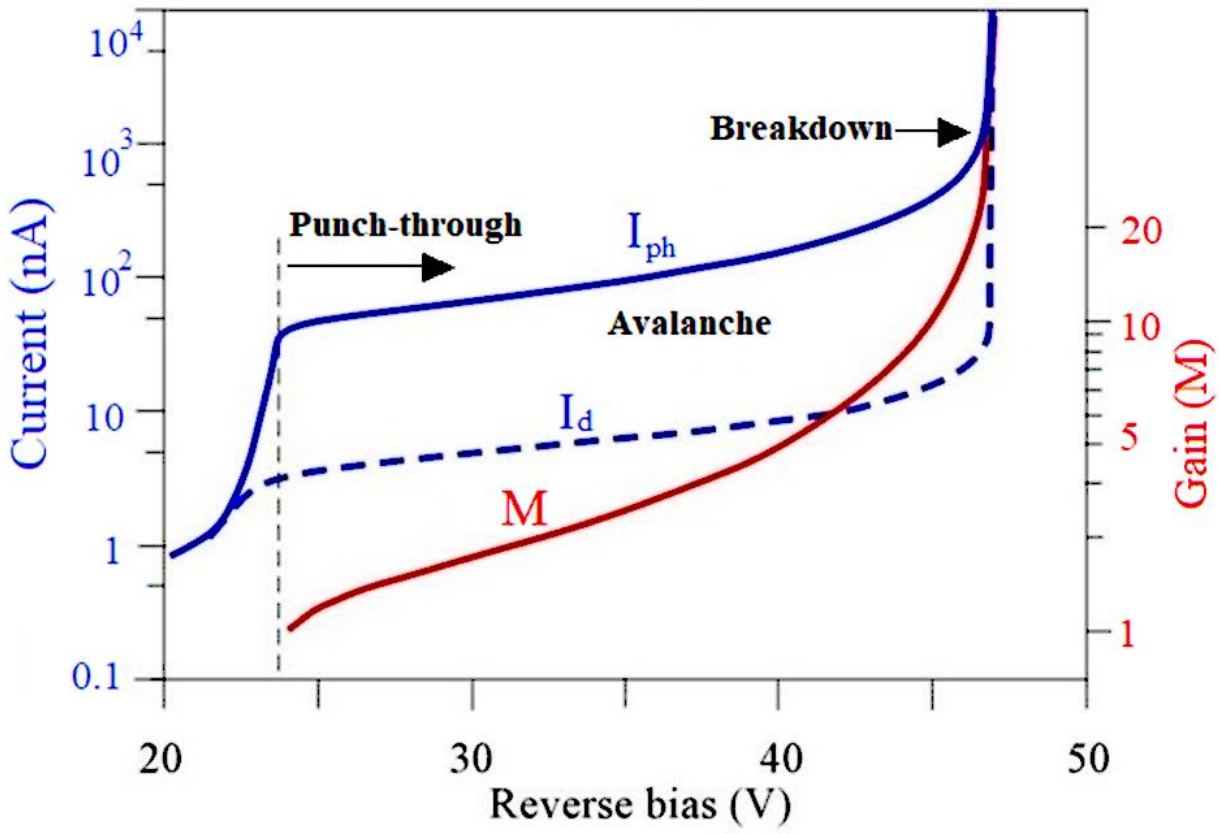

Figure 6.2: Illustration of typical current and gain, M versus reverse bias voltage MACS APD

The punch-through voltage can be determined by:

$$V_{punch} = \frac{1}{2}\Delta E_c x_c + \Delta E_m x_m \qquad (6.2)$$

where ΔE_c is the electric field of charge region, x_c is charge layer thickness, ΔE_c is the electric field of multiplication region, and x_m is multiplication layer thickness. The consideration of punch-through voltage have to be made carefully. The electric field across the absorption region will be too low at the reverse bias near breakdown if the punch-through voltage is too high, which can lead to a long carrier transit time and slow frequency response. However, if the punch-through voltage is too low, the electric field across the absorption region is too high at the reverse bias near breakdown, which will lead to both high tunnelling and dark currents. Regardless, the consideration have to fulfil the requirement of having an electric field of 10^5 kV/cm in the multiplication region in order to achieve impact ionisation.

Impact ionisation is another important phenomena in an APD because it is the process in which one energetic charge carrier can lose energy by the creation of other charge carriers. For example, an electron (or hole) with enough kinetic energy capable to knock a bound electron out of its bound state (in the valence band) and encourage it to a state in the conduction band, creating electron-hole pair. If this occurs under high electrical field, it can result in an avalanche breakdown as shown in Fig.6.2. This process is exploited in the APD, by which a small optical signal is amplified before entering an external electronic circuit where the original charge carrier is created by the absorption of a photon. The ability of electrons and holes to be ionised are characterised by the ionisation coefficients, $\alpha_e \ and \ \alpha_h$ and can be calculated as [3]:

$$\alpha_{e,h} = \frac{1}{(L_{int})_{avg}} \ (cm^{-1}) \qquad (6.3)$$

where L_{int} is the internal average distance retaliates between two successive collisions. These quantities represent ionisation probabilities per unit length (rates of ionisation, cm^{-1}). Hence, the ionisation ratio is used to characterise the performance of APD as given [4]:

$$k = \frac{\alpha_h}{\alpha_e} \qquad (6.4)$$

Most of the ionisation is achieved by electrons when holes do not ionise simultaneously. The avalanche process then proceeds principally from the p-side to the n-side. It is desirable to fabricate APD from materials that only permit one type of carrier either electrons or holes into multiplication region, as this improves the APD's speed and noise for multiplication materials generally utilised that have high ionisation coefficient ratios. For example, if electrons have a higher ionisation coefficient, optimal behaviour is achieved by injecting the electron of a photo carrier pair at the p side of the depletion layer and by using a material whose value of α_e is as low as possible. If holes are injected, the hole of a photo carrier pair should be injected at the n side of the depletion layer and k should be as large as possible. The ideal case of having single-carrier multiplication is achieved when k is zero or infinity. It is well known that the impact ionisation

process in APDs is strongly dependent on temperature and therefore an external biasing circuit to maintain a constant gain is necessary to achieve reproducible performance as shown in Fig. 6.3. In most wide bandgap semiconductors such as Si, GaAs, $Al_xGa_{1-x}As$, InP and InAlAs, the avalanche multiplication reduces with increasing temperature [5].

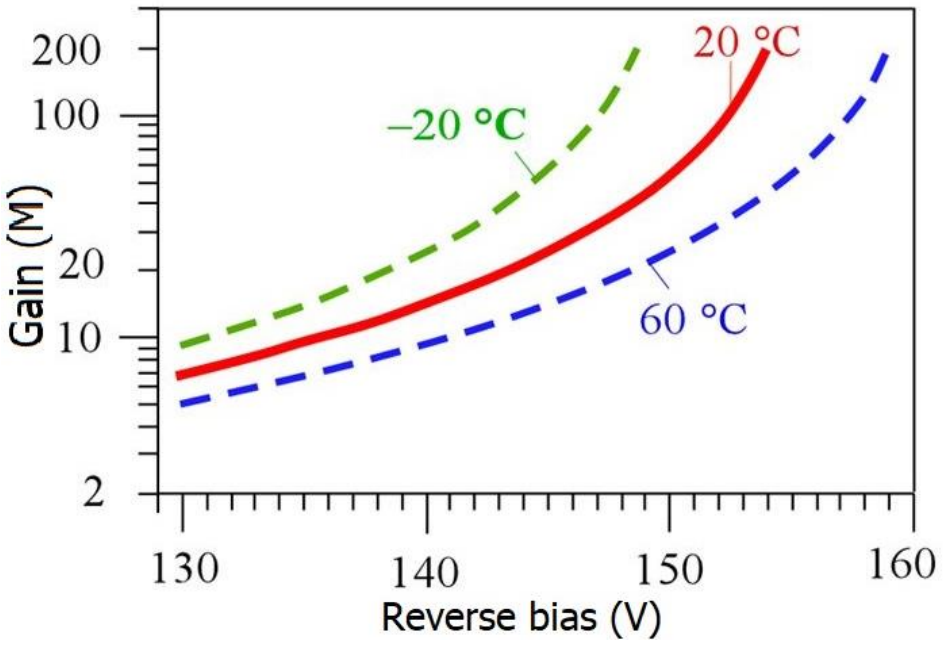

Figure 6.3: Illustration of gain at temperature dependent for Silicon APD [5]

It can be seen from Fig.6.3 that at lower temperatures, better gain is achieved compared to at higher temperatures. This is because the reduced temperature lowers the number of phonon scattering leading to a larger population of hot carriers that increases the impact ionisation. However, if applied bias continuously is increased at higher temperature operation, the gain will reach the exact gain as in lower temperature. In the case of narrow bandgap semiconductor, the gain increases as the temperature is raised. Fig.6.4 shows that the InAs APD exhibits exponentially rising gain at higher temperature. The narrow bandgap semiconductor normally require as low as around 15kV/cm to initiate the impact ionisation process [6].

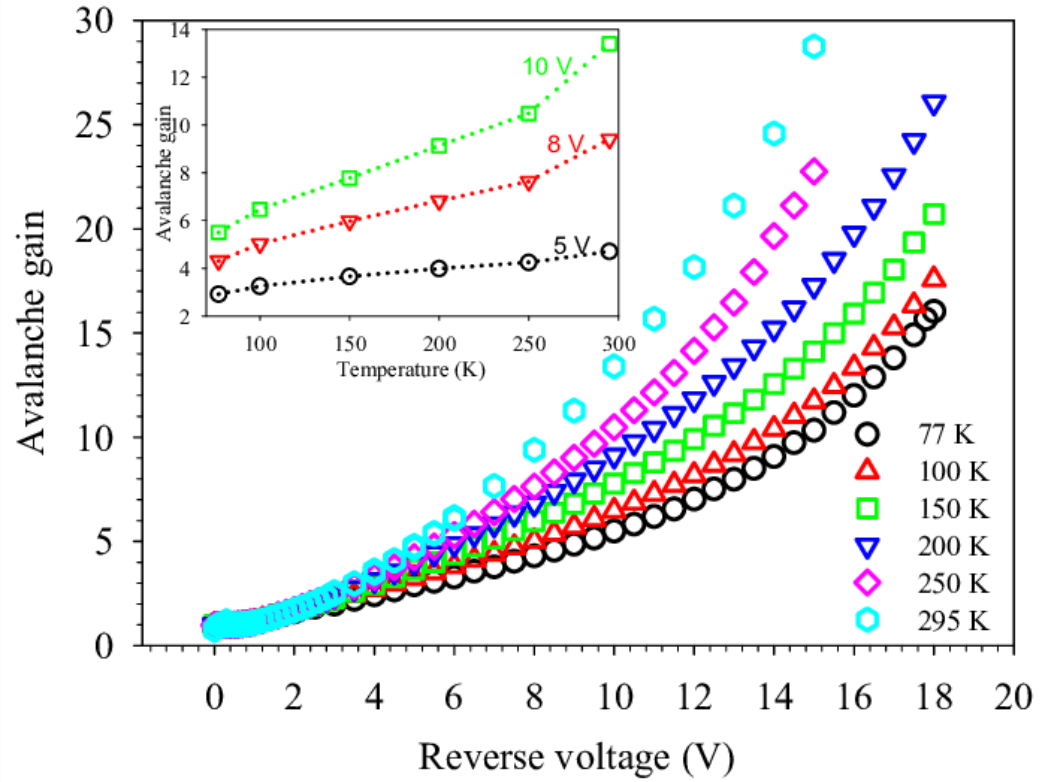

Figure 6.4: The temperature dependent avalanche gain at different bias voltages [6].

On the other hand, the multiplication region should be thin to minimize the possibility of localized uncontrolled avalanches (instabilities or micro plasmas) being produced by the strong electric field. Greater electric-field uniformity can be achieved in a thin region. A thin multiplication region will also provide low temperature coefficients of breakdown voltage thus improving the performance of the APD by lowering the excess noise via the dead space effects[7], and increasing the gain-bandwidth product (GBP), due to the reduction in the carrier transit time [8]. Consequently the gain increases at low frequency leading to a gain trade-off since the impact ionisation process takes time to build-up. For a properly designed APD, the bandwidth-limiting factor is carrier transit time at low gains and avalanche build-up time at high gains. Therefore, due to the trade-off between gain and bandwidth, GBP is commonly used as the figure of merit for APDs [9].

The noise of the APD is a very crucial factor when designing and determining the performance limits of light wave systems because it causes fluctuations in the output that cannot

be distinguished from the actual signal. An APD will normally be operating in one of the two noise-limited detection regimes, either detector noise limited at low power levels, or photon shot noise limited at higher powers. As an APD is designed to be operated under a reverse bias, sensitivity at low light levels will be limited by the shot noise, thermal noise, and leakage current. Shot noise, i^2_{shot} is a fundamental noise that exists in all optical detection processes due to fluctuations in the signal, while thermal noise, $i^2_{thermal}$ arises from the thermal motion in the resistors. Shot noise and thermal noise are intrinsic noise sources and cannot be eliminated. Both of them are statistically independent and total noise, i^2_{total} can be expressed as [10]:

$$\langle i_{total}^2 \rangle = \langle i_{shot}^2 \rangle + \langle i_{thermal}^2 \rangle = 2qIB + \frac{4kTB}{R_L} \qquad (6.5)$$

where q is the electron charge, I is the current flow, B is the effective bandwidth, k is the Boltzmann's constant, T is the absolute temperature, and R_L is the load resistance. For APD noise at higher light levels and biases, the ionisation of single carriers is not uniform such that a multiplication noise, $i^2_{multiply}$ known as excess noise is added when considering the impact ionisation process and can be written by [11]:

$$\langle i_{APD}^2 \rangle = \langle i_{multiply}^2 \rangle + \langle i_{thermal}^2 \rangle = 2q\big(I_{ph} + I_{DB} + I_{DS}\big)BM^2F + \frac{4kTB}{R_L} \qquad (6.6)$$

where I_{ph} is the photocurrent, I_{DB} is the bulk leakage current, I_{DS} is the surface leakage current, M is the multiplication gain, and F is the excess noise factor. McIntyre [11] introduced an elegant local model to calculate the excess noise factor versus multiplication for uniform electric field. For pure electron injection, the excess noise factor can be written as:

$$F = M - M(1-k)\left(\frac{M-1}{M}\right)^2 \qquad (6.7)$$

where $k=\beta/\alpha$. And α and β are impact ionisation coefficients of the electrons and holes. For pure hole injection, the relation is:

$$F = M - M\left(1-\frac{1}{k}\right)\left(\frac{M-1}{M}\right)^2 \qquad (6.8)$$

From Eq.6.8 and Eq.6.9, a low *k* (electron dominant ionisation) is desired for pure electron injection and a high *k* (hole dominant ionisation) is desired for pure hole injection in order to have low excess noise in the APDs. Fig.6.5 shows a plot of excess noise as a function of the k parameter. It can be seen that, to achieve low excess noise, a material with dissimilar ionisation coefficients ratio and the more strongly ionising carrier should be injected into the avalanche region.

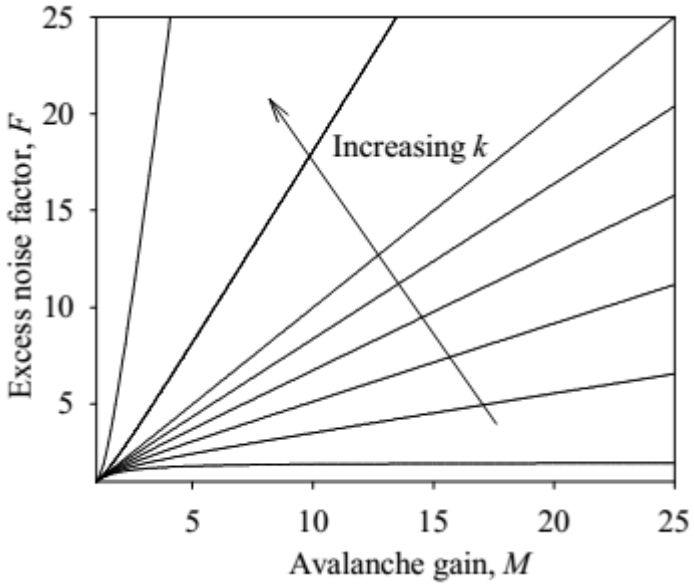

Figure 6.5: Excess noise factor prediction using McIntyre's local analysis for k=0, 0.2, 0.4, 0.6, 0.8, 1, 5 and 10 for electron injection and 1/k for hole injection [11].

Excess noise increases as the gain is increased. Since the gain exhibits wavelength-dependence, the excess noise differs according to the incident light wavelength. This is similar if the photocurrent generated by the signal light is also amplified by the gain. Hence, the best signal-to-noise ratio, S/N exists at certain gain. Together with the shot noise in the APDs, which arises from the random fluctuations in the motion of carriers and includes the shot noise from the surface leakage current (not multiplied), bulk dark current and photocurrent, the signal to noise ratio (SNR) in the APDs can be written as [12]:

$$\frac{S}{N} = \frac{I_{ph}^2 M^2}{2q\left(I_{ph}+I_{DB}+I_{DS}\right)BM^2F+\frac{4kTB}{R_L}} \qquad (6.9)$$

The signal-to-noise ratio, *S/N* of APD is improved at higher gain, *M*. But since excess noise factor *F* also depends on the gain *M*, the gain cannot be very high. There is an optimum value of gain *M* at which the *S/N* is maximized. Therefore, from the successful outcome of VCE samples described in previous chapter, the combination of both the vertical cavity and the MACS APD structure is expected to result in an AVCEP with a high quantum efficiency, high speed, low noise, and low dark current.

6.3 AVCEP Design and Modelling

In this thesis, the separation concept of multiplication and absorption of an APD has been taken as a design consideration. The APD concept that made use of the 9 QW VCEP structure described in chapter 3 is modelled based on the Multiplication-Absorption-Charge-Separation (MACS) method. As a start, the knowledge of impact ionisation coefficient value material of the multiplication layer is needed, so that possible gain can be estimated. GaAs material is used for the multiplication layer due to its wide bandgap and the fact that it is a commonly used material to derive α and β coefficient value over electric field dependence. The gain estimation is calculated based on α and β as below [13-14, 16]:

$$\alpha = 0.96 \times 10^5 e^{\left[-\left(\frac{4.47\times10^5}{E}\right)^{2.33}\right]} \ (cm^{-1}) \qquad (6.3)$$

$$\beta = 1.24 \times 10^5 e^{\left[-\left(\frac{4.99\times10^5}{E}\right)^{2.33}\right]} \ (cm^{-1}) \qquad (6.4)$$

$$M = \frac{(\alpha-\beta)e^{(\alpha-\beta)x_m}}{\alpha-\beta e^{(\alpha-\beta)x_m}} \qquad (6.5)$$

The relationship of electric field, *E* and multiplication, *M* with a variation of multiplication thicknesses, x_m is shown in Fig.6.6. Increment of multiplication thickness appears to attain lower electric field required for maximum multiplication. However, there is no significant behaviour of multiplication thickness and gain acquired. In order to achieve high

gain, x_m = 135nm is chosen to model the MACS-AVCEP. For x_m=135nm, the maximum gain value of 2246 is observed at 7.11x10^{5}V/cm while 1777 gain value is observed at 5.27 x10^{5}V/cm for x_m=200nm.

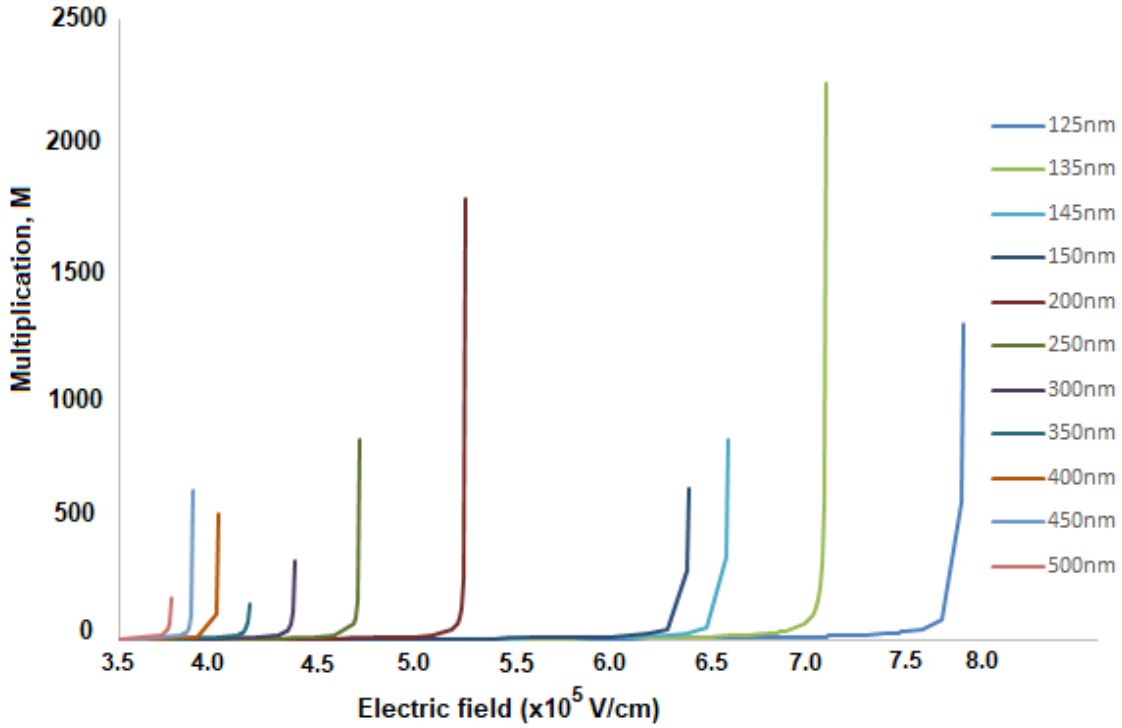

Figure 6.6: Electron multiplication due to electric field with different multiplication thickness

To achieve a high GBP, the multiplication and the absorption regions are separated into two different layers, such that the absorption occurs in a layer of narrow band-gap material, while a wider band-gap material is used for the multiplication layer. When the applied voltage is increased, the electric field is also increased in the multiplication region resulting in a secondary generation of free carriers. The surge of the applied voltage also increase the amplitude of the electric field in both the multiplication and the absorption layers. The electric field should be low enough to avoid the band to band tunnelling current in the narrow bandgap material [15], but high enough to achieve significant impact ionisation in the wide-bandgap materials. Therefore, another layer of space charge is placed between both the absorption and multiplication layers to vary the electric field in both layers. There are a few things that affect the electric field of multiplication layer, E_m and electric field of absorption layer, E_a. These are (1) the space charge

doping concentration (2) the reverse bias (3) the thickness of the multiplication layer, x_m and space charge layer, x_c and (4) the n^+ layer thickness and doping concentration.

All the electric field values were obtained by using the SimWindows software to design the AVCEP structure in this thesis. As shown in Fig.6.7, an increment of the space charge doping concentration will increase the E_m but decrease the E_a. This means that a high doping of the charge layer, x_c may result in a small electric field in the x_a so that the primary carriers may not move at their saturation velocity, resulting in a decrease of the bandwidth of the photodetector.

Furthermore, the electric field of the absorption layer, E_a and the multiplication layer, E_m will increase by increasing the applied bias as shown in Fig.6.8. The changes of multiplication layer, x_m and space charge layer x_c will effect the E_a and E_m. It was found that increasing the thickness of x_c has a similar effect of increasing the doping of x_c. By setting the bias at -15V, the addition of both the x_m and x_c will decrease E_a as shown in Table 6.1. E_m will reduce by elevating the x_m and reducing the x_c. It can also be seen that increasing the n^+ doping concentration will increase E_m and E_a as shown in Table 6.2. However, by increasing the thickness of the n^+ doping layer, there is no significant changes as shown in Table 6.3.

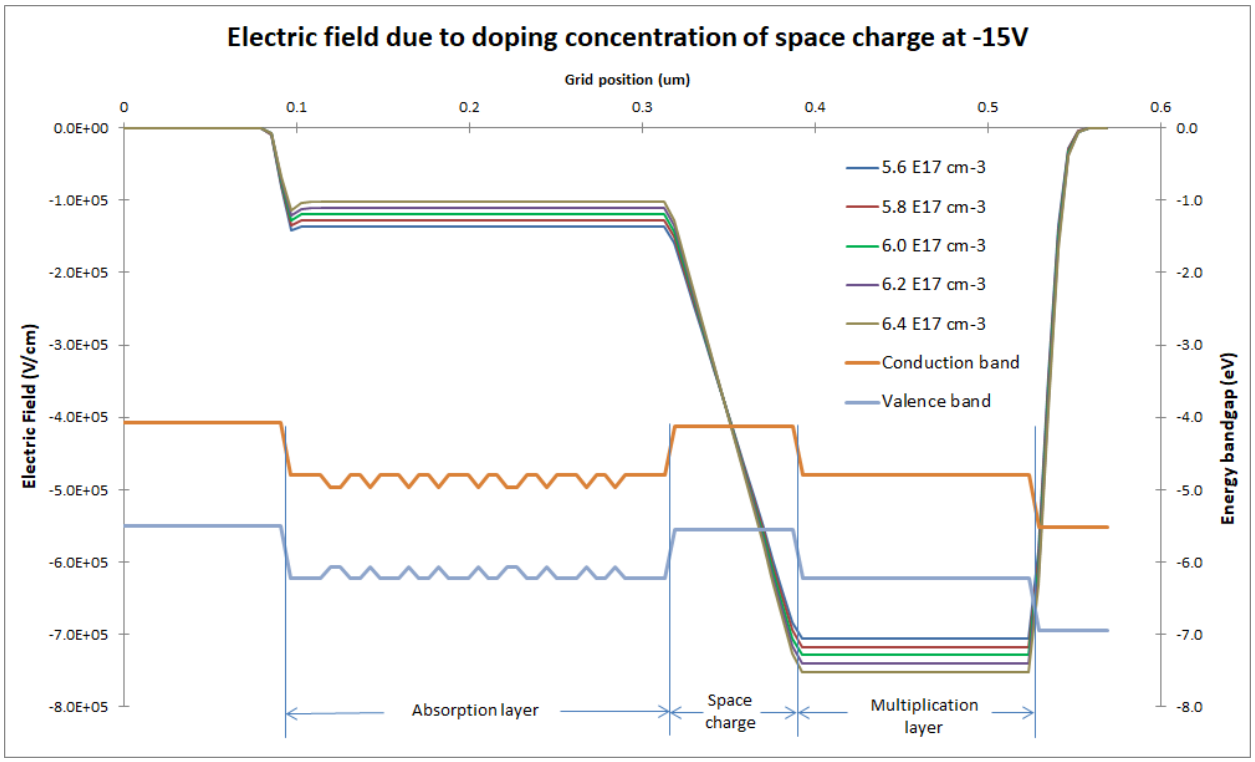

Figure 6.7: Electric field with different space charge concentration with x_m=135nm, x_c=76nm and n+ ($3.1x10^{18}$ cm^{-3}) layer thickness =45nm under -15V reverse biased.

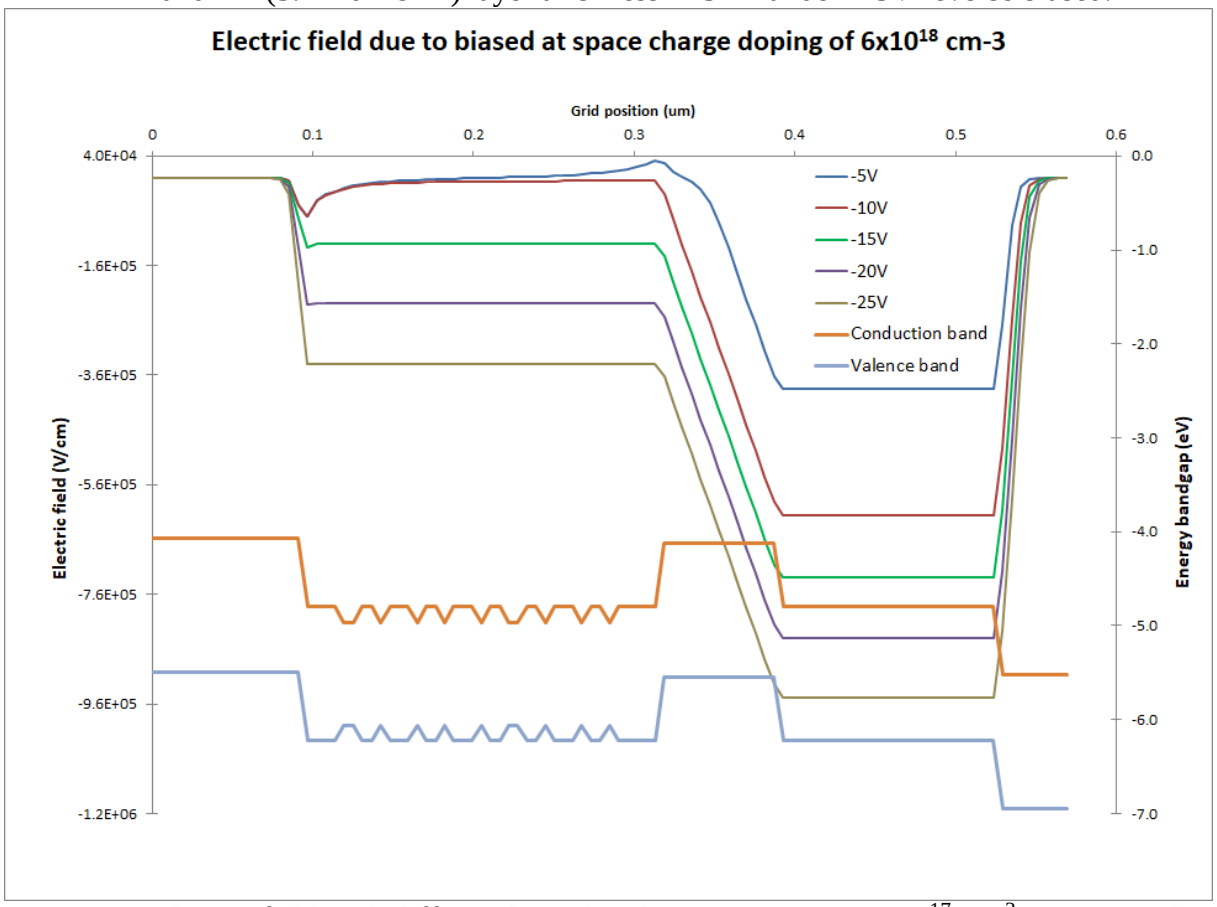

Figure 6.8: Electric field with different biased with x_m=135nm, x_c ($6x10^{17}$ cm^{-3}) =76nm and n+ ($3.1x10^{18}$ cm^{-3}) layer thickness =45nm.

Tab.6.1: Effect of x_m and x_c on E_a and E_m

	n+ ($3.1x10^{18}$ cm^{-3}) layer thickness = 45 nm, V = -15V					
	x_c = 76 nm			x_m = 135 nm		
	x_m = 125 nm	x_m = 135 nm	x_m = 145 nm	x_c = 66 nm	x_c = 76 nm	x_c = 86 nm
E_a (10^5 V/cm)	1.24	1.19	1.01	1.55	1.19	0.844
E_m (10^5 V/cm)	7.69	7.29	7.21	7.08	7.29	7.52

Tab.6.2: Effect of n^+ layer doping on E_a and E_m

	n+ layer thickness = 45 nm, x_c = 76 nm, x_m = 135 nm, V = -15V				
n+ layer doping (10^{18} cm^{-3})	2.0	2.5	3.1	3.5	4.0
E_a (10^5 V/cm)	1.12	1.16	1.19	1.21	1.23
E_m (10^5 V/cm)	7.21	7.25	7.29	7.31	7.32

Tab.6.3: Effect of n^+ layer thickness on E_a and E_m

	n+ =$3.1x10^{18}$ cm^{-3}, x_c = 76 nm, x_m = 135 nm, V = -15V,				
n+ layer thickness (nm)	25	35	45	55	65
E_a (10^5 V/cm)	1.3	1.05	1.19	1.2	1.2
E_m (10^5 V/cm)	7.18	7.5	7.29	7.4	7.5

The modelling of the band structure with bias at -14V for x_m=135nm, x_c ($3.1x10^{18}$ cm^{-3}) =76nm and n^+ ($3.1x10^{18}$ cm^{-3}) layer thickness of 45nm is used to estimate the possible result. The E_a of $9.72x10^5$ V/cm and E_m of $7.07x10^5$ V/cm were obtained which give estimated gain value of 166.7 as shown in Fig.6.9. Hence, for x_m of 135nm, the maximum gain can be estimated roughly between bias -14V and -15V. In order to achieve absorption and recombination process in QWs efficiently, the E_a is estimated not to surpass the avalanche field (≈$1x10^5$ V/cm). Table 6.4 shows the electric field value for different biases and space charge doping concentrations. Value grid position at 0.2μm is taken for E_a and 0.45μm for E_m. Once the thickness of multiplication has been investigated, the bandwidth and response time application is attained according to the possible radius of the mesa structure. The total capacitance of the AVCEP is considered by two series of junction capacitor, C_{j1} (p^+-p, absorption layer) and C_{j2} (p-n^+, multiplication layer). Since the thickness of the absorption is fixed at 218nm (9 QWs and barriers), the total capacitance will be affected only by the thickness of multiplication layer.

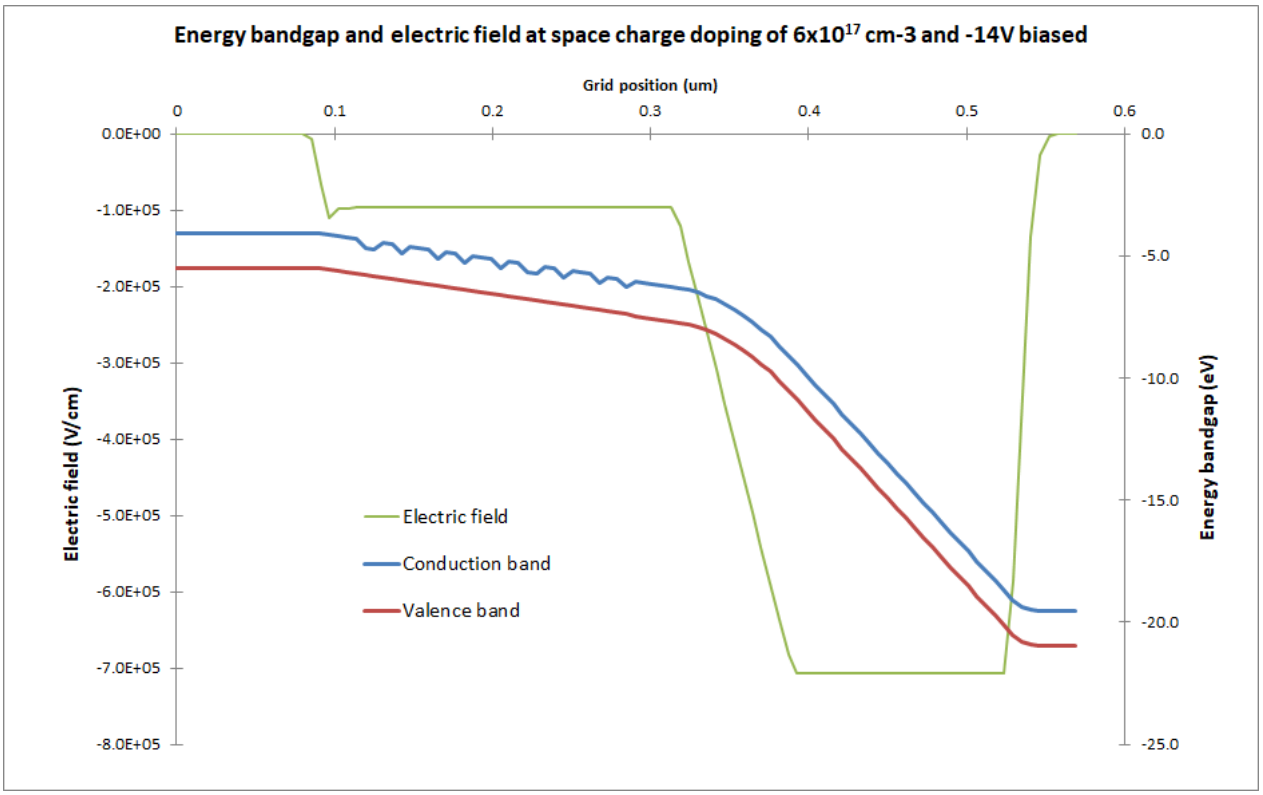

Figure 6.9: Electric field at -14V biased with x_m=135nm, x_c ($6x10^{17}$ cm^{-3}) =76nm and n+ ($3.1x10^{18}$ cm^{-3}) layer thickness =45nm.

Table 6.4: E_a and E_m value at x_c doping concentration and voltage dependent

Doping Xc \ Biased		-5V	-10V	-15V	-20	-25V
5.5×10^{17} cm^{-3}	**E_a (V/cm)**	8.35×10^2	2.86×10^4	1.41×10^5	2.51×10^5	3.6×10^5
	E_m (V/cm)	3.8×10^5	5.87×10^5	6.99×10^5	8.1×10^5	9.2×10^5
5.6×10^{17} cm^{-3}	**E_a (V/cm)**	8.3×10^2	2.4×10^4	$1.37x 10^5$	2.47×10^5	3.56×10^5
	E_m (V/cm)	3.81×10^5	5.9×10^5	7.05×10^5	8.16×10^5	9.25×10^5
5.7×10^{17} cm^{-3}	**E_a (V/cm)**	8.24×10^2	1.97×10^4	1.32×10^5	2.43×10^5	3.52×10^5
	E_m (V/cm)	3.82×10^5	6×10^5	7.1×10^5	8.21×10^5	9.31×10^5
5.8×10^{17} cm^{-3}	**E_a (V/cm)**	8.2×10^2	1.52×10^4	1.28×10^5	2.38×10^5	3.47×10^5
	E_m (V/cm)	3.83×10^5	6.04×10^5	7.17×10^5	8.27×10^5	9.37×10^5
5.9×10^{17} cm^{-3}	**E_a (V/cm)**	8.14×10^2	1.08×10^4	1.24×10^5	2.34×10^5	3.43×10^5
	E_m (V/cm)	3.84×10^5	6.1×10^5	7.22×10^5	8.33×10^5	9.42×10^5
6.0×10^{17} cm^{-3}	**E_a (V/cm)**	8.1×10^2	6.58×10^3	1.19×10^5	2.3×10^5	3.39×10^5
	E_m (V/cm)	3.85×10^5	6.15×10^5	7.29×10^5	8.39×10^5	9.48×10^5
6.1×10^{17} cm^{-3}	**E_a (V/cm)**	8.06×10^2	3.66×10^3	1.15×10^5	2.25×10^5	3.34×10^5
	E_m (V/cm)	3.86×10^5	6.2×10^5	7.35×10^5	8.45×10^5	9.54×10^5
6.2×10^{17} cm^{-3}	**E_a (V/cm)**	8.02×10^2	2.2×10^3	1.11×10^5	2.21×10^5	3.3×10^5
	E_m (V/cm)	3.87×10^5	6.23×10^5	7.4×10^5	8.51×10^5	9.6×10^5
6.3×10^{17} cm^{-3}	**E_a (V/cm)**	7.98×10^2	1.55×10^3	1.06×10^5	2.17×10^5	3.26×10^5
	E_m (V/cm)	3.87×10^5	6.26×10^5	7.46×10^5	8.56×10^5	9.66×10^5
6.4×10^{17} cm^{-3}	**E_a (V/cm)**	7.93×10^2	1.3×10^3	1.02×10^5	2.12×10^5	3.21×10^5
	E_m (V/cm)	3.88×10^5	6.28×10^5	7.52×10^5	8.62×10^5	9.71×10^5
6.5×10^{17} cm^{-3}	**E_a (V/cm)**	7.9×10^2	1.12×10^3	9.79×10^4	2.08×10^5	3.17×10^5
	E_m (V/cm)	3.89×10^5	6.3×10^5	7.58×10^5	8.68×10^5	9.77×10^5

In this thesis, the value of 135nm has been chosen for multiplication layer thickness due to reasonable capacitance value and bandwidth. Table 6.5 shows the effect of radius (1µm to 1000µm) on total capacitance, bandwidth and response time for fixed value of R_L = 50Ω, x_m = 135 nm, x_c ($6x10^{17}$ cm^{-3}) =76nm and n+ ($3.1x10^{18}$ cm^{-3}) layer thickness = 45nm. From Table 6.5, the capacitance and bandwidth will reduce by increasing the radius of the sample. Furthermore, the response time is expecting to be faster by reducing the radius. However, these outcome is limited to the trade-off between gain and bandwidth of GaAs material used as multiplication layer. The structure of the proposed AVCEP, shown in Table 6.6, contains 9 layers of 7 nm-thick $Ga_{0.68}In_{0.32}N_{0.015}As_{0.985}$ quantum wells separated by 13.5 nm GaAs barriers. The active region is enclosed between 95 nm-thick cladding layers C-doped ($p = 5 \times 10^{18}$ cm^{-3}) on the top side and 70 nm of Si-doped ($p = 3 \times 10^{18}$ cm^{-3}) on the bottom side.

Table 6.5: Effect of radius on total capacitance, bandwidth and response time

R_L = 50Ω, x_m = 135 nm, x_c ($6x10^{17}$ cm^{-3}) =76nm, n+ ($3.1x10^{18}$ cm^{-3}) layer thickness = 45nm			
Radius (µm)	**Total capacitance, C_T (F)**	**Bandwidth, f_{3dB} (Hz)**	**Response time, t_r (s)**
1	$1.05 x10^{-15}$	$3.01 x10^{12}$	$0.12 x10^{-12}$
2.5	$6.61 x10^{-15}$	$481.58 x10^{9}$	$0.73 x10^{-12}$
5	$26.44 x10^{-15}$	$120.39 x10^{9}$	$2.91 x10^{-12}$
7.5	$59.49 x10^{-15}$	$53.51 x10^{9}$	$6.54 x10^{-12}$
10	$105.76 x10^{-15}$	$30.10 x10^{9}$	$11.63 x10^{-12}$
25	$660.98 x10^{-15}$	$4.82 x10^{9}$	$72.68 x10^{-12}$
50	$2.64 x10^{-12}$	$1.20 x10^{9}$	$290.71 x10^{-12}$
75	$5.95 x10^{-12}$	$535.09 x10^{6}$	$654.10 x10^{-12}$
100	$10.58 x10^{-12}$	$301.00 x10^{6}$	$1.16 x10^{-9}$
250	$66.10 x10^{-12}$	$48.16 x10^{6}$	$7.27 x10^{-9}$
500	$264.39 x10^{-12}$	$12.04 x10^{6}$	$29.07 x10^{-9}$
750	$594.88 x10^{-12}$	$5.35 x10^{6}$	$65.41 x10^{-9}$
1000	$1.06 x10^{-9}$	$3.01 x10^{6}$	$116.29 x10^{-9}$

The space charge layer and multiplication layer thicknesses are 76nm and 135nm respectively and are placed between the bottom graded layer and n^+ doped layer. The charge layer is slightly doped at 6 x 10^{17} cm^{-3} which is lower than the p+ and n+ doped layer. The

structure is sandwiched between two DBRs. The top DBR has 10 pairs of GaAs/AlAs quarter-wave stacks and provides a reflectivity in excess of 98.14% at 1.3μm. On the other side, the bottom DBR has 15 pairs of AlAs/GaAs quarter-wave stacks giving around 99.21% reflectivity. This is higher than the top DBR, thus it might allow partial light emissions from the top surface when both DBRs are doped. The 98.01 nm thick GaAs capping layer is used to protect the AlAs layer from oxidation.

Considering the variation of gain estimated in Fig.6.6, an additional AVCEP structure is proposed using a different multiplication layer thickness. Another structure is having the same DBR and active layer as previous structure with few changes of layer thicknesses have been made to obtain the cavity at 1.3μm. The multiplication layer and the charge layer are changed to 200 nm and 55 nm respectively.

Table 6.6: Full structure of MACS-AVCEP with 135 nm multiplication layer

Notes	Doping	Repeats	Material	Thickness (nm)
p+ Doped GaAs / AlAs DBR	Be = 5 x 10^{18} cm^{-3}	10	GaAs	99.2
			AlAs	115.15
p+ Doped	Be = 5 x 10^{18} cm^{-3}	1	GaAs	**95**
Graded layer	Undoped	1	GaAs	10
Barrier	Undoped	9	$GaN_{0.035}As$	13.5
Intrinsic			$Ga_{0.733}In_{0.267}N_{0.025}As_{0.975}(Sb)$	7
Barrier	Undoped	1	$GaN_{0.035}As$	13.5
Graded layer	Undoped	1	GaAs	10
Space charge layer (p Doped)	**Be = 6 x 10^{17} cm^{-3}**	1	GaAs	**76**
Multiplication layer		1	GaAs	**135**
n+ Doped	Si = 3.1 x 10^{18} cm^{-3}	1	GaAs	**45**
n+ Doped GaAs / AlAs DBR	Si = 3 x 10^{18} cm^{-3}	15	AlAs	113.54
			GaAs	98.01
n+ Doped Substrate	Si = 3 x 10^{18} cm^{-3}	1	GaAs	350000

The p+ layer and n+ layer are reduced to 65nm and 30nm while the space charge doping is increased to 6.7 x 10^{17} cm^{-3}. The full structure for the 200nm multiplication layer can be seen in Table 6.7. Fig.6.10 shows -11.2V of applied bias is needed to acquire the E_a=5.56x10^3 V/cm,

E_m= 5.27x10^5 V/cm and 1777.9 of estimated gain value. Both of the structure reflectance spectra are identical and can be seen as in Fig.6.11.

Table 6.7: Full structure of MACS-AVCEP with 200 nm multiplication layer

Notes	Doping	Repeats	Material	Thickness (nm)
p+ Doped GaAs / AlAs DBR	Be = 5 x 10^{18} cm^{-3}	10	GaAs	99.2
			AlAs	115.15
p+ Doped	Be = 5 x 10^{18} cm^{-3}	1	GaAs	**65**
Graded layer	Undoped	1	GaAs	10
Barrier	Undoped	9	$GaN_{0.035}As$	13.5
Intrinsic			$Ga_{0.733}In_{0.267}N_{0.025}As_{0.975}$ (Sb)	7
Barrier	Undoped	1	$GaN_{0.035}As$	13.5
Graded layer	Undoped	1	GaAs	10
Space charge layer (p Doped)	**Be = 6.7 x 10^{17} cm^{-3}**	1	GaAs	**55**
Multiplication layer		1	GaAs	**200**
n+ Doped	Si = 3.1 x 10^{18} cm^{-3}	1	GaAs	**30**
n+ Doped GaAs / AlAs DBR	Si = 3 x 10^{18} cm^{-3}	15	AlAs	113.54
			GaAs	98.01
n+ Doped Substrate	Si = 3 x 10^{18} cm^{-3}	1	GaAs	350000

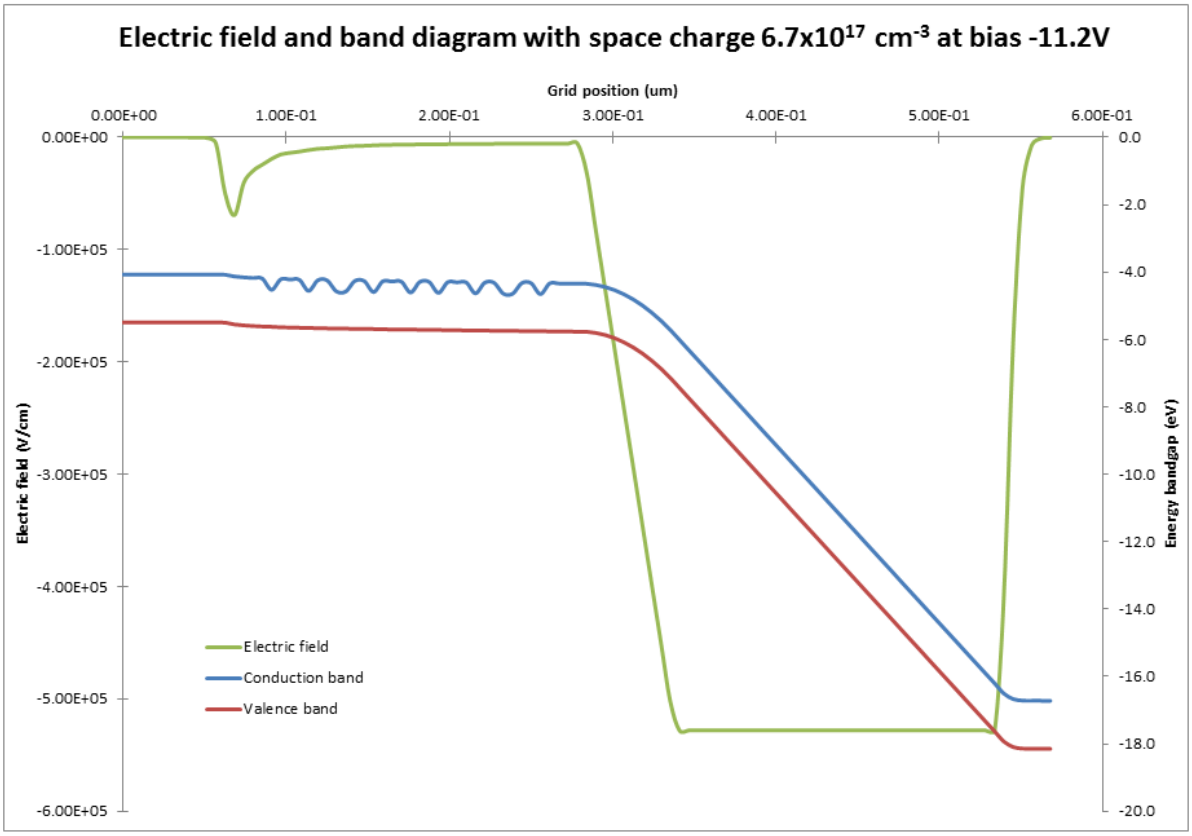

Figure 6.10: Electric field with -14V biased with x_m=135nm, x_c (3.1x10^{18} cm^{-3}) =76nm and n+ (3.1x10^{18} cm^{-3}) layer thickness =45nm.

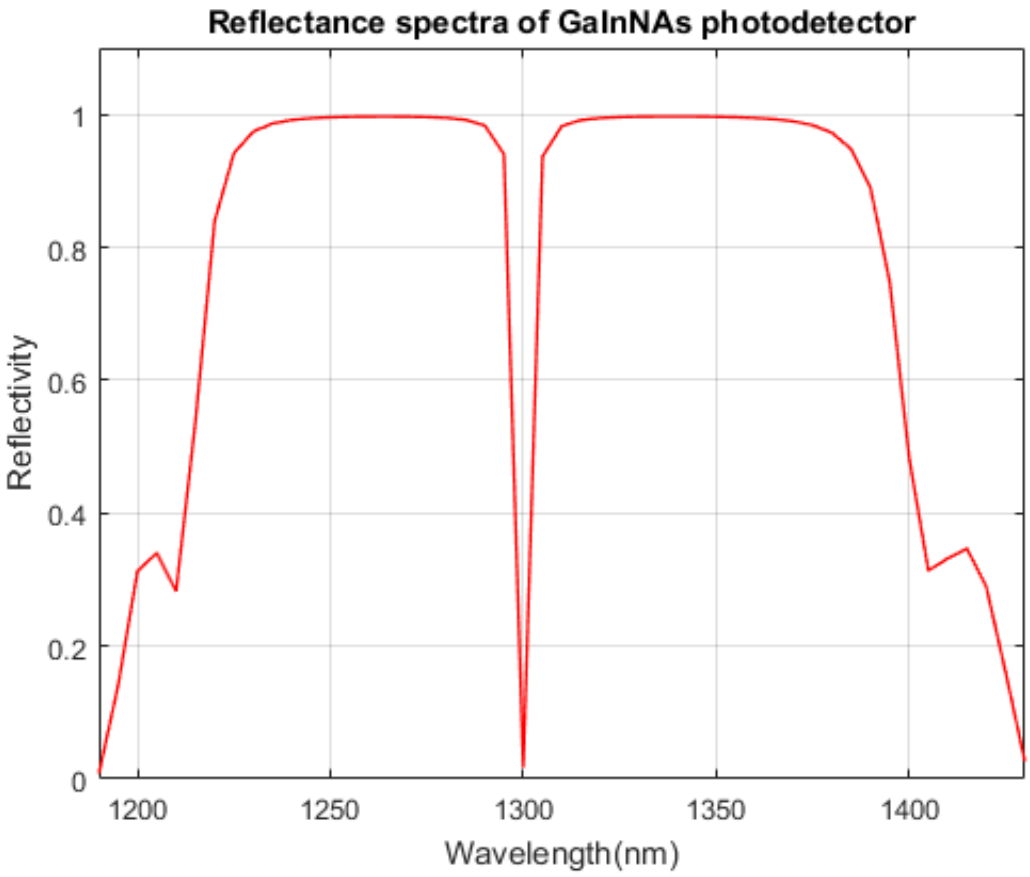

Figure 6.11: Resonance cavity for 9QWs with multiplication layer of 135nm or 200nm

6.4 Growth Structure

The structures in Table 6.6 and Table 6.7 have been sent for growth but only one that can be tested for initial measurement. The grown structure is shown in Table 6.8. The structure with the 200nm multiplication layer has been grown but unfortunately some parameter in the original structure has been changed due to growth constraint. The both top and bottom DBR thickness has been altered causing the cavity peak changed. The proposed absorption and barrier materials are changed to GaInNAs/GaAs. However, the most important parameter, the charge layer doping value has been reduced from $6.7 \times 10^{17} cm^{-3}$ to $1 \times 10^{17} cm^{-3}$. This change has been affecting the operation of the device as higher doping for charge layer is needed for higher electric field as discussed previously. Furthermore, the strain value of 0.00203 for this sample is nearly the same as for VCE GaInNAs/GaAs sample due to the usage of GaAs as the barrier. Nevertheless, we

have made some test measurements to observe the preliminary performance of the device. The sample is fabricated as described in chapter 4 in the shape of a mesa-structure, with top circular aperture of 1mm diameter.

Table 6.8: Full growth structure of MACS-AVCEP with 200 nm multiplication layer

Notes	Doping	Repeats	Material	Thickness (nm)
p+ Doped GaAs / AlAs DBR	Be = 5 x 10^{18} cm^{-3}	10	GaAs	95.85
			AlAs	112.46
p+ Doped	Be = 5 x 10^{18} cm^{-3}	1	GaAs	**65**
Graded layer	Undoped	1	GaAs	10
Barrier	Undoped	9	GaAs	13.5
Intrinsic			$Ga_{0.66}In_{0.34}N_{0.018}As_{0.982}$	7
Barrier	Undoped	1	GaAs	13.5
Graded layer	Undoped	1	GaAs	10
Space charge layer (p Doped)	**Be = 1 x 10^{17} cm^{-3}**	1	GaAs	**55**
Multiplication layer		1	GaAs	**200**
n+ Doped	Si = 3.1 x 10^{18} cm^{-3}	1	GaAs	**30**
n+ Doped GaAs / AlAs DBR	Si = 3 x 10^{18} cm^{-3}	15	AlAs	110.87
			GaAs	94.67
n+ Doped Substrate	Si = 3 x 10^{18} cm^{-3}	1	GaAs	350000

6.5 Device Measurements

In order to check an optical quality of the sample and confirm the bandgap is as expected, photoluminescence (PL) measurement is carried out on the samples. The relationship of bandgap energy between both peaks is shown in Fig.6.12. As temperature increases, both the active region and the cavity resonance are redshifted. However, the active region redshifts at a higher rate. The temperature-induced redshift rate of the effective bandgap of GaInNAs QW layer is determined to be 0.176nm/K and the cavity resonance shifts at rate of 0.063nm/K. These behaviours indicate that both samples are best to be operated near room temperature as active layer and cavity resonance retaliate with each other. It can be seen that the S-shape pattern for energy peak of the absorption region can be clearly observed where there is red shift between temperatures 50K to 77K. The origin of this S-shape is due to a large number of defects, impurities and structural compositions near the conduction band causing excitons to become

localised as discussed in chapter 5. The results of the PL measurements at T=300K are shown in Fig.6.13. The cavity resonant peak is measured to be at 1283nm while 1273nm is the peak for absorption region. The mismatch between both peaks is 10nm.

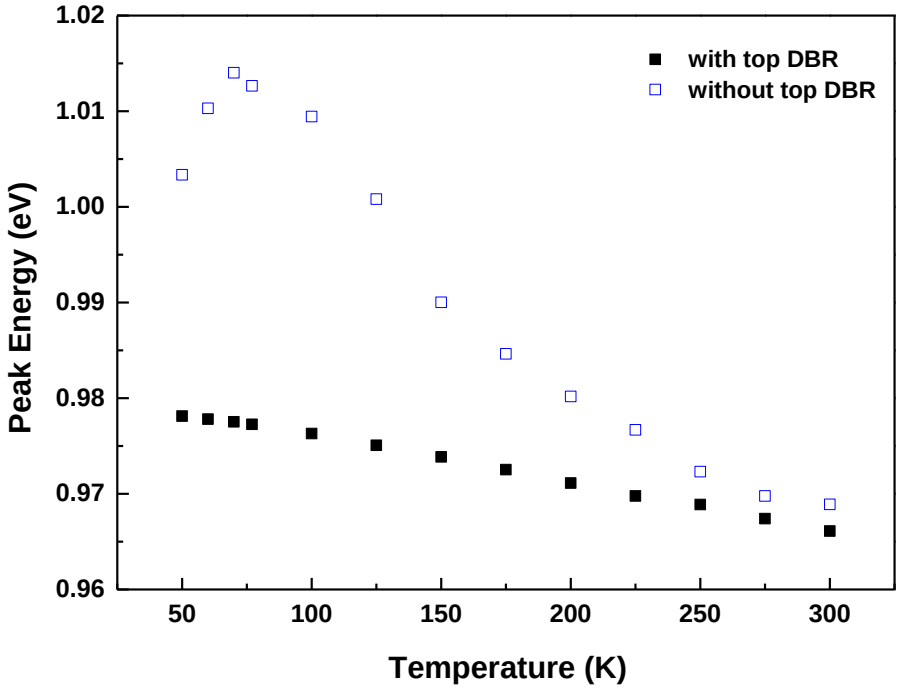

Figure 6.12: PL peak energy at temperature dependence for without top DBR (blue) and with top DBR (black)

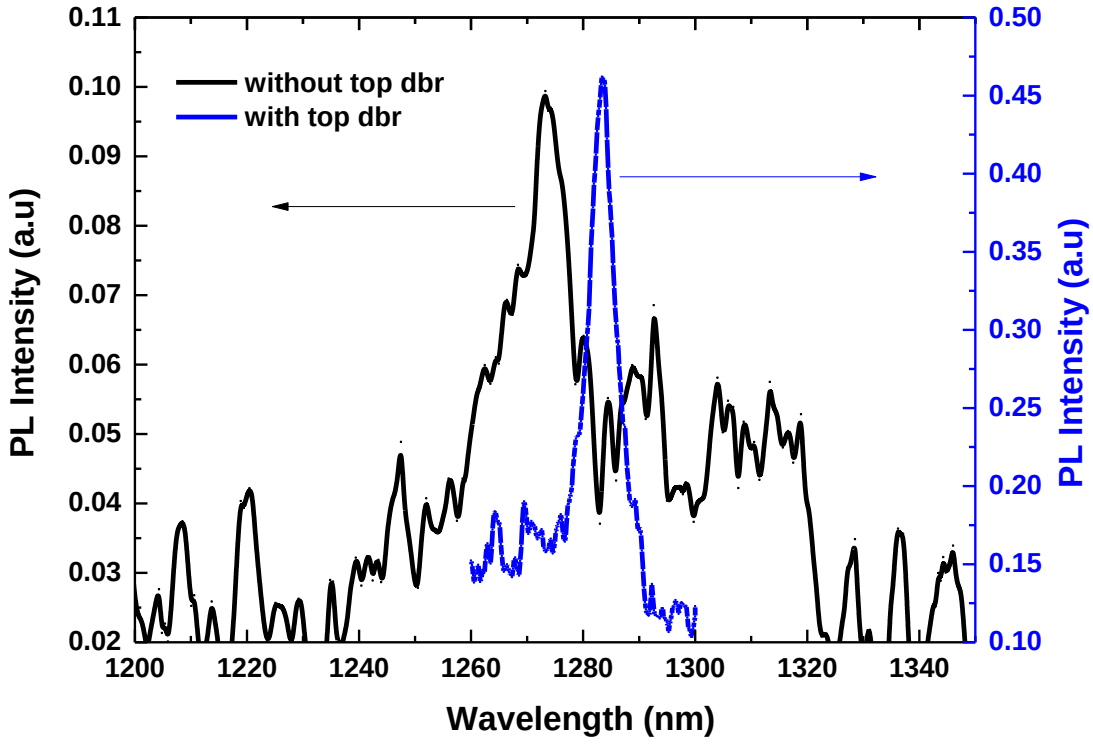

Figure 6.13: PL measurement at 300K for without top DBR (black) and with top DBR (blue)

The peak intensity of the sample is plotted in Fig.6.14 showing clearly a very large increase in intensity as the temperature is reduced. As the temperature drops from T=300K to T=100K the intensity steadily increases due to the escape probability of electrons decreasing resulting in more carriers recombining in the wells. Between T=100K to T=30K the PL intensity increases dramatically which attributing to the thermal escape time of holes dropping rapidly and approaching that of the recombination time. Furthermore, the behaviour is due to the effect of a phonon scattering mechanism increasing with temperature. This caused a non-radiative band to band transition which led the PL amplitude decrease with increasing temperature.

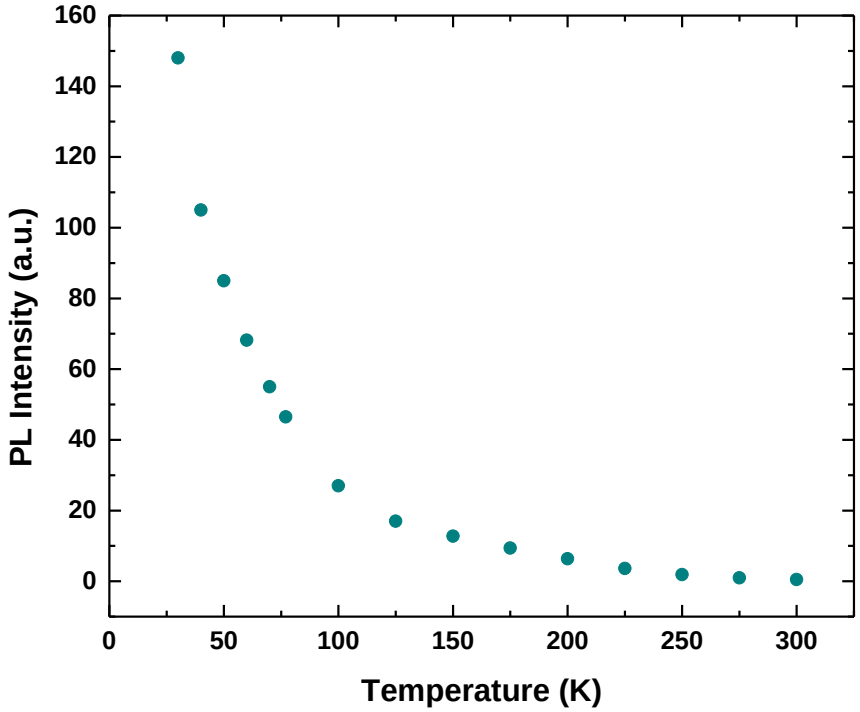

Figure 6.14: PL intensity versus temperature

I-V measurements were conducted to check the diode characteristic of the device. At bias of -0.5V, the dark current is observed to be 29pA and increased to 17nA at bias of -4V as shown in Fig.6.15. The device shows a good diode behaviour which produces a small dark current even at bias of -4V. The device under illumination is carried out but there is no response observed at low optical power. The optical power has been raised to maximum of 2.37mW but the response is not much as expected. At bias of -4V under illumination, the obtained photocurrent is 47nA.

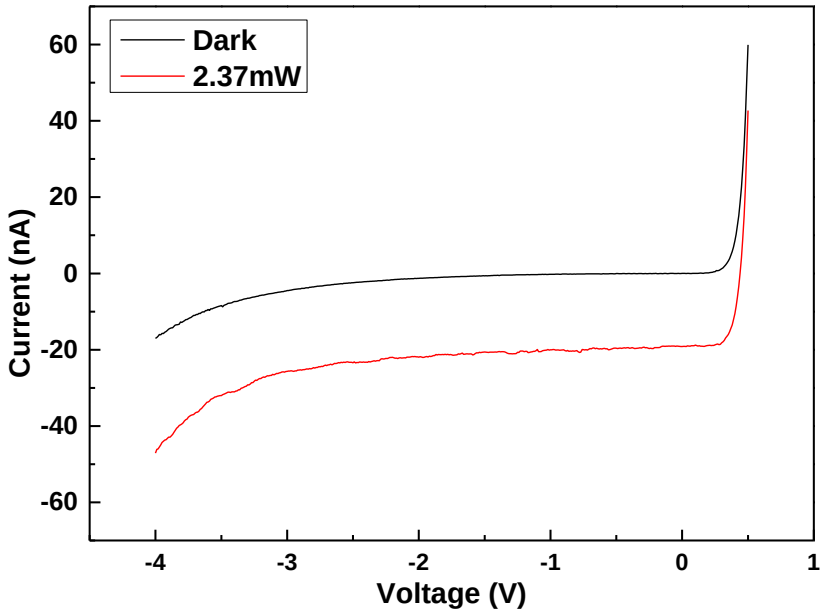

Figure 6.15: Room temperature I-V characteristic

The sample is considered as too Ohmic when only 30nA of increment with considerably high optical power of excitation at bias of -4V. However, when the first derivative is plotted for the illumination result, the oscillation can be observed even at room temperature. The oscillation shows that there is good confinement of electron in the quantum wells and there is a tunnelling effect occurring in the device. The oscillation shows 9 peaks corresponding to the number of quantum wells in the sample as depicted in Fig.6.16.

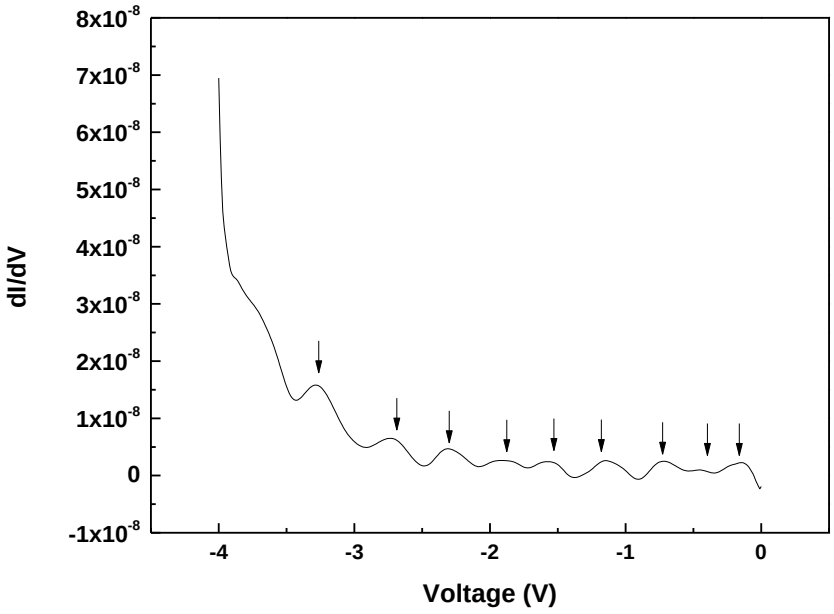

Figure 6.16: First derivative of the I-V characteristic

The preliminary photocurrent measurement is expected to give the same behaviour as the I-V measurement. At bias of -3V, the device just produces responsivity of 2.15mA/W as shown in Fig.6.17. The observed low responsivity could be due to low doping concentration for charge layer which produce low electric field in the multiplication region. Hence, there is no impact ionisation process occurred as expected.

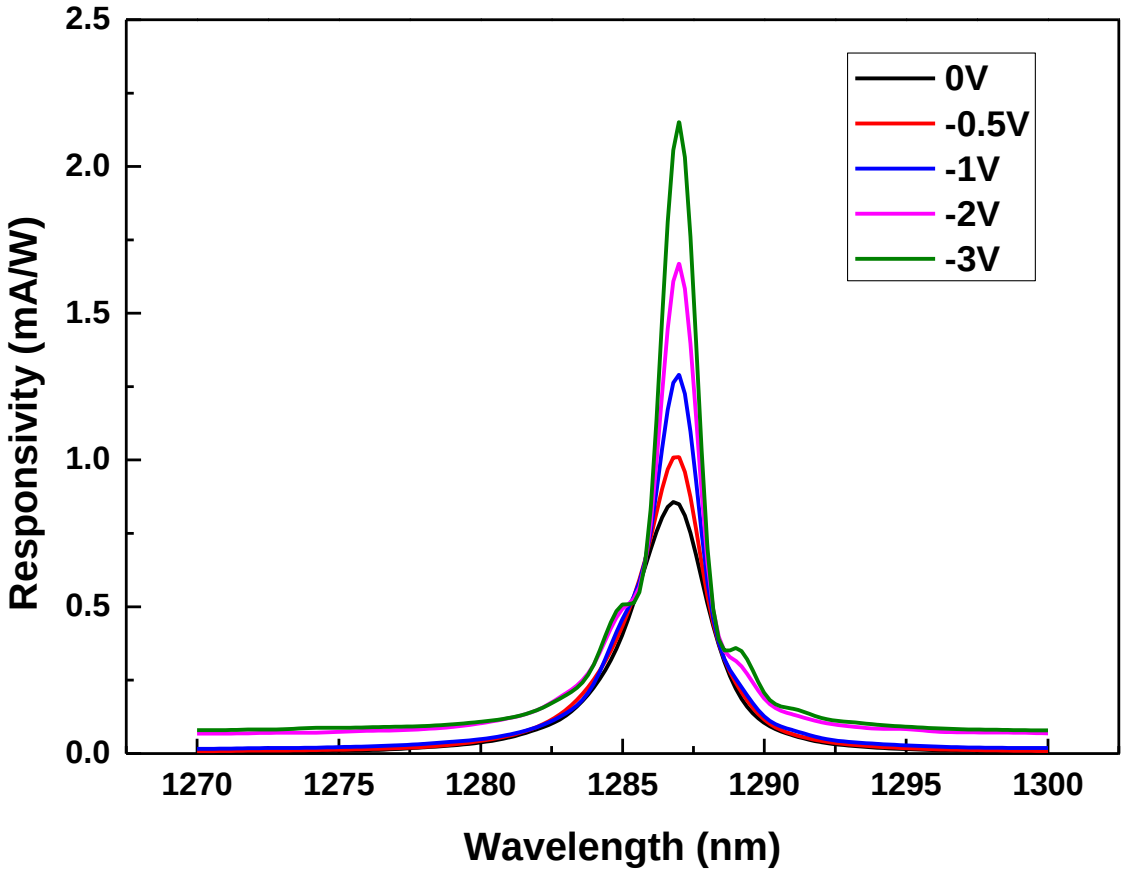

Figure 6.17: Responsivity at 300K at bias dependent

For TPC measurement, the rise time and decay time of the photodetector are shown in Fig.6.18. The pattern rise and decay time of the detector is exactly following the PL peak energy without top DBR as shown in Fig.6.12. This is because there is a drop of rise and decay time between T=50K to T=75K, that correlate with Pl measurement. The decay time is observed to be 49.1ns and the rise time is 3.56ns that correlate to 98MHz at room temperature operation. At

room temperature, the detectivity and NEP is calculated to be the 2.71 x 10^9 $\sqrt{Hz}/W$ and 1.05 x $10^{-9}W/\sqrt{Hz}$.

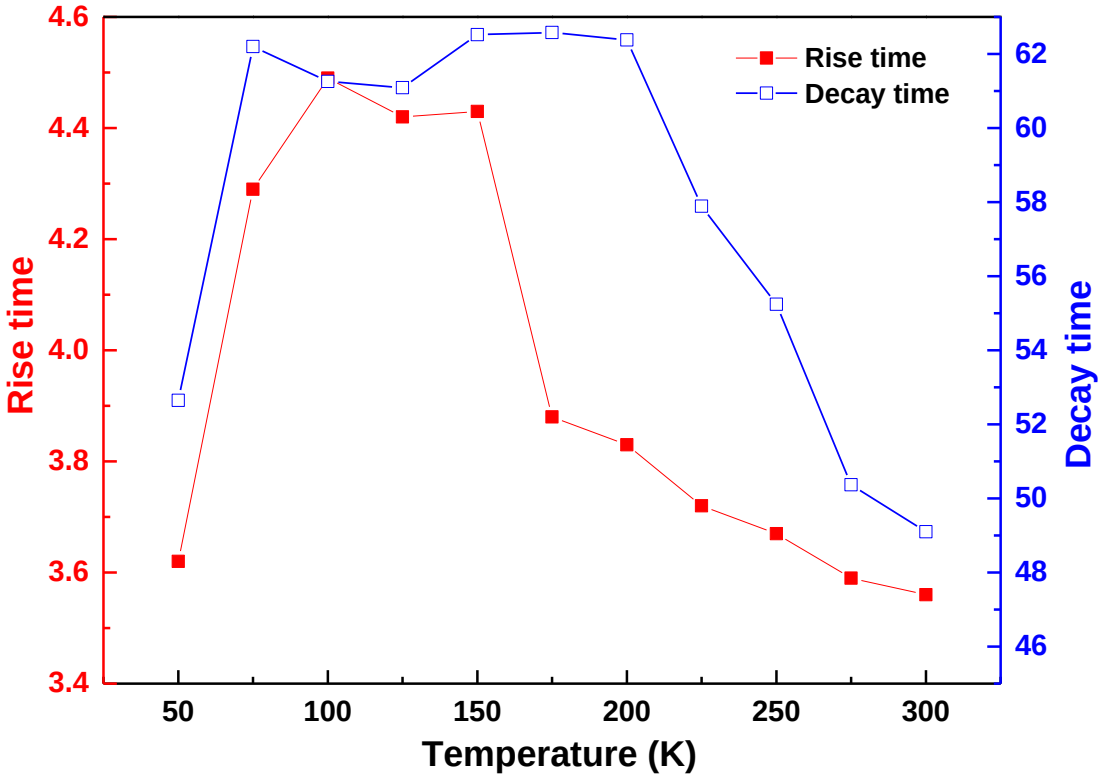

Figure 6.18: Rise and decay time at temperature dependence

6.6 Summary

The avalanche vertical cavity enhanced photodetector based on a dilute nitride GaInNAs/GaAs multi- quantum-well structure operating near 1.3μm has been demonstrated. PL measurements were performed on structures with and without top DBR to determine any deviation of the optical signal between 50K and 300K.The S-shape is observed in the GaInNAs material that indicate a defects near the conduction band causing excitons to become localised at very low temperature. An oscillation of conductance is observed during I-V measurement under optical power indicate the sample has very good electron confinement in quantum wells even at room temperature. The sample shows very low responsivity of 2.15mA/W, detectivity of 2.71 x 10^9 $\sqrt{Hz}/W$, NEP of 1.05 x $10^{-9}W/\sqrt{Hz}$ and corresponding bandwidth at 98MHz for room

temperature operation. The performance of the sample however is not as good as previous samples as described in chapter 5. Hence, further work is required on this sample to examine the oscillation and Ohmic behaviour of the device. The new fabrication step need to be done for p and n contact where they should be placed exactly on the p and n doped layer as in the sample structure.

References

1. J. L. Moll, Physics of Semiconductors, New York, McGraw-Hill, (1964)
2. X. Sun, J. Hsu, X.G. Zheng, J. C. Campbell, and A. L. Holmes, Jr., IEEE Photon. Technol. Lett., 5, 681 (2002)
3. K. A. Anselm, H. Nie, C. Hu, C. Lenox, P. Yuan, G. Kinsey, J. C. Campbell, and B. G. Streetman, Performance of Thin Separate Absorption, Charge, and Multiplication Avalanche Photodiodes, IEEE Journal of Quantum Electronics, 34, 3 (1998)
4. P. Yuan, C. C. Hansing, K. A. Anselm, C. V. Lenox, H. Nie, A. L. Holmes, Jr., B. G. Streetman and J. C. Campbell, Impact Ionization Characteristics of III–V Semiconductors for a Wide Range of Multiplication Region Thicknesses, IEEE Journal of Quantum Electronics, 36, 2 (2000)
5. P. Yuan, S. Wang, X. Sun, X. G. Zheng, A. L. Holmes, Jr., and J. C. Campbell, IEEE Photon. Technol. Lett., 10, 1370 (2000)
6. P. J. Ker, J. P. R. David and C. H. Tan, Optics Express, 28, 29568 (2012)
7. S. Xie and C. H Tan, IEEE J. of Quantum Electron., Nov. (2011)
8. S. Wang, R. Sidhu, X. G. Zheng, X. Li, X. Sun, A. L. Holmes, Jr., and J. C. Campbell, IEEE Photon. Technol. Lett., 2, 1346 (2001)
9. X. Zheng, J. Hsu, X. Sun, J. B. Hurst, X. Li, S. Wang, A. L. Holmes, and J. C. Campbell, IEEE J. Quant. Elec., 38, 1536 (2002)
10. X. G. Zheng, X. Sun, S. Wang, P. Yuan, G. S. Kinsey, A. L. Holmes, Jr., B. G. Streetman, and J. C. Campbell, Appl. Phys. Lett., 24, 3833 (2001)
11. R. J. McIntyre, IEEE Trans. on Electron Dev., 13, 164 (1966)
12. T. P. Pearsall and M. A. Pollack, Academic Press, Inc. 22, 173 (1985)
13. C. Groves, R. Ghin, J. P. R. David, and G. J. Rees, Temperature Dependence of Impact Ionization in GaAs, IEEE Transactions on Electron Devices, Vol. 50, 10, (2003)
14. Yasser M. El-Batawy and M. Jamal Deen, IEEE Transactions on Electron Devices, 50, 3 (2003)
15. X. Sun, Doctor of Philosophy: The University of Texas at Austin (2002)
16. Yasser M. El-Batawy and M. Jamal Deen,, IEEE Transactions on Electron Devices, 52, 3 (2005)
17. http://www.simwindows.com

CHAPTER 7

Conclusion and Future Work

This thesis is aimed at developing and demonstrating the performance of a vertical cavity enhanced photodetector for operation at room temperature. The work is focused on the main parameters of the photodetector such as quantum efficiency, selectivity, sensitivty, Noise Equivalent Power (NEP), and possible gain at room temperature operation. The active material used in this thesis is the quaternary dilute nitride which can be lattice matched to the GaAs substrate. The tunable selectivity is anticipated during the development of the VCE photodetector equipped to perform as tunable receiver. The photodetector structures reported in this thesis are entirely surface illuminated.

The p-i-n Multi Quantum Wells (MQWs) GaInNAs/GaAs based photodetector performance is compared between two structures with differing number of QWs. The temperature dependence of photoluminescence measurement is carried out where the S-shape behaviour is observed for the 10QW and the 20 QW samples at low temperature. The origin of this S-shape is due to the large number of defects, impurities and structural compositions near the conduction band, causing excitons to become localised. The photocurrent measurements are performed at a bias of -5V where the 20 QW sample produces a maximum quantum efficiency (QE) of 80.3%. This is the highest QE ever reported for operation at 1.0μm wavelength using the quaternary GaInNAs material. The dark current of the 20 QW sample is much lower compared to the 10 QW sample. This is due to the higher number of QWs used to achieve a longer intrinsic depletion length, hence contributing to a higher resistance, affecting the carriers passing through them. A higher QW number in the intrinsic region also will create traps in quantum wells which will reduce the response time. Both devices reached current saturation at -6V bias, limiting the operation of the photodetector. Transient photoconductivity measurements gave the best temperature to operate both devices, however the performance of both devices shows a

comparable sensitivity with that of the other commercial photodetectors at room temperature operation even at a larger diameter and area. A wider intrinsic region can increase the detectivity of the device due to more absorption and produces low noise, but it will reduce the speed of photodetector. The trade-off between speed and efficiency is important in making a reliable photodetector.

The VCE photodetector using GaInNAs/GaAs based material gives an overall QE of 67% with an internal gain of 1.55. The TPC performance for the smaller device shows that the speed of laser excitation is important to compensate with the transit time of the device material. The mismatch between cavity peak and absorption peak is crucial in order to enhance more the absorption and for temperature dependent applications. The growth quality of the Distributed Bragg reflector (DBR) mirrors is also important in order to achieve great selectivity and possible gain in the intrinsic region. The choice of an undoped top DBR is good for carrier transport but not quite suitable for temperature dependent applications.

The use of the Transmission Matrix method is important when designing the DBR mirrors. The addition of the temperature dependence parameter for layer material to help provide tunable selectivity, combined with the alignment of the peak cavity DBR resonance and peak energy absorption region, are amongst the essential elements to be considered when a photodetector is to operate at room temperature. The temperature dependence of the absorption region also needs to be taken into account while designing the DBRs as the thickness layer of the DBRs needs to be customised according to the temperature and bandgap of the absorption region.

The selection of GaNAs as the material for the barrier and the addition of Antimony flux during growth of the GaInNAs helped to overcome the strain issue, and improved the optical quality of the sample, where no “S-shape” behaviour was observed for the GaInNAs/GaNAs material. However, the close bandgap of the GaNAs and GaInNAs causes weak confinement of

electrons in the quantum wells, as the GaInNAs/GaNAs sample appears like a bulk material due to the well barrier height being just about 50meV in both the samples. Nevertheless, impressive gain is observed for 9QWs at really low bias, attributed to the existence of mid-gap As antisite defects (As_{Ga}) in the material which has been reported by many researchers for low temperature growth of dilute nitride material. The gain was obtained within 500meV before reaching the saturation level in the I-V measurement, and is related to the mid-bandgap of the dilute nitride material. However, less gain was observed for the 20 QW sample due to growth problems in terms of the DBR thickness and the huge mismatch between cavity resonant and absorption peak. The results from the GaInNAs/GaNAs samples have shown that the responsivity and FWHM of the responsivity have a strong temperature dependency. The incorporation of the temperature dependence of the DBR cavity at the design stage is crucial to determine the characteristic of operation of a vertical cavity device. In the case of a small mismatch between the cavity wavelength of the DBRs and the peak value of the absorption spectrum, the temperature modulation can be a solution to enhance the characteristic of devices that incorporate a vertical cavity.

The modelling and preliminary results of a VCE Avalanche photodetector are described based on the previous VCE GaInNAS/GaNAs performance. The change of parameter during the growth process has affected the performance of the sample, especially the charge layer, which is important in enhancing the electric field in the multiplication layer even at low bias. As a result, the I-V and photocurrent measurement are not showing the proper behaviour when the sample is excited with light. The sample characteristic tends to be more Ohmic than it should be. However, the oscillation was observed at room temperature when the first derivative is plotted with the number of peaks corresponding to the number of QWs. This shows that the samples have a good quantum well confinement which allows tunnelling current to occur under high field at room temperature.

One branch of further research to be taken into account is the C-V measurement of the samples which can explain the absorption coefficient of the samples and the capacitance of the device under an electrical influence, where the same measurement can be carried out for smaller mesa diameters of approximately 10μm to 100μm to observe the effect of response time. The TPC measurement could be re-taken by using a faster laser (down to femtosecond laser) to comply with the transit time of the material. Last but not least, the presence of gain at lower bias for the GaInNAs/GaNAs sample could help to explain the actual behaviour of the impact ionisation. The heating behaviour of the device which degrades the responsivity at high optical power could be extended towards looking at the carrier effect in the intrinsic region. The passivation technique could be applied to the samples to avoid the influence of the ambient temperature which can affect the device performance at both high bias voltage and optical power.

APPENDIX A

PUBLICATIONS

M.S. Nordin, F. Sarcan, M. Gunes, A. Boland-Thoms, A. Erol, and A.J. Vickers. Temporal Response of Dilute Nitride Multi-Quantum-Well Vertical Cavity Enhanced Photodetector. Journal of Electronic Materials (2017) DOI: 10.1007/s11664-017-5815-z

M.S. Nordin, F. Sarcan, A. Erol, A. Boland-Thoms & A.J. Vickers. *Response Time of Dilute Nitride MQW Vertical Cavity Enhanced Photodetectors*. Journal of Physics: Conference Series (2016) [Accepted]

F. Sarcan, **M.S. Nordin**, F. Kuruoğlu, A. Erol and A.J. Vikcers. *Characterization of temperature dependent operation of a GaInNAs-based RCEPD designed for 1.3μm*, *Superlattices and Microstructures*. Vol.102, December 2016. pp: 27–34

N. Balkan, A. Erol, F. Sarcan, L.F.F. Al-Ghuraibawi & **M.S. Nordin**. *Dilute nitride resonant cavity enhanced photodetector with internal gain for the λ ~ 1.3μm optical communications window*, *Superlattices and Microstructures*. Vol.86, October 2015. pp: 467–471

CONFERENCE PRESENTATIONS

M.S. Nordin, F. Sarcan, M. Evans, A. Erol, A. Boland-Thoms & A.J. Vickers. *GaInNAs (Sb) Multi Quantum Well Vertical Cavity Enhanced Photodetector* presented at Semiconductor and Integrated Opto-Electronics Conference, SIOE'17, Cardiff University, 31th April 2017 – 20th April 2017. (Oral)

M.S. Nordin, F. Sarcan, A. Erol, A. Boland-Thoms & A.J. Vickers. *Dilute Nitride MQW Vertical Cavity Enhanced Photodetector for 1.3μm Wavelength* presented at A Workshop on the Physics of Optoelectronic Materials and Devices, University of Essex; 27th – 28th March 2017. (Oral)

Fahrettin Sarcan, **M. Syahmi Nordin**, Furkan Kuruoğlu, Ayşe Erol & Anthony Vickers. *Design Issues and Characterization of a GaInNAs-based Resonance Cavity Enhanced Photodetector* presented at Nano Photonics and Micro/Nano Optics International Conference (NANOP) 2016, Paris, France; 7th – 9th December 2016. (Poster)

Fahrettin Sarcan, **M. Syahmi Nordin**, Ayse Erol, Anthony Vickers. *GaInNAs-based Resonance Cavity Enhanced Photodetector at Telecommunication Wavelengths* presented at Turkish Physical Society 32nd International Physics Congress 2016, Bodrum, Turkey; 6th – 9th September 2016. (Oral)

M.S. Nordin, F. Sarcan, A. Erol, A. Boland-Thoms & A.J. Vickers. *Response Time of Dilute Nitride MQW Vertical Cavity Enhanced Photodetectors* presented at 33rd International Conference on the Physics of Semiconductors (ICPS) 2016, Beijing, China; 31st July 2016 – 5th August 2016. (Oral)

M.S. Nordin, F. Sarcan, A. Erol, A. Boland-Thoms & A.J. Vickers. *Temporal Response of Dilute Nitride MQW Vertical Cavity Enhanced Photodetector* presented at 19th International Conference of Superlattices, Nanostructures and Nanodevices (ICSNN) 2016, Hong Kong; 26th – 30th July 2016. (Best Poster Award)

M.S. Nordin, N. Balkan, A. Erol, & F. Sarcan. *Design and Modelling of GaInNAs Resonant Cavity Enhanced Photodetector at λ=1.3 μm* presented at Semiconductor and Integrated Opto-Electronics Conference, SIOE'15, Cardiff University, 31st March 2015 – 2nd April 2015. (Oral)

APPENDIX B

Matlab code for resonance cavity of GaInNAs

```
% Ga1-x Inx Ny As1-y
for i=1:100;
a=32                    % Indium percentage
b=1.5                   % Nitrogen percentage
T=300                   % Temperature (K)

cAlGaAs=80              % Aluminium percentage for AlGaAs
cGaAs=0                 % Aluminium percentage for GaAs
cAlAs=100               % Aluminium percentage for AlAs

x=a/100                 % Indium concentration
y=b/100                 % Nitrogen concentration

zAlGaAs=cAlGaAs/100     % Aluminium concentration for AlGaAs
zGaAs=cGaAs/100         % Aluminium concentration for GaAs
zAlAs=cAlAs/100         % Aluminium concentration for AlAs

%%%%%%%%%%%%%%%%%%%%%%%%%% DILUTE NITRIDE BANDGAP ENERGY%%%%%%%%%%%%%%%%%%
Cnm1=2.3.*(1-x) + 1.9.*x - 4.2.*x.*(1-x)          % P. Seoung-Hwan (2004)
En1=1.7+ (3.89.*y)                                % P.J. Klar et. al. (2001)

Em1=(0.42 + 0.625.*(1-x))-(((5.8./(T+300))- (4.19./(T+271))).*10^-
4.*(T.^2).*(1-x))-((4.19E-4./(T+271)).*(T.^2))+(0.475.*(1-x).^2)
% S. Paul et. al. (1991)

E=(En1 + Em1 - (((En1-Em1).^2) + (4.*(Cnm1.^2).*y)).^0.5)./2
% W. Shan et. al. (1999,2001)

lamda=2.998E8.*6.626E-34./(E.*1.6E-19.*1E3)           % energy to wavelength
lam=lamda*1E9
lamd=round(lam*1E3)

%%%%%%%%%%%%%%%%%%%%%%%%%% REFRACTIVE INDEX %%%%%%%%%%%%%%%%%%%%%%%%%%%%%%

% C1= (0.52886 - (0.735.*zAlGaAs)).^2        % for any z < 0.36  towards GaAs
% C2= (0.30386 - (0.105.*zAlGaAs)).^2        % for any z > 0.36  towards AlAs

CAlAs= (0.30386 - (0.105.*zAlAs)).^2        % for any c > 0.36  towards AlAs
nAlAs1= (10.906 - 2.92.*zAlAs + (0.97501./(lam.^2 + CAlAs)) -
(0.002467.*((1.41.*zAlAs)+1).*(lam.^2))).^0.5
nAlAs2= ((T-273.15)-26).*(2.04 - 0.3.*zAlAs).*1E-4
nAlAs= nAlAs1+nAlAs2                        % AlAs Refractive index

CGaAs= (0.52886 - (0.735.*zGaAs)).^2        % for any c < 0.36  towards GaAs
nGaAs1= (10.906 - 2.92.*zGaAs + (0.97501./(lam.^2 + CGaAs)) -
(0.002467.*((1.41.*zGaAs)+1).*(lam.^2))).^0.5
nGaAs2= ((T-273.15)-26).*(2.04 - 0.3.*zGaAs).*1E-4
nGaAs= nGaAs1+nGaAs2                        % GaAs Refractive index

CAlGaAs= (0.30386 - (0.105.*zAlGaAs)).^2    % for any c > 0.36  towards AlAs
nAlGaAs1= (10.906 - 2.92.*zAlGaAs + (0.97501./(lam.^2 + CAlGaAs)) -
(0.002467.*((1.41.*zAlGaAs)+1).*(lam.^2))).^0.5
nAlGaAs2= ((T-273.15)-26).*(2.04 - 0.3.*zAlGaAs).*1E-4
nAlGaAs= nAlGaAs1+nAlGaAs2                  % AlGaAs Refractive index
```

```
nCavity=3.75            % refractive index of GaInNAs

dNdn=-2E-20;            % constant: differential refractive index
deln=2E18;              % change in carrier density
delN=deln*dNdn;         % change in refractive index due to change in carrier
concentration.

%%%%%%%%%%%%%%%%%%%%%% RESONANCE CAVITY %%%%%%%%%%%%%%%%%%%%%%%%%%%%%%%%%%%

n0=1;                   % refractive index of air
Pt=4;                   % number of period in the top DBR
Pb=14;                  % number of period in the bottom DBR
Pc=9;                   % number of period in the cavity
eps=8.854E-12;          % permittivity of free space by Farad/m
muo=pi*4E-7;            % permeability of free space by Henry/m
lam1=1050;              % minimum wavelength of spectrum (nm)
lam2=1550;              % maximum wavelength of spectrum (nm)
% lamd=1300;            % central wavelength(nm)
scanwid=5;              % step range(nm)

ani=0;                                          % incident angle in air
theta1=asin(n0/nGaAs*sin(ani));                 % angle in GaAs
theta2=asin(nGaAs/nAlGaAs*sin(theta1));         % angle in AlGaAs
theta3=asin(nAlGaAs/(nGaAs+delN)*sin(theta2)); % angle in GaAs (p-doped)
theta4=asin(nGaAs/nGaAs*sin(theta3));           % angle in GaAs spacer
theta5=asin(nGaAs/nCavity*sin(theta4));         % angle in cavity
theta6=asin(nCavity/nGaAs*sin(theta5));         % angle in GaAs spacer last
bottom
theta7=asin(nGaAs/(nGaAs+delN)*sin(theta6));    % angle in GaAs (n-doped)
theta8=asin(nGaAs/nAlAs*sin(theta7));           % angle in AlAs
theta9=asin(nAlAs/nGaAs*sin(theta8));           % angle in GaAs

meu0=sqrt(eps/muo)*n0*cos(ani);                  %characteristic inductance
meu1=sqrt(eps/muo)*nGaAs*cos(theta1);            %characteristic inductance
meu2=sqrt(eps/muo)*nAlGaAs*cos(theta2);          %characteristic inductance
meu3=sqrt(eps/muo)*nGaAs*cos(theta3);            %characteristic inductance
meu4=sqrt(eps/muo)*nGaAs*cos(theta4);            %characteristic inductance
meu5=sqrt(eps/muo)*nCavity*cos(theta5);          %characteristic inductance
meu6=sqrt(eps/muo)*nGaAs*cos(theta6);            %characteristic inductance
meu7=sqrt(eps/muo)*nGaAs*cos(theta7);            %characteristic inductance
meu8=sqrt(eps/muo)*nAlAs*cos(theta8);            %characteristic inductance
meu9=sqrt(eps/muo)*nGaAs*cos(theta9);            %characteristic inductance

d1=lamd/(4*nGaAs);          % thickness of GaAs layer (nm)
d2=lamd/(4*nAlGaAs);        % thickness of AlGaAs layer (nm)
d3=100;                     % thickness of GaAs (p-doped) layer (nm)
d4=13.5;                    % thickness of GaAs spacer layer (nm)
d5=7;                       % thickness of cavity layer (nm)
d6=13.5;                    % thickness of GaAs spacer last bottom layer (nm)
d7=80;                      % thickness of GaAs (n-doped)layer (nm)
d8=lamd/(4*nAlAs);          % thickness of AlAs layer (nm)
d9=lamd/(4*nGaAs);          % thickness of GaAs layer (nm)

h1=d1*cos(theta1);
h2=d2*cos(theta2);
h3=d3*cos(theta3);
h4=d4*cos(theta4);
h5=d5*cos(theta5);
h6=d6*cos(theta6);
h7=d7*cos(theta7);
```

```
h8=d8*cos(theta8);
h9=d9*cos(theta9);

% sigmam=2*pi*nm*dm*cos(thetam)/lamda
% the phase change of the beam of electromagnetic radiation traversing the
mth layer


for i=1:100;
steps=lam2-lam1;
spectrum(i)=lam1+(i-1)*scanwid;
wave=spectrum(i);
k=2*pi/wave;

M1row1=[cos(k*h1*nGaAs), j*sin(k*h1*nGaAs)/meu1];
M1row2=[j*meu1*sin(k*h1*nGaAs), cos(k*h1*nGaAs)];
M1=[M1row1;M1row2];
M2row1=[cos(k*h2*nAlGaAs), j*sin(k*h2*nAlGaAs)/meu2];
M2row2=[j*meu2*sin(k*h2*nAlGaAs), cos(k*h2*nAlGaAs)];
M2=[M2row1;M2row2];

MU=(M1*M2)^Pt;              % Top DBR characteristic matrix

M3row1=[cos(k*h3*nGaAs), j*sin(k*h3*nGaAs)/meu3];
M3row2=[j*meu3*sin(k*h3*nGaAs), cos(k*h3*nGaAs)];
M3=[M3row1;M3row2];

MDP=M3;                     % p-doped GaAs characteristic matrix

M4row1=[cos(k*h4*nGaAs), j*sin(k*h4*nGaAs)/meu4];
M4row2=[j*meu4*sin(k*h4*nGaAs), cos(k*h4*nGaAs)];
M4=[M4row1;M4row2];
M5row1=[cos(k*h5*nCavity), j*sin(k*h5*nCavity)/meu5];
M5row2=[j*meu5*sin(k*h5*nCavity), cos(k*h5*nCavity)];
M5=[M5row1;M5row2];

MC=(M4*M5)^Pc;              % Cavity and spacer characteristic matrix

M6row1=[cos(k*h6*nGaAs), j*sin(k*h6*nGaAs)/meu6];
M6row2=[j*meu6*sin(k*h6*nGaAs), cos(k*h6*nGaAs)];
M6=[M6row1;M6row2];
M7row1=[cos(k*h7*nGaAs), j*sin(k*h7*nGaAs)/meu7];
M7row2=[j*meu7*sin(k*h7*nGaAs), cos(k*h7*nGaAs)];
M7=[M7row1;M7row2];

MDN=(M6*M7);                % bottom spacer and n-doped GaAs characteristic
matrix

M8row1=[cos(k*h8*nAlAs), j*sin(k*h8*nAlAs)/meu8];
M8row2=[j*meu8*sin(k*h8*nAlAs), cos(k*h8*nAlAs)];
M8=[M8row1;M8row2];
M9row1=[cos(k*h9*nGaAs), j*sin(k*h9*nGaAs)/meu9];
M9row2=[j*meu9*sin(k*h9*nGaAs), cos(k*h9*nGaAs)];
M9=[M9row1;M9row2];

ML=(M8*M9)^Pb;              % Bottom DBR characteristic matrix

MT=(MU*MDP*MC*MDN*ML);      % Total characteristic matrix
```

```
M11=MT(1,1);
M12=MT(1,2);
M21=MT(2,1);
M22=MT(2,2);
r1(i)=(M11*meu0+M12*meu0*meu9-M21-
M22*meu9)/(M11*meu0+M12*meu0*meu9+M21+M22*meu9);
R1(i)=r1(i)*conj(r1(i));
end;

plot(spectrum,R1);
title('Reflectance spectra of GaInNAs photodetector')
xlabel('Wavelength(nm)')
ylabel('Reflectivity')
axis([lam1 lam2 0.0 1.1])
grid on
hold on
```